

The North Atlantic Ocean: A force for change at Earth's Greenhouse-Icehouse Transition



Amy Victoria Thomas-Sparkes

School of Earth & Ocean Sciences
Cardiff University

Thesis submitted in partial fulfilment of the requirements
for the degree of
Doctor of Philosophy

September 2019

Declaration

Statement 1

This thesis is being submitted in partial fulfilment of the requirements for the dress of PhD.

Signed _____.

Date _____.

Statement 2

This work has not been submitted in substance for any other degree or award at this or any other university or place of learning, nor is it being submitted concurrently for any other degree or award (outside of any formal collaboration agreement between the University and a partner organisation).

Signed _____.

Date _____.

Statement 3

I hereby give consent for my thesis, if accepted, to be available in the University's Open Access repository (or, where approved, to be available in the University's library and for inter-library loan), and for the title and summary to be made available to outside organisations, subject to the expiry of a University-approved bar on access if applicable.

Signed _____.

Date _____.

Declaration

This thesis is the result of my own independent work, except where otherwise stated, and the views expressed are my own. Other sources are acknowledged by explicit references. The thesis has not been edited by a third party beyond what is permitted by Cardiff University's Use of Third Party Editors by Research Degree Students Procedure.

Signed _____.

Date _____.

Word count _____.

(Excluding summary, acknowledgements, declarations, contents pages, appendices, tables, diagrams and figures, references, bibliography, footnotes and endnotes).

Abstract

Earth's landmark greenhouse-icehouse transition at the Eocene Oligocene Transition (EOT) is arguably one of the most important climatic events in geological history. The dominant global geochemical signature of this dramatic shift in Earth's climate (approximately 33.7 million years ago), a 1.2 - 1.5‰ increase in the stable oxygen isotope ratio ($\delta^{18}\text{O}$) of benthic foraminifera, represents a significant period of global cooling that occurred contemporaneously with the initiation of widespread Antarctic glaciation. The EOT represents the first establishment of a widespread, continental-scale, somewhat stable ice sheet on Antarctica and yet significant debate remains as to the forcing mechanism responsible for this substantial perturbation marking the end of the Eocene greenhouse world. Initiation of the step-wise shift in $\delta^{18}\text{O}$ occurred during an interval of low eccentricity and low-amplitude change in obliquity; an orbital configuration considered the ultimate trigger for glaciation at the EOT and the pacemaker for subsequent ice sheet growth. However, some other forcing mechanism(s) must have been important in conditioning the climate leading up to the EOT as these orbital configurations are found at other points in geological history where such large-scale changes in climate are absent.

The overall aim of this thesis is to explore the evolution of temperature, ice volume and ocean circulation, the interactions between these key climatic parameters and the relative importance of different forcing and feedback mechanisms across the EOT. This thesis will place particular emphasis on paleoceanographic changes that occurred in the Atlantic Ocean region across this interval and their subsequent impacts. To this end, multiple records of foraminiferal stable isotopes and trace elements, and fish teeth neodymium isotopes are presented from sediment cores largely within the Atlantic Ocean or subject to its influence at the EOT.

Findings of this thesis suggest a fascinating link between deep water formation in the North Atlantic Ocean and Antarctic ice sheet dynamics at the EOT. A new high-resolution ϵNd record derived from fossil fish teeth at ODP Site 1263 (Walvis Ridge) in the South Atlantic provides evidence for a significant strengthening of Northern Component Water (NCW), a paleo pre-cursor to North Atlantic Deep Water (NADW), at 34.7 Ma one million years prior to the onset of the EOT. The increasing influence of northern-sourced deep waters, and associated cross-hemisphere heat piracy, provided optimal conditions for landmark climate change prior to the occurrence of the orbital parameters considered to be the ultimate trigger of the EOT. From this point on, NCW played a significant role in the distribution of heat and salinity within the Atlantic Ocean basin and is likely partly responsible, along with enhanced production of Antarctic Bottom Water (AABW) due to Antarctic glaciation, for the interhemispheric temperature asymmetry documented within this thesis. Benthic foraminiferal Mg/Ca-derived bottom water temperatures from IODP Site U1406 (Newfoundland Sediment Drifts) in the North Atlantic show a much lesser degree of cooling in the high northern latitudes when compared to their southern counterparts; in line with previous evidence from records of sea surface temperature (SST).

Benthic foraminiferal trace element data from IODP Site U1406, along with ODP Site 925 (Ceara Rise) in the Equatorial Atlantic, demonstrate a regional, transient excursion in primary productivity that begins coeval with Antarctic glaciation at the EOT. Arctic Ocean continental shelves served as a nutrient-rich source fuelling the

productivity pulse in the Atlantic at the EOT when glaciation-induced sea level fall exposed organic-rich shelf sediment nutrients to weathering. This new source of bioavailable nutrients was efficiently distributed through the North Atlantic region by surface water overflows between the Greenland and Norwegian Seas and the North Atlantic causing increased primary productivity and associated export production leading to a steepening of the overall decline in $p\text{CO}_2$ and hence acting as a positive feedback on Antarctic Ice Sheet (AIS) growth.

Overall this thesis makes significant strides in clarifying the timeline of key climatic events in the Atlantic Ocean in the lead up to and across the EOT and highlights the importance of the influence of the Arctic Ocean and North Atlantic in modulating climate and ocean chemistry at the EOT.

Abbreviations

$\Delta[\text{CO}_3^{2-}]$	Carbonate saturation state
$\delta^{11}\text{B}$	Boron isotope ratio
$\delta^{13}\text{C}$	Carbon isotope ratio
$\delta^{13}\text{C}_{\text{DIC}}$	Carbon isotope ratio of dissolved inorganic carbon
$\delta^{13}\text{C}_{\text{SW}}$	Carbon isotope ratio of seawater
$\delta^{18}\text{O}$	Oxygen isotope ratio
$\delta^{18}\text{O}_{\text{SW}}$	Oxygen isotope ratio of seawater
AABW	Antarctic Bottom Water
AAIW	Antarctic Intermediate Water
ACC	Antarctic Circumpolar Current
AIS	Antarctic Ice Sheet
AMOC	Atlantic Meridional Overturning Circulation
BFAR	Benthic foraminifera accumulation rate
BWO	Bottom water oxygen
BWT	Bottom water temperature
CCD	Calcite Compensation Depth
CDW	Circumpolar Deep Water
CHUR	Chondritic Uniform Reservoir
CIE	International Commission on Illumination
DIC	Dissolved inorganic carbon
DSDP	Deep Sea Drilling Program
DSOW	Denmark Strait Overflow Water
DWBC	Deep Western Boundary Current
EAC	East Australian Current
EEOC	Early Eocene Climatic Optimum
EMIC	Intermediate Complexity Earth System Model
EOGM	Eocene Oligocene Glacial Maximum
EOT	Eocene Oligocene Transition
GSR	Greenland-Scotland Ridge
GSSP	Global Stratotype Section Point
HR-ICP-MS	High Resolution Inductively Coupled Mass Spectrometry
IODP	International Ocean Discovery Program

ISOW	Iceland-Scotland Overflow Water
ITCZ	Intertropical convergence zone
kyr	Thousand years
L*	Colour reflectance
LSW	Labrador Sea Water
Ma	Million years ago
mbsf	Metres below sea floor
mbsl	Metres below sea level
MC-ICP-MS	Multi-collector Inductively Coupled Mass Spectrometer
MECO	Middle Eocene Climatic Optimum
myr	Million years
NADW	North Atlantic Deep Water
NCW	Northern Component Water
NOC	National Oceanography Centre
ODP	Ocean Drilling Program
$p\text{CO}_2$	Atmospheric carbon dioxide
PHT	Poleward heat transport
ppb	Parts per billion
ppm	Parts per million
ppmv	Parts per million volume
PrOM	Priabonian Oxygen Isotope Maximum Event
PWO	Pore water oxygen
REE	Rare earth element
SAF	Subantarctic Front
SAMW	Subantarctic Mode Water
SEM	Scanning electron microscope
SPM	Suspended particulate matter
SST	Sea surface temperature
SWI	Sediment water interface
TISW	Tethyan-Indian Saline Water
VPDB	Vienna Pee Dee Belemnite
VSMOW	Vienna Standard Mean Ocean Water

Acknowledgements

Firstly, I would like to thank my supervisor Carrie Lear for her unwavering support and guidance during the last five years. Your patience, encouragement and belief in me has been a source of constant reassurance to me through the duration of my PhD. In my moments of self-doubt, of which there were several, you always knew what to say. You only ever made me feel confident, capable and deserving of this opportunity. I could not have wished for a better supervisor, mentor and friend. Thank you for everything, Carrie. I hope we will continue to work together in the future.

I have come to learn that a successful PhD project is underpinned by a legion of other people besides the PhD student and their supervisor without whom the entire experience would be a slower, more stressful and much less enjoyable process.

To Tina Van de Fliert, Katharina Kressig and Claire Huck – thank you for your hospitality and tutelage during my time in the MAGIC labs at Imperial College, and for your unwavering patience in the face of my questions thereafter. Thank you to Marc-Alban Millet for your guidance and teaching in the CELTIC laboratory. The help and support you have given since your arrival at Cardiff have been invaluable; my knowledge and confidence in the laboratory have benefited enormously.

The technical support I have received during my time at Cardiff has been outstanding. Thank you to Sandra Nederbragt for generating all stable isotope data. Thank you to Lindsey Owen for all your lab-based support and guidance during my time as a laboratory technician employed by the school. A huge thank you must go to Anabel Morte-Rodenas for her endless patience when providing countless hours of teaching and support in my use of the ICP-MS.

Thank you to everyone in the School of Earth & Ocean Sciences that has offered a scientific, friendly and supportive ear during the last five years. The department, but especially the 'Changing Earth and Ocean' research group, has made my PhD experience a wholly enjoyable one. I am grateful to all the office mates I have had over the course of the last five years who have shared in my highs, supported me in my lows and provided a seemingly endless supply of sweet treats. You have been wonderful friends and colleagues, and I wish you all every success in the future. A special mention must go to Elaine Mawbey who, from the moment I arrived in Cardiff, has been a source of scientific guidance, personal support and genuine friendship. I must also thank my most recent home-based office mate, Grizzly, who has kept me sane in recent months and forced me to get outside and relax at some point every day during the write up process.

To Micky and Hennie – my PhD experience would not have been the same without you both. You have been instrumental in my success during my time at Cardiff and your support means more than I can ever say. You have motivated me, inspired me and made me laugh on the most stressful of days. You are both incredible scientists and lifelong friends.

To my Grandparents, Roland and Roma, without whom this thesis would not have been possible. You have always supported me and believed in me. You have given me the best possible start to my post-PhD life and for that I will be forever grateful.

Even though neither of you will see me become Dr Amy Sparkes, I promise I will continue to make you proud.

To Andrew – the soon-to-be other Dr A. Thomas-Sparkes – your love and support knows no end. I will spend the rest of my life offering the same love and support to you. Together we can go anywhere and achieve anything.

Finally, I would like to thank my parents, Sally and Steve Sparkes. I dedicate this thesis to you. You have been a constant pillar of support, guidance and love. You have always told me I can achieve whatever I set my mind to. It is your unfailing belief in me and encouragement to believe in myself that have carried me this far. My success, now and in the future, is as much a product of your hard work as it is mine.

Table of Contents

1. Introduction	1
1.1 Cenozoic Climate	2
1.2 The Eocene Oligocene Transition	4
1.2.1 <i>The Isotope Shift: Global Cooling and Growing Ice</i>	4
1.2.2 <i>Carbon Cycle Dynamics</i>	5
1.3 Causes of the EOT	6
1.3.1 <i>Drawdown of Atmospheric Carbon Dioxide</i>	6
1.3.2 <i>Changing Ocean Gateways</i>	7
1.3.3 <i>Deep Water Formation</i>	9
1.4 Aims and Objectives	10
1.5 Thesis Outline	11
2. Materials and Methods	14
2.1 Site Selection	15
2.1.1 <i>IODP Site U1406 – Newfoundland Sediment Drifts</i>	16
2.1.1.1 <i>Setting</i>	16
2.1.1.2 <i>Chronology</i>	16
2.1.2 <i>ODP Site 925 – Ceara Rise</i>	17
2.1.2.1 <i>Setting</i>	17
2.1.2.2 <i>Chronology</i>	17
2.1.3 <i>ODP Site 1263 – Walvis Ridge</i>	17
2.1.3.1 <i>Setting</i>	17
2.1.3.2 <i>Chronology</i>	18
2.1.4 <i>ODP Site 756 – Ninety East Ridge</i>	19
2.1.4.1 <i>Setting</i>	19
2.1.4.2 <i>Chronology</i>	19
2.2 Sample Preparation	19
2.3 Benthic Foraminifera	20
2.4 Benthic Foraminiferal Stable Isotopes	21
2.4.1 <i>Oxygen Isotopes</i>	21
2.4.2 <i>Carbon Isotopes</i>	22
2.4.3 <i>Species Selection</i>	23
2.4.4 <i>Sample Cleaning for Isotope Analysis</i>	24
2.4.5 <i>Stable Isotope Sample Analysis</i>	24
2.5 Benthic Foraminiferal Trace Elements	24
2.5.1 <i>Species Selection</i>	24
2.5.2 <i>Sample Preparation</i>	25
2.5.3 <i>Sample Cleaning for Trace Element Analysis</i>	26
2.5.4 <i>Trace Element Analysis by Solution HR-ICP-MS</i>	26
2.5.5 <i>Trace Element Analysis by Laser Ablation ICP-MS</i>	27
2.6 Fish Teeth Neodymium Isotopes	29
2.6.1 <i>Sample Cleaning</i>	30
2.6.2 <i>Digestion of Basaltic Rock Standard</i>	30
2.6.3 <i>Ion Exchange Column Chromatography</i>	30
2.6.4 <i>Isotopic Analysis</i>	31
2.6.5 <i>Age Correction for ¹⁴⁷Sm to ¹⁴⁴Nd Decay</i>	32
2.7 Contributions to this Thesis	32

3. The Link between Atlantic Meridional Overturning Circulation and Antarctic Ice Sheet Dynamics across the Eocene Oligocene Transition	34
3.1 Introduction	35
3.1.1 <i>The Modern Thermohaline Circulation</i>	35
3.1.2 <i>Deep Water Formation at the EOT</i>	35
3.1.3 <i>Neodymium Isotopes</i>	40
3.1.3.1 <i>Variation in the Modern Ocean</i>	40
3.1.3.2 <i>Deep Sea Archives</i>	41
3.2 Methodology	44
3.2.1 <i>Geological Setting</i>	44
3.2.2 <i>Chronology</i>	45
3.2.3 <i>Sample Preparation and Analysis</i>	45
3.3 Results	47
3.3.1 <i>ODP Site 925 – Ceara Rise</i>	47
3.3.2 <i>ODP Site 1263 – Walvis Ridge</i>	49
3.4 Discussion	52
3.4.1 <i>ϵNd at ODP Site 925: Water Mass or Weathering?</i>	52
3.4.1.1 <i>Sources of Non-Radiogenic Weathered Material to Ceara Rise</i>	56
3.4.1.2 <i>Eccentricity-Paced Oscillations in Amazonian Weathering Flux</i>	57
3.4.2 <i>Evolution of Atlantic Ocean Circulation over Cenozoic Timescales: Landmark Change at the EOT</i>	58
3.4.2.1 <i>Strengthening of NCW Formation prior to the EOT</i>	59
3.4.2.2 <i>Glaciation-Induced ϵNd Variability from 33.8 Ma to 32.7 Ma</i>	65
3.4.2.3 <i>Renewed Intensity of NCW Formation from 32.7 Ma Onwards</i>	68
3.5 Chapter Summary	69
4. Productivity Changes across the Eocene Oligocene Transition	71
4.1 Introduction	72
4.1.1 <i>Productivity Change at the Eocene Oligocene Transition</i>	72
4.1.2 <i>Paleoproductivity Proxies</i>	74
4.1.2.1 <i>Benthic Foraminiferal Trace Elements</i>	74
4.1.2.1.1 <i>U/Ca</i>	74
4.1.2.1.2 <i>Mn/Ca</i>	75
4.2 Methodology	76
4.2.1 <i>Geological Setting</i>	76
4.2.2 <i>Chronology</i>	77
4.2.3 <i>Sample Preparation and Analysis</i>	78
4.3 Results	79
4.3.1 <i>North Atlantic</i>	79
4.3.1.1 <i>IODP Site U1406 – The Newfoundland Sediment Drifts</i>	79
4.3.1.2 <i>The Wider North Atlantic</i>	81
4.3.2 <i>Equatorial Atlantic</i>	84
4.3.2.1 <i>ODP Site 925 – Ceara Rise</i>	84

4.3.2.2 <i>The Wider Equatorial Atlantic</i>	86
4.4 Discussion	88
4.4.1 <i>Atlantic Ocean Change at the EOT</i>	88
4.4.1.1 <i>A Late Eocene Incursion of Arctic-Sourced Waters</i>	88
4.4.1.2 <i>Changing Redox Conditions at the EOT: Primary Production or Bottom Water Oxygen?</i>	88
4.4.2 <i>A Basin-Wide Atlantic Ocean Productivity Increase</i>	91
4.4.3 <i>Forcing of the Early EOGM Productivity Pulse</i>	95
4.4.3.1 <i>Glaciation-Induced Silicate Weathering</i>	95
4.4.3.2 <i>The Shelf-Nutrient Hypothesis</i>	98
4.4.4 <i>Implications for the Carbon Cycle at the EOT</i>	100
4.5 Chapter Summary	106
5. Refining Estimates of Deep Ocean Temperature Across the Eocene Oligocene Transition	107
5.1 Introduction	108
5.1.1 <i>Foraminiferal Mg/Ca</i>	108
5.1.1.1 <i>Mg/Ca-derived Paleotemperatures across the EOT</i>	109
5.1.1.2 <i>Secondary Factors on Foraminiferal Mg/Ca</i>	110
5.1.1.2.1 <i>The Carbonate Ion Hypothesis</i>	110
5.1.1.2.2 <i>Mg/Ca in Seawater</i>	111
5.1.1.2.3 <i>Diagenesis</i>	114
5.2 Methodology	116
5.2.1 <i>Geological Setting</i>	116
5.2.2 <i>Chronology</i>	117
5.2.3 <i>Sample Preparation and Analysis</i>	117
5.2.3.1 <i>Benthic Foraminiferal Stable Isotopes</i>	117
5.2.3.2 <i>Foraminiferal Trace Elements</i>	118
5.3 Results	120
5.3.1 <i>Foraminiferal Sr/Ca as an Indicator of Diagenesis</i>	120
5.3.2 <i>Foraminiferal Mg/Ca and Mn/Ca Covariance</i>	124
5.3.3 <i>Correcting for Mg/Ca_{sw}</i>	128
5.3.4 <i>Mg/Ca Change Across the EOT</i>	131
5.3 Discussion	134
5.4.1 <i>Influence of Saturation State at IODP Site U1406</i>	134
5.4.2 <i>Indian Ocean Circulation</i>	138
5.4.2.1 <i>Temperature Disparity in the Indian Ocean: The Influence of Tethyan-Sourced Waters or NCW?</i>	139
5.4.2.2 <i>A Regional Indian Ocean Warming?</i>	144
5.4.3 <i>Ice Growth at the EOT</i>	148
5.5 Chapter Summary	151
6. Synthesis	153
6.1 Major Findings	154
6.1.1 <i>Strengthening of NCW Conditioned Climate for Landmark Change at the EOT</i>	154
6.1.2 <i>A Glacially-Induced Transient Productivity Increase</i>	155
6.1.3 <i>Refined Estimates of Temperature Change at the EOT</i>	156
6.2 Implications	158
6.2.1 <i>The Chronology of the EOT</i>	158

<i>6.2.2 Climate System Feedbacks</i>	161
7. References	163
8. Appendices	202

List of Figures and Tables

Figure 1.1 $\delta^{18}\text{O}$ across the EOT and wider Cenozoic	3
Figure 2.1 Location of ocean drilling sites used in this study	15
Figure 2.2 Fossil fish teeth	29
Figure 3.1 Cenozoic ϵNd from ODP Sites 689 and 1263	37
Figure 3.2 Location of ocean drilling sites used in chapter three	44
Figure 3.3 ϵNd and $\delta^{18}\text{O}$ from ODP Site 925	48
Figure 3.4 ϵNd and $\delta^{18}\text{O}$ from ODP Site 1263	51
Figure 3.5 ϵNd across the EOT	52
Figure 3.6 ϵNd , $\delta^{18}\text{O}$, B/Ca and L^* from ODP Site 925	55
Figure 3.7 ϵNd across the EOT subdivided by ocean basin	62
Figure 3.8 $\delta^{13}\text{C}$ from the Atlantic Ocean region and ϵNd from ODP Sites 647 and 1263 across the EOT	65
Figure 4.1 Location of ocean drilling sites used in chapter four	76
Figure 4.2 Stable isotopes, Mn/Ca and U/Ca from IODP Site U1406	80
Figure 4.3 Stable isotopes and productivity proxies from the wider North Atlantic	83
Figure 4.4 Stable isotopes and U/Ca from ODP Site 925	85
Figure 4.5 Stable isotopes and productivity proxies from the wider Equatorial Atlantic	87
Figure 4.6 Stable isotopes and productivity proxies across the EOT subdivided by Atlantic Ocean region	94
Figure 4.7 Late Eocene paleogeography	99
Figure 4.8 Schematic of the phosphorus cycle	101
Figure 4.9 Stable isotopes, productivity proxies and $p\text{CO}_2$ across the EOT	104
Figure 5.1 Location of ocean drilling sites used in chapter five	116
Figure 5.2 Mg/Ca and Sr/Ca from IODP Site U1406	121
Figure 5.3 Mg/Ca and Sr/Ca from ODP Site 756	122
Figure 5.4 Mg/Ca and Sr/Ca from ODP Site 925	123
Figure 5.5 Mg/Ca and Mn/Ca from IODP Site U1406	125
Figure 5.6 LA-ICP-MS-derived Mn/Ca from IODP Site U1406	126
Figure 5.7 Mg/Ca corrected for Mn/Ca contaminant phase	127
Figure 5.8 Mg/Ca-derived BWT corrected for $\text{Mg}/\text{Ca}_{\text{sw}}$ from IODP Site U1406	128
Figure 5.9 Mg/Ca-derived BWT and SST corrected for $\text{Mg}/\text{Ca}_{\text{sw}}$ from IODP Site U1406	129
Figure 5.10 Mg/Ca-derived BWT and SST corrected for $\text{Mg}/\text{Ca}_{\text{sw}}$ from ODP Site 756	130
Figure 5.11 Mg/Ca-derived BWT and $\delta^{18}\text{O}$ from IODP Site U1406	131
Figure 5.12 Mg/Ca-derived BWT and SST from ODP Site 756	132
Figure 5.13 Mg/Ca, Li/Ca, and $\delta^{18}\text{O}$ from IODP Site U1406	135
Figure 5.14 Modelling simulation of temperature change due to Arctic gateway closure	142
Figure 5.15 $\delta^{18}\text{O}$, $\delta^{18}\text{O}_{\text{sw}}$, BWT and SST from Indian Ocean sites across the EOT	143
Figure 5.16 Mg/Ca, Li/Ca, and $\delta^{18}\text{O}$ from IODP Site 756	145
Figure 5.17 $\delta^{18}\text{O}_{\text{sw}}$ from Indian Ocean sites across the EOT	149

Figure 6.1 A summary of the EOT	160
Table 2.1 Summary of ocean drilling sites used in this study	16
Table 2.2 ODP Site 925 chronology	17
Table 2.3 ODP Site 1263 chronology	18
Table 2.4 Long term precision and accuracy for standards	27
Table 2.5 LA-ICP-MS parameters	28
Table 2.6 Contributions to work	33
Table 5.1 Calibration components used to calculate Mg/Ca _{sw} -corrected temperatures	113
Table 5.2 Values used to calculate saturation state and temperature influence at IODP Site U1406	136
Table 5.3 Values used to calculate saturation state and temperature influence at ODP Site 756	146

Chapter One

Introduction

1. Cenozoic Climate

The Cenozoic era plays host to some of the most fundamental changes in Earth's climate history. Arguably one of the most important is the Eocene-Oligocene Transition (EOT). The EOT, marking the transition from the Priabonian stage of the latest Eocene to the Rupelian stage of the earliest Oligocene, is defined as an interval of approximately 500 kyr in duration that begins before and ends after the Eocene Oligocene Boundary (EOB). This thesis will adopt the terminology laid out by Coxall and Pearson (2007). The EOT, when on the timescale of Cande and Kent (1995), is defined as the interval between 34 Ma and 33.5 Ma (all age models within this thesis are presented according to this timescale). The EOB, defined by the last stratigraphic occurrence of the planktic foraminifera family *Hantkeninidae* with its GSSP fixed at Massignano, Italy (Silva and Jenkins, 1993), is placed at 33.7 Ma according to this timescale. This boundary sits within the 200 kyr plateau that separates steps one and two of the positive excursion in $\delta^{18}\text{O}$ commonly referred to as 'the shift' (Coxall and Pearson, 2007). The interval following the isotope shift, characterised by the highest values of $\delta^{18}\text{O}$, is here referred to as the Eocene Oligocene Glacial Maximum (EOGM) following Liu *et al.* (2004) and is considered a separate interval to the previously defined EOT.

The EOT is widely regarded as one of the most dramatic perturbations of the Earth's climate system during the last 100 myr and is often referred to as the greenhouse-icehouse transition. This critical climate transition marks a period of significant climatic change between early Cenozoic warmth and a glaciated climate more akin to that of the modern (Lear *et al.* 2008) and has remained of significant interest to paleoceanographers over recent decades.

Prior to this landmark shift, early Cenozoic warmth was characterised by significantly higher atmospheric carbon dioxide concentrations ($p\text{CO}_2$) than that of today (Pagani *et al.* 2011). Global temperatures peaked during the Early Eocene Climate Optimum (EECO) (53 – 51 Ma) at around 12°C above modern (Zachos *et al.* 2008) when Antarctica was covered with temperate flora and fauna and longitudinal planetary temperature gradients were much lower. Following the EECO, Eocene temperature and $p\text{CO}_2$ underwent a long term decline (Zachos *et al.* 2001), punctuated only by

the transient high of the Middle Eocene Climatic Optimum (MECO) (c. 40 Ma (Bohaty and Zachos, 2003; Bohaty *et al.* 2009)). As shown in figure 1.1a, this long-term cooling trend culminated in the EOT. Only after the transition, in the earliest Oligocene (34 – 23 Ma) did temperature and ice volume remain within the icehouse remit of the modern, glaciated climate.

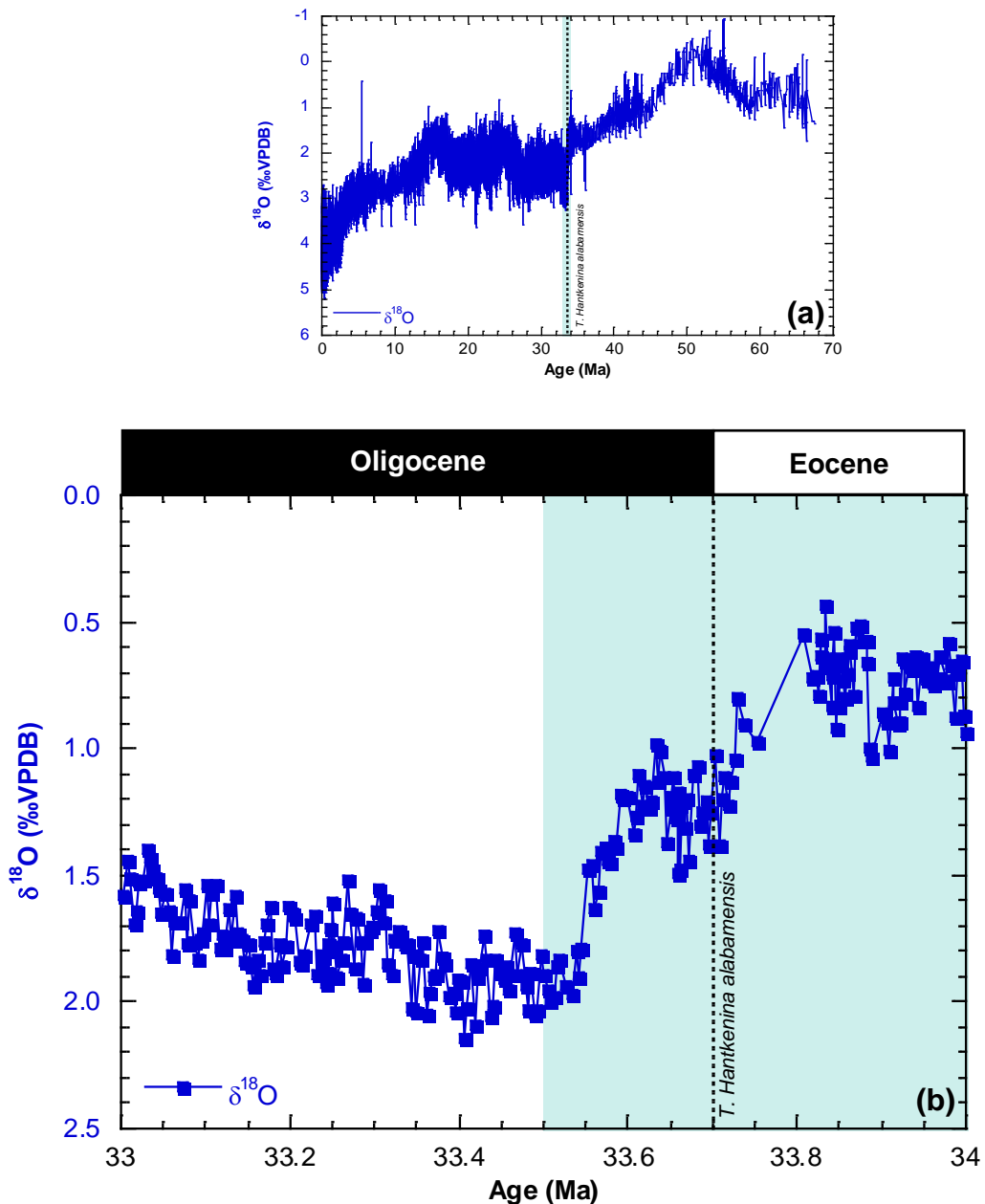


Figure 1.1 – (a) $\delta^{18}\text{O}$ across the Cenozoic from Zachos *et al.* (2008) and (b) $\delta^{18}\text{O}$ across the late Eocene and early Oligocene from Coxall *et al.* (2005). The approach taken by Zachos *et al.* (2008) is one of compiling and averaging time-equivalent data from different sites. More recently an alternative ‘megasplice’ approach has been proposed by Vleeschouwer *et al.* (2017) which uses single-site data from any given point in time spliced together to produce a longer term paleoclimate record. In both panels, pale blue shaded panels indicate the duration of the EOT. EOB marked by top of *Hantkenina alabamensis*. Age model calibrated to Cande and Kent (1995).

1.2 The Eocene Oligocene Transition

Much of the effort into better defining the nature and timing of the EOT in recent years has relied on the use of paleoclimate proxies derived from deep sea sediment cores extracted through the Ocean Drilling Program (ODP) and International Ocean Discovery Program (IODP).

1.2.1 The Isotope Shift: Global Cooling and Growing Ice

The dominant global geochemical signature of the EOT is a 1.2 - 1.5‰ increase in the stable oxygen isotope ratio ($\delta^{18}\text{O}$) that occurred in two steps of approximately 40 kyr each (Coxall *et al.* 2005; Coxall and Wilson, 2011) over the course of around 300 kyr (Liu *et al.* 2009; Mudelsee *et al.* 2014) and separated by a plateau of around 200 kyr (Coxall *et al.* 2005; Coxall and Pearson, 2007). The isotope shift terminates with the onset of the EOGM; an interval of the highest values of $\delta^{18}\text{O}$ of ~ 500 kyr in duration (Liu *et al.* 2004).

This step-wise transition occurred contemporaneously with the initiation of widespread Antarctic glaciation and an approximately 60 - 70 metre eustatic sea level fall (Kominz and Pekar, 2001; Katz *et al.* 2008; Miller *et al.* 2008; Houben *et al.* 2012). Whilst there is evidence for smaller scale ice growth in the Late Eocene (e.g. Priabonian Oxygen Isotope Maximum Event (PrOM) (Scher *et al.* 2014)), the EOT represents the first establishment of a widespread, continental-scale, somewhat stable ice sheet on Antarctica (Galeotti *et al.* 2016). Paired analysis of foraminiferal stable isotopes and trace element ratios have enabled the temperature and ice volume components of $\delta^{18}\text{O}$ to be deconvolved. It is widely believed that the first step of the isotope shift is largely due to cooling on the order of 2°C (Lear *et al.* 2008; Wade *et al.* 2012), while the second step is representative of a large increase in continental ice volume (~ 0.6‰) resulting in an ice sheet on Antarctica largely equivalent to that of the modern (Lear *et al.* 2008; Bohaty *et al.* 2012). Understanding the scale of ice growth that occurred at the EOT, under conditions warmer than today, and the behaviour of associated climate parameters is vital to understanding ice sheet stability under likely conditions of future warming.

1.2.2 Carbon Cycle Dynamics

The role of various carbon cycle parameters is of keen interest across the EOT. A significant decline in atmospheric CO₂ occurred in the lead up to the EOT. In addition, coeval with the increase in $\delta^{18}\text{O}$ an increase of $\sim 1\text{‰}$ in $\delta^{13}\text{C}$ occurred. Contemporaneous with the isotope shift across the EOT, a two-step, one kilometre-deepening of the calcite compensation depth (CCD) occurred (Coxall *et al.* 2005). The CCD is the depth in the deep ocean where the rate of carbonate accumulation equals that of dissolution. At the lysocline, the rate of carbonate dissolution rapidly increases; however, below the CCD waters are undersaturated. There have been several hypotheses proposed as to the cause of the CCD deepening across the EOT (Merico *et al.* 2008; Armstrong-McKay *et al.* 2016) including:

- i) an increase in the rate of organic carbon sequestration lead to the extraction of CO₂ from the ocean-atmosphere system by more fervent mixing in a cooler climate, causing an acceleration of the biological pump and an increased nutrient supply (Zachos *et al.* 1996; Salamy and Zachos, 1999). This drawdown of CO₂ lead to increased pH, increased deep ocean CO₃²⁻ concentration and a deepening of the CCD.
- ii) an increase in the weathering of silicate rocks, due to Antarctic glaciation, served as a sink for atmospheric CO₂ causing a drawdown of $p\text{CO}_2$, an increase in the alkalinity of the oceans and a deepening of the CCD (Zachos *et al.* 1999; Zachos and Kump, 2005; Basak and Martin, 2013).
- iii) developing thermohaline circulation and deep-basin ventilation lead to a decrease in oceanic residence time and deep-ocean acidity allowing carbonate to be preserved at greater depths and a deepening of the CCD (Miller *et al.* 2009).
- iv) the eustatic sea level fall characteristic of the EOT caused a reduction in the global shelf area and a decrease in the amount of shallow CaCO₃ burial. Simultaneously, the sea level fall lead to an increase in newly exposed previously submarine shelves, and weathering of CaCO₃ which rapidly discharged to the oceans causing an increase in the CO₃²⁻ concentration and a deepening of the CCD (Coxall *et al.* 2005; Merico *et al.* 2008; Griffith *et al.* 2011).

Carbon cycle box models have been used in attempts to identify the mechanism likely responsible for CCD deepening. However, modelling efforts have been unable to reconcile the CCD deepening with any one single forcing mechanism. It is more likely that a shift in carbonate burial from shallow to deep water along with an increase in ocean ventilation was responsible for the transient $\delta^{13}\text{C}$ perturbation and a permanent deepening of the CCD (Armstrong McKay *et al.* 2016).

1.3 Causes of the EOT

Debate remains rife within the scientific literature as to the cause of the EOT. Substantial glaciation has only occurred in geological history when one or both of the poles have been less than 1000 kilometres from a large land mass (Smith and Pickering, 2003) however, given that large parts of the Cretaceous were characterised by a non-glaciated, polar land mass (Smith *et al.* 1994), it has been suggested that a pole-based continent is a necessary, yet insufficient in isolation, precondition for the development of an 'icehouse' world (Kennett, 1977; Smith and Pickering, 2003). The initiation of the $\delta^{18}\text{O}$ step change occurred during an interval of low eccentricity and low-amplitude change in obliquity; an orbital configuration that is considered the ultimate trigger for glaciation at the EOT and the pacemaker for subsequent ice sheet growth (DeConto and Pollard, 2003a; Coxall *et al.* 2005). However, other forcing mechanism(s) must have been important in conditioning the climate, or increasing the sensitivity of the climate to astronomical forcing due to changes in key boundary conditions (Vleeschouwer *et al.* 2017) leading up to the EOT as these orbital configurations do not seem to have been notably different to patterns of obliquity and eccentricity at any other time (Coxall *et al.* 2005). Both drawdown of $p\text{CO}_2$ (DeConto and Pollard, 2003a; Pearson *et al.* 2009; Pagani *et al.* 2011) and tectonic changes in ocean gateways (Kennett, 1977) have been popularly cited as causal mechanisms. The cause of the EOT represents an unresolved knowledge gap that this study aims to contribute towards filling.

1.3.1 Drawdown of Atmospheric Carbon Dioxide

In many model simulations, when combined with the orbital configuration of the EOT, significant and persistent change in atmospheric CO_2 leads to significant cooling and

the development of large-scale continental ice sheets on Antarctica (DeConto and Pollard, 2003a; 2003b; Lefebvre *et al.* 2012; Goldner *et al.* 2014; Ladant *et al.* 2014; Hutchinson *et al.* 2018) when $p\text{CO}_2$ levels fell below a critical threshold. Constraining the timing and nature of $p\text{CO}_2$ change across the EOT is therefore crucial in deciphering the relative strength and importance of different forcing mechanisms across this crucial climate transition.

Studies using different proxies provide variable estimates of $p\text{CO}_2$ change across the EOT (Pagani *et al.* 2005; Pearson *et al.* 2009; Pagani *et al.* 2011; Heurreux and Rickaby, 2015). Alkenone-based estimates of $p\text{CO}_2$ change over a 20 myr period, from the middle Eocene to the late Oligocene, depict relatively high $p\text{CO}_2$ of between 1000 to 1500 parts per million volume (ppmv) before and during the EOT (Pagani *et al.* 2005); values between two and three times that of the modern (Pagani *et al.* 2002). This was followed by a sizeable decline in $p\text{CO}_2$ at approximately 32 Ma (Pagani *et al.* 2005). Boron isotope records of $p\text{CO}_2$ from particularly well-preserved planktonic foraminifera, *Turborotalia ampliapertura*, in a shelf/slope environment in Tanzania suggest declining $p\text{CO}_2$, from 1100 to 760 ppmv, which was seemingly coupled with global cooling and occurred in advance of the main period of ice volume increase (Pearson *et al.* 2009). This was followed by a rebound to pre-EOT $p\text{CO}_2$ values of 1150 ppmv. It is suggested that the Antarctic ice sheet (AIS) survived this return to higher $p\text{CO}_2$ levels due to the hysteresis effect, although some waning in ice extent may have occurred. A subsequent, more gradual decline in $p\text{CO}_2$, to 625 ppmv occurred, over the 500 kyr immediately following the EOT. The period of maximum ice growth was characterised by $p\text{CO}_2$ concentrations of between 450 and 1500 ppmv with a central estimate of 760 ppmv at 33.6 Ma (Pearson *et al.* 2009). However, it is worth noting that significant uncertainty remains as to the pattern and magnitude of CO_2 change across the EOT due to the sparse availability of records across this interval.

1.3.2 Changing Ocean Gateways

A sound understanding of the history of global ocean circulation patterns is required to provide a scientifically significant evaluation of the hypotheses that link the EOT, and its associated expansion of the AIS, to tectonically-driven changes in ocean

gateways. It has long been suggested that tectonically-driven opening of ocean gateways served as the predominant forcing mechanism responsible for the EOT (Kennett, 1977). Smith and Pickering (2003) state that Milankovitch forcing, $p\text{CO}_2$ and other processes only became significant after a revised ocean gateway configuration was established. Continents previously joined to Antarctica were identified as being obstructive masses until tectonic changes separated South America and Australia from Antarctica allowing the opening of Drake Passage and the Tasman Gateway, respectively (Kennett, 1977). The resultant changes in Southern Ocean circulation patterns are suggested to have had a significant influence on the initiation and expansion of the AIS.

In the early Eocene, characterised by an unglaciated Antarctica surrounded by a warm Southern Ocean, the tectonic configuration of the Southern Ocean region included South America and Australia adjoined to the Antarctic continent. Kennet (1977) suggests that at approximately 50 Ma Australia began its separation from Antarctica; the South Tasman Rise was breached at around 39 Ma and the Tasman Gateway was characterised by a shallow water connection between the southern Indian and Pacific oceans. A deep-water connection is not thought to have developed here until the EOT as the South Tasman Rise served as a barrier of some kind. It is argued that this tectonic separation thermally isolated Antarctica due to the development of an Antarctic Circumpolar Current (ACC) (Barker and Burrell, 1976). This was potentially compounded by the opening of Drake Passage between South America and Antarctica, which may have already been characterised by a shallow seaway (Barker and Burrell, 1976; Smith and Pickering, 2003). Subsequent studies loan support to the hypothesis that the Tasman Gateway prompted development of the ACC and initiation of AIS glaciation (Exon *et al.* 2001; Bijl *et al.* 2013). Exon *et al.* (2001) suggest that the opening of the Tasman Gateway barred the Eastern Australian Current (EAC), a tropical sourced current, from reaching Antarctic shores prompting a regional cooling of Antarctica and ice sheet formation. However, it has more recently been suggested that the AIS was not warmed by an EAC but rather was cooled by an equatorward Tasman current (Huber *et al.* 2004) and that opening of the Tasman Gateway actually preceded AIS glaciation by 2 myr (Stickley *et al.* 2004). Huber *et al.* (2004) suggest that deflection of the EAC by the ACC cannot be

the dominant forcing mechanism of the EOT and question the premise that changing ocean gateways coinciding with AIS glaciation was anything more than a coincidence.

Other studies suggest that the opening of Drake Passage was the driving force behind the EOT (Livermore *et al.* 2004; 2005; Eagles *et al.* 2006; Livermore *et al.* 2007). However, there is significant disagreement over the timing of the opening of Drake Passage; estimates range from the Middle Eocene (Livermore *et al.* 2007; Katz *et al.* 2011), through the Early (Livermore *et al.* 2004; 2005) and Late Oligocene (Lyle *et al.* 2007) to the Middle Miocene (Barker, 2001). Further study is required to better constrain the timing of the opening of Drake Passage. In addition, various modelling efforts have reduced the emphasis on the role played by changing ocean gateways in facilitating the EOT (e.g. DeConto and Pollard, 2003a; Lefebvre *et al.* 2012; Hill *et al.* 2013).

1.3.3 Deep Water Formation

The configuration of the thermohaline circulation has changed significantly across geological timescales (Ferreira *et al.* 2018). During the earliest Eocene the Southern Ocean and mid-latitudes were accountable for a greater proportion of deep water formation than in the modern ocean. It was not until much later that a switch to bipolar deep water formation occurred. While some studies have dated this switch to the early and middle Eocene (Hohbein *et al.* 2012; Boyle *et al.* 2017; Vahlenkamp *et al.* 2018a; 2018b) and the middle Miocene (Wright and Miller, 1996), significant evidence now exists to suggest that the formation of a proto-North Atlantic Deep Water (NADW) known as Northern Component Water (NCW) occurred around the EOT (Davies *et al.* 2001; Via and Thomas, 2006; Abelson and Erez, 2017; Coxall *et al.* 2018). Other studies have linked the changes in ocean gateways discussed above to the onset and/or intensification of deep water formation in the Atlantic Ocean (Lear and Lunt, 2016; Elsworth *et al.* 2017); although gateway configuration has been shown to be one of the largest sources of uncertainty in determining ocean circulation patterns at the EOT (Kennedy *et al.* 2019).

However, given that the resolution and spatial coverage of current records is insufficient to accurately date the onset of NCW, significant debate remains over the timing of this deep water formation. For example, much of the evidence for a middle Eocene onset stems from high latitude evidence such as drift deposits. Therefore, while the onset of NCW may date to this earlier interval, the EOT may represent a secondary phase in the evolution of northern sourced deep water formation. An intensification or strengthening of NCW may have served as a forcing or feedback mechanism at the EOT. Many studies have implicated NCW onset in a reduction of heat transport to the high latitudes of the Southern Ocean and the glaciation of Antarctica (Sijp and England, 2003; Abelson *et al.* 2008; Hutchinson *et al.* 2019). In contrast, some modelling efforts have suggested that growth of the AIS altered the distribution of heat and salt in the world's oceans and hence significantly changed patterns of ocean circulation (Goldner *et al.* 2014). In any case, the role of NCW at the EOT and its link with widespread glaciation of the Antarctic is a key area of investigation within this thesis.

1.4 Aims and Objectives

The overall aim of this thesis is to explore the evolution of temperature, ice volume and ocean circulation across the EOT and the interactions between these key climatic parameters. This is vital to facilitating understanding of the relative importance of different forcing and feedback mechanisms across this landmark climate transition. This thesis will place particular emphasis on paleoceanographic changes that occurred in the Atlantic Ocean region across this interval by addressing the following key research questions:

- i) Do changes in bottom water mass properties suggest a change in Atlantic Ocean circulation between the Late Eocene and Early Oligocene? If so, do these changes pre- or post-date growth of the Antarctic Ice Sheet?
- ii) What magnitude of bottom water temperature change is associated with the EOT at the high northern latitudes of the Atlantic Ocean? How does this change compare to cooling seen in the high latitudes of the Southern Ocean?

- iii) Was a change in the regional carbon cycle or productivity regime in the North Atlantic associated with the EOT?

These research questions will be addressed by achieving the following objectives:

- i) Develop benthic foraminiferal stable isotope and/or trace element records from IODP Site U1406 (North Atlantic), ODP Site 925 (Equatorial Atlantic), ODP Site 1263 (South Atlantic) and ODP Site 756 (Indian Ocean).
- ii) Generate high resolution records of fossil fish teeth ϵNd from ODP Site 925 and ODP Site 1263.

1.5 Thesis Outline

The methodological approach taken by this thesis is detailed in chapter two. The principle findings of this work are outlined in chapters three, four and five.

Chapter three investigates the link between deep water formation in the North Atlantic Ocean and Antarctic ice sheet dynamics at the EOT. This chapter documents an ϵNd record derived from fossil fish teeth at ODP Site 1263 (Walvis Ridge) in the South Atlantic and provides evidence for a significant strengthening of NCW, a paleo pre-cursor to NADW, shortly before the onset of the EOT at c. 34.7 Ma. This is the first record without ambiguity that shows the geochemical signature of NCW penetrating the South Atlantic prior to the EOT and hence is the first to document the evolution of NCW into a system featuring interhemispheric AMOC. This evidence suggests that the increasing influence of northern-sourced deep waters, and associated northern hemisphere heat piracy, provided optimal conditions for landmark climate change prior to the occurrence of the ultimate trigger of the Earth's greenhouse-icehouse transition; the coincidence of low eccentricity and low-amplitude change in obliquity.

Chapter four presents benthic foraminiferal trace element data from IODP Site U1406 (Newfoundland Sediment Drifts) in the North Atlantic and ODP Site 925 (Ceara Rise) in the Equatorial Atlantic. These records demonstrate a regional, transient excursion in primary productivity that begins coeval with Antarctic glaciation

at the EOT. Evidence suggests that Arctic Ocean continental shelves served as the nutrient-rich source fuelling the productivity pulse in the Atlantic at the EOT when glaciation-induced sea level fall exposed organic-rich shelf sediment nutrients to weathering. This new source of bioavailable nutrients was distributed through the North Atlantic region causing increased primary productivity and associated export production leading to a steepening of the overall decline in $p\text{CO}_2$ and acting as a positive feedback on AIS growth.

Chapter five examines new foraminiferal Mg/Ca-derived ocean temperatures from IODP Site U1406 in the North Atlantic and ODP Site 756 (Ninety East Ridge) in the Indian Ocean. This chapter recognises the advantages and pitfalls associated with this proxy and provides evidence to suggest that secondary controls can be successfully corrected for with the right approach. Mg/Ca data are corrected for manganese-rich contaminant phases, the Mg/Ca of seawater and the effect of carbonate saturation change. In applying these corrections, this thesis provides the first record of North Atlantic bottom water temperature change across the EOT. Records of sea surface temperature (SST) from this region show an absence of cooling across the EOT. Similarly the new record of bottom water temperature (BWT) at IODP Site U1406 suggests a cooling of 0.98°C supporting earlier conclusions that a transient interhemispheric temperature asymmetry occurred coeval with glaciation at the EOT (Liu *et al.* 2018) whereby BWT and SST cooled to a much greater degree in the high southern latitudes than in their northern counterparts. Onset of glaciation on Antarctica has been suggested to enhance production of Antarctic Bottom Water (AABW) and hence would enhance cooling in the high southern latitudes and diminish cooling in the North Atlantic. This effect is likely also responsible for the warming associated with the isotope shift in the Indian Ocean region.

Chapter five also provides insight into changing ocean circulation by comparative study of foraminiferal trace elements within the Indian Ocean basin. A BWT cooling of $2 - 3^\circ\text{C}$ over 400 kyr between 34.7 Ma and 34.3 Ma seen at ODP Site 756 is unparalleled at other high latitude Southern Ocean sites and likely represents a change in water mass bathing this region of the Indian Ocean; either (i) the

diminishing influence of Tethyan-Indian Saline Water (TISW) following the onset of the gradual closure of the Tethys gateway at c. 35 Ma or (ii) displacement of Southern Ocean-derived bottom water to the Indian Ocean due to newly onset NCW filling the Atlantic. In both scenarios, the replacement water mass was likely derived from the Southern Ocean; the formation of which intensified following cooling and associated glaciation of Antarctica. A 0.4°C cooling and increase in $\Delta[\text{CO}_3^{2-}]$ of approximately $20 \mu\text{mol kg}^{-1}$ is associated with the increased northern influence of this southerly-derived water mass across the isotope shift – likely akin to Subantarctic Mode Water (SAMW). These high latitude sourced cold waters carry northward an abundance of weathered nutrients from the Antarctic continent resulting in a regional pulse of primary productivity and associated increase in organic carbon burial. This may explain the lower $\Delta[\text{CO}_3^{2-}]$ response of the Indian Ocean compared to the Pacific and warrants further investigation into regional controls on CCD deepening at the EOT.

Chapter six integrates all findings and discusses their implications for current understanding of one of the most landmark climate transitions in Earth's history. In addition, potential scope for further work in light of these new findings is discussed.

Chapter Two

Materials and Methods

2.1 Site Selection

This thesis uses pelagic deep-sea sediment material retrieved as part of the Ocean Drilling Program (ODP) and International Ocean Discovery Program (IODP) from various open ocean sites around the globe (see figure 2.1 and table 2.1). Sites were chosen based on several criteria; (i) geographical location places them along a north—south transect through the Atlantic Ocean basin (ii) optimised sedimentation rate for an expanded EOT, and (iii) paleo water depth that places sites above the CCD at the EOT.

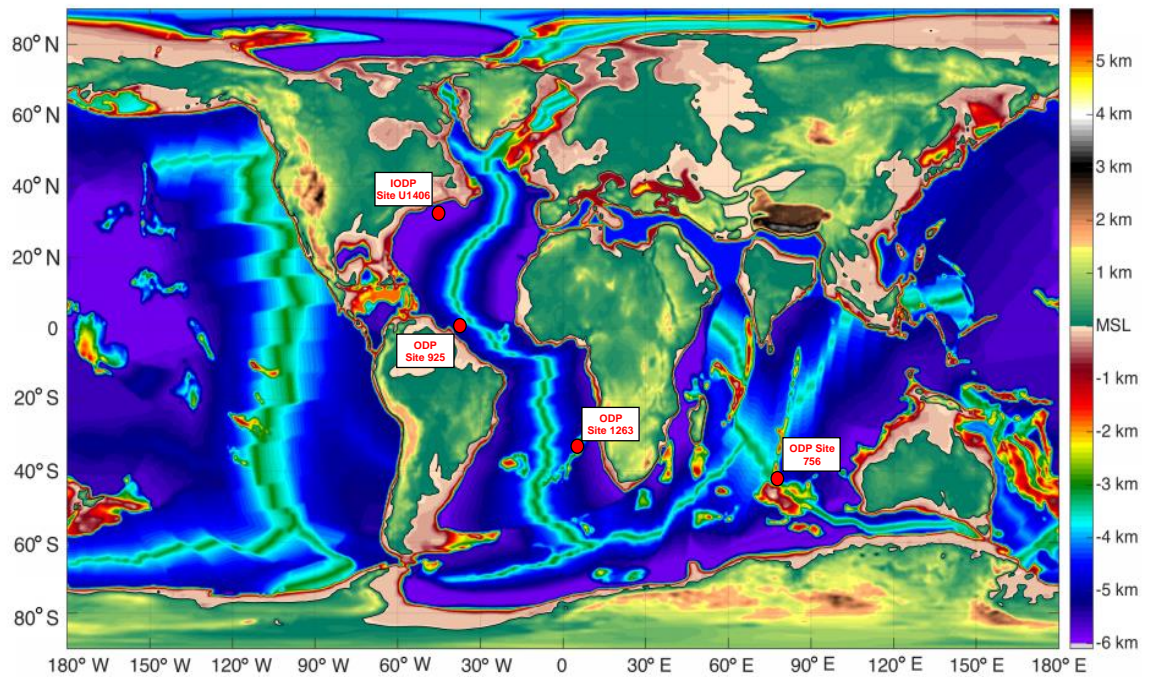


Figure 2.1 – Location of ocean drilling sites used in this study displayed on paleogeographic map from Baatsen *et al.* (2016).

ODP/IODP Expedition	Site	Ocean Basin	Latitude	Longitude	Sediment Depth (mbsf)	Modern Water Depth (m)
342	U1406 - Newfoundland Sediment Drifts	North Atlantic	40°21.0'N	51°39.0'W	187.66 - 206.48	3813
154	925 - Ceara Rise	Equatorial Atlantic	4°12.249'N	43°29.334'W	746.43 - 850.14	3042
208	1263 - Walvis Ridge	South Atlantic	28°31.98'S	2°46.77'E	69.57 - 90.28	2717
121	756 – Ninety East Ridge	Indian Ocean	27°21.330'S	87°35.805'E	113.66 – 130.60	1519

Table 2.1 – Summary of ocean drilling sites used in this study.

2.1.1 IODP Site U1406 – Newfoundland Sediment Drifts

2.1.1.1 Setting

The Newfoundland ridges (J-Anomaly Ridge and Southeast Newfoundland Ridge) lie offshore of Newfoundland, north western Canada. These plastered ridges are mantled with contourite, pelagic carbonate drift deposits (Norris *et al.* 2014). IODP Site U1406 is located in the North Atlantic Ocean on J-Anomaly Ridge placing it directly underneath the path of the Atlantic Deep Western Boundary Current (DWBC). Samples of 20 cm³ from IODP Site U1406 were taken using a combination of an extended core barrel and an advanced piston corer between 187.66 and 206.48 metres below sea floor (mbsf) at an average temporal resolution of 10 kyr but with intervals of higher resolution sampling (~ 2 – 5 kyr) across key intervals including the step-wise change in $\delta^{18}\text{O}$ and the EOGM.

2.1.1.2 Chronology

Chronology for IODP Site U1406 is based on shipboard biostratigraphic datums (Norris *et al.* 2014) and revised magnetostratigraphy (Van Peer *et al.* 2017) calibrated to the timescale of Cande and Kent (1995).

2.1.2 ODP Site 925 – Ceara Rise

2.1.2.1 Setting

ODP Site 925 is the shallowest site drilled as part of Leg 154 on Ceara Rise, an aseismic rise bounded by the Ceara abyssal plain to the west and the Amazon cone to the east, in the western equatorial Atlantic Ocean. Sediments were retrieved using a rotary core barrel. Samples of 20 cm³ from ODP Site 925 were taken between 746.43 and 850.14 mbsf at an average temporal resolution of 50 kyr.

2.1.2.2 Chronology

Chronology for ODP Site 925 is based solely on biostratigraphy as magnetostratigraphic age control was unavailable for sites collected during Leg 154. Sample ages are based on the planktonic foraminifera biostratigraphic framework presented by Pearson and Chaisson (1997). The datums presented therein have been updated to those published by Wade *et al.* (2011) calibrated to Cande and Kent (1995) as shown in table 2.2. The age model was constructed by linear interpolation between reliable biostratigraphic datums. In the absence of magnetostratigraphic age control, this represents the best age model available.

Datum	Depth (mbsf)	Age (Ma)
T <i>Turborotalia ampliapertura</i>	652.20	30.30
B <i>Paragloborotalia</i>	663.75	30.60
T <i>Pseudohastigerina naguewichiensis</i>	728.30	32.00
T <i>Hantkenina alabamensis</i>	776.65	33.70
T <i>Turborotalia cerroazulensis</i>	777.23	33.80

Table 2.2 – Biostratigraphic datums used to construct ODP Site 925 chronology. Datum depths are taken from Pearson and Chaisson (1997) and have been updated to ages presented by Wade *et al.* (2011) calibrated to Cande and Kent (1995).

2.1.3 ODP Site 1263 – Walvis Ridge

2.1.3.1 Setting

Walvis Ridge is an aseismic ridge formed by hotspot volcanism that runs from the northeast to southwest and divides the South Atlantic into two basins; the Angola and Cape Basins to the north and south, respectively (Zachos *et al.* 2004). The ridge is mostly draped with pelagic deposits that increase in thickness with increasing

proximity to the continental margin (Zachos *et al.* 2004). ODP Site 1263 sits on the north-south segment of Walvis Ridge at a water depth of 2717 mbsf making it the shallowest site drilled as part of Leg 208. Sediments were retrieved using an advanced piston corer. Samples of 40 cm³ from ODP Site 1263 were taken between 69.57 and 90.28 mbsf at an average temporal resolution of 40 kyr but with intervals of higher resolution sampling (~ 10 - 20 kyr) across key intervals including the isotope shift and the EOGM.

2.1.3.2 Chronology

Chronology for ODP Site 1263 is based on biostratigraphic and magnetostratigraphic datums (Zachos *et al.* 2004) calibrated to the timescale of Cande and Kent (1995).

These are shown in table 2.3

Datum	Depth (mbsf)	Age (Ma)
B <i>Sphenolithus ciperoensis</i>	41.25	27.55
B <i>Paragloborotalia opima</i>	52.28	30.54
B <i>Sphenolithus distentus</i>	55.29	30.32
C12n (y)	54.98	30.48
T <i>Subbotina angiporoides</i>	58.41	29.67
C12n (o)	60.10	30.94
T <i>Globigerina ampliapertura</i>	62.10	30.12
T <i>Pseudohastigerina spp</i>	62.10	32.00
T <i>Reticulofenestra umbilicus</i>	65.48	31.70
C13n (y)	74.11	33.06
T <i>Ericsonia formosa</i>	74.23	32.90
C13n (o)	78.81	33.55
Increase <i>Ericsonia obruta</i>	82.98	33.70
T <i>Turborotalia cerroazulensis</i>	85.96	33.80
T <i>Hantkenina spp</i>	92.26	33.70
T <i>Globigerinatheka index</i>	92.26	34.30
T <i>Discoaster saipanensis</i>	90.93	34.00
T <i>Globigerinatheka semiinvoluta</i>	100.63	35.30
B <i>Istmolithus recurvus</i>	102.85	36.60
T <i>Acarinina primitiva</i>	108.56	39.00
T <i>Chiasmolithus grandis</i>	107.25	37.10
B <i>Dictyococcites bisectus</i>	118.05	38.50
B <i>Dictyococcites scrippsae</i>	122.52	40.30
C19n (y)	128.06	41.26
C19n (o)	129.56	41.52

Table 2.3 – Biostratigraphic and magnetostratigraphic datums used to construct ODP Site 1263 chronology. Datum depths taken from Zachos *et al.* (2004) calibrated to Cande and Kent (1995).

2.1.4 ODP Site 756 – Ninety East Ridge

2.1.4.1 Setting

ODP Site 756 lies on Ninetyeast Ridge in the eastern Indian Ocean. Ninetyeast Ridge is a 5000 km north-south lineament stretching from 10°N to 34°S (Pierce *et al.* 1989). The 100 – 200 km wide ridge is composed of basalts that erupted onto a young, weak oceanic Indian plate in shallow waters (Zachos *et al.* 1992). Basement ages increase northward illustrating how the ridge formed near its present southern end due to the Kerguelen and Ninetyeast Ridge hotspot and gained its current south-north alignment by the northward movement of the Indian plate over the hotspot. The ridge is topped by sediments derived from the Bengal Fan. ODP Site 756 is the southernmost site drilled on Ninetyeast Ridge as part of Leg 121 in a water depth of 1519 metres. Sediments were retrieved using an extended core barrel. The EOT section at ODP Site 756 is complete and composed of nannofossil ooze; samples were taken from between 113.67 and 142.66 mbsf. These washed samples were inherited from H. Coxall, Stockholm University.

2.1.4.2 Chronology

Chronology for ODP Site 756 is based on biostratigraphic datums including planktonic foraminifera (Martina Vinco, MSc project, 2016) and nannofossils (Pierce *et al.* 1989) calibrated to the timescale of Cande and Kent (1995).

2.2 Sample Preparation

Core samples used in this study were weighed and dried in the oven overnight at 40°C. They were reweighed the next day to obtain an accurate dry bulk sediment weight. Samples were washed through a 63 µm sieve with pressurised 15 MΩ deionised water. For samples that were difficult to disaggregate additional measures were taken to ensure efficient and effective sample washing. Some samples were soaked in a buffered sodium hexametaphosphate solution (calgon) prior to washing.

The coarse >63 µm fraction was subsequently dried in the oven and weighed before being picked for benthic foraminifera. The <63 µm fraction was washed into sample bags and, once material was settled and dried, this fine fraction material was also

weighed. The percent coarse of each sample was calculated using the weights of the $>63\ \mu\text{m}$ and $<63\ \mu\text{m}$ fractions.

Benthic foraminifera required for stable isotope and trace element analyses were picked from the 250 – 355 μm size fraction. Each sample was crushed in 18 M Ω deionised water to open individual foraminifer chambers and facilitate effective cleaning. Any visible contaminants were removed with a fine paintbrush. Once the sample fragments were homogenised, they were separated into two 500 μl acid-cleaned centrifuge tubes; one portion for stable isotope analysis and the other for trace element analysis.

2.3 Benthic Foraminifera

The main paleoceanographic archive employed in the toolkit of this thesis is that of foraminifera. Foraminifera are ubiquitous, single-celled protists composed of calcium carbonate (CaCO_3) tests that they precipitate themselves. Their test is formed gradually over the course of the lifespan of an individual foraminifer (varying from weeks to months in duration) and consists of sequential chambers. It is the distinct form and morphology of a foraminifer test that makes a particular species uniquely identifiable. The test forms from an internal calcification pool of minimally altered ambient seawater. Therefore, the test of any given foraminifer incorporates and preserves a geochemical signature representative of the chemical and physical conditions of the seawater in which it calcified providing a useful tool to reconstruct past oceanic and climatic variability. Foraminifera are generally subdivided into planktonic and benthic varieties; planktonic species occupy the surface and upper water column while benthic species live at the seafloor (epifaunal species) or burrowed within the top few centimetres of seafloor sediment (infaunal species). Therefore, the water depth or sediment microhabitat preferences of individual species can be used to selectively reconstruct geochemical and physical changes from specific oceanographic settings.

2.4 Benthic Foraminiferal Stable Isotopes

2.4.1 Oxygen Isotopes

Without doubt the longest established and most reputable proxy record of past climate change is that of stable oxygen isotope ratios from benthic foraminiferal calcite tests (Urey, 1947; Urey *et al.* 1951; Epstein *et al.* 1951; Epstein *et al.* 1953). It is this proxy that provides evidence of changes in continental ice volume, temperature and salinity (Chappell and Shackleton, 1986; Shackleton, 1987) based on the fractionation between ^{16}O and ^{18}O during the precipitation of carbonate and the $\delta^{18}\text{O}$ of seawater ($\delta^{18}\text{O}_{\text{sw}}$). In studies using benthic foraminiferal calcite to develop paleoceanographic records, the ratio of a sample is expressed relative to an international reference standard (Vienna Pee Dee Belemnite (VPDB)) as:

$$\delta^{18}\text{O} (\text{‰}) = \left(\frac{\left[\left(\frac{^{18}\text{O}}{^{16}\text{O}} \right)_{\text{sample}} - \left(\frac{^{18}\text{O}}{^{16}\text{O}} \right)_{\text{standard}} \right]}{\left(\frac{^{18}\text{O}}{^{16}\text{O}} \right)_{\text{standard}}} \right) \times 1000$$

Eq. 1

The two primary controls exerting influence over $\delta^{18}\text{O}$ of biogenic calcite are temperature and the $\delta^{18}\text{O}$ of the surrounding seawater ($\delta^{18}\text{O}_{\text{sw}}$). $\delta^{18}\text{O}$ of benthic foraminiferal calcite displays an inverse relationship with the temperature of the water in which it precipitates at a sensitivity of $\sim 0.23\text{‰}$ per 1°C (Bemis *et al.* 1988). The sensitivity of $\delta^{18}\text{O}$ to changes in $\delta^{18}\text{O}_{\text{sw}}$ is more straightforward in that a change in the latter causes an equal change in the former. Therefore, changes in $\delta^{18}\text{O}$ of benthic foraminifera provide a signal of both change in ice volume and BWT. $\delta^{18}\text{O}_{\text{sw}}$ records changing continental ice volume as, when polar ice sheets expand, the lighter oxygen isotope (^{16}O) is preferentially evaporated at lower latitudes and precipitated over the poles due to Rayleigh fractionation where it is stored in the ice sheet. This leaves the heavier oxygen isotope (^{18}O) at a greater relative abundance in the therefore isotopically heavier ocean.

This somewhat complex signal provided by $\delta^{18}\text{O}$ rather limits its use alone in interpreting past changes in climatic parameters (Billups and Schrag, 2003). During times of ice-free conditions, such as the Early Eocene, the record of $\delta^{18}\text{O}$ can be easily applied in the interpretation of temperature and salinity changes. However, this

is not so straightforward during times of large-scale changes in ice volume, such as the EOT. An independent proxy of either ice volume or temperature is required to deconvolve the temperature and $\delta^{18}\text{O}_{\text{sw}}$ components of $\delta^{18}\text{O}$ (Lear *et al.* 2000; Rosenthal *et al.* 2000; Martin *et al.* 2002); Mg/Ca ratios of benthic foraminifera can serve this purpose, as will be the case in this study.

2.4.2 Carbon Isotopes

The partitioning of carbon between the ocean, atmosphere and terrestrial realms exerts great influence over the $\delta^{13}\text{C}$ of the dissolved inorganic carbon (DIC) of the ocean. The terrestrial biosphere is depleted in ^{13}C ($\sim -25\text{‰}$ $\delta^{13}\text{C}$ (Park and Epstein, 1960)) due to the preferential uptake of ^{12}C during photosynthesis; breaking the bonds of this lighter isotope requires less energy. Therefore, the ocean and atmosphere tend to have increased $\delta^{13}\text{C}$ values. Any change in the flux of carbon between these individual reservoirs results in changes in the $\delta^{13}\text{C}$ signature of seawater ($\delta^{13}\text{C}_{\text{sw}}$). At any given point in the ocean the $\delta^{13}\text{C}_{\text{sw}}$ is influenced by both large-scale changes in carbon sources and sinks, and more localised factors including the balance between photosynthesis and respiration, air-sea exchange, and the mixing of water masses with different $\delta^{13}\text{C}_{\text{sw}}$. In studies using foraminiferal calcite to develop paleoceanographic records, the ratio is expressed relative to an international reference standard (Vienna Pee Dee Belemnite (VPDB)) as:

$$\delta^{13}\text{C} (\text{‰}) = \left(\frac{\left[\left(\frac{^{13}\text{C}}{^{12}\text{C}} \right)_{\text{sample}} - \left(\frac{^{13}\text{C}}{^{12}\text{C}} \right)_{\text{standard}} \right]}{\left(\frac{^{13}\text{C}}{^{12}\text{C}} \right)_{\text{standard}}} \right) \times 1000$$

Eq. 2

This $\delta^{13}\text{C}_{\text{sw}}$ signature is incorporated into the tests of foraminifera in a similar manner to $\delta^{18}\text{O}$. However, foraminiferal $\delta^{13}\text{C}$ is not at precise equilibrium with $\delta^{13}\text{C}_{\text{DIC}}$ as they calcify from an internal pool. The pH, DIC concentration and $\delta^{13}\text{C}_{\text{DIC}}$ of this microenvironment can all be different from that of the surrounding ambient seawater (Spero *et al.* 1997; Zeebe *et al.* 1999). Given the relatively rapid rate of CaCO_3 precipitation, abiotic kinetic fractionation also occurs causing an enrichment of test $\delta^{13}\text{C}$ relative to seawater (McConnaughey, 1989). In addition, biological vital effects and microhabitat preferences can cause species-specific offsets from $\delta^{13}\text{C}_{\text{DIC}}$. These

secondary factors need to be considered when making interpretations about paleoecological or paleoceanographic changes using foraminiferal $\delta^{13}\text{C}$.

A critical component governing the $\delta^{13}\text{C}_{\text{sw}}$ at a regional scale is the balance between photosynthesis and respiration. A $\delta^{13}\text{C}_{\text{sw}}$ profile common around the world's ocean is one of low DIC and high $\delta^{13}\text{C}_{\text{DIC}}$ in the surface ocean and the reverse with depth due to the dominance of photosynthesis in the photic zone and respiration of organic matter at the seafloor. This gradient will become stronger or weaker dependent on the efficiency of the biological pump. For example, should the rate of photosynthesis in surface waters increase due to higher primary productivity, $\delta^{13}\text{C}_{\text{sw}}$ in these waters increases because of the preferential biological fixation of ^{12}C over ^{13}C . Simultaneously, bottom water $\delta^{13}\text{C}_{\text{sw}}$ decreases as a result of the remineralisation of an increased flux of organic matter to the seafloor. Thus, the gradient between the $\delta^{13}\text{C}$ of planktonic (surface or near-surface dwellers) and benthic (seafloor dwelling) foraminifera have been used to provide insights into paleoproductivity changes in various regions of the world's oceans (e.g. Zachos *et al.* 1999).

Mixing of different water masses is an additional influence on $\delta^{13}\text{C}_{\text{sw}}$. In the modern ocean, deep water forms in the high latitudes where surface waters cool and sink. These deep waters obtain their initial $\delta^{13}\text{C}$ signature from the surface waters in the area of sinking, which reflects both biological and air-sea exchange processes (Lynch-Stieglitz *et al.* 1995). These signatures can be further modified by the biological pump as the water masses move around the thermohaline circulation system. This leads to a disparity in $\delta^{13}\text{C}$ of deep waters around the world; nutrient-poor NADW has higher $\delta^{13}\text{C}$ than nutrient-rich AABW. Subsequent mixing of these water masses around the thermohaline circulation results in a heterogeneous pattern of $\delta^{13}\text{C}$ around the globe.

2.4.3 Species Selection

In this thesis, two different species of benthic foraminifera are used to generate stable isotopes. *Cibicidoides* species are a popular choice for the production of stable isotope data. They more accurately record the stable isotope value of the seawater

and are reliably consistent in their deviation from equilibrium values (Katz *et al.* 2003). *Oridorsalis umbonatus* is a popular choice for the production of paleoclimate data as it has a wide geographic distribution allowing easy inter-site comparison. In addition, *Oridorsalis umbonatus* is very easily identifiable thus avoiding confusion with similar morphotypes. Taxonomic identification was aided by use of reliable reference material (Pearson *et al.* 2006; Holbourn *et al.* 2013) and the author's attendance at a Natural Environment Research Council (NERC) short course in Cenozoic planktonic foraminifera taxonomy (Natural History Museum, London, November 2015).

2.4.4 Sample Cleaning for Isotope Analysis

Benthic foraminifera were soaked in 300 μ l of 3% hydrogen peroxide for 30 minutes in order to oxidise any organic material. All samples were then subjected to the clay removal step from the cleaning protocol of Boyle and Keigwin (1985). Samples were repeatedly ultrasonicated in both 18 M Ω deionised water and methanol to remove any clay fragments inside the test.

2.4.5 Stable isotope Sample Analysis

Benthic foraminiferal samples were analysed at several institutions; including Cardiff University on a ThermoFinnigan MAT252 with online sample preparation by an automated Kiel II carbonate device, the National Oceanography Centre (NOC) in Southampton and Stockholm University. Analytical error for the IODP Site U1406 data set, based on repeat analysis of in-house standard GS1, isotopically similar to NBS-19, is 0.03‰ for $\delta^{18}\text{O}$ and 0.04‰ for $\delta^{13}\text{C}$. Analytical error for the ODP Site 925 data set, based on repeat analysis of standard NBS-19 is 0.04‰ for $\delta^{18}\text{O}$ and 0.02‰ for $\delta^{13}\text{C}$. Analytical error for the ODP Site 1263 data set, based on repeat analysis of standard BCT63 is 0.029‰ for $\delta^{18}\text{O}$ and 0.013‰ for $\delta^{13}\text{C}$.

2.5 Benthic Foraminiferal Trace Elements

2.5.1 Species Selection

In this thesis, several different species of benthic foraminifera are used to generate trace element data. *Oridorsalis umbonatus* is a popular choice for the production of paleoclimate data as it has a wide geographic distribution allowing easy inter-site comparison; indeed, this species was used to generate geochemical data from

multiple sites in this study. The infaunal habitat of *Oridorsalis umbonatus* makes it far less sensitive to changes in bottom water saturation state (Mawbey and Lear, 2013). *Cibicidoides havanensis* was also chosen for the generation of trace element data. This epifaunal species complements the use of *Oridorsalis umbonatus* perfectly as it is well suited to monitoring changes in bottom water saturation state; its B/Ca values are commonly fourfold greater than those of *Oridorsalis umbonatus* (Yu and Elderfield, 2007). *Oridorsalis umbonatus* is extant meaning that core-top calibrations can be applied, and Mg/Ca-derived bottom water temperatures generated. It is worth noting that the application of modern, core-top calibrations to Cenozoic aged sediments relies on the uniformitarianism principle; that the past relationship between foraminiferal Mg/Ca and temperature has remained unchanged through time. Should this assumption be false, greater uncertainty is associated with the estimates of absolute temperature generated. However, less uncertainty is associated with the interpretation of relative temperature changes over shorter timescales.

2.5.2 Sample Preservation

An important consideration when analysing foraminiferal calcite for both stable isotope and trace element composition is whether the primary signal has been effectively preserved or whether the calcite has been subjected to diagenetic effects that may have caused overprinting of that primary signal. Post-mortem alterations to the primary geochemical signal can occur in a number of ways that are discussed in more detail in the introduction to chapter five of this thesis. The most effective way to reduce the impact of post-mortem alteration is to select clay-rich sediment sections where primary calcite is best preserved; the reduced permeability of clays reduces the impact of diagenesis on test calcite (Pearson *et al.* 2001). However, these so-called 'glassy' foraminifer tests (so-called because of their translucent appearance under a light microscope) are rare in open ocean settings and geochemical records from foraminiferal calcite more commonly stem from recrystallised tests.

Intense scrutiny of test microstructure in images generated by scanning electron microscopy (SEM) is one of the most effective ways to evaluate whether a foraminifer test remains unaltered by diagenetic processes. However, even a standard light microscope is sufficient to show some signs of diagenetic alteration. Of the samples used in this thesis, foraminifera from both ODP Site 925 and ODP Site

756 could be considered 'frosty' in appearance. This is not surprising given the significant burial depth of the EOT section at ODP Site 925 (c. 750 mbsf). Samples from IODP Site U1406 were much better preserved and seem much closer to 'glassy' in appearance. Significant consideration is given to foraminiferal preservation in chapter five of this thesis when interpreting paleotemperature change across the EOT.

2.5.3 Sample Cleaning for Trace Element Analysis

Samples were cleaned according to a modified version of the four-step cleaning protocol outlined in Boyle and Keigwin (1985). Steps include:

- i. Clay removal by repeated ultrasonication in 18 M Ω deionised water and methanol
- ii. Reduction of metal oxides using a buffered solution of hydrous hydrazine and citric acid in ammonia solution
- iii. Oxidation of organic matter using hydrogen peroxide in sodium hydroxide solution
- iv. Acid leach using Optima ultra-clean 0.02 M nitric acid

A detailed version of this cleaning protocol can be found in appendix 1.

2.5.4 Trace Element Analysis by Solution HR-ICP-MS

Following completion of the cleaning protocol, samples were dissolved in 120 μ l of Optima ultra-clean 0.065 M nitric acid with the aid of a vortex mixer. 10 μ l and 100 μ l aliquots of the dissolved samples were extracted into new acid-cleaned 500 μ l centrifuge tubes for calcium and trace element analysis respectively. All analyses were carried out using a Thermo Element XR HR-ICP-MS in the CELTIC laboratory at Cardiff University.

190 μ l of Optima ultra-clean 0.5 M nitric acid was added to the 10 μ l portion designated for calcium analysis. Each sample's calcium concentration was determined by comparing their intensity counts (drift- and blank-corrected) of ^{43}Ca to that of an in-house analytical standard, MCS-B. In-house standards were made gravimetrically using single element standards from Greyhound Chromatography and Allied Chemicals.

250 µl of Optima ultra-clean 0.5 M nitric acid was added to the 100 µl portion designated for trace element analysis. Each sample was followed by an MCS-B standard of equivalent ^{43}Ca concentration to counter matrix effects. Intensity counts are recorded for the following elements: ^6Li , ^7Li , ^{11}B , ^{24}Mg , ^{25}Mg , ^{27}Al , ^{43}Ca , ^{46}Ca , ^{48}Ca , ^{55}Mn , ^{87}Sr , ^{88}Sr , ^{111}Cd , ^{138}Ba , ^{146}Nd and ^{238}U . Samples with a boron intensity signal of less than five times that of the analytical blank were disregarded in all further analysis and interpretation of their B/Ca ratio. Elemental ratios were calculated using blank-corrected intensity counts (by subtraction of the intensity count of the last analytical blank in the sequence) of the sample and its matrix-matched standard counterpart.

At the start and end of each analytical run, two independent in-house consistency standards, CS1 and CS2 (also compiled from single element standards from Greyhound Chromatography and Allied Chemicals), were analysed against MCS-B to allow calculation of the long-term precision and accuracy of each element. Analytical precision and external reproducibility are shown in table 2.4.

	CS1		CS2	
	Precision (RSD)	Accuracy (%)	Precision (RSD)	Accuracy (%)
Mg/Ca	1.02	0.52	0.95	0.60
Li/Ca	1.60	0.08	1.78	0.46
Sr/Ca	1.09	0.58	0.73	0.31
U/Ca	2.71	1.30	2.11	1.75
Mn/Ca	1.84	1.42	1.72	0.37
B/Ca	7.24	11.51	2.20	0.21
Fe/Ca	3.29	1.40	2.09	1.31

Table 2.4 – Long term precision and accuracy for standards CS1 and CS2 measured by HR-ICP-MS over the course of this study.

2.5.5 Sample Analysis by Laser Ablation ICP-MS

Laser ablation ICP-MS (LA-ICP-MS) allows the development of foraminiferal trace element records of high spatial resolution. In this study, specimens of benthic foraminifera were mounted on double-sided carbon tape on glass slides in the sample cell of an ArF excimer (193 nm) LA-system with dual-volume laser ablation cell (RESOLUTION S-155, Australian Scientific Instruments) coupled to the Thermo

Element XR HR-ICP-MS in the CELTIC laboratory at Cardiff University. Prior to analysis, specimens were not subjected to the cleaning protocol outlined in section 2.5.2 of this chapter as, due to the very nature of laser ablation techniques and the aims of this method, not only are contaminant phases easily identifiable, but their identification is desired.

Optimal laser ablation parameters are those that maximise the spatial resolution of the depth profile through a test wall. The ideal parameters would be a fluence and repetition rate low enough to ablate only a small amount of test material per pulse and yet generate a sufficient signal. These parameters were selected by testing various fluence settings, spot sizes and repetition rates. Ultimately, the parameters selected are shown in table 2.5. In the interest of a statistically robust method, six different spots on each of six specimens per sample were ablated (Nairn, 2018). Each spot is placed in the centre of a different chamber of the foraminifer. Geochemical heterogeneity exists within a given foraminifer test and also between different foraminifer tests from the same sample. This heterogeneity is masked in a homogenised sample analysed by solution-based HR-ICP-MS. The idea of generating profiles from six different spots on six different foraminifera is to obtain a statistically representative trace element to calcium ratio that can be compared to the solution-based value or, in the case of Mg/Ca, be used to generate a paleotemperature for a given sample. In this thesis, given the findings of the LA-ICP-MS work, the Mg/Ca values generated by laser ablation were not used for the calculation of paleotemperatures.

The NIST SRM 610 standard was measured after each specimen and the NIST SRM 612 standard was measured at the beginning and end of every analytical sequence. The latter was calibrated using NIST SRM 610 for external reproducibility. The precision of measurements carried out for this study is 1.58% for Mg/Ca.

	Sample	Standard
Fluence (Jcm⁻²)	3.0	4.5
Spot Size (µm)	50	64
Repetition Rate (Hz)	2	4

Table 2.5 – Parameters chosen for trace element analysis of benthic foraminifera using LA-ICP-MS.

Data reduction was conducted according to the long-established protocol of Longerich *et al.* (1996) whereby blank corrected element counts were calculated for both standard and individual foraminiferal sample spots by the subtraction of mean background intensity counts from the mean gross intensity counts of each element. Analysis of bracketing NIST SRM 610 standards allowed for linear correction of instrumental drift. Ablation profiles were normalised to ^{43}Ca as means of an internal standard, which corrects for any differences in the relative yield of ablation between samples. Mg/Ca ratios representative of each of the six spots on each of six specimens per sample was developed by calculating a mean Mg/Ca value for the time interval covered by every spot on every specimen in a sample. Each profile was given equal weighting in the calculation of this mean value. These corrected, integrated ratios were then converted to mmolmol^{-1} using known concentrations of trace elements in the standard NIST SRM 610 (GeoRem – Jochum *et al.* 2011).

2.6 Fish Teeth Neodymium Isotopes

An introduction to neodymium (Nd) isotopes is given in the introduction to chapter three of this thesis along with a discussion of the sources of Nd to the sediment and the need to consider these sources when interpreting Nd isotope data. Sediment samples used in this study were prepared according to the protocol outlined in section 2.2 of this chapter. Fossil fish teeth were picked from the $>63\ \mu\text{m}$ size fraction. An image of fish teeth analysed in this study are shown in figure 2.2.



Figure 2.2 – Example of fossil fish teeth analysed for neodymium isotope content in this study. Teeth were picked from the $>63\ \mu\text{m}$ fraction of sediment.

2.6.1 Sample Cleaning

Samples were cleaned according to a modified version of the four-step cleaning protocol outlined in Boyle and Keigwin (1985). Steps include:

- i. Clay removal by repeated ultrasonication in 18 M Ω deionised water and methanol
- ii. Reduction of metal oxides using buffered solution of hydrous hydrazine and citric acid in ammonia solution
- iii. Oxidation of organic matter using hydrogen peroxide in sodium hydroxide solution
- iv. Acid leach using Optima ultra-clean 0.02 M nitric acid

A detailed version of this cleaning protocol can be found in the appendix 1.

2.6.2 Digestion of Basaltic Rock Standard

100 μ g of BCR-2, a basaltic rock standard containing 28.26 μ g/g Nd (Jochum *et al.* 2016), was digested in a mixture of 300 μ l of concentrated HNO₃ and 150 drops of HF before being refluxed on the hotplate at 90°C for 48 hours. The standard was then evaporated at 120°C. Once dry, 600 μ l of HNO₃ was added and evaporated three times. Once dry, 5 ml of concentrated HCl was added before being evaporated. The standard was taken up in 1 ml of 1 M HCl and left on the hotplate at 120°C overnight before being ready to load onto columns.

2.6.3 Ion Exchange Column Chromatography

For ODP Site 925, samples were processed in the MAGIC laboratory of the Department of Earth Science and Engineering at Imperial College London according to the ion exchange column chromatography procedure outlined in appendix 2. The first stage of the chemical protocol extracts the Rare Earth Elements (REEs) from the rest of the sample matrix using BioRad AG50W-X8 cation exchange resin (200 – 400 mesh size, hydrogen form, 8% cross-linkage) in BioRad gravity flow poly-prep chromatography columns. The REEs were progressively separated from the matrix using subsequent additions of 1 M, 3 M and 6 M HCl. These samples were dried down on a hotplate at 120°C. The second stage of the chemical protocol extracts Nd from the remaining REEs using Eichrom Ln-Spec resin (50 – 100 μ m bead size) in

Savillex 5 ml reservoir microcolumns. Nd was separated from the other REEs by the gradual addition of 0.2 M HCl.

For ODP Site 1263 samples were processed according to the ion exchange chromatography procedure outlined in McCoy-West *et al.* (2017) (see appendix 3) in the CELTIC laboratory of the School of Earth & Ocean Sciences at Cardiff University. The first stage of the chemical protocol extracts the REEs from the rest of the sample matrix using BioRad AG50W-X8 cation exchange resin (200 – 400 mesh size, hydrogen form, 8% cross-linkage) in BioRad gravity flow poly-prep chromatography columns. Samples were loaded in 2 ml of 1 M HCl. The REEs were progressively separated from the matrix using subsequent additions of 10 ml of 1 M HCl + 1 M HF, 12 ml of 2.5 M HCl, 8 ml of 2 M HNO₃, with the REE fraction collected in 14 ml of 6 M HCl. These samples were dried down on a hotplate at 120°C. The second stage of the chemical protocol extracts Nd from the remaining REEs using Eichrom Ln-Spec resin (50 – 100 µm bead size) in in-house manufactured micro-columns. Samples were loaded in 0.5 ml of 0.2 M HCl before Nd was separated from the other REEs by the addition of 6 ml of 0.2 M HCl and collected in a subsequent 6 ml of 0.2 M HCl. These samples were dried down on a hotplate at 70°C.

2.6.4 Isotopic Analysis

Neodymium isotope ratios from ODP Site 925 and ODP Site 1263 were measured on a Nu Plasma Multi-Collector Inductively Coupled Mass Spectrometer (MC-ICP-MS) at Imperial College London and a Nu Plasma II MC-ICP-MS at Cardiff University, respectively. Instrumental bias was corrected for using a ¹⁴⁶Nd/¹⁴⁴Nd ratio of 0.7219. Internal reproducibility was monitored using the ¹⁴³Nd/¹⁴⁴Nd of the JNd_i Nd standard. External reproducibility was monitored using a basaltic rock standard BCR-2, yielding a value of 0.512632 ± 0.000015 over the course of multiple runs ($n=3$) for ODP Site 1263. A value of 0.512640 ± 0.00009 was obtained for ODP Site 925 ($n=5$). Both of these values are in excellent agreement with the published value of 0.512634 (Weis *et al.* 2006). Procedural blanks were consistently below 30 pg of Nd. Corrections were made for Samarium interference on ¹⁴⁴Nd as levels of ¹⁴⁴Sm were consistently below 0.1% of the total 144 signal.

2.6.5 Age Correction for ^{147}Sm to ^{144}Nd Decay

Given the age of the samples analysed in this study, it is important to correct for the decay of the parent isotope ^{147}Sm to its daughter isotope ^{144}Nd to account for any in situ production of ^{144}Nd . In order to do so, an average value of 0.131 was applied. This value is derived from mean values of $^{147}\text{Sm}/^{144}\text{Nd}$ from DSDP Site 527 on Walvis Ridge (Thomas *et al.* 2003) and is the same approach adopted by Via and Thomas (2006). This value is in line with existing published values (e.g. Martin and Scher, 2006; Coxall *et al.* 2018).

2.7 Contributions to this Thesis

Given the wide range of geochemical proxies employed during the course of this research and the large number of samples used, it is necessary to clarify the contribution of other scientists and the use of any external, unpublished datasets. Hence, table 2.6 provides the name of the analyst and the institution at which the analysis took place for each site and geochemical proxy.

Site	Geochemical Proxy	Sample Washing	Sample Picking	Geochemical Analysis
IODP Site U1406	Benthic Foraminiferal Stable Isotopes	Vicki Taylor, NOC Southampton	Vicki Taylor, NOC Southampton	Vicki Taylor, NOC Southampton
	Benthic Foraminiferal Trace Elements	Vicki Taylor, NOC Southampton	Vicki Taylor, NOC Southampton	Amy Sparkes, Cardiff University
ODP Site 925	Benthic Foraminiferal Stable Isotopes	Amy Sparkes, Cardiff University	Amy Sparkes, Cardiff University	Amy Sparkes, Cardiff University
	Benthic Foraminiferal Trace Elements	Amy Sparkes, Cardiff University	Amy Sparkes, Cardiff University	Amy Sparkes, Cardiff University
	Fossil Fish Tooth Neodymium Isotopes	Amy Sparkes, Cardiff University	Amy Sparkes, Cardiff University	Amy Sparkes, Imperial College London
ODP Site 1263	Benthic Foraminiferal Stable Isotopes	Amy Sparkes, Cardiff University	Amy Sparkes, Cardiff University	Amy Sparkes, Cardiff University
	Fossil Fish Tooth Neodymium Isotopes	Amy Sparkes, Cardiff University	Amy Sparkes, Cardiff University	Amy Sparkes, Cardiff University
ODP Site 756	Benthic Foraminiferal Stable Isotopes	Max Holmström, Stockholm University	Max Holmström, Stockholm University	Max Holmström, Stockholm University
	Benthic Foraminiferal Trace Elements	Max Holmström, Stockholm University	Amy Sparkes, Cardiff University	Amy Sparkes, Cardiff University

Table 2.6 – Contributions to the work outlined in this chapter. Contributions in bold relate to those made by the author of this thesis.

Chapter Three

The Link between Atlantic Meridional Overturning Circulation and Antarctic Ice Sheet Dynamics across the Eocene Oligocene Transition

3.1 Introduction

3.1.1 The Modern Thermohaline Circulation

In the modern ocean, NADW is predominantly formed in the cyclonic subpolar gyres of the Norwegian and Greenland Seas. This water flows out from the Nordic Seas in the form of Denmark Strait Overflow Water (DSOW) and Iceland-Scotland Overflow Water (ISOW) across the Greenland-Scotland Ridge (GSR). These two water masses form lower and upper NADW respectively. Upon flowing through the Irminger Basin the less dense Labrador Sea Water (LSW) joins to form the upper arm of NADW. These three water masses flow southward along the western edge of the North Atlantic as a DWBC. In the southern reaches of the Atlantic Ocean, NADW overlies AABW, a colder and denser water mass, and is overlain by Antarctic Intermediate Water (AAIW). At the southern high latitudes, the ACC entrains NADW and exports it through the Indian and Pacific Oceans. These deep waters are upwelled and returned to the North Atlantic region in the intermediate and surface layers of the thermohaline circulation. The warmer, saltier North Atlantic Current (NAC) cools in the high northern latitudes of the Atlantic and sinks once again. In the Atlantic Ocean this loop-like connection between the high northern and southern latitudes and the surface and deep ocean is referred to as the Atlantic Meridional Overturning Circulation (AMOC). This deep ocean circulation is responsible for a substantial proportion of global heat transport.

3.1.2 Deep Water Formation at the EOT

The configuration of the thermohaline circulation has not always been this way. Indeed, during the early Cenozoic, including the earliest Eocene, the Southern Ocean and mid-latitudes were accountable for a greater proportion of deep water formation (Wright and Miller, 1996; Tigchelaar *et al.* 2011). At some point in geological history, a transition from a southern source to a bipolar source of deep water formation in the Atlantic Ocean occurred; representing the greatest change in ocean circulation that has occurred over the last 50 myr (Miller *et al.* 2009). This switch has previously been dated to various time periods; from the early and middle Eocene (e.g. Hohbein *et al.* 2012; Boyle *et al.* 2017; Vahlenkamp *et al.* 2018a; 2018b) to the middle Miocene (e.g. Wright and Miller, 1996).

Chapter Three: The Link between Atlantic Meridional Overturning Circulation and Antarctic Ice Sheet Dynamics across the Eocene Oligocene Transition

It has more recently been suggested that the formation of a proto-NADW, NCW, coincided with the EOT (Davies *et al.* 2001; Via and Thomas, 2006; Abelson and Erez, 2017; Coxall *et al.* 2018). Davies *et al.* (2001) provide evidence from early Oligocene-age sediment drift deposits in the Faroe-Shetland Channel that imply a southerly-flowing, North Atlantic sourced, deep water mass. This is supported by seabed erosional patterns in the North Atlantic (Howe *et al.* 2001). Evidence from neodymium isotopes (ϵNd), a deep-water mass proxy, also supports this theory (e.g. Martin and Scher, 2004; Via and Thomas, 2006). Via and Thomas (2006) date the initiation of northern-sourced deep water formation to 33 Ma using ϵNd data from Walvis Ridge in the southeast Atlantic. ϵNd values at Walvis Ridge (ODP Site 1263 - South Atlantic) and Maud Rise (ODP Site 689 - Weddell Sea, Southern Ocean) diverge (figure 3.1) where by Southern Ocean values remain relatively radiogenic while values from Walvis Ridge become less radiogenic, and as such acquire a more 'Atlantic' signature, suggesting a gradual increase in NCW. This is also suggested by a significant divergence in the $\delta^{18}\text{O}$ values of benthic and planktic foraminifera, which implies a greater degree of stratification in the ocean, expansion of the thermocline and, therefore, development of the thermohaline circulation and psychrosphere (Abelson *et al.* 2008).

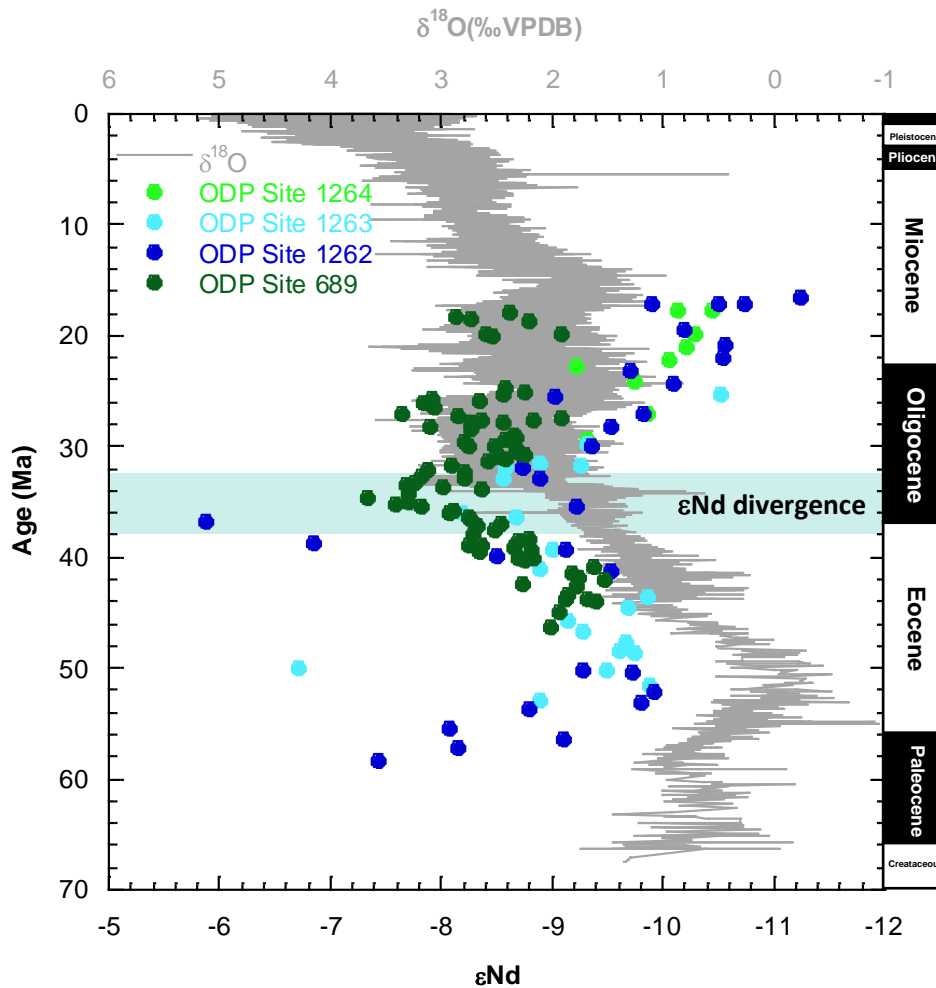


Figure 3.1 – Existing ϵNd records from Walvis Ridge (ODP Sites 1262, 1263 and 1264) and Maud Rise (ODP Site 689) plotted against the $\delta^{18}\text{O}$ compilation of Zachos *et al.* (2008). Data for Walvis Ridge and Maud Rise from Via and Thomas (2006) and Scher and Martin (2004) respectively. Age model calibrated to Cande and Kent (1995).

Despite the evidence outlined above, the sparse resolution and spatial coverage of available records is insufficient to accurately date the onset of NCW. Hence, significant debate remains as to both (i) the timing of the onset of NCW and (ii) the pattern of change associated with its subsequent evolution. Given that evidence for a middle Eocene NCW onset stems from solely high latitude evidence (e.g. Coxall *et al.* 2018; Vahlenhamp *et al.* 2018a; 2018b), it is possible that the evidence associated with the EOT suggests a critical subsequent stage in the evolution of NCW as opposed to its onset. Debate remains as to whether changes in northern-sourced deep water formation played an integral role in the climatic evolution of the EOT and, if so, whether it could be described as cause or consequence.

Various efforts have been made to model NCW formation in the hope of resolving the timing and mechanism behind its initiation and its impact on global climate. It has been suggested that the formation of NCW was associated with a weakening of AABW formation, a reduction in Poleward Heat Transport (PHT) to the Southern Ocean and facilitated growth of the AIS (Sijp and England, 2003; Abelson *et al.* 2008; Sijp *et al.* 2011). It has also been suggested that changes in NCW caused invigoration of the thermohaline circulation, acceleration of upwelling and productivity and a drawdown of $p\text{CO}_2$ (Abelson *et al.* 2008) in line with work suggesting that changing intensity of the AMOC due to Drake Passage opening altered ocean carbon storage (Fyke *et al.* 2015). Conversely, other modelling studies suggest that Antarctic glaciation may have led to changing global distribution of heat and salt, and hence global circulation (e.g., Goldner *et al.* 2014). In any case, such changes likely impacted the stability of the Antarctic ice sheet and acted as powerful feedbacks in the climate system (Goldner *et al.* 2014). Indeed, the intensification of AMOC has even been proposed as a link that connects two other competing hypotheses as to the cause of the EOT; changing Southern Ocean gateways and drawdown of $p\text{CO}_2$ (Lear and Lunt, 2016; Elsworth *et al.* 2017). However, results are largely model-dependent based on differences in prescribed boundary conditions (e.g. paleogeography, atmospheric CO_2 concentrations) and the models resolution. More recent efforts by David Hutchinson and colleagues (Hutchinson *et al.* 2018; 2019) have emphasised the importance of accurate Late Eocene paleogeography and a model resolution able to resolve changes in ocean gateways and boundary current heat transport. These recent efforts, using climate model GFDL CM2.1, adopt the paleogeography of Baatsen *et al.* (2016) and an improved ocean horizontal resolution of $1^\circ \times 1.75^\circ$ compared to the 3° resolution typically seen in EOT modelling efforts. Hutchinson *et al.* (2018) investigated EOT climate sensitivity to different levels of CO_2 . While a halving of atmospheric CO_2 raised Arctic salinities by 1 – 2 psu as a result of weaker precipitation and run-off in the Arctic, this increase in salinity was insufficient alone to cause the initiation of a sinking regime in the North Atlantic; a result that perhaps suggests an increased likelihood that a tectonic forcing was at play across this interval.

Chapter Three: The Link between Atlantic Meridional Overturning Circulation and Antarctic Ice Sheet Dynamics across the Eocene Oligocene Transition

Historically, the most commonly cited cause for the reorganisation of thermohaline circulation is that it occurred synchronous with a rapid suppression of the Iceland Plume (Poore *et al.* 2011; Parnell-Turner *et al.* 2014); a convective upwelling, mantle feature of 1500°C potential temperature (White, 1997) and a 1200 kilometre radius (Rickers *et al.* 2013). This rapid suppression caused an abrupt deepening of the Greenland-Scotland Ridge (GSR). The GSR is a bathymetric sill extending from southeast Greenland through Iceland to the Scottish continental shelf (Hohbein *et al.* 2012). It is thought that the subsidence of the GSR from a subaerial to submarine rise served to control the ocean gateway and water exchange between the Arctic and North Atlantic oceans (Stärz *et al.* 2017); a flow path that represents a significant proportion of the modern day NADW. A decrease in the height of the GSR allowed the development of a bidirectional seaway between the Nordic Sea and the North Atlantic once a critical depth was breached; namely below the surface-subsurface interface (~ 50 metres below sea level (mbsl)) (Stärz *et al.* 2017); a hypothesis supported by recent modelling efforts by Abelson and Erez (2017). Records of the subsidence history of the GSR date this breach to approximately 32 Ma (e.g. Clift, 1996). However, a second potential tectonic forcing has more recently been suggested by Hutchinson *et al.* (2019) who, following the work of Hutchinson *et al.* (2018), proposed closure of the Arctic-North Atlantic gateway as a mechanism by which control state salinities of the North Atlantic could be raised. These efforts not only prompted sinking in the North Atlantic by blocking Arctic freshwater access to the North Atlantic but also shutdown sinking in the North Pacific by salt-advection feedbacks in line with evidence from recent low resolution records from the Pacific Ocean region (e.g. Thomas *et al.* 2014; McKinley *et al.* 2019).

Some studies suggest that the timing of changes to NCW and the EOT are merely coincidental (e.g. Via and Thomas, 2006). In any case, whilst the resolution of records is currently not high enough to explicitly constrain the timing of this relationship (e.g. Via and Thomas, 2006) (i.e. whether the change in ocean circulation preceded or post-dated ice sheet growth) records suggest a tantalising link between Antarctic glaciation and the formation of NCW. Coxall *et al.* (2018) provided evidence of substantial change in the North Atlantic region prior to the EOT, but were unable to establish a direct impact on the wider AMOC. The aim of this

work is to better constrain the timing of any reorganisation in North Atlantic Ocean circulation associated with the EOT and growth of the AIS.

3.1.3 Neodymium Isotopes

Neodymium (Nd), a light rare earth element (REE) naturally occurs in seven different isotopes. Of keenest interest to paleoclimatologists is the geochemical ratio of radiogenic ^{143}Nd to stable ^{144}Nd . ^{143}Nd is the radiogenic daughter of the radioactive Samarium (Sm) isotope, ^{147}Sm , from which it slowly decays over a half-life of 106 Ga. By using equation 3, $^{143}\text{Nd}/^{144}\text{Nd}$ is normalized by a measure of the deviation of a geological sample from the bulk Earth value (the chondritic uniform reservoir (CHUR) value of 0.512638 (Jacobsen and Wasserburg, 1980)) in parts per 10,000.

$$\epsilon\text{Nd} = \left(\frac{^{143}\text{Nd}/^{144}\text{Nd}_{\text{sample}}}{0.512638 \times 10\,000} \right) - 1$$

Eq. 3

3.1.3.1 Variation in the Modern Ocean

Bedrock material with differing ϵNd values is eroded and delivered to the oceans by aeolian and fluvial transport processes. In combination with the short residence time of Nd in the oceans (c. 1000 years; Tachikawa *et al.* 1999; 2003) compared to timescales of oceanic mixing (c. 1500 years; Broecker and Peng, 1982), this leads to a heterogeneity in the Nd isotopic composition of the oceans. Variations in the isotopic composition of Nd in surface waters occur primarily as a result of differences in weathered continental rocks that drain into a given ocean basin. Intermediate and deep water masses subsequently acquire the signature of surface waters in their respective areas of subduction or down welling (Thomas, 2004). These signatures are subsequently modified by mixing with other water masses.

Therefore, distinctive inter-basin differences exist in the modern ocean (Piepgras *et al.* 1979) somewhat mirroring global deep water circulation. The most negative, non-radiogenic ϵNd values are found in NADW where mixing of dense waters formed in the Nordic and Labrador Seas, with values of ~ -9 and ~ -16 respectively, result in values of ~ -12 to -13 (Piepgras and Wasserburg, 1987) due to drainage of older, Canadian rocks. The mixing of NADW with eastward flowing waters from Drake Passage give AABW and AAIW more radiogenic values of ~ -8.5 (Piepgras and

Wasserburg, 1982). The most radiogenic values are found in the North Pacific where values of around -4 (Piepgras and Jacobsen, 1988) are derived from circum-Pacific arc terranes and very slow deep water renewal. The North Atlantic and North Pacific represent the ϵNd endmembers within the modern thermohaline circulation; values within the Southern and Indian Oceans fall between them.

3.1.3.2 Deep Sea Archives

Nd isotopes have been identified as quasi-conservative tracers of water masses (Piepgras and Wasserburg, 1980) and have been widely applied over the last 30 years in paleoceanographic studies. The different fractions of a deep sea sediment sample will represent Nd isotopic ratios derived from a number of sources. These fractions can be adsorbed onto mineral surfaces (known as the exchangeable fraction), associated with carbonates, bound to organic compounds, scavenged by iron and manganese oxides or leftover in the detrital residue (Tessier *et al.* 1979). The continental-sourced, typically clay-rich, detrital fraction, based on an assumption that an authentic Nd isotopic signature is retained during subsequent transportation and diagenesis, represents the minerals weathered from nearby continents and thus can be used to deduce the continental provenance of deep sea material. Modifications to this baseline Nd isotopic ratio commonly represent an authigenic seawater signal. Any changes in source region or ocean circulation can be identified in the detrital and authigenic signals respectively and evaluated against changes in global and regional climate parameters or ice sheet dynamics.

While the dominant source of Nd to the oceans is the weathering and erosion of continental material, there remains a lack of understanding of the contribution of particulate inputs to the dissolved Nd distribution in the oceans. Hence, one important uncertainty in the use of Nd isotopes as a water mass tracer is 'boundary exchange'; namely the exchange between particulate and dissolved fractions that occurs most commonly at continental margins. Given its potential to affect the quasi-conservative behaviour of Nd in the oceans, it is an important process to consider when making interpretations as to the source of a ϵNd signal. Significant evidence for a contribution to oceanic Nd by boundary exchange is derived from both modern observational studies (e.g. Lacan and Jeandel, 2005; Grasse *et al.* 2017) and

modelling simulations (e.g. Arsouze *et al.* 2008; 2009). Furthermore, comparison of these two types of study illustrate a lack of understanding of the precise mechanism that controls boundary exchange (Wilson *et al.* 2013). Boundary exchange is most commonly found to influence deep water settings close to continental margins and, hence, was not thought to be a process likely to influence the open ocean sites used in the work presented in this thesis. However, a greater discussion of the possible influence of boundary exchange on ϵNd at Ceara Rise can be found in section 3.4.1 of this chapter.

One significant difficulty in the application of Nd isotopes to paleoceanographic studies lies in identifying a ubiquitous, dateable marine proxy archive that accurately records an authigenic Nd signal that remains unchanged through time when subjected to burial and lithification (Martin and Haley, 2000). The proxy mostly widely accepted as a reliable recorder of the seawater Nd signal is that of fossil fish teeth. The hydroxyapatite of living fish teeth contains parts per billion (ppb) Nd, compared to between 100 and 1000 (parts per million) ppm of the hydroxyfluorapatite of fossil teeth (Wright, 1984; Shaw and Wasserburg, 1985). Work pioneered in the early 1980s (e.g. Staudigel *et al.* 1985) discovered that this post-mortem increase in Nd concentration occurs during very early diagenesis at the sediment water interface (SWI) by processes including adsorption and substitution (Reynard *et al.* 1999). This overwhelming incorporation of Nd during early diagenesis ensures that fish teeth record the isotopic signature of the bottom water, removing any ambiguity associated with the habitat depth of different fish species (Martin and Scher, 2004).

Fossil fish teeth are limited only by stratigraphic resolution making them better suited to resolving rapid or shorter term changes in ocean circulation. Thus, the use of fish teeth affords much better spatial and temporal resolution than that previously afforded by ferromanganese (Fe-Mn) crusts. The use of fish teeth is limited to samples larger than 10 ng Nd, but sample sizes typically range between 30 and 100 ng. Larger abundances can be targeted by selecting cores with specific sedimentological attributes. Indeed, teeth are best preserved in low carbonate content material with slower sedimentation rates (Martin and Haley, 2000). Slower sedimentation rates lead to a longer exposure of fish teeth to bottom water and

hence to higher Nd concentrations (Elderfield and Pagett, 1986; Martin and Scher, 2004).

One potential pitfall of Nd isotopes in fish teeth raised by Toyoda and Tokomani (1990), suggested that differences between seawater Nd and the concentrations recorded in fish teeth were indicative of continuous post-burial uptake of Nd from pore water within the sediment despite a lack of correlation between age and Nd concentration in the earliest studies (e.g. Grandjean *et al.* 1987). However, subsequent studies have clearly illustrated no systematic increase in Nd concentrations with burial depth (Martin and Scher, 2004). In addition, Nd is highly particle reactive and concentrations in pore water are so low that they are below detection limits of modern analytical capabilities (Martin and Scher, 2004). Thus, incorporation of Nd into fish teeth must occur while pore waters are directly interacting with bottom water.

The use of Nd isotopes as a proxy for changes in global water mass configuration is the perfect addition to the research toolkit employed in fulfilling the overarching aims and objectives of this thesis. Therefore, in this chapter records of ϵNd will be presented from fossil fish teeth from two Atlantic Ocean sites; ODP Site 925 (Ceara Rise) in the Equatorial Atlantic and ODP Site 1263 (Walvis Ridge) in the South Atlantic.

3.2 Methodology

3.2.1 Geological Setting

Samples spanning the Eocene Oligocene boundary were analysed from sediment cores recovered from ODP Site 1263 (Walvis Ridge - 28°31.98'S, 2°46.77'E) and ODP Site 925 (Ceara Rise - 4°12.249'N, 43°29.334'W). These sites and others discussed in this chapter are shown in figure 3.2 and extensive site information is provided in chapter two of this thesis.

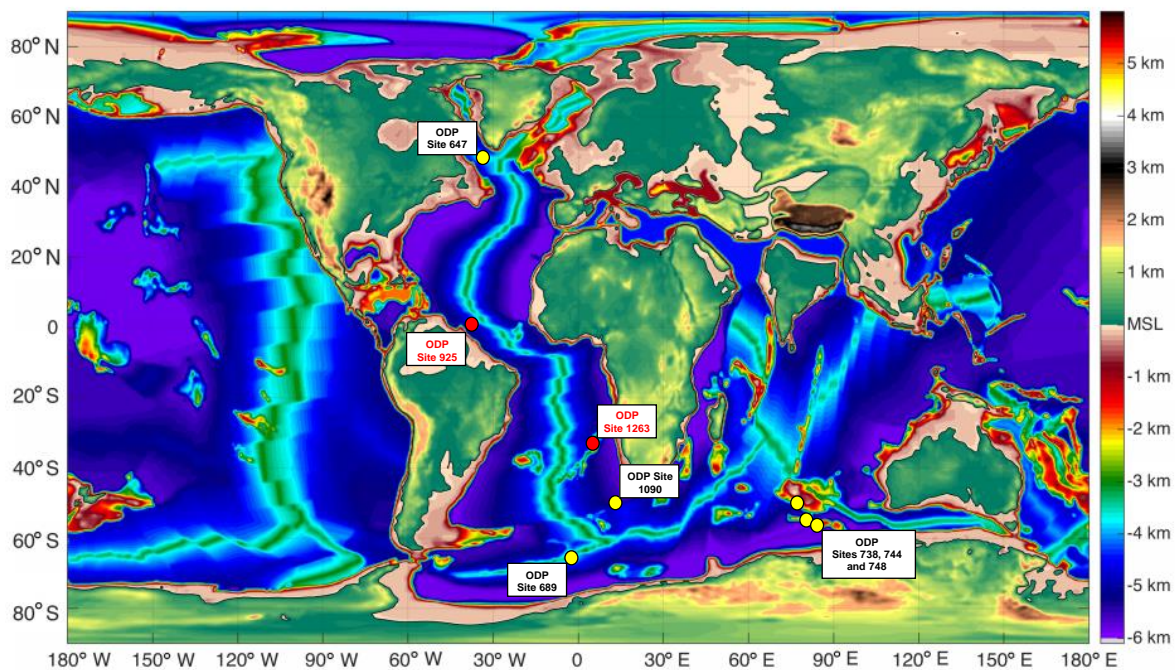


Figure 3.2 – Location of ocean drilling sites used, or discussed, in this study displayed on paleogeographic map from Baatsen *et al.* (2016). Red dots indicate sites from which new data has been generated in this thesis. Yellow dots indicate sites from which existing published data is presented for comparison purposes.

ODP Site 925 is the shallowest site drilled as part of Leg 154 on Ceara Rise, an aseismic rise bounded by the Ceara abyssal plain to the west and the Amazon cone to the east, in the western equatorial Atlantic Ocean. Its paleo water depth of 2500 metres places it directly within the core of modern NADW at the EOT making it an ideal site to monitor the increasing influence of any proto-NADW in the latest Eocene and earliest Oligocene. Samples of 20 cm³ from ODP Site 925 were taken between 746.43 and 850.14 mbsf at an average temporal resolution of 50 kyr. ϵ Nd data are provided from samples at an average temporal resolution of 200 kyr.

Walvis Ridge is an aseismic ridge formed by hotspot volcanism that runs from the northeast to southwest and divides the South Atlantic into two basins; the Angola and Cape Basins to the north and south, respectively (Zachos *et al.* 2004). The ridge is mostly draped with pelagic deposits that increase in thickness with increasing proximity to the continental margin (Zachos *et al.* 2004). ODP Site 1263 sits on the north-south segment of Walvis Ridge at a water depth of 2717 mbsf making it the shallowest site drilled as part of Leg 208. Samples of 40 cm³ from ODP Site 1263 were taken between 69.57 and 90.28 mbsf at an average temporal resolution of 40 kyr but with intervals of higher resolution sampling (~ 10 - 20 kyr) across key intervals including the isotope shift and the EOGM. These samples were analysed for ϵNd from fossil fish teeth. An initial subset of samples (17 at a resolution of ~ 100 kyr) were analysed for their benthic foraminiferal $\delta^{18}\text{O}$ to allow comparison with an existing published record of $\delta^{18}\text{O}$ from ODP Site 1263; this was to establish whether a second benthic foraminiferal stable isotope record from ODP Site 1263 warranted generation.

3.2.2 Chronology

Chronology for ODP Site 925 is based solely on biostratigraphy as magnetostratigraphic age control was unavailable for sites collected during Leg 154. Chronology for ODP Site 1263 is based on biostratigraphic and magnetostratigraphic datums. Both age models are calibrated to the timescale of Cande and Kent (1995) and are presented in greater detail in chapter two of this thesis.

3.2.3 Sample Preparation and Analysis

Benthic foraminifera samples used in this study were prepared and cleaned according to the protocol outlined in sections 2.2 and 2.4 of chapter 2 of this thesis. For ODP Site 925 and ODP Site 1263, a minimum of five individuals of *Cibicidoides havanensis* and *Oridorsalis umbonatus* respectively were run from specimens picked from the 250 – 355 μm size fraction. These samples were analysed at Cardiff University on a ThermoFinnigan MAT252 with online sample preparation by an automated Kiel II carbonate device. Analytical error for the ODP Site 925 data set, based on repeat analysis of standard NBS-19 (n=172), is 0.043‰ for $\delta^{18}\text{O}$ and

Chapter Three: The Link between Atlantic Meridional Overturning Circulation and Antarctic Ice Sheet Dynamics across the Eocene Oligocene Transition

0.020‰ for $\delta^{13}\text{C}$. Analytical error for the ODP Site 1263 data set, based on repeat analysis of standard BCT63 (n=94), is 0.029‰ for $\delta^{18}\text{O}$ and 0.013‰ for $\delta^{13}\text{C}$.

Fossil fish teeth were picked from the >63 μm size fraction. A minimum of 200 μg of teeth were cleaned according to the protocol outlined in section 2.6.1 of chapter two of this thesis. Samples were dissolved and subjected to chemical separation by ion exchange column chromatography techniques outlined in section 2.6.3 of chapter two of this thesis in order to isolate Nd from both the REEs and the wider matrix. Isotope ratios from ODP Site 925 and ODP Site 1263 were measured on a Nu Plasma MC-ICP-MS at Imperial College London and a Nu Plasma II MC-ICP-MS at Cardiff University, respectively. Instrumental bias was corrected for using a $^{146}\text{Nd}/^{144}\text{Nd}$ ratio of 0.7219. Internal reproducibility was monitored using the $^{143}\text{Nd}/^{144}\text{Nd}$ of the JNd_i Nd standard. External reproducibility was monitored using a basaltic rock standard BCR-2, yielding a value of 0.512632 ± 0.000015 over the course of multiple runs (n=3) for ODP Site 1263. A value of 0.512640 ± 0.00009 was obtained for ODP Site 925 (n=5). Both of these values are in excellent agreement with the published value of 0.512634 (Weis *et al.* 2006). Procedural blanks were consistently below 30 pg of Nd. Corrections were made for Samarium interference on ^{144}Nd as levels of ^{144}Sm were consistently below 0.1% of the total 144 signal.

3.3 Results

3.3.1 ODP Site 925 – Ceara Rise

Benthic foraminiferal stable isotope and fossil fish teeth neodymium isotope data obtained from 56 samples from ODP Site 925 are presented in figure 3.3. $\delta^{18}\text{O}$ values are relatively stable during the pre-boundary interval averaging -0.45‰ between 35.68 Ma and 34.05 Ma. The isotopic shift at ODP Site 925 is characterised by a $\sim 0.8\text{‰}$ increase in $\delta^{18}\text{O}$. Thus, whilst absolute values of $\delta^{18}\text{O}$ are somewhat unusual when compared to other Atlantic records, the relative change across the shift is comparable in magnitude. The heavier values of $\delta^{18}\text{O}$ persist into the early Oligocene.

The ϵNd record from ODP Site 925 demonstrates very negative, non-radiogenic values across the interval studied with an average of -13.9 for the entire dataset. Values of ϵNd oscillate on the order of $0.5 - 1.5$ ϵ units between -15 and -13 . The greatest oscillation is associated with step one of the isotope shift prior to the EOB; an interval most commonly associated with the cooling phase of the transition. Here ϵNd increases from -14.89 to -13.11 between 34.35 Ma and 33.90 Ma before subsequently decreasing from -13.19 to -15.07 between 33.82 Ma and 33.55 Ma. This latter value is the least radiogenic of the record and is reached during step two of the isotope shift. The values shown in this record from Ceara Rise represent the least radiogenic record generated from fish teeth thus far across the EOT from anywhere in the global ocean.

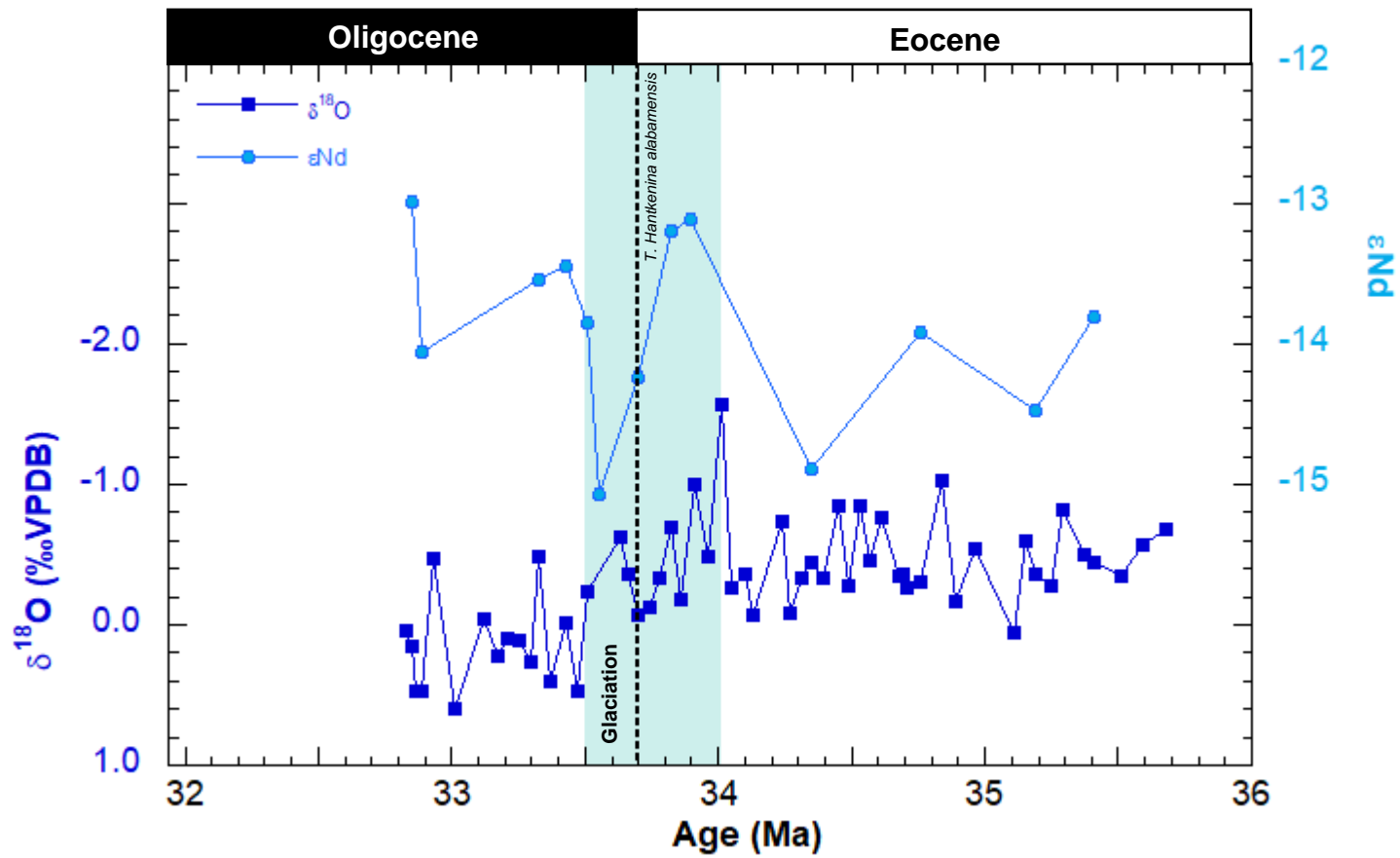


Figure 3.3 – Benthic foraminiferal stable isotope and fossil fish teeth ϵNd from ODP Site 925. Shaded bar shows duration of EOT. Top of *Hantkenina alabamensis* used to show position of EOB. Age model calibrated to Cande and Kent (1995).

3.3.2 ODP Site 1263 – Walvis Ridge

Benthic foraminiferal stable isotope data obtained from 17 samples of *Oridorsalis umbonatus* from ODP Site 1263 are presented in figure 3.4 alongside the pre-existing record also developed from *Oridorsalis umbonatus* by Riesselman *et al.* (2007). This small subset of samples was processed for $\delta^{18}\text{O}$ initially to ensure that they corroborated the previously published high-resolution record (~ 6 kyr resolution). Good agreement of the $\delta^{18}\text{O}$ values of samples analysed in this study with those analysed by Riesselman *et al.* (2007) (as shown in figure 3.4) suggested the development of a further benthic foraminiferal stable isotope record from ODP Site 1263 across the time interval of interest was unnecessary.

The isotopic shift at ODP Site 1263 is characterised by a ~ 1.77‰ increase in $\delta^{18}\text{O}$ from 1.31‰ at 33.82 Ma to 3.08‰ at 33.56 Ma (Riesselman *et al.* 2007). The $\delta^{18}\text{O}$ values generated as part of this study are in close agreement with the absolute values of the neighbouring samples from Riesselman *et al.* (2007). However, the coarse resolution of the record fails to capture the true magnitude of the isotope shift. The representation of the isotope shift provided by the coarse resolution original record presented by this study is of a ~ 0.7‰ increase between 34 Ma and 33.46 Ma. Therefore, subsequent discussions of the isotope shift will refer to the record of Riesselman *et al.* (2007) where both steps one and two of the isotope shift are resolvable due to the high resolution; step one is shown as a ~ 0.5‰ increase across 80 kyr and step two as a ~ 0.6‰ increase across 90 kyr. The higher post-boundary values of $\delta^{18}\text{O}$ persist into the early Oligocene and do not recover to pre-excursion levels.

The ϵNd record developed from ODP Site 1263 depicts absolute values in close agreement with those previously published as part of longer-term record of ϵNd covering a greater portion of the Cenozoic; the entire Eocene and Oligocene in addition to the late Paleocene and early Miocene by Via and Thomas (2006). The resolution of this original record was too coarse to document the detailed changes in ϵNd shown here in figure 3.4. The greatest change across the time interval analysed predates the isotope shift at the EOT. Between 34.76 Ma and 34.3 Ma ϵNd

Chapter Three: The Link between Atlantic Meridional Overturning Circulation and Antarctic Ice Sheet Dynamics across the Eocene Oligocene Transition

decreases by 1.1 ϵ units from -7.6 to -8.7. This change leads the oxygen isotope shift by almost 1 myr. Across the oxygen isotope shift, ϵ Nd stabilises, and values remain below -8.5; these are the least radiogenic values of the record. The lowest value, -8.9 at 33.69 Ma, is documented between steps one and two of the oxygen isotope shift. Following the onset of glaciation on Antarctica, during the EOGM, greater variability is seen where by ϵ Nd values oscillate to a greater extent, on the order of 0.4 to 0.5 ϵ units. This period of greater variability lasts for around 1 myr; from the onset of glaciation at c. 33.8 Ma until 32.7 Ma. During the latter half of this interval ϵ Nd values become slightly more radiogenic from 33.3 Ma onward, but fail to recover to pre-transition values. From 32.8 Ma onwards, ϵ Nd at Walvis Ridge decreases once again from -7.99 to -8.66.

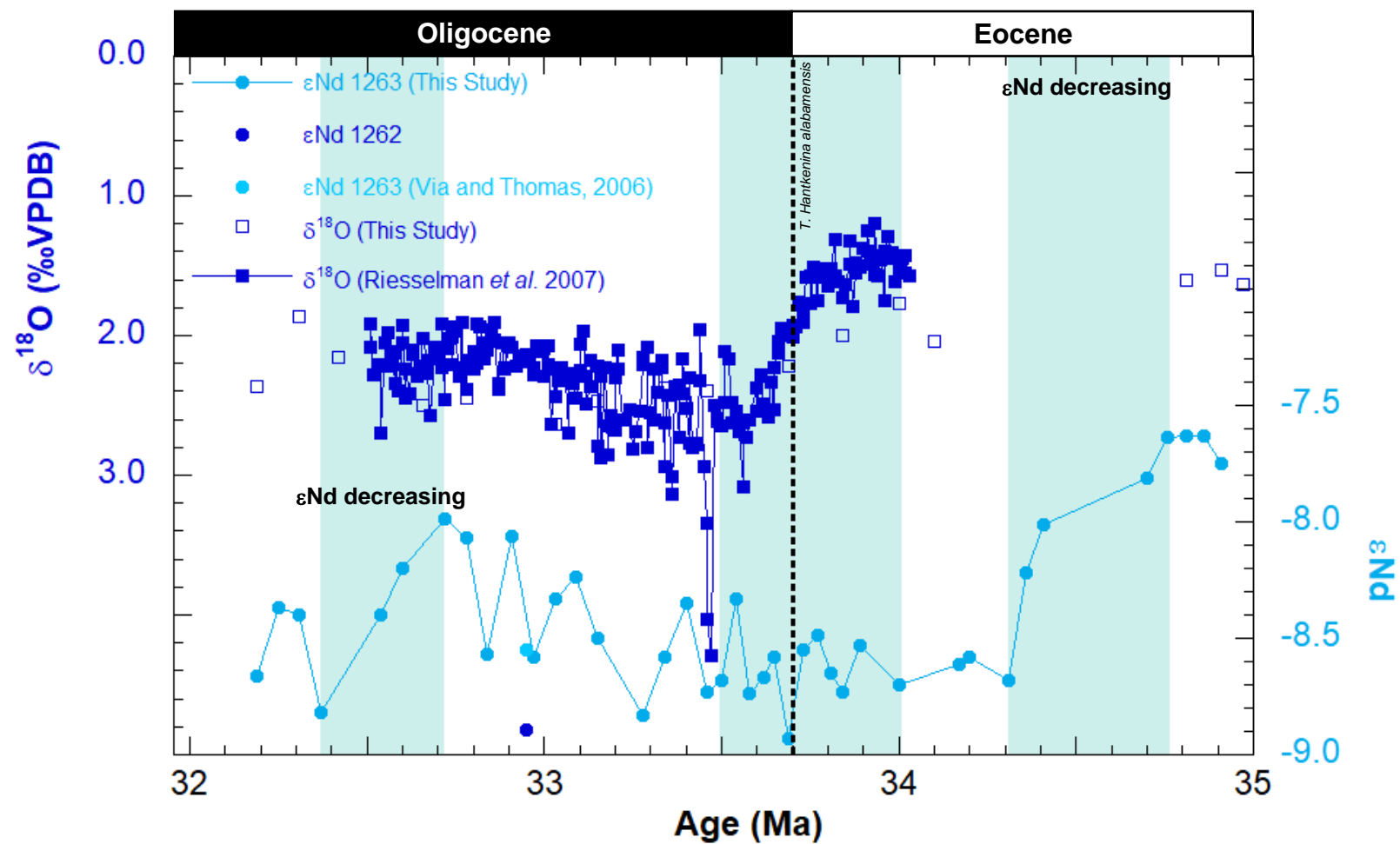


Figure 3.4 – Benthic foraminiferal stable isotope and fossil fish teeth ϵ Nd from ODP Site 1263. Previously published data from ODP Sites 1262 and 1263 (ϵ Nd data points without line) are from Via and Thomas (2006). Middle shaded bar shows duration of EOT. Top of *Hantkenina alabamensis* used to show position of EOB. Age model calibrated to Cande and Kent (1995). Age model calibrated to Cande and Kent (1995).

3.4 Discussion

In order to effectively interpret the ϵNd records generated during this study consideration must be given to the continental configuration at the EOT, the regional geology surrounding each ocean basin and the paleo isotopic composition of the various different water masses at the EOT. Figure 3.5 shows existing published records from multiple site locations (as shown in figure 3.2).

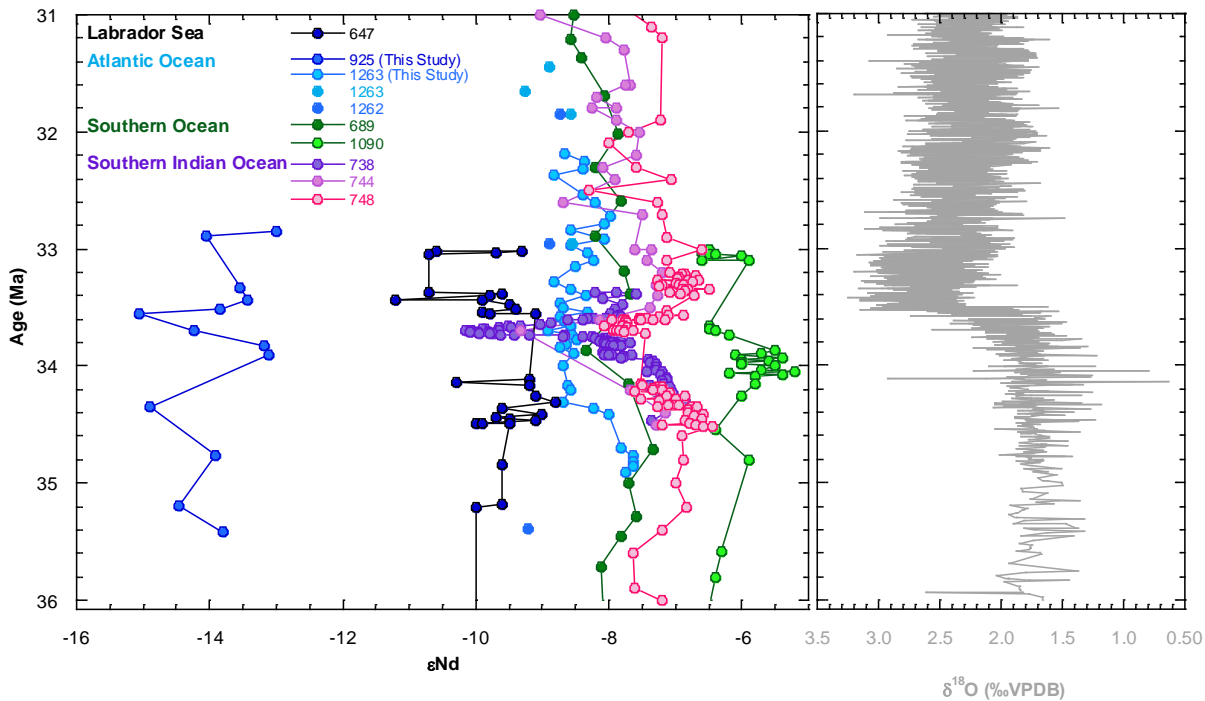


Figure 3.5 – ϵNd records across the EOT. Data shown from Labrador Sea (ODP Site 647 – Coxall *et al.* 2018); Equatorial Atlantic (ODP Site 925 – this study); South Atlantic (ODP Site 1263 – Via and Thomas (2006) and this study); Atlantic sector of Southern Ocean (ODP Site 689 – Scher and Martin, 2004; ODP Site 1090 – Scher and Martin, 2006); Indian sector of Southern Ocean (ODP Site 738 – Scher *et al.* 2011; ODP Sites 744 and 748 – Wright *et al.* 2018). Oxygen isotope record presented from Zachos *et al.* (2008) and references therein.

3.4.1 ϵNd at ODP Site 925: Water Mass or Weathering?

One of the most striking elements of figure 3.5 is the extent to which the record of ODP Site 925 differs from the others. The ϵNd signatures of water masses bathing modern equatorial Atlantic regions are determined by mixing of northern-sourced NADW and southern-sourced AABW deep waters. The Northeastern Atlantic is surrounded by continental bedrock made up of the early Proterozoic and late Archean provinces of the Canadian Shield (Hoffman, 1988) from which its bottom water derives its characteristically low ϵNd (c. -12 (Piepgras and Wasserburg, 1987)). In contrast, Southern Ocean deep waters are influenced by the comparably

radiogenic ϵNd of the volcanic island arcs of the Pacific Ocean region (c. -4) (Piepgras and Wasserburg, 1982). It is the mixing of northern-sourced deep waters and radiogenic Pacific surface waters sinking in the Southern Ocean to which AABW ϵNd values of c. -8 may be attributed.

At the EOT the ϵNd endmembers of the world's ocean basins differed to those of today. North Atlantic waters appeared to be more radiogenic (c. -9 to -11) than those of its modern counterpart likely due to the absence of a significant contribution from the Labrador Seas (Coxall *et al.* 2018). In the South Atlantic and Southern Ocean fish teeth ϵNd values have been documented between -7 and -8.5 (e.g. Via and Thomas, 2006) and -5 to -8 (e.g. Scher and Martin, 2004; 2008) respectively. In the late Eocene oceans the Tethys Ocean featured ϵNd values of c. -9 to -10 (e.g. Grandjean *et al.* 1987; Stille *et al.* 1990).

ϵNd values at ODP Site 925 are the least radiogenic thus far documented across the EOT. The record presented here demonstrates very negative, non-radiogenic values with an average ϵNd of -13.9. As shown in figure 3.5, these values lie outside the typical array of ϵNd values that might be expected given the water masses influencing this equatorial Atlantic site in both the modern (Piepgras and Wasserburg, 1987) ocean and at the EOT (Scher and Martin, 2004; 2006; 2008; Via and Thomas, 2006).

ϵNd values at ODP Site 925 are more akin to those found in the modern Labrador Sea. LSW is the least radiogenic water mass influencing the modern Atlantic ocean (c. -14 to -16) (Lambelet *et al.* 2016; Van de Flierdt *et al.* 2016). In addition to debate over the timing of the onset of LSW (Thomas and Via, 2007; Borrelli *et al.* 2014; Coxall *et al.* 2018), there are several further reasons why it is unlikely to be responsible for the non-radiogenic values at Site 925 across the EOT. In the modern ocean the density of LSW is not high enough for it to sink beyond intermediate water depths (~2000 metres) and the non-radiogenic values attributed to LSW are not seen beyond 35°N (Lambelet *et al.* 2016) making its influence limited at an equatorial site with a paleo water depth of 2500 metres at the EOT. Moreover, LSW is formed by seasonal convective mixing whereby winter heat loss from regional surface

waters destabilises the water column and mixes surface water downwards to form dense bottom water masses (Marshall and Schott, 1999; Straneo, 2006). There is substantial evidence to suggest that longer-term freshening of surface waters in the subpolar North Atlantic has previously substantially inhibited LSW formation (Hillaire-Marcel *et al.* 2001; Straneo, 2006; Gelderloos, 2012); a plausible scenario given evidence for an Arctic-sourced freshwater influence on North Atlantic surface waters at the EOT (Coxall *et al.* 2018). Therefore, the values presented here are beyond those which might reasonably be explained by simple mixing of northern and southern-sourced deep waters.

Therefore it is far more likely that the extremely non-radiogenic values of ϵNd at Ceara Rise represent a regional weathering signal whereby weathered material from nearby continents impart a local ϵNd signal onto deep waters at Ceara Rise by a process termed boundary exchange. As can be seen from figure 3.6, there is a distinct synchronicity between the oscillations in ϵNd and those in the shipboard record of colour reflectance (L^*) collected during ODP Leg 154 (Curry *et al.* 1995). Colour reflectance (in this case based on the CIE (International Commission on Illumination) L^* colour parameter) can be used to track changes in sediment colour; an indication of changes in sediment composition, which may reflect changing weathering regime. L^* can also represent changes in dissolution whereby a darkening of sedimentary material illustrates increased dissolution of the sedimentary carbonate component. However, this is ruled out here due to an absence of synchronicity with benthic foraminiferal B/Ca (figure 3.6), which one could reasonably expect to show a significant decrease under conditions of increased dissolution (Yu *et al.* 2010).

Chapter Three: The Link between Atlantic Meridional Overturning Circulation and Antarctic Ice Sheet Dynamics across the Eocene Oligocene Transition

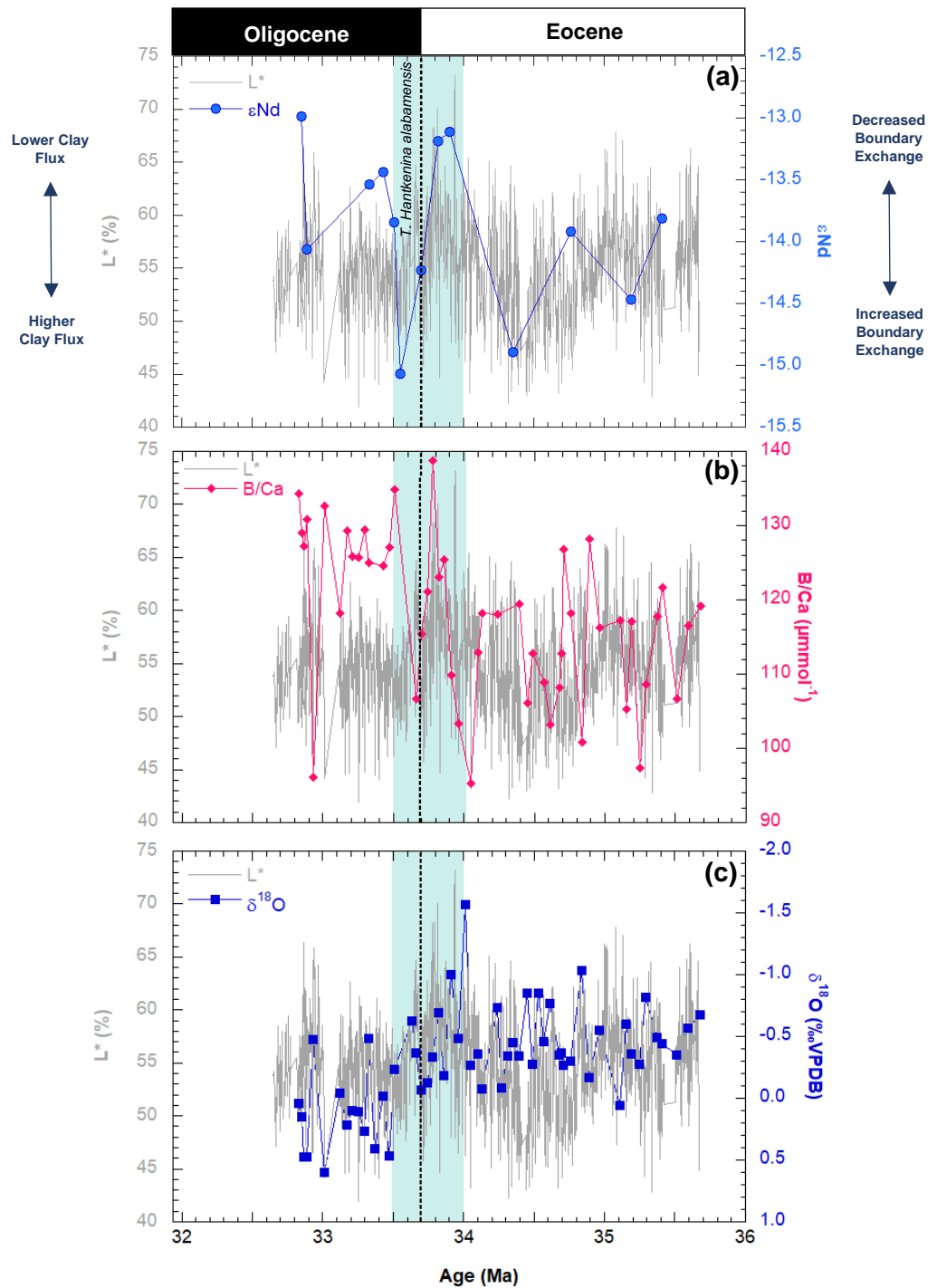


Figure 3.6 – (a) Fossil fish teeth ϵ_{Nd} and sediment colour reflectance, (b) benthic foraminiferal B/Ca and sediment colour reflectance (c) benthic foraminiferal $\delta^{18}\text{O}$ and sediment colour reflectance from ODP Site 925. Shaded bar shows duration of EOT. Top of *Hantkenina alabamensis* used to show position of EOB. Age model calibrated to Cande and Kent (1995).

3.4.1.1 Sources of Non-Radiogenic Weathered Material to Ceara Rise

Boundary exchange is the interchange of particulate and dissolved fractions at sites close to continental margins; namely the exchange of Nd between seawater and sediments on the continental shelf (Jeandel *et al.* 1995; Lacan and Jeandel, 2001; Lacan and Jeandel, 2005). The mechanisms behind this process remain poorly constrained (Wilson *et al.* 2013) but it is now thought that boundary exchange exerts a considerable control on the oceanic Nd budget (Van de Flierdt *et al.* 2016). Ceara Rise lies 800 kilometres east of the mouth of the Amazon River. Recent work has provided evidence of boundary exchange between sediments derived from the Amazon basin and the modern Atlantic Ocean that is dominated by the release of REEs from suspended particulate matter (SPM) (Rousseau *et al.* 2015). Modern ϵNd values of Amazonian SPM are around -10.7 (Allègre *et al.* 1996; Viers *et al.* 2008; Rousseau *et al.* 2015), derived from the weathering of a mix of radiogenic (~ -8) material from Phanerozoic sedimentary rocks in the west of the Amazon basin and much older cratonic material in the eastern Amazon basin (~ -20).

Differences in the paleotopography of the South American continent in the latest Eocene meant that drainage patterns were substantially different to those of today and that it is likely that the Amazon basin served as the source of non-radiogenic weathered material at the EOT. From the middle Eocene onwards the Amazon basin was divided in two by the Purus Arch, which was not incised by the Amazon river until the Late Miocene (Hoorn *et al.* 1995) by which time a transcontinental Amazon system had been established (Figueiredo *et al.* 2009). Prior to its incision, the Purus Arch isolated the eastern basin from the western basin and restricted the areas drained to the equatorial Atlantic continental shelves to the older, cratonic material of the Guiana Shield (Dobson *et al.* 2000). The Guiana Shield is one of three ancient cratons that make up the South American plate and underlies Guyana, Suriname, Venezuela and areas of both Brazil and Colombia thus forming much of the eastern Amazonian basin. This ancient craton has ϵNd values of as low as -20 making it a likely weathering source for the non-radiogenic ϵNd at Ceara Rise across the EOT.

Indeed, it has previously been suggested that Amazon basin drainage exerted an influence on the ϵNd of sediments at Ceara Rise later in the Cenozoic (Stewart *et al.*

2016; van Soelen *et al.* 2017). Therefore, the implications of the data presented here are two-fold: (i) that the influence of the Amazon basin on ϵNd at Ceara Rise has persisted over much longer Cenozoic timescales than previously thought; and (ii) that the effect of boundary exchange has the potential to affect open ocean sites to a greater degree than previously thought.

3.4.1.2 *Eccentricity-Paced Oscillations in Amazonian Weathering Flux*

Spectral analysis previously conducted on the biogenic barium and reactive phosphorus components of the sedimentary record from ODP Site 925 has identified eccentricity-paced oscillations across the EOT (Nilsen *et al.* 2003). The location of ODP Site 925 places it under great influence of changes in ocean-atmosphere heat exchange. The equatorial regions are readily influenced by changes in Earth's meridional temperature gradients by shifts in the Intertropical Convergence Zone (ITCZ). The ITCZ is a tropically located belt that represents Earth's thermal equator. This region is a low-latitude, low-pressure, high-rainfall confluence of the North and South trade winds. The axis of global atmospheric circulation is far from static and migrates over many timescales; from seasonally (between 9°N in boreal summer and 2°S in boreal winter) to longer paleo timescales (Schneider *et al.* 2014). The ITCZ migrates towards the differentially warming hemisphere taking increased precipitation with it and leaving behind more arid conditions. A movement of the ITCZ would significantly alter the hydrological cycle in the Amazonian region. A more intense hydrological cycle would make the basin area more susceptible to significant weathering causing an increased flux of weathered clay-rich material to Ceara Rise. Indeed it is clear from figure 3.6 that during phases of low L^* , ϵNd values become less radiogenic suggesting a greater flux from the extremely non-radiogenic regions of the Amazon basin identified above. Evidence of regional climate change associated with the northward movement of the ITCZ has been documented from the Amazon Basin at the onset of the Bølling Allerød warm episode in the northern hemisphere and the Antarctic Cold Reversal in the southern hemisphere (c. 14 Ka) (Arz *et al.* 1998; Blard *et al.* 2011).

It is worth considering why the greatest oscillation in ϵNd begins coeval with the isotope shift and reaches peak values in the early EOGM. There are three possible

explanations for this: (i) that the glaciation-induced sea level fall associated with the isotope shift exposed greater areas of continental shelf fronting the region of Amazon outflow, forcing the deposition of weathered sediments to deeper waters causing a subsequent increase in the flux of non-radiogenic material to Ceara Rise; (ii) that a large scale shift of the ITCZ occurred at the EOT aligned with previous evidence for a north-ward shift of the ITCZ in the Pacific at this time (Hyeong *et al.* 2016); or (iii) that the efficiency of boundary exchange was enhanced in response to decreasing bottom water oxygen (BWO) (Jeandel *et al.* 2007) associated with increased primary productivity (see chapter four of this thesis). It is also possible that a combination of all three factors contributed to the larger oscillation associated with the EOT, but it is beyond the current scope to identify their relative contributions. The first explanation is unlikely given that the main ϵNd oscillation occurs prior to the second step of the isotope shift which represents the main phase of ice growth and associated sea level fall. The second explanation is perhaps the most likely given that synchronous changes in the position of the ITCZ in the Pacific record of Hyeong *et al.* (2016) have been documented in phase with first step of the $\delta^{18}\text{O}$ shift. This record may therefore lend support to the idea that EOT cooling was less pronounced in the northern hemisphere than in its southern counterpart hence causing a northward migration of the ITCZ during the first step of the EOT.

3.4.2 Evolution of Atlantic Ocean Circulation over Cenozoic Timescales:

Landmark Change at the EOT?

Several recent efforts have been made to develop long-term records of the evolution of the thermohaline circulation through the Cenozoic to facilitate a clearer understanding of the link between changing ocean circulation and fundamental changes in the wider climate system. In the earlier Cenozoic, during the Paleocene and earlier Eocene, deep water formation in the North Atlantic Ocean was impeded as the development of the basin towards its modern configuration was still in its infancy. Long-term records of Atlantic Ocean change have focused primarily on the South Atlantic and Southern Ocean (e.g. Scher and Martin, 2004; 2006; 2008). Indeed records developed from Walvis Ridge (ODP Site 1263) (Via and Thomas, 2006; Thomas and Via, 2007) depict a long-term increase in ϵNd values from c. 53 Ma to 36 Ma whereby values become much more radiogenic (from -9.11 at 56.5 Ma

to -5.87 at 36.8 Ma). These increasingly radiogenic values of ϵNd represent a change from the homogeneity of the early Eocene oceans due to the increasing influence of Pacific-sourced waters following the opening of Drake Passage. By the late Eocene greater homogeneity in the ϵNd values of the global ocean is seen. Beyond the EOT this long term trend appears to reverse at Walvis Ridge with ϵNd values decreasing to -11.20 by 16.5 Ma. This long-term decrease in values beyond the EOT has been mirrored at other sites in the Atlantic and Indian sectors of the Southern Ocean (e.g. Scher and Martin, 2008; Wright *et al.* 2018) and attributed to the increasing flux and southward influence of NCW on Circumpolar Deep Water (CDW). This interpretation is in line with stratigraphic and sedimentary evidence from drift deposits (Davies *et al.* 2001) and seabed erosional patterns (Howe *et al.* 2001) in the North Atlantic. These records all appear to suggest that the EOT marked a momentous change in ocean circulation, yet their resolution has as of yet been too coarse to conclude whether a reorganisation of Atlantic Ocean circulation pre- or post-dated Antarctic glaciation. Via and Thomas (2006) have previously described the coincidence of this reorganisation with landmark climate change at the EOT as just that; a coincidence. However, this study presents a record of ϵNd from Walvis Ridge that clearly depicts a substantial decrease in ϵNd unique to the South Atlantic region prior to the $\delta^{18}\text{O}$ shift characteristic of the EOT. This trend to less radiogenic ϵNd in the South Atlantic is interpreted here as a significant strengthening of NCW formation whereby NCW matures to include a system of cross-hemispheric AMOC for the first time.

3.4.2.1 Strengthening of NCW Formation Prior to the EOT

In order to attribute this change in ϵNd at Walvis Ridge to a change in ocean circulation, continental-derived run-off due to changes in weathering flux or source region of weathered material must be ruled out. This study suggests that a change in weathering regime is unlikely given that the ϵNd shift occurs (i) significantly prior (c. 1 myr) to the widespread growth of the AIS, (ii) much later than late Eocene small-scale glaciation events such as Priabonian Oxygen Isotope Maximum (PrOM) at c. 37.3 Ma (Scher *et al.* 2014) that may have prompted glacial weathering of nearby continents, and (iii) sites of closer proximity to significant sources of glacially weathered material show a much smaller magnitude of change or no change at all

across this interval. It is also vital to determine that the ϵNd shift represents a regional water mass signal and not simply part of a wider global trend in whole ocean ϵNd . Whilst any change in NCW flux would be propagated throughout the entire thermohaline circulation, it is reasonable to expect that any related signal would be most evident at sites in the immediate flow path of the northern-sourced water mass and greatest at those sites closest to its source. It is evident from figure 3.7 that this is indeed the case. The appearance of this $> 1 \epsilon$ unit shift in ϵNd between 34.76 Ma and 34.2 Ma appears to be isolated to the Atlantic Ocean region. The magnitude of ϵNd change is unmatched outside of the Atlantic Ocean region and the timing does not correlate with a substantial change at sites dominated by alternative water masses at the EOT.

In the previously published low resolution record of ϵNd from Walvis Ridge, Via and Thomas (2006) document a shift to more 'Atlantic' values around the time of the EOT compared to an absence of significant change in the ϵNd record from Maud Rise (ODP Site 689) in the Atlantic sector of the Southern Ocean (Scher and Martin, 2004). Similarly, comparison with the new high resolution record generated in this study suggests that the magnitude of change is much less across the same time interval at Maud Rise ($< 0.5 \epsilon$ unit between 34.7 Ma and 34.15 Ma) when compared to the $> 1 \epsilon$ unit of change at Walvis Ridge. The magnitude of change is not the only difference between the two sites. ϵNd at Maud Rise is consistently at least 0.5ϵ units more radiogenic than Walvis Ridge across this interval and therefore more akin to those documented at sites on Kerguelen Plateau in the Indian sector of the Southern Ocean across this time interval (Scher *et al.* 2011; Wright *et al.* 2018). The magnitude of change at all of the Kerguelen Plateau sites (ODP Sites 738, 744 and 748) is more comparable to that seen at Maud Rise; at ODP Site 748 ϵNd changes by 0.36ϵ units between 34.8 Ma and 34.3 Ma (Wright *et al.* 2018). It has been suggested that the decrease in ϵNd values on Kerguelen Plateau is likely as a result of the increasing influence of NCW on the composition of CDW (Wright *et al.* 2018). Similarly, it is likely that the differences between Maud Rise and Walvis Ridge are due to the relative proximity of the former to Antarctica. Its location places it within greater influence of proto-CDW. The small increase documented in values at Maud Rise and Kerguelen Plateau compared to the larger change at Walvis Ridge is likely

still as a result of the increasing influence of NCW on the composition of CDW (Wright *et al.* 2018). However, the main constituents of CDW at this time would have been Southern Ocean-derived bottom waters and Pacific throughflow from Drake Passage; both of these water masses are more radiogenic than true NCW. Thus the signal of NCW strengthening is diminished at these sites by mixing with these more radiogenic water masses that also make up proto-CDW.

One possible anomaly in the Atlantic sector of the Southern Ocean lies at ODP Site 1090 on Agulhas Ridge. Given that its latitudinal position places it between Walvis Ridge and Maud Rise (see figure 3.2), it might reasonably be expected that ϵNd values on Agulhas Ridge would lie between those found at the other two sites, hence documenting the diminishing southward influence of NCW. However, ϵNd appears to be even more radiogenic at Agulhas Ridge than at Maud Rise. Due to its significantly greater paleodepth (3400 metres) Site 1090 is likely subject to greater influence from the influx of Pacific-derived radiogenic Nd through Drake Passage to areas of deep water formation, such as the Weddell Sea, in the Southern Ocean (Scher and Martin, 2006). This signal is not mirrored at Maud Rise due to greater stratification of the late Eocene ocean where proto-AABW underlay the mid-depths of Maud Rise (1900 metres) (Scher and Martin, 2006).

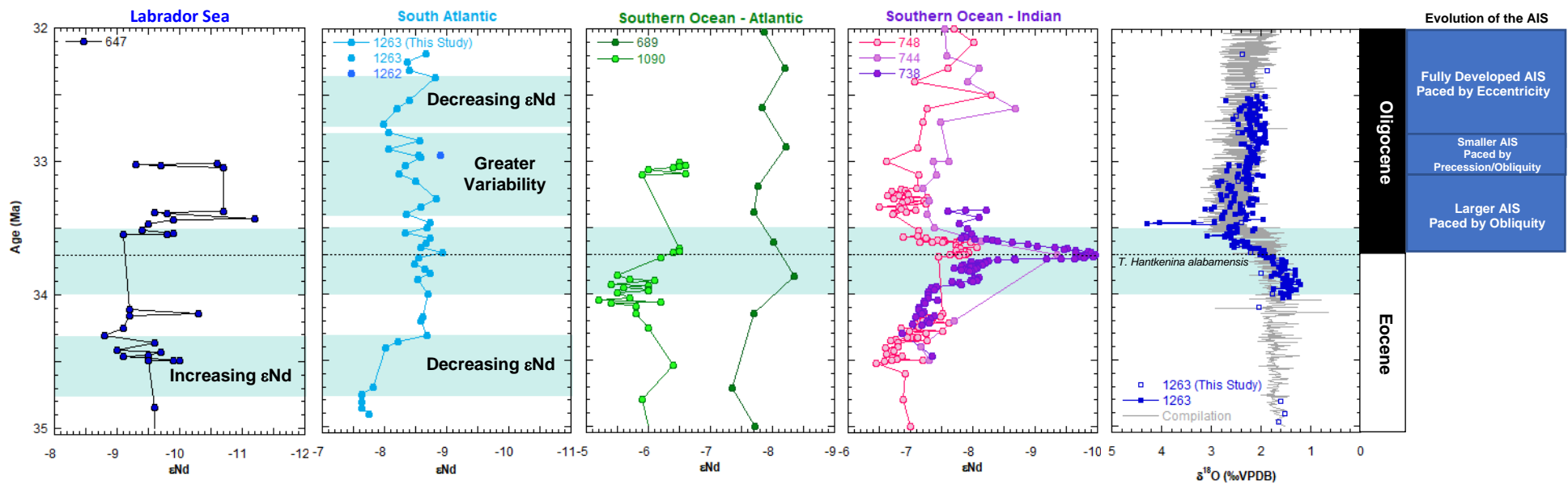


Figure 3.7 – ϵNd records from across the late Eocene and early Oligocene subdivided by ocean basin region. Records presented from the Labrador Sea (ODP Site 647 – Coxall *et al.* 2018); South Atlantic (ODP Site 1263 – Via and Thomas (2006) and this study); Atlantic sector of Southern Ocean (ODP Site 689 – Scher and Martin, 2004; ODP Site 1090 – Scher and Martin, 2006); Indian sector of Southern Ocean (ODP Site 738 – Scher *et al.* 2011; ODP Sites 744 and 748 – Wright *et al.* 2018). Oxygen isotope record presented from ODP Site 1263 (Rieselmann *et al.* (2007) and this study). Stages of Antarctic ice sheet evolution presented from Galeotti *et al.* (2016). Middle shaded bar shows duration of EOT. Top of *Hantkenina alabamensis* used to show position of EOB.

One location where a similar magnitude of change is seen is at ODP Site 647 in the Labrador Sea. Data from Coxall *et al.* (2018) demonstrate a change in ϵNd of equal magnitude (from -10.2 to -9.1) yet opposing direction across the same time interval as that documented at Walvis Ridge. ϵNd values become more radiogenic in the Labrador Sea as values in the South Atlantic become less so. This converging trend of ϵNd between ODP Site 647 and ODP Site 1263 suggests a common water mass source influencing both of these sites at this time lending support to an increased influence of NCW; this is a reinterpretation of the data from Coxall *et al.* (2018). This also provides useful insight into the likely source region from which NCW stems. Coxall *et al.* (2018) have identified that ϵNd values in the Labrador Sea do not reach modern values of NADW across the EOT and, as at Walvis Ridge, become more akin to values found in ISOW and DSOW (see figure 3.8). An absence of a contribution from LSW to NCW reinforces the idea that the evolution of modern-like NADW occurred later in the Cenozoic (after c. 10 Ma (Thomas and Via, 2007)) whilst NCW in the latest Eocene was predominantly derived from the Nordic Seas. As shown in figure 3.8, the timing of this increased influence of NCW lags the onset of the North Atlantic Ocean basin-wide negative $\delta^{13}\text{C}$ excursion (Coxall *et al.* (2018) and chapter four of this thesis); the source of which is attributed to the leakage of organic-rich fossil carbon from the Arctic Ocean. Not only do these ϵNd records support a northerly source for the isotopically-depleted carbon, but suggest that leakage of nutrient-rich, isotopically-depleted Arctic-sourced waters preceded the formal strengthening of NCW at 34.76 Ma.

Given the coherent picture from sites in the Atlantic and Southern Ocean regions, this study confidently attributes the decrease in ϵNd at Walvis Ridge to the strengthening of NCW formation prior to the EOT. Prior modelling work of Hutchinson *et al.* (2018) claims that a halving of atmospheric CO_2 leads to an increase in Arctic and North Atlantic salinities of c. 1 - 2 and 2 psu, respectively. However, this effect alone is insufficient to trigger sinking in the North Atlantic but could provide a forcing if the climate conditions were closer to a sinking regime due to a further forcing mechanism not represented in their model. The significant change in ϵNd coincides with the initial deepening of the GSR in the latest Eocene suggesting that the strengthening of NCW formation and its influence throughout the

Chapter Three: The Link between Atlantic Meridional Overturning Circulation and Antarctic Ice Sheet Dynamics across the Eocene Oligocene Transition

Atlantic Ocean basin was tectonically rather than climatically driven. Indeed, significant communication between the Nordic Seas and the rest of the Atlantic is a precondition that must be met for deep water formation to occur in the region. It is possible that this strengthening of NCW occurred as a result of both GSR deepening and CO₂ drawdown. However, it is unlikely that it would have occurred due to the latter alone.

Given the approximately 1 myr lag between the strengthening of NCW (34.76 Ma) and the onset of glaciation (33.7 Ma), it is clear that changing heat and salt distribution due to ocean circulation change was insufficient alone to cause growth of the AIS and associated climate change at the EOT. However, a more likely scenario is that a significant strengthening of NCW formation provided the pre-conditioning of the climate required for landmark climate change at the EOT when its ultimate trigger occurred (the coincidence of low eccentricity and low-amplitude change in obliquity). This orbital configuration was not unprecedented and does not seem to have been notably different to patterns of obliquity and eccentricity at other nodes which lack associated ice growth (Coxall *et al.* 2005). Thus it has long been acknowledged that, whilst it is considered the ultimate trigger of the EOT, some other forcing mechanism was required to condition the climate around the EOT to make it more susceptible to landmark change. The manner in which the intensification of NCW pre-conditioned the climate for landmark change and growth of the AIS at the EOT is likely due to changes in ocean heat transport; a process that plays a role in the regulation of global climate on long timescales (hundreds to thousands of years) and moderating interhemispheric temperature gradients. In the modern ocean NADW plays a key role in maintaining the heat balance between the northern and southern hemisphere (Broecker, 1991). The lower, cooler, southward flowing arm of the AMOC is counterbalanced by the northward flow of much warmer surface waters creating a constant transfer of heat across the equator from the southern to northern hemisphere that would, in the absence of the AMOC, build up in the Southern Ocean. Therefore, the waxing and waning of NADW, and this associated 'heat piracy' (Seidov and Maslin, 2001), can modulate the heat balance between the two hemispheres in what is known as the 'bipolar seesaw'; when AMOC is strongest the northward transfer of heat is greatest and the Southern Ocean cools relative to the North Atlantic, and vice versa. This study suggests that this mechanism primed the

climate for change under the orbital configurations of the EOT and led to the climatic effects of this landmark climate transition (e.g. deep and surface water cooling, and substantial growth of continental ice) being most greatly expressed in the high southern latitudes. Significant evidence in support of this theory lies within the absence of cooling in sea surface temperature records from the high northern latitudes compared to significant cooling in their southern counterparts (e.g. Liu *et al.* 2018). Chapter five of this thesis will discuss temperature asymmetry across the EOT in greater detail.

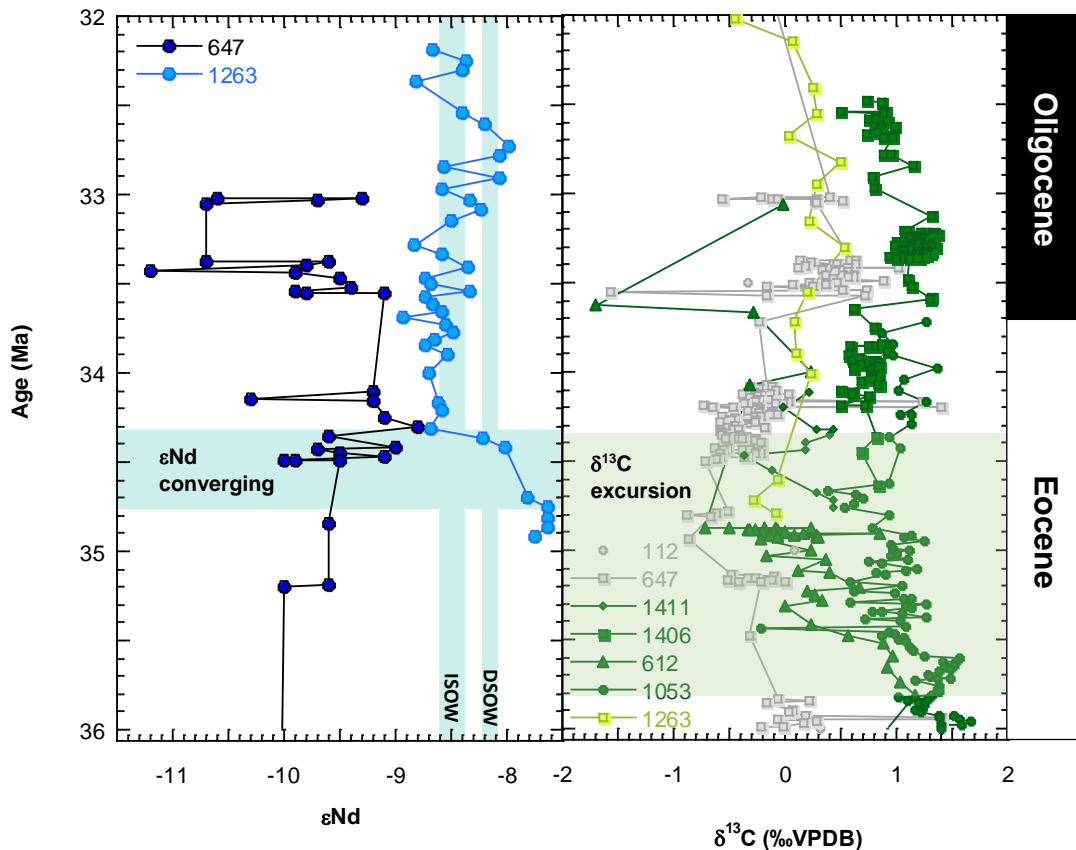


Figure 3.8 – Benthic foraminiferal carbon isotope records from the Labrador Sea (ODP Sites 112 and 647 (Coxall *et al.* 2018) in grey), the North Atlantic (IODP Site U1411, ODP Site 612 (Coxall *et al.* 2018), ODP Site 1053 (Borrelli *et al.* 2014), IODP Site U1406 (this study) in dark green) and the South Atlantic (ODP Site 1263 (this study) in light green) plotted with ϵ Nd from ODP Site 647 (Coxall *et al.* 2018) and ODP Site 1263 (this study). Age model calibrated to Cande and Kent (1995). Shaded vertical bars represent published values of DSOW and ISOW (Lacan and Jeandel, 2004a; 2004b). Shaded blue and green horizontal panels represent periods of ϵ Nd convergence between the Labrador Sea and the South Atlantic and the $\delta^{13}\text{C}$ excursion in the North Atlantic identified by Coxall *et al.* (2018).

3.4.2.2 Glaciation-Induced ϵ Nd Variability from 33.8 Ma to 32.7 Ma

Following the strengthening of NCW formation, ϵ Nd at Walvis Ridge stabilises until the onset of glaciation on Antarctica when greater variability is seen. ϵ Nd undergoes oscillations on the order of 0.4 – 0.5 ϵ units. This period of greater variability lasts for

around 1 myr; from the onset of glaciation at c. 33.8 Ma until 32.7 Ma. Greater variability in ϵNd following the growth of the AIS has been found in other records. Scher *et al.* (2011) document a large two-step ϵNd excursion at ODP Site 738 on Kerguelen Plateau between 33.9 Ma and 33.6 Ma synchronous with the two-step $\delta^{18}\text{O}$ increase. It is unlikely that this excursion is related to changes in NCW formation as: (i) it does not coincide with an excursion of similar or greater magnitude at sites closer to the source region of NCW; (ii) the second step of this excursion coincides with the presence of ice-rafted debris (IRD); and (iii) an excursion in ϵNd values of such a magnitude in the Indian sector of the Southern Ocean would require a 78% contribution of NCW to CDW (Scher *et al.* 2011), an unlikely composition of the circumpolar water mass in the earliest Oligocene. Scher *et al.* (2011) attribute this excursion to much more radiogenic values to an increase in the glacial-derived weathering flux of material from the newly developing continental ice sheet on Antarctica which wanes when the size of the ice sheet becomes self-limiting in its weathering capability. In a similar vein of thought, smaller oscillations on the order of 0.5 ϵ units at sites on Kerguelen Plateau following glaciation have been attributed to the locality of these sites to Antarctica and the regional influence of glacial variability in the earliest Oligocene (Wright *et al.* 2018). Kerguelen Plateau is located within close proximity to Prydz Bay, a major outlet for Antarctic-derived, weathered terrigenous material that is delivered to the southern end of Kerguelen Plateau by the Prydz Bay Gyre; an idea supported by the fact that the more southerly sites (those of closest proximity to the AIS) on Kerguelen Plateau exhibit the lowest ϵNd values (Wright *et al.* 2018). Therefore, it is valid to consider whether the increased variability in the Walvis Ridge record following glaciation could have occurred as a result of the same mechanism; did the waxing and waning of an early Oligocene AIS induce weathering-derived ϵNd oscillations in the South Atlantic record presented here? This study suggests that an Antarctic-derived weathering influence is unlikely due to: (i) the absence of significant change seen coeval with the large pulse documented by Scher *et al.* (2011); (ii) the increased distance between Walvis Ridge and Kerguelen Plateau from the AIS and its discharge outlets; and (iii) the overall trend exhibited at Walvis Ridge during this interval is opposing to that seen at other Southern Ocean sites.

However, comparison of the Walvis Ridge ϵNd record with records documenting the waxing and waning of the AIS (e.g. Galeotti *et al.* 2016) does reveal some interesting insights into a possible control of NCW variability by Antarctic ice sheet dynamics. As shown in figure 3.7, the interval of greatest variability in ϵNd immediately follows glaciation at the high southern latitudes. The initial phase coincides with a period of a larger-sized AIS, the waxing and waning of which is governed over obliquity time-scales. ϵNd oscillates on the order of 0.4 – 0.5 ϵ units, but these oscillations remain around an average value of -8.61; a value closely aligned with those depicting maximum NCW formation during its pre-EOT strengthening (-8.7). Across the second half of this interval between 33.15 Ma and 32.8 Ma, a small increase in ϵNd to more radiogenic values occurs; although over the course of these 350 kyr values do not recover to those of the interval prior to 34.76 Ma.

The new work presented here proposes two plausible mechanisms by which the AIS may exert control over NCW formation. Firstly, it is likely that the highly dynamic nature of the AIS during its infancy prompted oscillations in the relative strengthening and weakening of the two polar-sourced water masses whereby intensification of deep-water formation at one pole may have occurred at the expense of deep water formation at the other. Increasing ice volume on Antarctica is known to enhance production of AABW by the growth of sea ice and associated brine rejection (Ohshima *et al.* 2016). Under conditions of decreasing ice volume, increased freshwater run-off in to the Southern Ocean may freshen and impede formation of AABW. Sea ice extent is highly sensitive to orbital forcing (DeConto *et al.* 2007); it is possible therefore that this particular feedback exerted significant control over the balance of deep water formation during an interval when AIS extent was governed by higher frequency orbital forcing. The sensitivity of the thermohaline circulation to changes in AIS extent has been modelled previously; the addition of this AIS-ocean feedback mechanism has been found to align the drawdown of atmospheric CO_2 hypothesis with both the heterogeneity of temperature and $\delta^{18}\text{O}$ records across the EOT and the timing of the event (Goldner *et al.* 2014). A second mechanism by which the changing extent of the AIS may influence the flux of NCW is due to sea level oscillations associated with the growth and decay of the AIS. Relative sea level change with respect to sill depth at the GSR has previously been modelled to

modulate the strength of the gyre in the high northern latitudes and thus impact the flux of NCW across the GSR (Stärz *et al.* 2018). This hypothesis closely aligns with the series of short-term excursions to more negative ϵNd values at ODP Site 647 which have been attributed to increased weathering of old continental material surrounding the North Atlantic basin (Coxall *et al.* 2018). It is perhaps beyond the scope of the current study to clearly define which of these mechanisms plays the dominant role in influencing NCW formation. However, evidence presented in subsequent chapters of this thesis will highlight the importance of glacial-induced sea level-related weathering feedbacks in the high northern latitudes across the EOT. In addition suggestions for further work that might further explore these ideas are presented in the thesis synthesis in chapter six.

3.4.2.3 Renewed Intensity of NCW Formation from 32.7 Ma Onwards

From 32.7 Ma onwards, ϵNd at Walvis Ridge decreases once again from -7.99 to -8.66. It is only after 32.7 Ma once a fully developed, stable AIS exhibiting progressively stronger ice sheet hysteresis behaviour over enhanced long eccentricity cycles (Galeotti *et al.* 2016) that NCW intensifies once again. Interestingly the GSR also sinks below the surface-subsurface interface (> 50 metres below sea level) at around 32 Ma (Clift, 1996; Stärz *et al.* 2017); an age that slightly post-dates the renewed intensity of NCW formation in the ϵNd record from Walvis Ridge. At this point a fully-developed bi-directional seaway was established across the ridge most likely facilitating the long-term trend of strengthening NCW flux seen in both the South Atlantic and Southern Ocean during the later Oligocene and beyond. It is possible that the stabilisation of the AIS plays a greater role in the onset of a more mature and stable form of NCW given the change in ϵNd predates the deepening of the GSR. However, the latter cannot be ruled out given the crude resolution of the tectonic history of the dynamics of the GSR.

3.5 Chapter Summary

One striking realisation of the development of neodymium isotope records from around the world's oceans is the relative similarity of ϵNd water mass end members earlier in geological history. If figure 3.5 is examined with the exclusion of ODP Site 925, it becomes apparent that end members during the late Eocene and early Oligocene are much more similar to each other than those of the modern ocean. To some extent this has previously complicated the identification of individual source water masses and changes in competing water masses within paleo records. However, comparative examination of the newly developed ϵNd record from Walvis Ridge with existing records taking into consideration geographical location, paleo water depth and proximity to both the source of NCW and the AIS have allowed a convincing and exciting interpretation of changing ocean circulation at the EOT.

Evidence presented here from the South Atlantic substantiates previous suggestions that the evolution of modern NADW occurred in two distinct phases; the initial phase of which was dominated by a paleo-precursor to NADW known as NCW that stemmed primarily from the Nordic sea region. Evidence from the high northern latitudes had previously suggested that the onset of NCW occurred in the middle Eocene. Given the significant evidence presented here from a high resolution record of ϵNd from Walvis Ridge in the South Atlantic a significant strengthening of this primary phase of northern-sourced deep water formation can now be accurately identified as occurring in the latest Eocene; just under 1 myr prior to the EOT. This is the first record without ambiguity that shows the geochemical signature of NCW penetrating into the South Atlantic prior to the EOT and hence is the first to document the evolution of NCW into a system featuring cross-hemispheric AMOC. This evidence refutes the idea that a significant reorganisation of the thermohaline circulation occurred in response to global cooling at the EOT and rather suggests that the increasing influence of northern-sourced deep waters provided optimal conditions for landmark climate change prior to the occurrence of the ultimate trigger of the Earth's greenhouse-icehouse transition; the coincidence of low eccentricity and low-amplitude change in obliquity. It is suggested here that priming of the climate system by the intensification and interhemispheric transport of NCW and associated northern hemisphere heat piracy made it more susceptible to undergo previously

Chapter Three: The Link between Atlantic Meridional Overturning Circulation and Antarctic Ice Sheet Dynamics across the Eocene Oligocene Transition

unparalleled changes in Cenozoic climate most greatly expressed in the high southern latitudes through deep and surface water cooling, and the initiation of substantial volumes of continental ice on Antarctica. Whilst this strengthening of NCW was likely tectonically driven, the record generated during this study suggests that it was subsequently climatically modulated with a strong control exerted by the orbitally-paced waxing and waning of the AIS. The role of the AIS in controlling ocean circulation and associated global climate changes has serious implications given the likely magnitude of future changes in polar ice melt and a greater understanding of the processes that link the two is imperative.

Chapter Four

Productivity Changes across the Eocene Oligocene Transition

4.1 Introduction

4.1.1 Productivity Change at the Eocene Oligocene Transition

An extensive perturbation to the carbon cycle is expressed through the $\sim 1\text{‰}$ increase in benthic $\delta^{13}\text{C}$ and significant decrease in $p\text{CO}_2$ (Pearson *et al.* 2009; Pagani *et al.* 2011) at the EOT. The complex array of interactions responsible for forcing this fundamental change in Earth's climate 33.8 million years ago remains the topic of much debate and disentangling the precise mechanisms that tie the carbon cycle to the growth of the AIS presents significant challenges.

One such mechanism hypothesised to cause increased carbon sequestration (and hence drawdown of $p\text{CO}_2$) is enhanced primary productivity and associated export production. Primary production is defined as the synthesis of organic compounds from CO_2 ; this occurs largely by photosynthetic (using sunlight as its energy source) or, to a lesser extent, by chemosynthetic (using energy derived from the redox reactions of inorganic compounds) autotrophs in the photic zone of the upper water column. Net primary productivity is defined as the portion leftover after that necessary to sustain current producers has been consumed for respiration and existing cell maintenance; namely the total amount of organic carbon produced by autotrophs less the amount oxidised back to CO_2 during respiration (Bender *et al.* 1987). Secondary production in the ocean is defined as the amount of growth of heterotrophic biomass. Heterotrophs derive their energy solely from respiration of organic matter supplied by autotrophs. Hence, changes in overall oceanic biological productivity are largely due to changes in net primary productivity. It is within these terms that this chapter discusses changes in primary productivity. Export production is the portion of organic biomass that is successfully transferred from the surface (avoiding upper ocean recycling) to deep ocean. The proportion of material exported varies dependent on marine setting, but surface productivity is generally proportional to burial flux (Tribovillard *et al.* 2006). Changes in primary productivity and export production in the global ocean can occur due to changes in external and internal feedback mechanisms, including temperature, $p\text{CO}_2$, nutrient availability and ocean circulation. Similarly, changing productivity can serve as a feedback mechanism by releasing carbon to, or sequestering carbon from, the atmosphere. Thus,

understanding changes in export production can aid comprehension of the sensitivity of the biological pump under conditions of future climate change.

Numerous studies have detailed changes in primary productivity and export production from the Late Eocene to Early Oligocene. However, the timing and extent of change depends both on the study site location and the choice of paleoproductivity proxy used (Ladant *et al.* 2018). Indeed, reconstructions of paleoproductivity suggest a heterogeneous pattern of change at the EOT. At first glance, this heterogeneity would appear to be determined by latitude. Records from the high southern latitudes indicate increasing productivity across the EOT (e.g. Diester-Haas and Zahn, 1996; 2001; Salamy and Zachos, 1999; Schumacher and Lazarus, 2004; Villa *et al.* 2014) while, despite some suggestion of high-low latitude coupling (Coxall and Wilson, 2011), most records from lower latitudes and the tropics document either no change (e.g. Schumacher and Lazarus, 2004; Siesser *et al.* 1995) or decreasing productivity (e.g. Griffith *et al.* 2010; Erhardt *et al.* 2013; Moore *et al.* 2014).

Significantly, there is a distinct lack of records from the northern high latitudes; a region thought to have undergone significant oceanographic changes at this time. Primary productivity and associated export production exhibit significant geographical heterogeneity in the modern ocean. Decoupling of the productivity signal can occur between different ocean basins, particularly in response to variation in nutrient availability due to ocean circulation changes.

Recent research has warranted a greater investigation of the role played by the Arctic and North Atlantic in productivity changes at the EOT. Coxall *et al.* (2018) document the southward export of nutrient-rich, low $\delta^{13}\text{C}$ water imprinted by Arctic-sourced fossil carbon to the North Atlantic region in the million years leading up to the EOT. The authors suggest this initial pulse of NCW (the paleo precursor to NADW) could have played a role in preconditioning the climate for the EOT.

Therefore, the primary objective of this chapter is to investigate changes in primary productivity and export production change in the North Atlantic at the EOT. How did the initiation or intensification of a proto-NADW mass impact primary productivity and

export production in the Atlantic Ocean? What role did changes in primary productivity have on the carbon cycle perturbation at the EOT? What was its impact on $p\text{CO}_2$?

4.1.2 Paleoproductivity Proxies

Reconstructing changes in productivity through the geological past represents a complicated effort. Many proxies have been used in previous studies, but almost all are complicated by the presence of secondary effects and differing preservation of biogenic components and chemical indicators at the seafloor (Coxall and Wilson, 2011). Records taken to measure productivity changes through time must make every effort to account for these other factors. A record, or comparison of records, that apply multiple proxy measurements to samples may instil greater confidence in interpretations made about paleoproductivity (Moore *et al.* 2014). In this chapter, a suite of new benthic foraminiferal trace element data (including U/Ca and Mn/Ca) is presented from the North and Equatorial Atlantic and compared to a range of other proxies from sites in the Atlantic Ocean region.

4.1.2.1 Benthic Foraminiferal Trace Elements

4.1.2.1.1 U/Ca

Uranium (U) is conservative in seawater with a residence time of 250 kyr (Ku, 1977). Common benthic foraminiferal uranium concentrations are approximately 0.02 ppm (Ku, 1965; Delaney and Boyle, 1983) and between 1.2 – 4 ppm (Bertine *et al.* 1970; Bacon and Rosholt, 1982) for lattice-bound and authigenic coatings, respectively. It was originally claimed that foraminiferal U/Ca was dependent solely on the seawater uranium content with a small post-depositional effect from dissolution in samples taken above the lysocline (Russell *et al.* 1994). Subsequent studies however identified secondary effects on lattice-bound U/Ca; these include carbonate saturation state ($\Delta[\text{CO}_3^{2-}]$) (Russell *et al.* 1996; Russell *et al.* 2004; Raitzsch *et al.* 2011; Keul *et al.* 2013) and temperature (Russell *et al.* 2004; Yu *et al.* 2008). Uranium exists in seawater in three different carbonate complexes whereby one, two or three carbonyl groups are attached to a central uranyl ion (Clark *et al.* 1995). Although the latter form is the most common for uranium in seawater, their relative abundance depends on $\Delta[\text{CO}_3^{2-}]$. The abundance of those complexes with less

carbonate groups decreases with increasing $\Delta[\text{CO}_3^{2-}]$, hence the inverse relationship between planktic and benthic foraminiferal U/Ca and $\Delta[\text{CO}_3^{2-}]$ (Russell *et al.* 2004; Raitzsch *et al.* 2011).

U/Ca is also associated with changes in seafloor redox conditions (Barnes and Cochran, 1990). The primary mechanism by which uranium is removed from bottom water is by sediment uptake across the SWI (McManus *et al.* 2005). In low oxygen conditions, soluble uranium (U^{6+}) is reduced to insoluble uranium (U^{4+}) which forms authigenic coatings on the sediment (Boiteau *et al.* 2012). Uranium flux between the sediment and bottom water is controlled by both organic carbon flux and oxygen concentration. Uranium accumulates in its reduced form due to oxygen consumption during the degradation of organic matter. Hence, an increase in productivity and associated export production and/or a decrease in bottom water oxygen (BWO) would prompt shoaling of the oxygen penetration depth resulting in enhanced flux of insoluble uranium (U^{4+}) to the sediment. It can be difficult to disentangle the effects of BWO and productivity, but can be facilitated by use of other proxies (Boiteau *et al.* 2012).

4.1.2.1.2 Mn/Ca

Manganese (Mn) is also a redox-sensitive element (Glock *et al.* 2012), but has almost opposing redox behaviour when compared to uranium. Under oxic conditions soluble manganese (Mn^{2+}) is oxidised to form solid-phase manganese oxides (MnO_x) in the sediment. In low oxygen conditions, solid manganese oxides (MnO_x) are reduced to soluble manganese (Mn^{2+}). Therefore, in low BWO conditions, pore water Mn^{2+} concentration is higher and benthic foraminiferal lattice-bound Mn/Ca is higher.

Several studies have attempted to use benthic foraminiferal Mn/Ca as a proxy for past changes in BWO (e.g. Klinkhammer *et al.* 2009; Chun *et al.* 2010; Ni Fhlaithearta *et al.* 2010; Pälike *et al.* 2014). However, many studies have highlighted both the need for species-specific considerations such as microhabitat preferences (Koho *et al.* 2008; 2015; 2017) and the complexity of deconvolving the effects of BWO and productivity (McKay *et al.* 2015). Hence, this chapter will combine the use of both benthic foraminiferal U/Ca and Mn/Ca.

4.2 Methodology

4.2.1 Geological Setting

Samples spanning the Eocene Oligocene boundary were analysed from sediment cores recovered from IODP Expedition 342 Site U1406 (Newfoundland Sediment Drifts - 40°21.0'N, 51°39.0'W) and ODP Leg 154, Site 925, Hole A (Ceara Rise - 4°12.249'N, 43°29.334'W). Sites discussed in this chapter are shown in figure 4.1.

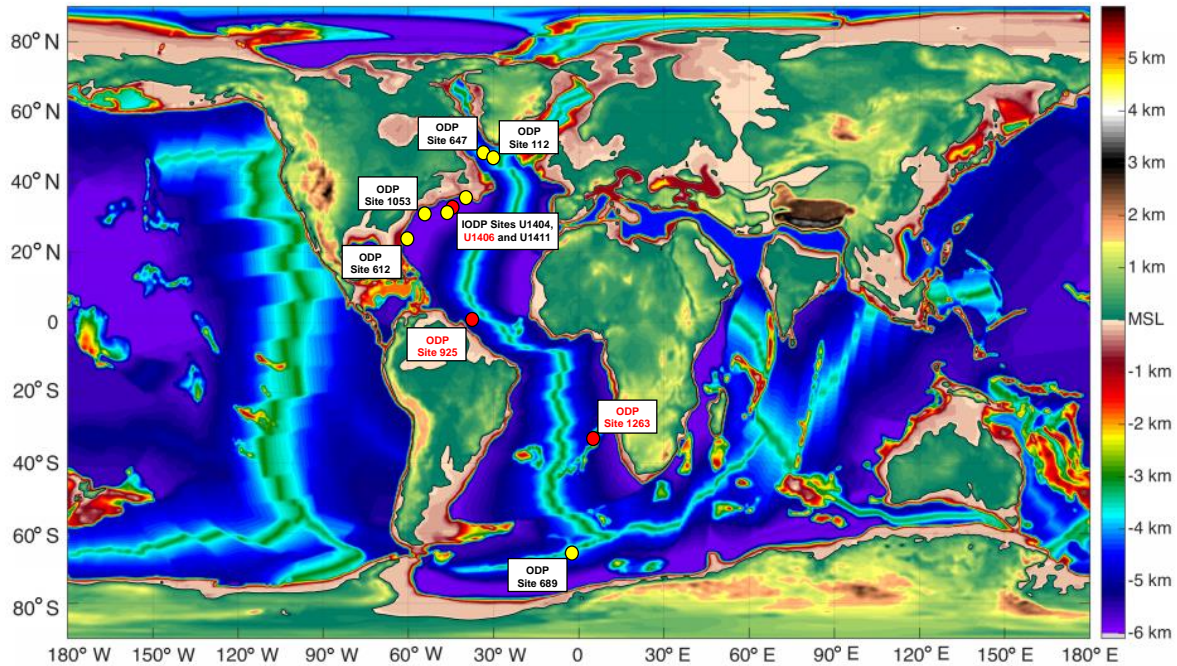


Figure 4.1 – Location of ocean drilling sites used, or discussed, in this study displayed on paleogeographic map from Baatsen *et al.* (2016). Red dots indicate sites from which new data has been generated in this thesis. Yellow dots indicate sites from which existing published data is presented for comparison purposes.

ODP Site 925 is the shallowest site drilled as part of Leg 154 on Ceara Rise, an aseismic rise bounded by the Ceara abyssal plain to the west and the Amazon cone to the east, in the western equatorial Atlantic Ocean. Its paleo water depth of 2500 metres places it directly within the core of modern NADW at the EOT making it an incredibly well-placed site to monitor the increasing influence of any proto-NADW in the latest Eocene and earliest Oligocene. In its modern, low-latitude, oceanographic setting the productivity regime at ODP Site 925 remains relatively constant throughout the year. Productivity tends to be low due to a relatively deep mixed layer, convergence and downwelling (Peterson and Stramma, 1991). Some small seasonal variations in the mixed layer depth can be attributed to changes in the relative strength of the north and southeastern trade winds due to the shifting position

of the ITCZ; productivity increases when weaker trade winds allow a shallowing of the thermocline. Samples of 20 cm³ from ODP Site 925 were taken between 746.43 and 850.14 mbsf at an average temporal resolution of 50 kyr.

The Newfoundland ridges (J-Anomaly Ridge and Southeast Newfoundland Ridge) lie offshore of Newfoundland, north western Canada. These plastered ridges are mantled with contourite, pelagic carbonate drift deposits (Norris *et al.* 2014). IODP Site U1406 is located in the North Atlantic Ocean on J-Anomaly Ridge placing it directly underneath the path of the Atlantic DWBC. The modern productivity regime in the Northwestern Atlantic is dominated by a distinct seasonality; the North Atlantic spring bloom is one of the largest in the global ocean due to a combination of oceanographic and biological forcing (Tilstone *et al.* 2014). The slowdown of intensified wintertime convective mixing, restratification of the water column and shoaling of the mixed layer depth leads to increased nutrient availability in the photic zone that are rapidly consumed due to increasing daylight hours (Sundby *et al.* 2016). Following the cessation of the spring bloom, boreal summertime productivity is much lower. Its location and paleo water depth of 3300 metres at c. 50 Ma make in an ideal site to monitor changing ocean circulation and deep-water formation in the North Atlantic through time (Boyle *et al.* 2017). With this in mind, samples of 20 cm³ from IODP Site U1406 were taken between 187.66 and 206.48 mbsf at an average temporal resolution of 10 kyr but with intervals of higher resolution sampling (~ 2 – 5 kyr) across key intervals including the step-wise change in $\delta^{18}\text{O}$ and the EOGM.

4.2.2 Chronology

Chronology for ODP Site 925 is based solely on biostratigraphy as magnetostratigraphic age control was unavailable for sites collected during Leg 154. Sample ages are based on the planktonic foraminifera biostratigraphic framework presented by Pearson and Chaisson (1997). The datums presented therein have been updated to those published by Wade *et al.* (2011). Chronology for IODP Site U1406 is based on shipboard biostratigraphic datums (Norris *et al.* 2014) and revised magnetostratigraphy (Van Peer *et al.* 2017). Both age models are calibrated to the timescale of Cande and Kent (1995) and are presented in greater detail in chapter two of this thesis.

4.2.3 Sample Preparation and Analysis

Samples were prepared and cleaned prior to analysis as outlined in chapter two of this thesis according to a condensed version of the cleaning protocol of Boyle and Keigwin (1985). For ODP Site 925, benthic foraminiferal stable isotopes were generated from a minimum of five individuals of *Cibicidoides havanensis* from a homogenised sample picked from the 250 – 355 μm size fraction. These samples were analysed at Cardiff University on a ThermoFinnigan MAT252 with online sample preparation by an automated Kiel II carbonate device. Analytical error for this data set, based on repeat analysis of standard NBS-19, is 0.04‰ for $\delta^{18}\text{O}$ and 0.02‰ for $\delta^{13}\text{C}$. For IODP Site U1406, between five and ten individuals of *Cibicidoides mundulus* were run from the 150 – 250 μm size fraction. These samples were analysed at the National Oceanography Centre (NOC) Southampton. Analytical error for this dataset, based on analysis of in-house standard GS1, isotopically similar to NBS-19, is 0.03‰ for $\delta^{18}\text{O}$ and 0.04‰ for $\delta^{13}\text{C}$.

For analysis of their trace element content samples were prepared and cleaned prior to analysis as outlined in chapter two of this thesis according to the cleaning protocol of Boyle and Keigwin (1985). The full oxidative and reductive clean was carried out on these samples as this study aimed to utilise the full suite of trace element data, not only the U/Ca and Mn/Ca data presented here. For ODP Site 925 and IODP Site U1406, a minimum of five individuals of *Oridorsalis umbonatus* were picked from the 250 - 355 μm size fraction to be analysed for their trace element composition. *Oridorsalis umbonatus* is a popular choice for the production of trace element data as it has a wide geographic distribution allowing easy inter-site comparison. It is also a species present in the modern ocean allowing the development of accurate core-top calibrations. For ODP Site 925, a minimum of five individuals of *Cibicidoides havanensis* were also analysed for their trace element composition to enable precisely paired stable isotope and trace element data to be produced from a single homogenised sample. In addition, due to their epifaunal habitat, *Cibicidoides* species are more sensitive to changes in bottom water saturation state than shallow infaunal *Oridorsalis umbonatus*; an important consideration when developing trace element records across the EOT.

4.3 Results

4.3.1 North Atlantic

4.3.1.1 IODP Site U1406 – The Newfoundland Sediment Drifts

Benthic foraminiferal stable isotope and trace element data obtained from 142 samples from IODP Site U1406 are presented in figure 4.2. In the late Eocene, centred on 35 Ma, the record shows a negative $\delta^{13}\text{C}$ excursion that reaches a minimum of 0.49‰ at 34.85 Ma. Isotopically lighter values last until the base of the isotope shift at 33.63 Ma. During this late Eocene period values of $\delta^{18}\text{O}$ average just under 1‰.

The isotopic shift at IODP Site U1406 is characterised by a ~ 0.7‰ and 1‰ increase in $\delta^{13}\text{C}$ and $\delta^{18}\text{O}$, respectively. The $\delta^{13}\text{C}$ excursion is somewhat temporary in nature with values recovering to pre-shift values of approximately 0.8‰ by 33 Ma. In contrast, the now isotopically heavier $\delta^{18}\text{O}$ values of between approximately 1.5‰ and 2‰ persist into the early Oligocene. Coincident with the increase in $\delta^{18}\text{O}$, benthic foraminiferal U/Ca begins to increase from consistently less than 50 nmolmol⁻¹ to almost 200 nmolmol⁻¹. Shortly thereafter during the EOGM, c. 33.2 Ma, peak U/Ca values of 531 nmolmol⁻¹ are reached. Values decline rapidly before a smaller, secondary maxima in U/Ca of 343 nmolmol⁻¹ occurs at 32.68 Ma (figure 4.2).

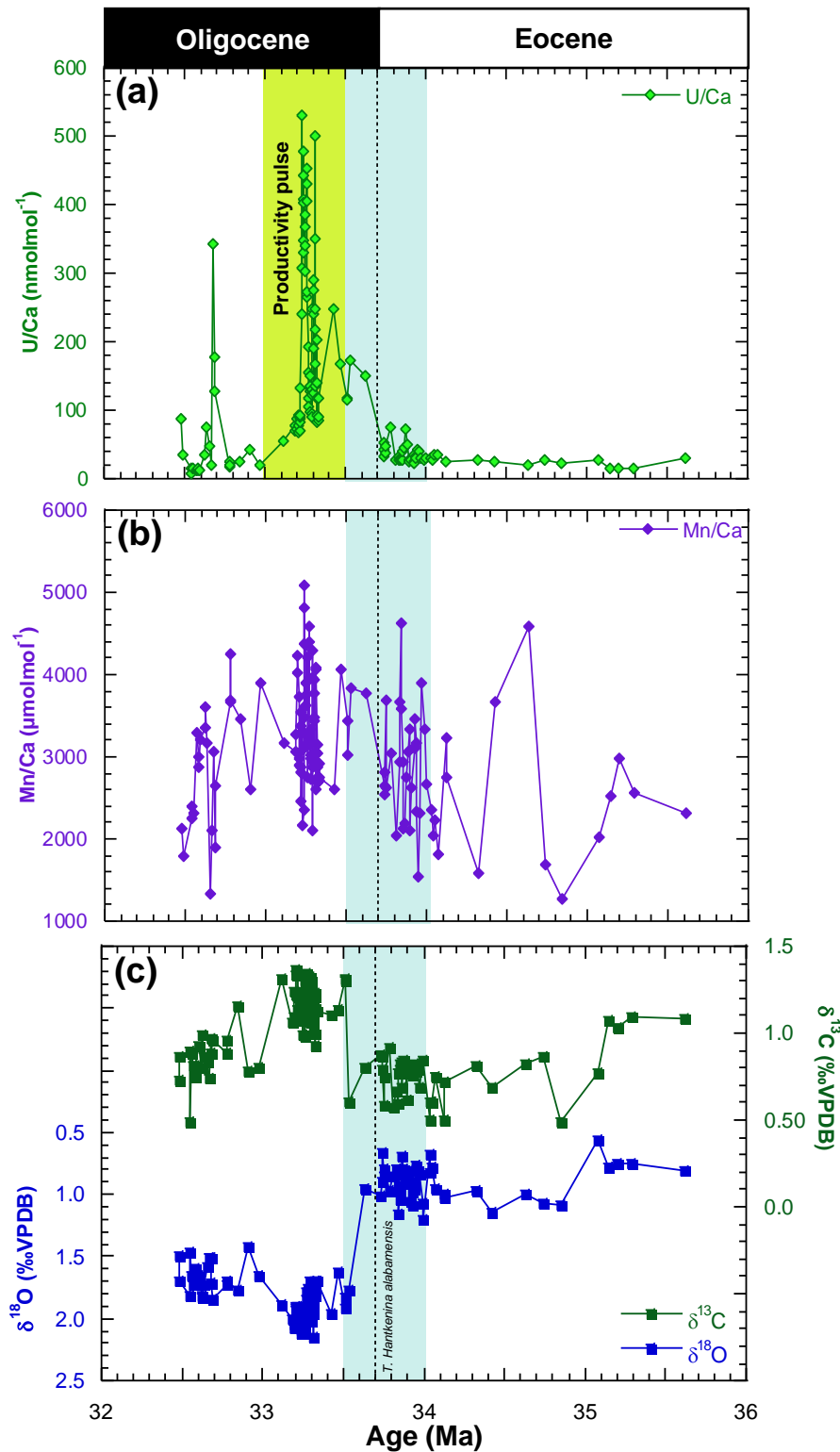


Figure 4.2 – Benthic foraminiferal U/Ca (a), Mn/Ca (b) and stable isotopes (c) from IODP Site U1406 generated as part of this study. Stable isotope data generated from *Cibicidoides havanensis* and trace elements from *Oridorsalis umbonatus*. Pale blue shaded bar indicates EOT. EOB marked by top of *Hantkenina alabamensis*. Green shaded bar indicates pulse of productivity pulse. Age model calibrated to Cande and Kent (1995).

4.3.1.2 The Wider North Atlantic

The results obtained from IODP Site U1406 in this study are compared to the existing published records from the North Atlantic region in figure 4.3. Benthic foraminiferal stable isotope records are presented from ODP Site 647 and DSDP Site 112 in the southern Labrador Sea (Coxall *et al.* 2018), and IODP Site UU1411, DSDP Site 612 (Coxall *et al.* 2018) and ODP Site 1053 (Borrelli *et al.* 2014) in the North Atlantic. Abundance of alkenone C³⁷ at IODP Site U1404 in the North Atlantic across the EOT is taken from Liu *et al.* (2018). Benthic foraminiferal U/Ca from ODP Site 647 is also shown (H.K. Coxall and C.H. Lear, unpublished). These latter two proxies are used as productivity indicators.

In the late Eocene, values of $\delta^{18}\text{O}$ at IODP Site U1406 are comparable to those from ODP Site 1053 (Borrelli *et al.* 2014) and IODP Site U1411 (Coxall *et al.* 2018). This observed array of North Atlantic values vary between 0.4 and 1.2‰. $\delta^{18}\text{O}$ values from ODP Site 647 in the Labrador Sea deviate significantly from this trend where, prior to 35.8 Ma, values are between 1‰ and 3‰ lower than at more southerly sites. Values only start to increase following 35.8 Ma when they become more akin to other North Atlantic sites around 34.3 Ma. During this same period, $\delta^{13}\text{C}$ values at ODP Site 647 are also substantially different. Prior to 35.8 Ma, they are approximately 0.5‰ to 1‰ lower than other North Atlantic sites, including IODP Site U1406. Between 35.8 Ma and 33.8 Ma, a negative $\delta^{13}\text{C}$ excursion of between 0.5‰ and 1‰ is documented at all North Atlantic sites, including IODP Site U1406. The exact magnitude and precise timing of this excursion varies based on the site location. The latter is likely dictated by small differences in age models. Coxall *et al.* (2018) determined that the largest excursions occur at those sites sitting directly downstream of ODP Site 647 in the DWBC where values become more akin to those seen in the Labrador Sea. IODP Site U1406 fits with this conclusion where the magnitude of the $\delta^{13}\text{C}$ excursion is around 0.6‰.

The shift in $\delta^{18}\text{O}$ at c. 33.65 Ma is relatively uniform across the North Atlantic basin. At ODP Site 647 $\delta^{18}\text{O}$ increases by 1.22‰, from 0.22‰ to 1.44‰, between 33.72 Ma and 33.57 Ma; a similar magnitude to the 1‰ shift seen at IODP Site U1406. $\delta^{13}\text{C}$ increases at the two sites by 0.95‰ and 0.7‰, respectively. Whilst values of

Chapter Four: Productivity Changes across the Eocene-Oligocene Transition

$\delta^{18}\text{O}$ remain relatively stable at c. 1.5‰ across the EOGM, values of $\delta^{13}\text{C}$ recover to pre-shift values by approximately 33 Ma at IODP Site U1406. At ODP Site 647, $\delta^{13}\text{C}$ values remain higher than those of the late Eocene but do undergo a decrease.

The benthic foraminiferal U/Ca increase at IODP Site U1406, described in the previous section, is mirrored by an increase in U/Ca at ODP Site 647 and an increase in alkenone abundance at IODP Site U1404 indicating a regionally coherent trend (figure 4.3). ODP Site 647 U/Ca increases from 33 nmolmol⁻¹ at 34 Ma to 133 nmolmol⁻¹ at 33.5 Ma. Alkenone abundance increases from 0.9 to 7.9 ngg⁻¹ across the isotope shift. Peak values are reached at 33 Ma. A secondary peak of 44 ngg⁻¹ is seen at 32.2 Ma.

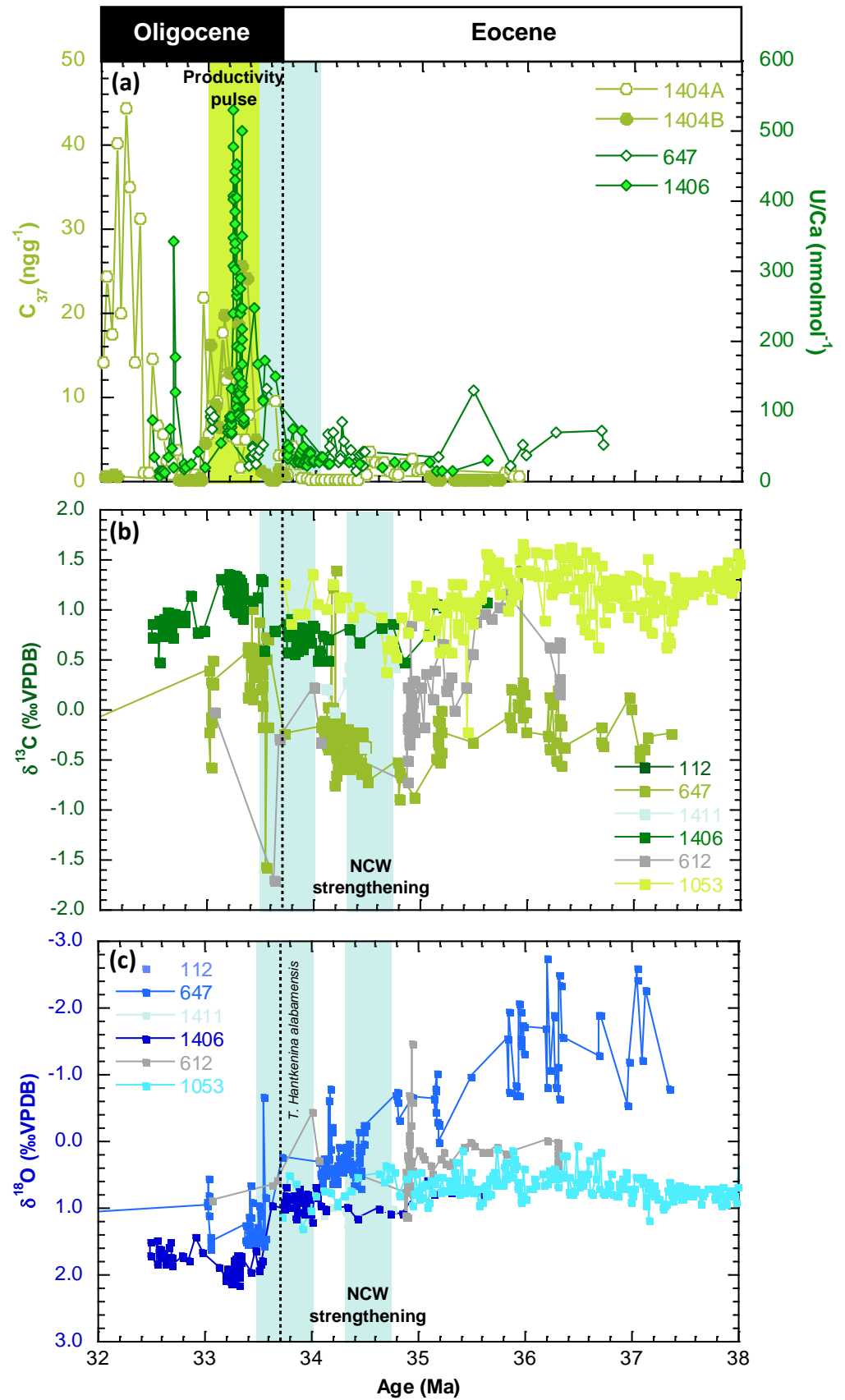


Figure 4.3 – Productivity indicators (a), benthic foraminiferal $\delta^{13}C$ (b) and $\delta^{18}O$ (c) from the North Atlantic. Stable isotope data presented from Sites 112, 647, UU1411, 612 (Coxall *et al.* 2018), 1053 (Borrelli *et al.* 2014) and U1406 (this study). Productivity indicator data includes benthic foraminiferal U/Ca (U1406 – this study, 647 – H.K. Coxall and C.H. Lear, unpublished) and alkenone abundance (UU1404 – Liu *et al.* 2018). Pale blue shaded bars indicate duration of EOT and NCW strengthening. EOB marked by top of *Hantkenina alabamensis*. Green shaded bar indicates pulse of productivity pulse. Age model calibrated to Cande and Kent (1995).

4.3.2 Equatorial Atlantic

4.3.2.1 ODP Site 925 – Ceara Rise

Benthic foraminiferal stable isotope and trace element data obtained from 56 samples from ODP Site 925 are presented in figure 4.4. In the late Eocene, centred on 35.5 Ma, the record shows a negative $\delta^{13}\text{C}$ excursion that persists for around 800 kyr similar to that identified in the North Atlantic records. A 0.4‰ minima occurs at 35.59 Ma. U/Ca of *Cibicidoides havanensis* increases during this minimum.

$\delta^{13}\text{C}$ values recover to 1.4‰ by 34.89 Ma. From this point to the base of the isotope shift at 33.9 Ma $\delta^{13}\text{C}$ values slowly decrease to 0.72‰. $\delta^{18}\text{O}$ values are relatively stable during this time averaging around -0.5‰. This places ODP Site 925 outside of the typical array of North Atlantic $\delta^{18}\text{O}$ values discussed in the previous section. It is not currently clear why these values are lower than most other North Atlantic sites, sitting closer to values seen in the Labrador Sea in the late Eocene. Most likely this is a result of recrystallization of the geothermal gradient at high burial depths (~ 850 mbsf for the deepest sample at ODP Site 925) whereby elevated temperature leads to lower $\delta^{18}\text{O}$ values. $\delta^{18}\text{O}$ will be much more sensitive to processes that cause recrystallization than $\delta^{13}\text{C}$.

The isotopic shift at ODP Site 925 is characterised by a ~ 1.0‰ increase in $\delta^{13}\text{C}$ and $\delta^{18}\text{O}$. Thus, whilst absolute values of $\delta^{18}\text{O}$ are somewhat unusual when compared to other North Atlantic records, the relative change across the isotope shift is indeed comparable. The now higher values of $\delta^{18}\text{O}$ persist into the early Oligocene, whereas the positive $\delta^{13}\text{C}$ excursion is more transient in nature with values recovering to pre-shift values of approximately 0.9‰ by 33.2 Ma.

Similar to the trends identified in the North Atlantic that are coincident with the substantial increase in $\delta^{18}\text{O}$, the U/Ca of all three benthic foraminifera species increases. The greatest increase of U/Ca occurs in *Oridorsalis umbonatus*, a shallow infaunal species, whereby values increase from 23 nmolmol⁻¹ at 33.9 Ma to 179 nmolmol⁻¹ at 33.5 Ma.

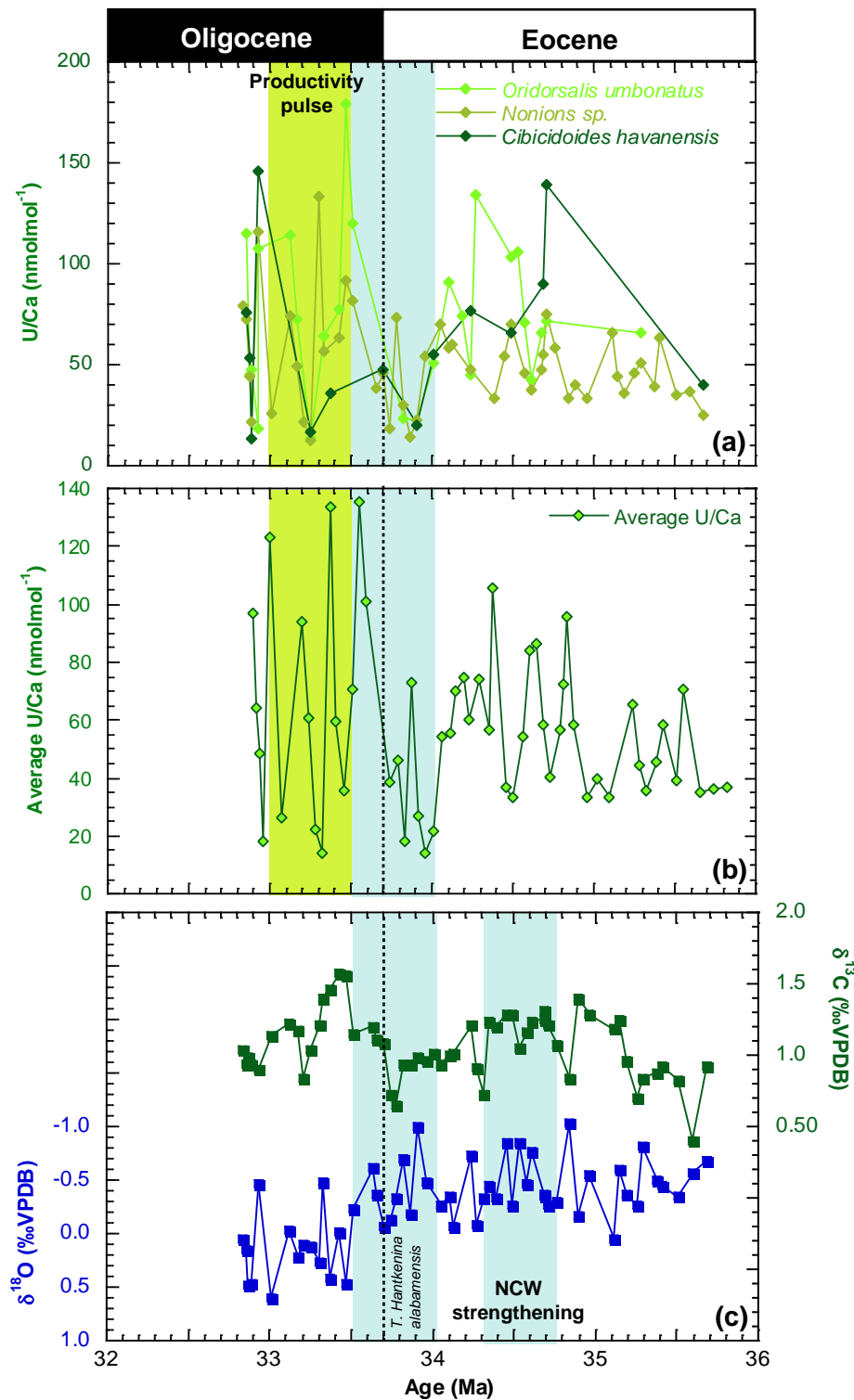


Figure 4.4 – Benthic foraminiferal stable isotope and U/Ca data from ODP Site 925 generated as part of this study. U/Ca generated from *Cibicidoides havanensis*, *Nonions sp* and *Oridorsalis umbonatus* (a). Average U/Ca calculated as the mean of the U/Ca value from each of the three species for any given sample (b). Stable isotope data generated from *Cibicidoides havanensis* (c). Pale blue shaded bars indicate duration of EOT and NCW strengthening. EOB marked by top of *Hanfkenina alabamensis*. Green shaded bar indicates pulse of productivity pulse. Age model calibrated to Cande and Kent (1995).

4.3.2.2 The Wider Equatorial Atlantic

The results obtained from ODP Site 925 in this study are compared to the existing published records from Ceara Rise of Diester-Haas and Zachos (2003) and Nilsen *et al.* (2003) in figure 4.5. Nilsen *et al.* (2003) presented records of biogenic barium, total reactive phosphorus, biogenic silica and calcium carbonate with the aim of reconstructing export production, nutrient burial and the ratio of organic to inorganic carbon burial in the Equatorial Atlantic. Similarly, Diester-Haas and Zachos (2003) presented records of bulk sediment carbon isotope ratios, percent coarse fraction, radiolarian accumulation rates and benthic foraminiferal accumulation rates (BFAR).

In figure 4.5, the increase in U/Ca associated with both the $\delta^{13}\text{C}$ minima centred around 35.5Ma and with the isotope shift coincide with key changes in productivity indicators presented by these two previous studies. Diester-Haas and Zachos (2003) document two distinct increases in the accumulation of radiolaria across the study interval of interest. The first, an increase from $1.94 \text{ mgcm}^{-2}\text{ky}^{-1}$ to $40.1 \text{ mgcm}^{-2}\text{ky}^{-1}$, occurred between 35.69 Ma and 34.54 Ma. The start of this increase coincides with the $\delta^{13}\text{C}$ minima and increasing U/Ca presented in this study. The second interval occurs in sync with the isotope shift. Radiolarian accumulation rate increases from $0.35 \text{ mgcm}^{-2}\text{ky}^{-1}$ to $35.82 \text{ mgcm}^{-2}\text{ky}^{-1}$ between 33.6 Ma and 33.14 Ma. Concurrently, Nilsen *et al.* (2003) document an increase in biogenic silica abundance from 3.49% to 19.20% between 33.61 Ma and 33.13 Ma.

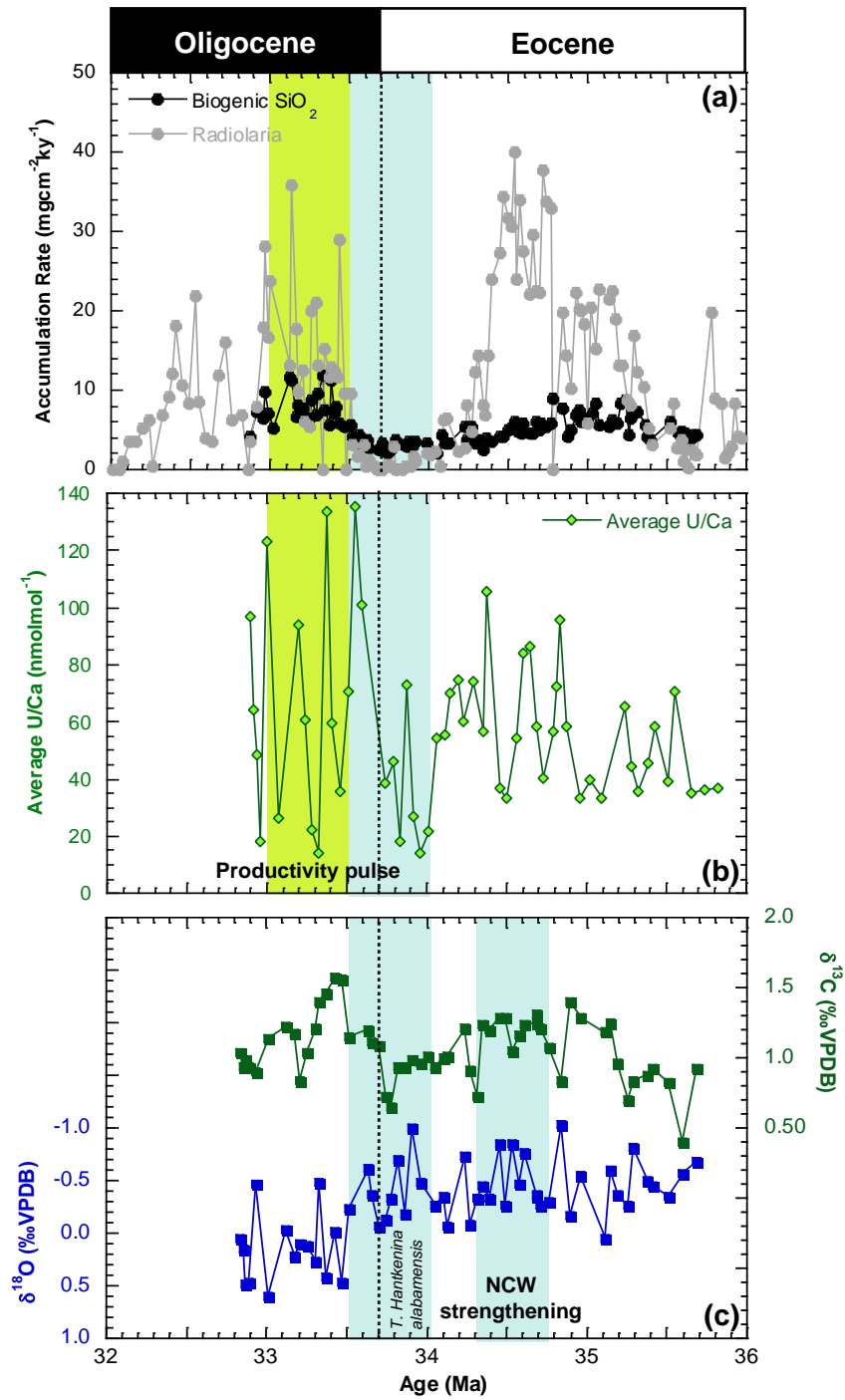


Figure 4.5 – Benthic foraminiferal stable isotopes and productivity indicator data from ODP Site 925 in the equatorial Atlantic. Productivity indicator data includes benthic foraminiferal U/Ca (this study) (a), biogenic silica accumulation rate (Nilsen *et al.* 2003) and radiolaria accumulation rate (Diester-Haas and Zachos, 2003) (b). Stable isotope data presented from ODP Site 925 (this study) (c). Pale blue shaded bars indicate duration of EOT and NCW strengthening. EOB marked by top of *Hantkenina alabamensis*. Green shaded bar indicates pulse of productivity pulse. Age model calibrated to Cande and Kent (1995).

4.4 Discussion

4.4.1 Atlantic Ocean Change at the EOT

Based on the trends identified in the previous section, it would appear that the northeastern and equatorial Atlantic Ocean region responded reasonably consistently across latitudes at several key intervals through the latest Eocene and earliest Oligocene. In this section, the northern hemisphere (north and equatorial) Atlantic Ocean will be discussed as one region.

4.4.1.1 A Late Eocene Incursion of Arctic-Sourced Waters

An Atlantic Ocean wide negative $\delta^{13}\text{C}$ excursion of between 0.5‰ and 1‰ is identified at all sites in the latest Eocene. The exact magnitude and precise timing of this excursion varies based on the site location. The latter is likely dictated by small differences in age models. Recent work by Coxall *et al.* (2018) suggests that this low benthic foraminiferal $\delta^{13}\text{C}$ signal results from older, poorly ventilated and nutrient-rich Arctic-sourced waters flowing into the North Atlantic in an initial pulse of NCW. Results presented in chapter three of this thesis show that the leakage of nutrient and organic-rich waters from the Arctic Ocean preceded the formal onset of NCW at 34.76 Ma. Contrary to the enriched $\delta^{13}\text{C}$ signal of well-ventilated and nutrient-depleted modern NADW, it is proposed that this early NCW was imprinted by nutrient stocks derived from fossil carbon in a fresher (Brinkhuis *et al.* 2006), more isolated Arctic basin with a strong hydrological system and high fluvial input. An absence of Pacific-Arctic Ocean throughflow forced the outflow of nutrient-rich, low $\delta^{13}\text{C}$ water through the Nordic Seas (Onodera *et al.* 2008; O'Regan *et al.* 2011). The conformity of the results presented here from IODP Site U1406 and ODP Site 925 substantiate this idea. Both sites lie within the typical Atlantic $\delta^{13}\text{C}$ array during this excursion and show excursions of smaller magnitude than the northern-most sites present by Coxall *et al.* (2018) lending support to the idea that this signal was propagated from the north and flowed southward through the Atlantic.

4.4.1.2 Changing Redox Conditions at the EOT: Primary Production or Bottom Water Oxygen?

A transient increase in benthic foraminiferal U/Ca along with a smaller increase in benthic foraminiferal Mn/Ca is seen in association with the EOT in both the North and

Equatorial Atlantic. U/Ca and Mn/Ca begin to increase synchronous with increasing ice volume at the isotope shift with peak U/Ca values reached very early in the EOGM.

Manganese and uranium are both highly redox sensitive elements that can be influenced by both changes in organic carbon flux and changing BWO. Therefore, the changes in redox conditions reconstructed in this study could be driven by i) increased productivity, ii) decreased oxygen concentration of bottom waters or iii) a combination of both. Whilst it can be difficult to disentangle the effects of BWO and productivity on redox conditions as they are inherently inter-related (McKay *et al.* 2015) and hypoxic conditions occur naturally in areas of high productivity (Groenvelde and Filipsson, 2013) within only millimetres of the SWI (McKay *et al.* 2015) a multi-proxy approach can facilitate interpretations (Boiteau *et al.* 2012).

Uranium flux between the sediment and pore water is controlled by both organic carbon flux and oxygen concentration. In low oxygen conditions, soluble uranium (U^{6+}) is reduced to insoluble uranium (U^{4+}) which forms authigenic coatings on the sediment (Boiteau *et al.* 2012). Uranium accumulates in its reduced form due to oxygen consumption during the degradation of organic matter. Hence, an increase in productivity and associated export production and/or a decrease in BWO would prompt shoaling of the oxygen penetration depth resulting in enhanced flux of insoluble uranium (U^{4+}) to the sediment and increasing benthic foraminiferal U/Ca. Porewater manganese has also been shown to reflect changes in BWO and organic carbon flux. Under oxic bottom water conditions, manganese is transported to the seafloor in the form of oxides. When these oxides breach the redox boundary in the sediment, where pore water oxygen (PWO) is depleted due to organic matter remineralization, they are reduced to soluble Mn^{2+} which diffuses upwards towards the SWI and reprecipitates as manganese oxides under oxygenated conditions once again.

In this study, it is clear that Mn/Ca systematics can help to deconvolve the signal depicted by the U/Ca record as, while crucial calibration work for benthic foraminiferal Mn/Ca is lacking (Koho *et al.* 2015; Barras *et al.* 2018), the importance of considering

changes in faunal assemblage is well documented (McKay *et al.* 2015). Some efforts have been made to investigate the effect of benthic foraminifera microhabitat preferences on test Mn/Ca values (e.g. Reichart *et al.* 2003; Koho *et al.* 2008; Koho *et al.* 2015; Koho *et al.* 2017). Subsequent conceptual modelling efforts (e.g. TROXCHEM – Koho *et al.* 2015) have combined benthic foraminiferal ecology with test Mn/Ca to deconvolve past BWO and productivity changes. This work has shown that under BWO conditions bordering on hypoxic, shallow infaunal species of benthic foraminifera (such as *Oridorsalis umbonatus*) incorporate little Mn unless the flux of organic matter to the sediment is high. Such species show little response to changes in BWO (Glock *et al.* 2012; Koho *et al.* 2017) as they rarely calcify under oxygen-depleted conditions (Koho *et al.* 2015). However, if the oxygen penetration depth shoals due to enhanced remineralisation under conditions of increased organic matter loading, yet bottom waters remain oxic, shallow infaunal species tolerant of low oxygen conditions are exposed to increased Mn^{2+} and possess higher values of Mn/Ca (Koho *et al.* 2015) as documented on the Newfoundland margin at the EOT where peak values of Mn/Ca are associated with the same of U/Ca. This suggests that the U/Ca excursion documented at IODP Site U1406 and ODP Site 925 is likely a result of increased organic flux to the seafloor rather than significant changes in BWO. Here, a shoaling of the redoxcline would occur due to the increased delivery of organic matter thus increasing the flux of insoluble U^{4+} into the sediment and benthic foraminiferal U/Ca.

This conclusion is supported by the coincidence of U/Ca with increased alkenone abundance (shown in figure 4.3) in the North Atlantic. The alkenone abundance data, originally published by Liu *et al.* (2018) and used to calculate a 25 million year record of SST changes in the North Atlantic based on their degree of saturation ($U^{K_{37}}$), can be used to make inferences about primary productivity at IODP Site U1404 across the time interval of interest. Indeed, these C_{37} alkenones (long-chain unsaturated ketones synthesised by near-surface dwelling microalgae) have been used to reconstruct primary productivity over much younger timescales in other ocean basins (e.g. Jasper and Gagosian, 1989; Rostek *et al.* 1997; Wernke *et al.* 2000). Furthermore, an increase in the supply of organic matter is far more logical than BWO depletion under conditions of Atlantic Ocean circulation change at the

EOT. It is hardly feasible to invoke BWO depletion when $\delta^{13}\text{C}$ values suggest that regional bottom waters became less stagnant and NCW became more akin to the better ventilated modern NADW.

Other factors shown to influence benthic foraminiferal U/Ca include $\Delta[\text{CO}_3^{2-}]$ (Russell *et al.* 1996; Russell *et al.* 2004; Raitzsch *et al.* 2011; Keul *et al.* 2013) and temperature (Russell *et al.* 2004; Yu *et al.* 2008). However, it is unlikely that changing $\Delta[\text{CO}_3^{2-}]$ is responsible for this transient increase. Firstly, based on the documented inverse relationship between $\Delta[\text{CO}_3^{2-}]$ and U/Ca, the increase in U/Ca would suggest decreasing $\Delta[\text{CO}_3^{2-}]$. This is contrary to the trend of a deepening CCD shown in many records to be associated with the EOT. Based on the established relationship between B/Ca and $\Delta[\text{CO}_3^{2-}]$ (Yu and Elderfield, 2007; Yu *et al.* 2010) an absence of change in benthic foraminiferal B/Ca from this site (see appendix 4) also refutes any implied CCD changes. Moreover, the transient nature of the U/Ca excursion contradicts the permanent change in the CCD across the EOT. Temperature is not a probable cause either given the absence of cooling at this site evident from benthic foraminiferal Mg/Ca (see appendix 4 and chapter five of this thesis). Additionally, recent studies have cast doubt over the temperature control on U/Ca (Raitzsch *et al.* 2011). Moreover, the absolute values of both U/Ca and Mn/Ca at these sites suggest that they are not likely lattice-bound trace element ratios representative of a primary bottom water signal. Benthic foraminifera with high ($>100 \mu\text{molmol}^{-1}$) Mn/Ca, such as those recorded here, are commonly associated with high ($> 300 \text{ nmolmol}^{-1}$) U/Ca (Chen *et al.* 2017). Both more likely signify changes in the extent of authigenic coatings and therefore a change in sedimentary redox conditions at these sites that this study attributes predominantly to increasing primary productivity.

4.4.2 A Basin-Wide Atlantic Ocean Productivity Increase

A substantial body of research has focused on establishing the link between productivity change and the glaciation of Antarctica at the EOT. Simply growing an ice sheet on the Antarctic continent causes a steepening of latitudinal thermal gradients which intensifies upwelling-induced productivity by a wind and ocean circulation driven 'spinning up' of the oceans (Diester-Haas and Zahn, 1996; Salamy and Zachos, 1999; Miller *et al.* 2009). The efficiency of wind and ocean circulation driven upwelling in the Southern Ocean has also been linked to both the onset (c. 41

Ma) and strengthening (associated with AIS growth) of the ACC (Latimer and Filippelli, 2002; Scher and Martin, 2006). Both of these have been identified as positive feedbacks on the climate system by drawing down atmospheric CO₂ and, in the latter case, reducing PHT to Antarctica. In any case this body of work highlights the role that might have been played by glaciation-induced productivity changes in regulating important climate feedbacks.

The timing and extent of productivity change at the EOT depends both on the study site location and the choice of paleoproductivity proxy used (Ladant *et al.* 2018). Previous work detailing paleoproductivity reconstructions suggest a heterogeneous pattern of change at the EOT that appears to be determined by latitude. Records from the high southern latitudes indicate increasing productivity across the EOT (e.g. Diester-Haas and Zahn, 1996; 2001; Salamy and Zachos, 1999; Schumacher and Lazarus, 2004; Villa *et al.* 2014) while, despite some suggestion of high-low latitude coupling (Coxall and Wilson, 2011), most records from lower latitudes and the tropics document either no change (e.g. Schumacher and Lazarus, 2004; Siesser *et al.* 1995) or decreasing productivity (e.g. Griffith *et al.* 2010; Erhardt *et al.* 2013; Moore *et al.* 2014). However, the results presented in this chapter do not necessarily conform to this high-low latitude contrast in productivity changes. Instead, this study has presented a regional increase in primary productivity across the EOT in the north and equatorial regions of the Atlantic Ocean. It is important to consider, however, whether this trend is mirrored in records from the southern high latitudes. In figure 4.6, records of primary productivity from ODP Site 689 (Maud Rise in the Atlantic Ocean Sector of the Southern Ocean) are compared to those presented in this study.

Figure 4.6 suggests that there was a homogenous productivity response occurring at the EOT within the Atlantic Ocean. As discussed earlier, in the North and Equatorial Atlantic productivity starts to increase synchronous with glaciation; a trend mirrored at ODP Site 689 where primary productivity (export productivity in the surface waters calculated from benthic foraminiferal abundance according to the method of Herguera and Berger (1991)) increases coeval with the onset of glaciation. Similarly, a return to pre-excursion values is also seen to be synchronous between the

northern and southern regions of the basin. These results suggest a basin-wide productivity response of the Atlantic Ocean at the EOT; in contrast to the decreasing productivity documented in the Pacific Ocean (e.g. Griffith *et al.* 2010; Erhardt *et al.* 2013; Moore *et al.* 2014). This significant decoupling of productivity changes by basin likely occurred as a result of basin-specific changes in ocean circulation and, hence, a redistribution of the nutrient inventory. By the time nutrient-rich waters are transported through the Atlantic and Southern Oceans and northward through the Pacific, they become nutrient-depleted due to nutrient uptake in the Southern Ocean. This idea is consistent with both model results that show an increased uptake of nutrients in the Southern Ocean limits northward transport in to the Pacific (Sarmiento *et al.* 2004) and a latitudinal gradient of BFAR showing a northward decrease through the Pacific (Griffith *et al.* 2010; Erhardt *et al.* 2013).

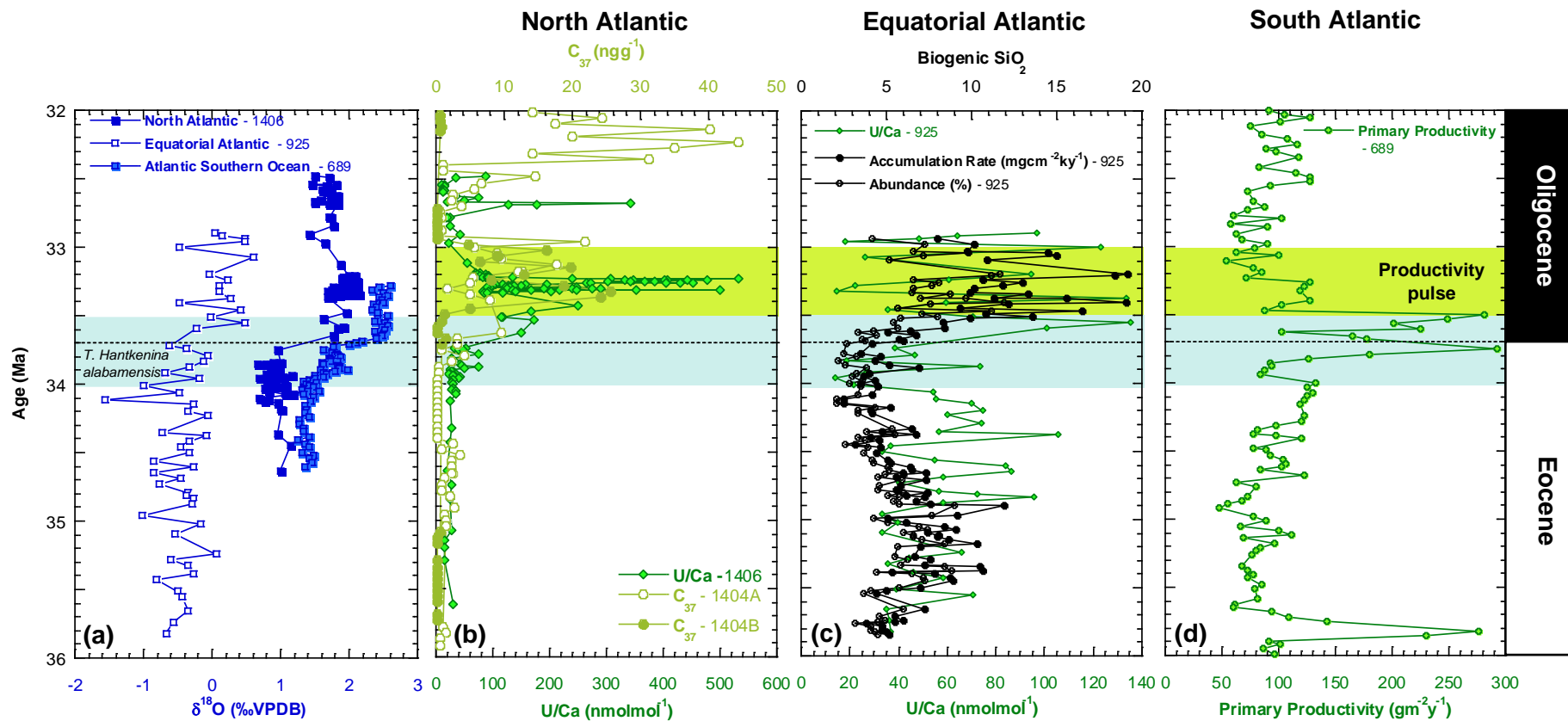


Figure 4.6 – (a) Benthic foraminiferal stable isotopes from IODP Site U1406 (Newfoundland Sediment Drifts, North Atlantic – this study), ODP Site 925 (Ceara Rise, Equatorial Atlantic – this study) and ODP Site 689 (Maud Rise, South Atlantic sector of Southern Ocean – Bohaty *et al.* (2012)). Productivity data taken from this study and Liu *et al.* (2018) for North Atlantic (b); this study and Nilsen *et al.* (2003) for Equatorial Atlantic (c); Diester-Haas and Zahn (1996) for Atlantic sector of Southern Ocean (d). Pale blue shaded bar indicates duration of EOT. EOB marked by top of *Hantkenina alabamensis*. Green shaded bar indicates pulse of productivity pulse. Age model calibrated to Cande and Kent (1995).

4.4.3 Forcing the Early EOGM Productivity Pulse

This section will discuss the likely forcing mechanism behind the productivity pulse associated with the isotope shift. Productivity changes can be driven by both internal (e.g. more efficient nutrient recycling, shifts in upwelling regime) and external (e.g. changes in continental weathering flux) processes. Previous studies of paleoproductivity across the EOT have suggested an external forcing mechanism is most likely based on apparent eccentricity paced cycles identified in records of biogenic barium, reactive phosphorus (Nilsen *et al.* 2003) and BFAR (Diester-Haas and Zachos, 2003) from Ceara Rise. In addition, these same records demonstrate a coincidence of increasing export production and increasing nutrient burial. Under conditions determined by changes in internal feedback mechanisms, such as more efficient nutrient recycling, increased export production would not equal increased nutrient burial. Increased preservation of organic matter could be caused by an increased sedimentation rate, reduced BWO, or regional cooling. However, the regional nature of the productivity increase, the absence of evidence for cooling across the shift at IODP Site U1406 and a lack of substantial increase in sedimentation rate suggests better preservation of organic matter is not a factor at play here. Therefore, an external forcing mechanism such as increased nutrient supply or intensification of weathering rates is more likely.

The differentiation between an internal and external feedback mechanism also has important implications for the likely effect on the carbon cycle and the subsequent drawdown or release of $p\text{CO}_2$. The amount of externally sourced nutrients responsible for what is commonly termed 'new production' can determine the capability of the deep ocean to sequester carbon (Bristow *et al.* 2017); a key area of interest across the EOT.

4.4.3.1 Glaciation-Induced Silicate Weathering

The carbonate-silicate cycle, namely the balance between silicate weathering and decarbonation reactions, is largely responsible for pacing oscillations in atmospheric CO_2 concentration over geological timescales and has the greatest potential for sequestering carbon in the deep ocean (Kelly *et al.* 2010). Weathering of silicate rocks serves as a sink for CO_2 and a source of alkalinity to the oceans through

delivery of Ca^{2+} and HCO_3^- ions. Some of this CO_2 is released during carbonate mineral precipitation. The remaining CO_2 is eventually released when the carbonate sediments are exposed to temperatures high enough to prompt its release during decarbonation reactions. Hence, enhanced silicate weathering leads to decreased atmospheric CO_2 content.

Several studies have suggested a link between silicate weathering, atmospheric CO_2 and glaciation of Antarctica. Elsworth *et al.* (2017) suggested that atmospheric CO_2 drawdown across the EOT can be explained by an intensification of silicate weathering due to a 5% increase in precipitation over land due to a strengthening AMOC associated with the opening of Drake Passage. Other studies have suggested that increased silicate weathering at the EOT due to Antarctic glaciation may explain the significant CCD deepening and provide a positive feedback on glaciation by drawing down atmospheric CO_2 (Zachos and Kump, 2005; Basak and Martin, 2013) or have linked the associated increase in silicate flux to the ocean with documented increases in primary productivity across the climate transition (Zachos *et al.* 1999). Indeed, many Southern Ocean records show increasing biogenic silica accumulation associated with the EOT (Diester-Haas *et al.* 1995; Diester-Haas and Zahn, 1996; Diester-Haas and Zahn, 2001). This could explain the link between enhanced silicate weathering, primary productivity increase and the positive excursion in $\delta^{13}\text{C}$ by invoking an increase in the ratio of organic to inorganic carbon burial.

However, it is unlikely that the regional pulse in productivity documented in this study occurred due to increased silicate weathering. In the first instance, figure 4.6 shows that primary productivity begins to increase immediately following the EOB, coeval with the onset of glaciation across step two of the isotope shift at 33.7 Ma. Peak productivity values are reached early in the EOGM (c. 33.3 Ma). The importance of this timing is two-fold. Firstly, any change in silicate weathering associated with the intensification of AMOC would likely coincide with the NCW strengthening dated to 34.7 Ma (identified in chapter one of this thesis); a delay of 1 My between NCW strengthening and the primary productivity increase and associated CO_2 drawdown renders this hypothesis unlikely. Secondly, several studies have investigated the

timescales over which the silicate weathering negative feedback on $p\text{CO}_2$ operates (e.g. Sundquist, 1991; Lenton and Britton, 2006). Most recently Colbourn *et al.* (2015), using a new weathering model (Rock-Geochemical Model (RokGeM)) in combination with the GENIE Earth System Model, provided new estimates of the timescale over which the climate re-equilibrates, through weathering action, following a sizeable carbon perturbation. This study identified an e -folding timescale, namely the time for which it would take the $p\text{CO}_2$ level to be reduced by a factor of e , to lie within the range of 170 to 380 kyr. However, it is also worth noting that this approach assumes an instantaneous release of CO_2 emissions to the atmosphere rather than an increase occurring over longer timescales. Even the upper estimate is therefore likely an underestimate of the timescale over which the climate re-equilibrates. Therefore, if enhanced silicate weathering associated with Antarctic glaciation were responsible for increased primary productivity and the drawdown of atmospheric CO_2 , one would expect the interval between the onset of glaciation and the stabilisation of CO_2 to be greater than the timeframe documented here.

In addition, the manner in which silicate weathering is both physically and chemically moderated make it an unlikely candidate here. Physical weathering exposes a greater surface area of silicate rocks to chemical weathering. When physical weathering rates are low, the amount of chemical weathering is limited by the supply of newly exposed surfaces (West *et al.* 2005). However, when physical weathering rates are higher, the chemical weathering rate becomes limiting. Under these latter conditions, the role of increasing temperature, precipitation and acidity becomes much more important (Colbourn *et al.* 2015). Hence, it is unlikely that silicate weathering served as the forcing mechanism for increased primary productivity and drawdown of CO_2 given that: (i) the increase in weathering associated with glaciation is likely physical; (ii) the likely increase in temperature, precipitation and acidity associated with AMOC strengthening that would increase chemical weathering predates this interval by around 1 my, and (iii) the interval of increased primary productivity and accelerated drawdown of atmospheric CO_2 immediately follows widespread cooling associated with step one of the isotope shift.

4.4.3.2 The Shelf-Nutrient Hypothesis

Given the heterogeneous biogeochemical response of the ocean at the EOT, the forcing mechanism responsible for this basin-wide pulse of productivity associated with glaciation is likely also regional in nature. If the forcing mechanism responsible for this pulse in productivity is likely external, then the source from which it stems is vitally important. Previous studies have highlighted the potentially important source of organic and nutrient-rich material provided by the Arctic around this time. As already discussed, Coxall *et al.* (2018) propose that isotopically light fossil carbon sourced from the relatively isolated Paleogene Arctic basin can be held responsible for the negative $\delta^{13}\text{C}$ excursion centred around 35 Ma. During the Eocene, the Arctic Ocean was far more isolated than in its modern tectonic configuration (Onodera *et al.* 2008). No throughflow from the Arctic to the Pacific Ocean akin to modern existed until the Pliocene (O'Regan *et al.* 2011) and, with a strong hydrological cycle and high fluvial input (Brinkhuis *et al.* 2006), the Arctic served as a semi-isolated sink for nutrient-rich organic matter. Any signal derived from changes in the Arctic Ocean would be propagated southward through the North Atlantic.

Results from this study suggest that this very same region served as the nutrient-rich source fuelling the productivity pulse in the Atlantic at the EOT. However, given the lag between the onset of NCW and the pulse in productivity, the nutrient-rich source is seemingly locked up until another forcing prompts its release into the local Arctic waters which are then propagated southwards by the already established NCW. Continental shelf sediments abundant around Arctic Ocean margins served as a vast sink for nutrient accumulation in the latest Eocene by storing huge amounts of solid organic matter. Following glaciation, and the associated sea level fall, organic matter formerly residing on the shelf would have been exposed to weathering and its high nutrient content was redistributed to local Arctic waters and propagated southward through the North Atlantic region by surface water overflows that formed part of the bidirectional seaway established between the Arctic and North Atlantic Ocean across the GSR by this time (Stärz *et al.* 2017). Indeed northern hemisphere salinity profiles from the Atlantic basin document evidence of a freshwater Arctic Ocean influence on North Atlantic surface waters alongside increasing incursion of NCW at depth (Coxall *et al.* 2018). The increased bioavailable oceanic nutrient inventory carried southward

Chapter Four: Productivity Changes across the Eocene-Oligocene Transition

in cold, fresh Arctic surface waters, further enhanced by the decreased capacity of the continental shelf sink, would have increased primary productivity and associated export production.

This mechanism was originally proposed to explain the link between Pleistocene glacial sea level low stands and peaks in marine productivity (Broecker, 1982). Many subsequent studies have focused on this so-called Shelf-Nutrient Hypothesis as a feedback mechanism linking glaciations, primary productivity and atmospheric CO₂ (Filippelli *et al.* 2007; Tamburini and Föllmi, 2009; Tshumi *et al.* 2011). Many of the Pleistocene modelling studies focus solely on the reorganisation of burial sinks and fail to account for any resultant increase in weathering flux which would only have compounded the effect seen in the Shelf-Nutrient Hypothesis (Flores *et al.* 2012). This potential additive effect is extremely relevant in this case given the extensive evidence of increased flux of weathered continental material at the EOT, particularly in the high northern latitudes associated with intensification of North Atlantic overturning (e.g. Elsworth *et al.* 2017).

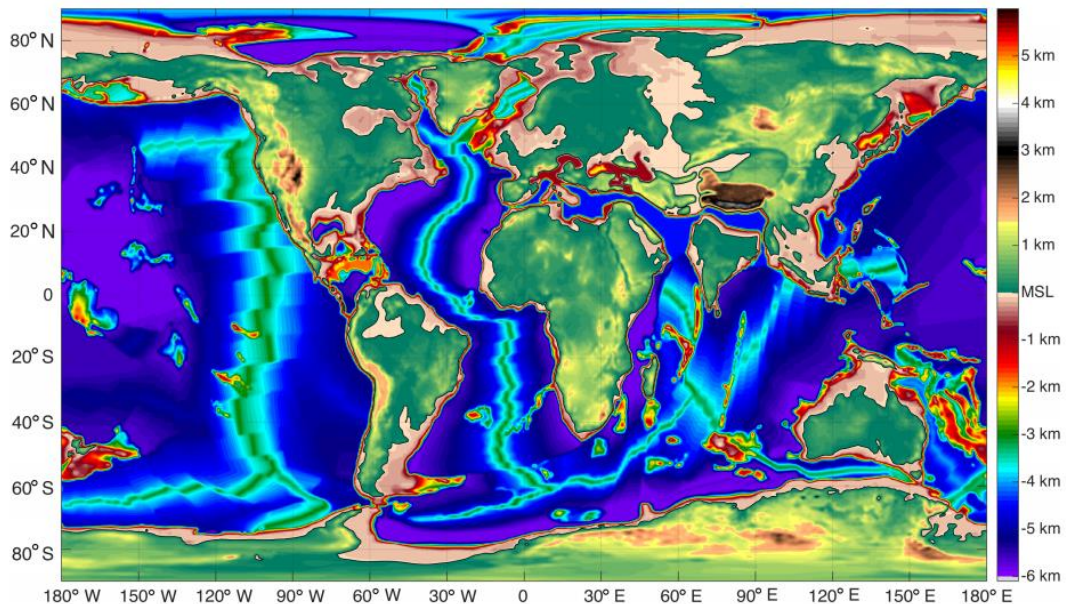


Figure 4.7 – Map of Late Eocene paleogeography (c.38 Ma) showing paleo- topography and bathymetry. Paleogeography map from Baatsen *et al.* (2016).

Given that this discussion has already demonstrated significant heterogeneity in the biogeochemical response of the ocean at the EOT, it is prudent to question why this process did not cause a globally uniform pulse of productivity and why the Arctic Ocean could influence regional primary productivity to such an extent. The modern Arctic Ocean is significantly influenced by the composition of the material at its margin sources. While the current flux of shelf-derived eroded sediment is roughly equivalent to that of other ocean basins, continental shelves account for more than 50% of the area of the Arctic Ocean basin (Kipp *et al.* 2018). Indeed, shelf regions are tenfold larger in the Arctic than those surrounding its southern counterpart (Walsh, 1989) meaning any changes in shelf input from northern high latitudes have a disproportionately large impact when normalised to basin area (Kipp *et al.* 2018). This is especially true at the EOT when northern hemisphere shelf regions were much larger due to differences in paleogeography (see figure 4.7). In addition, many studies have demonstrated the geographically heterogeneous response of sea level to changes in ice volume dependent on the dominant region of ice growth or ice loss (e.g. Mitrovica *et al.* 2001). It has been repeatedly shown that when the mass of continental ice changes in Antarctica, the greatest sea level response will be seen in far-field regions (Bamber *et al.* 2009; Mitrovica *et al.* 2009; Gomez *et al.* 2010) suggesting that the sea level-induced exposure of continental shelves would have been greatest in the Arctic and North Atlantic regions. Therefore, the effect of the Shelf-Nutrient Hypothesis is likely heightened in the Arctic Ocean at the EOT compared to other ocean basins or at other times in geological history. Hence, it is likely that the Arctic region plays a vitally important and previously understudied role in influencing the ocean chemistry of the North Atlantic region at the EOT.

4.4.4 Implications for the Carbon Cycle at the EOT

Implications for the carbon cycle at the EOT as a result of increased primary productivity are interesting given: (i) the widespread perturbation to the carbon cycle that occurred at this time represented by the ~1‰ increase in $\delta^{13}\text{C}$ and significant decrease in atmospheric CO_2 ; and (ii) the fact that it is now thought that the modern Arctic Ocean is responsible for around 14% of the global ocean uptake of atmospheric CO_2 (Bates and Mathis, 2009). Broecker (1982) initially proposed that the Shelf-Nutrient Hypothesis would serve as a positive feedback loop in times of

glaciation where by increased nutrient supply would increase productivity, drawdown atmospheric CO₂ and further enhance climatic conditions favourable to glaciation.

Certainly this mechanism would have a huge impact on the phosphorus cycle given that the continental margin sink for reactive phosphorus is almost equal to that of the deep ocean despite accounting for less than 10% of total ocean area (Flores *et al.* 2012). This is likely due to high sedimentation rates, lower nutrient recycling, high marginal productivity (Filipelli *et al.* 2007) and the increased solubility of reactive phosphorus containing material under the acidic conditions of subaerial exposure caused by sea level fall (Guidry and Mackenzie, 2003). Phosphorus is a key limiting nutrient for productivity in the global ocean (Wu *et al.* 2000) and is suggested to be the ultimate control acting on primary productivity over geological timescales (Tyrell, 1999; Compton *et al.* 2000). Specifically, the potential impact of changes to the biological availability of reactive phosphorus (phosphorus that enters the ocean and is available for uptake (Compton *et al.* 2000)) is huge; an increase in phosphorus entering the ocean would likely impact primary productivity, the oxidation and burial of organic matter-derived carbon and pCO₂.

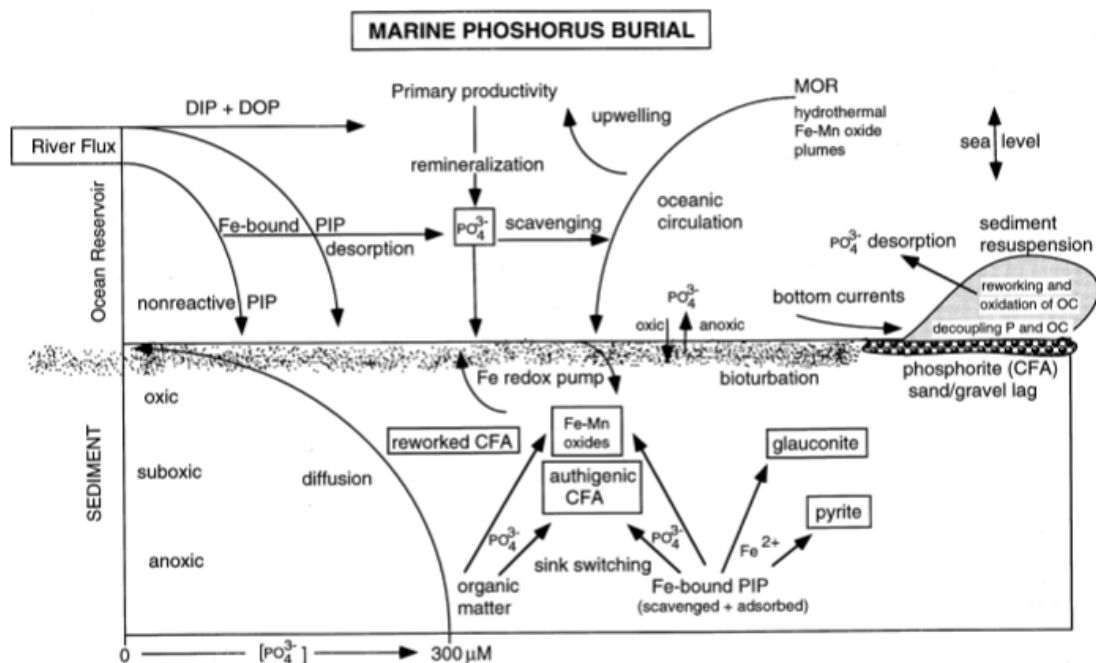


Figure 4.8 –Schematic showing processes regulating the marine phosphorus cycle. Figure extracted from Compton *et al.* (2000).

As shown in figure 4.8, the early stages of sediment diagenesis of organic matter decouple the phosphorus and carbon cycles. While some phosphorus is buried along with a portion of carbon as organic matter, a certain amount is remineralised and used in the precipitation of carbonate fluorapatite. Conversely, the organic carbon is oxidised and returned to the oceans. The amount of phosphorus buried in this manner is heightened when higher sea levels increase shelf area and zones of higher productivity shift to these shallow water regions. The effect of a falling sea level on the phosphorus cycle in shelf regions is two-fold. Firstly, less reactive phosphorus is trapped nearshore and a greater proportion is deposited in deeper waters. Secondly, increased weathering and reworking of shelf sediments due to glaciation-induced sea level retreat remobilises the extensive amounts of buried phosphorus before it is delivered to off-shore regions of the deep ocean further fuelling new production.

As a result of the falling sea level and decrease in shelf area, zones of higher productivity have migrated to regions over deeper waters causing a greater regeneration of phosphorus in the water column where intensified upwelling fosters continued high rates of primary productivity in the surface waters. This increased primary productivity and associated export production serves to drawdown $p\text{CO}_2$. As shown in figure 4.9, a long-term decline in atmospheric CO_2 occurs leading up to the climate transition (Pearson *et al.* 2009; Pagani *et al.* 2011). However, a steeper period of decline is associated with the onset of glaciation and pulse of productivity. The alkenone-derived record of Pagani *et al.* (2011) documents a decline of around 500 ppm from 33.9 Ma to 33.1 Ma, whereas the boron-derived record of Pearson *et al.* (2009) suggests an overall decline from 959 ppm at 33.96 Ma to 624 ppm at 32.90 Ma. Following the decline in productivity, $p\text{CO}_2$ appears to rebound by between 150 and 200 ppm. The transient nature of this steepened decline in $p\text{CO}_2$ is readily explained by its being forced by a pulse of primary productivity caused by the Shelf-Nutrient Hypothesis. Interestingly, the end of this period of sharply declining $p\text{CO}_2$ and high primary productivity occurs at a time when the AIS is thought to have become significantly more stable (Galeotti *et al.* 2016). Once sea level stabilised, rivers would have been in equilibrium with their new base level and it is likely that the

previously plentiful supply of shelf sediment-derived phosphorus was no longer a force fuelling productivity.

Given that there are so many plausible explanations for a decrease in $p\text{CO}_2$ at this time, it is important to explore the potential magnitudes of change that would occur. While studies that invoke the weathering of organic matter in shelf material over glacial-interglacial timescales imply relatively small changes in atmospheric CO_2 that are much smaller than the scale of change documented in records of CO_2 across the EOT (Pagani *et al.* 2005; Pearson *et al.* 2009; Pagani *et al.* 2011), the boundary conditions at the EOT are very different. Figure 4.7 shows the extent of flooding of northern hemisphere continents in the Late Eocene where vast amounts of organic matter would have been sequestered. The warm, humid conditions of the Early Eocene greenhouse would have prompted significant chemical weathering and riverine flux of phosphorus. This increased input was likely associated with increased trapping of phosphorus in marginal coastal environments, precipitation of carbonate fluorapatite across substantial shelf areas and scavenging of phosphorus in the water column by Fe-Mn oxides (Compton *et al.* 2000). These processes led to the accumulation of much greater stores of organic matter in shelf regions than those of the modern day or during Pleistocene interglacials. Therefore, it is not unreasonable to suggest that the scale of the effect of the Shelf-Nutrient Hypothesis would have been much greater at the EOT than at other intervals in the geological past. An interdisciplinary approach using an Intermediate Complexity Earth System Model (EMIC) would effectively test these ideas and offer an insight into the scale of the possible effect on $p\text{CO}_2$ of each of these mechanisms; including the weathering of organic-rich shelf sediments from the Arctic Ocean basin.

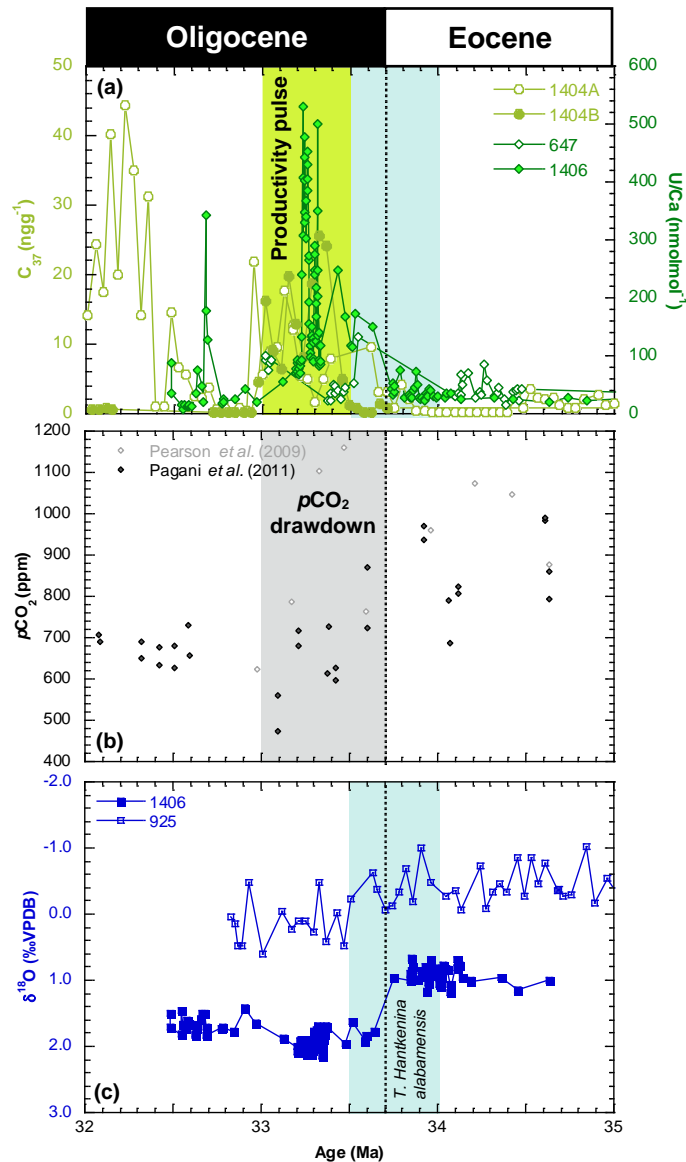


Figure 4.9 – (a) Productivity indicator data from the North Atlantic region including benthic foraminiferal U/Ca (IODP Site U1406 – this study, ODP Site 647 – Helen Coxall, unpublished) and alkenone abundances (ODP Site U1404 – Liu *et al.* 2018). (b) Atmospheric carbon dioxide generated from boron isotopic data of planktic foraminifera *Turborotalia ampliapertura* from the Tanzania Drilling Project and calculated using a seawater $\delta^{11}\text{B}$ value of 38‰ and a variable $[\text{CO}_3^{2-}]$ determined by a simple box model (Pearson *et al.* 2009). Alkenone-based atmospheric carbon dioxide generated by Pagani *et al.* (2011). (c) Benthic foraminiferal stable isotopes from IODP Site U1406 (Newfoundland Sediment Drifts, North Atlantic – this study) and ODP Site 925 (Ceara Rise, Equatorial Atlantic – this study). Pale blue shaded bar indicates duration of EOT. EOB marked by top of *Hantkenina alabamensis*. Green shaded bar indicates pulse of productivity pulse. Grey shaded bar indicates enhanced drawdown of $p\text{CO}_2$. Age model calibrated to Cande and Kent (1995).

Given that the increasing $\delta^{13}\text{C}$ signal is found in records of the EOT from across the globe, it is worthwhile considering what role the increase in primary productivity documented here in the Atlantic Ocean could have on $\delta^{13}\text{C}$. Over the timescales discussed in this study, the exchange of carbon between organic and carbonate reservoirs plays a vital role in balancing the carbon budget (Berner, 1982; Zachos *et al.* 1996). In areas of high organic matter delivery to the seafloor, a greater proportion evades oxidation and gets buried in the sediment. Thus, when a substantial increase in primary productivity and export production occurs, and flux of organic matter to the ocean floor is high, a greater proportion of ^{12}C is locked up and a resultant increase in $\delta^{13}\text{C}$ occurs. Indeed, this increase in the ratio of organic to inorganic carbon burial has been proposed to explain the c. 1‰ global change in $\delta^{13}\text{C}$ across the EOT (Zachos *et al.* 1996; Salamy and Zachos, 1999; Zachos and Kump, 2005). Although, when tested using biogeochemical box models this forcing mechanism alone does not seem to explain the magnitude or nature of the $\delta^{13}\text{C}$ shift (e.g. Merico *et al.* 2008; Armstrong-McKay *et al.* 2016). In any case, the associated acceleration of the biological pump under such circumstances as those described here would cause a drawdown of $p\text{CO}_2$ and hence increase the $\delta^{13}\text{C}$ of the oceans.

4.5 Chapter Summary

This chapter has presented benthic foraminiferal stable isotope and trace element data from two sites in the Atlantic Ocean; IODP Site U1406 in the north of the basin and ODP Site 925 in the equatorial Atlantic region. These records have demonstrated a transient excursion in primary productivity that begins coeval with Antarctic glaciation at the EOT. Comparison with existing published data have revealed this to be a region-wide phenomena in the Atlantic Ocean that is not mirrored elsewhere in the global ocean (e.g. the Pacific and Southern Oceans). Here, it is proposed that the Arctic Ocean continental shelves served as the nutrient-rich source fuelling the productivity pulse in the Atlantic at the EOT. Glaciation-induced sea level fall exposed organic-rich shelf sediment nutrients to weathering. This new source of bioavailable nutrients was distributed through the North Atlantic region causing increased primary productivity and associated export production. This interval of enhanced export production is associated with a steepening of the overall decline in $p\text{CO}_2$. This transient acceleration in the decline in $p\text{CO}_2$ came to an end coeval with declining primary productivity. Once the AIS and associated sea level oscillations stabilised, the rivers reached equilibrium with their new base level and the mechanism fuelling this increased new production was halted. The implications of these findings are threefold: (i) the biological pump in the Atlantic Ocean region acted as a positive feedback on the carbon cycle and AIS growth across Earth's Greenhouse-Icehouse Transition; (ii) the potential impact of the Shelf-Nutrient Hypothesis on atmospheric CO_2 change is much larger than suggested over glacial-interglacial cycles given the differing boundary conditions of the EOT; and (iii) a greater emphasis should be placed on the importance of changes in the Arctic and North Atlantic Oceans at this time warranting further investigation of changes in the high northern latitudes across this critical climate transition.

Chapter Five

Refining Estimates of Deep Ocean Temperature across the Eocene Oligocene Transition

5.1 Introduction

5.1.1 Foraminiferal Mg/Ca

A foraminiferal calcite lattice hosts magnesium (Mg); the amount hosted is largely determined by the temperature dependent nature of the partition coefficient of Mg^{2+} . This reaction is endothermic meaning that the partition coefficient of Mg^{2+} increases with temperature exponentially. It was first suggested by Chave (1954) that the Mg content of biogenic calcite positively covaries with latitude, and hence temperature; a claim that has subsequently been supported by countless studies (Izuka, 1988; Nürnberg *et al.* 1996; Rosenthal *et al.* 1997; Lea *et al.* 1999; Lear *et al.* 2002).

When compared to the thermodynamic relationship in inorganic calcite, biogenic calcite exhibits a much higher sensitivity (Rosenthal *et al.* 2000). The difference in temperature sensitivity between biogenic (~ 6 - 10% per °C (Lea *et al.* 1999; Elderfield and Ganssen, 2000; Gray *et al.* 2018)) and inorganic ($3.1 \pm 0.4\%$ per °C (Katz, 1973) calcite suggests a biologically derived process exerts a control on the incorporation of Mg into biogenic calcite. These subsequently named vital effects appear to exert greater influence in benthic than planktic species and highlight the need for species-specific temperature calibrations. Most of the calibrations presented in the literature are expressed in an exponential form:

$$Mg/Ca = B \exp(A \times \text{temperature})$$

Eq. 4

Use of Mg/Ca ratios in foraminiferal calcite as a paleotemperature proxy can help to deconvolve the complex signal provided by $\delta^{18}O$. During times of ice-free conditions, such as the Early Eocene, the record of $\delta^{18}O$ can be easily applied in the interpretation of temperature changes. However, this is not so straightforward during times of large scale changes in ice volume, such as the EOT. Therefore, Mg/Ca ratios can serve as an independent proxy of temperature to deconvolve the temperature and $\delta^{18}O_{sw}$ components of $\delta^{18}O$ (Lear *et al.* 2000; Rosenthal *et al.* 2000; Martin *et al.* 2002).

5.1.1.1 Mg/Ca-derived Paleotemperatures across the EOT

Past periods of substantial changes in global climate provide natural, geological archives suited to testing current understanding of the climate system; the EOT serves as one such prime opportunity. Efforts to quantitatively reconstruct both surface and deep ocean temperatures across this pivotal climate transition have been long ongoing.

Early studies that adopted Mg/Ca ratios as a BWT paleothermometer failed to recognise any deep ocean cooling signal across the EOT. A low resolution, 50 million year record of BWT that depicts a 12°C cooling over the Cenozoic failed to illustrate any cooling across the higher-resolution EOT interval and suggested that the majority of the oxygen isotope signal might be attributed to ice volume increase (Lear *et al.* 2000); a suggestion made by several other early studies (e.g. Billups and Schrag, 2003; Lear *et al.* 2004). However, this interpretation raises issues of ice accommodation on Antarctica. A 1.5‰ increase in $\delta^{18}\text{O}$ attributed solely to ice volume increase would require a continental ice volume of between 1.5 and 3 times that of the modern day AIS prompting the hypothesis that there were extensive northern hemisphere ice sheets present at the EOT, much earlier than previously thought (Billups and Schrag, 2003; Coxall *et al.* 2005). While it has previously been suggested that substantial evidence existed for the presence of northern hemisphere glaciation at the EOT by estimates of eustatic sea level fall that could not be ascribed to the AIS alone (Tripathi *et al.* 2005), this hypothesis has more recently been reliably refuted (Edgar *et al.* 2007; Spray *et al.* 2019). It is thought much more likely that previously identified drop stones off Greenland's coast line are the product of small valley glaciers and ephemeral ice caps (Eldrett *et al.* 2007) as opposed to widespread glaciation. Moreover, substantial bipolar glaciation cannot be reconciled with climate model simulations. An isotope enabled, coupled global climate-ice sheet model, that accounts for declining $p\text{CO}_2$ and the impact of orbital forcing, is unable to simulate bipolar glaciation at the atmospheric CO_2 concentrations suggested across the EOT (DeConto *et al.* 2008). Indeed, the presence of extensive northern hemisphere ice sheets can only be simulated when atmospheric CO_2 concentrations fall below 280 ppmv, compared to the initiation of the AIS at atmospheric CO_2 concentrations of between ~560 and 920 ppmv (Gasson *et al.* 2014). In the absence

of bipolar glaciation at the EOT, there must have been some degree of cooling. Later studies that have failed to establish BWT cooling across the EOT have recognised the influence of secondary controls on benthic foraminiferal Mg/Ca ratios (e.g. Lear *et al.* 2004; Peck *et al.* 2010; Pusz *et al.* 2011; Lear *et al.* 2010).

The most reliable records of planktic foraminiferal Mg/Ca-derived SST across the EOT to date stem from well-preserved shelf sediments and suggest a cooling of between 2.5°C and 4°C across step one of the isotope shift (Lear *et al.* 2008; Wade *et al.* 2012). Available records from other proxy indicators have documented a disparity between the high southern and high northern latitudes whereby no significant surface ocean cooling is associated with the isotope shift in the high northern latitudes (Liu *et al.* 2018). A record of Mg/Ca-derived BWT is lacking from this region; the work presented here aims to provide one from IODP Site U1406. There is a much greater abundance of BWT records from the Southern Ocean regions across the EOT (Peck *et al.* 2010; Pusz *et al.* 2011; Bohaty *et al.* 2012). It is thought that deep waters cooled by approximately 2°C across the EOT; a change largely occurring across step one. Step two of the $\delta^{18}\text{O}$ shift is considered to be predominantly caused by an increase in continental ice volume equivalent to an increase in $\delta^{18}\text{O}$ of $\sim 0.6\text{‰}$ (Lear *et al.* 2008; Bohaty *et al.* 2012).

5.1.1.2 Secondary Factors on Foraminiferal Mg/Ca

Some efforts have been made to isolate the temperature-dependency of Mg/Ca by correcting for secondary controls but further strides in this area are required. While the dominant control on foraminiferal Mg/Ca is temperature, the main secondary factors that have been identified as complicating the use of this paleotemperature proxy include the influence of: (i) changes in $\Delta[\text{CO}_3^{2-}]$; (ii) secular changes in the Mg/Ca ratio of seawater; and (iii) post-mortem diagenetic alteration of the chemical composition of the calcite test.

5.1.1.2.1 The Carbonate Ion Hypothesis

It has long been suggested that various trace elements in benthic foraminiferal calcite are influenced by the $\Delta[\text{CO}_3^{2-}]$ of the surrounding sea water (Elderfield *et al.* 2006) where by the trace element partition coefficient decreases with decreasing seawater

carbonate saturation state (Elderfield *et al.* 1996; Lear, 2007) or indeed, in the case of U/Ca, are inversely related (Russell *et al.* 2004). This is especially important across the EOT where the CCD deepened by one kilometre over the same timeframe as the two step $\delta^{18}\text{O}$ shift (Coxall *et al.* 2005) and rapidly altered the saturation state of the deep ocean. This CCD deepening has been identified as a somewhat unique and extreme event; it is not thought that $\Delta[\text{CO}_3^{2-}]$ exerts such a strong effect on Mg/Ca ratios at other times in geological history (Lear *et al.* 2004). The carbonate saturation state effect has now been widely proposed as the cause of the absence of cooling within many benthic Mg/Ca paleotemperature records across the EOT (Martin *et al.* 2002; Lear *et al.* 2004). This effect readily explains why, in areas of lower carbonate saturation, a cooling signal cannot be identified, yet a cooling is reconstructed from study sites in shelf and slope environments (e.g. Katz *et al.* 2008; Lear *et al.* 2008). The $\Delta[\text{CO}_3^{2-}]$ effect is now recognised as being far more influential than previously thought (Rosenthal *et al.* 2006) and is thought to explain the steepening of calibration curves at temperatures below 3°C (Elderfield *et al.* 2006), an effect previously attributed to increased temperature sensitivity (Martin *et al.* 2002). Rather, the $\Delta[\text{CO}_3^{2-}]$ effect is far more dominant in deep ocean waters because, whilst temperatures remain relatively constant beyond one or two kilometres depth, $\Delta[\text{CO}_3^{2-}]$ decreases rapidly below around 3°C (Elderfield *et al.* 2006). The effect of $\Delta[\text{CO}_3^{2-}]$ serves to change the $\delta^{18}\text{O}_{\text{sw}}$, deconvolved from $\delta^{18}\text{O}$ by Mg/Ca ratios, by as much as 0.01 to 0.03‰ per $\mu\text{mol kg}^{-1}$ (Elderfield *et al.* 2006). Therefore, to accurately deconvolve BWT from foraminiferal $\delta^{18}\text{O}$ in deep water settings, the effect of $\Delta[\text{CO}_3^{2-}]$ must be quantified and accounted for (Yu and Elderfield, 2008).

5.1.1.2.2 Mg/Ca in Seawater

The isotopic composition of benthic foraminifera reflects that of the surrounding seawater at the time of test precipitation. Ca^{2+} in the calcite lattice is substituted by Mg^{2+} ; the extent to which this happens depends on both the partition coefficient (D_{Mg}) and the concentration of the Mg^{2+} cation relative to Ca^{2+} in the seawater ($\text{Mg}/\text{Ca}_{\text{sw}}$) (Lear, 2007). Therefore, absolute values of Mg/Ca-derived paleotemperature also depend on any assumptions made about $\text{Mg}/\text{Ca}_{\text{sw}}$. The residence times of Mg^{2+} and Ca^{2+} ions in the ocean are 10 Ma and 1 Ma, respectively (Broecker and Peng, 1982).

Many studies have focused on Pleistocene timescales as this secondary factor does not influence records of less than one million years in duration. However, past changes in Mg/Ca_{sw} are poorly constrained on geologically older timescales and thus when Mg/Ca ratios are used on timescales longer than one million years inaccuracies may become incorporated into the temperature data as a result of changes in Mg/Ca_{sw} . The generation of absolute temperature estimates becomes impeded and thus it is difficult to calculate accurate values of $\delta^{18}O_{sw}$ and changes in continental ice volume. Studies have chosen to either adopt an estimate to constrain Mg/Ca_{sw} or assume unchanged Mg/Ca_{sw} through time.

Various methods have been adopted to generate estimates of Mg/Ca_{sw} . Simple geochemical models provide estimates of 1.6 molmol^{-1} (Demicco *et al.* 2005) and 3.9 molmol^{-1} (Wilkinson and Algeo, 1989) for Mg/Ca_{sw} at 50 Ma. Evidence from the composition of fluid inclusions in evaporite minerals suggests seawater ratios of between 2.5 and 3.5 molmol^{-1} at 50 Ma (Lowenstein *et al.* 2001). Echinoderm fossils, when well-preserved, have also been shown to provide broadly corroborating evidence of fluctuations in seawater chemistry. Dickson *et al.* (2004) found similarities between results yielded from echinoderm samples and those of geochemical models and fluid inclusions. However, more sizeable discrepancies are evident when considering shorter timescales (e.g. 10^6 myr). A more recently developed method to estimate past Mg/Ca_{sw} uses hydrothermal calcium carbonate veins (CCVs) that have precipitated from seawater-derived fluids in ocean ridge flank basalts of the upper crust (e.g. Coggon *et al.* 2010; Coggon and Teagle, 2011). This method also provides evidence of a lower Mg/Ca_{sw} value for the Eocene; between 1.5 and 2.5 molmol^{-1} (Coggon *et al.* 2010). More recently, paired analysis of clumped isotopes (Δ_{47}) and foraminiferal Mg/Ca have been used to reconstruct Mg/Ca_{sw} (Evans *et al.* 2018).

More recent studies have questioned the assumption that the distribution coefficient of Mg^{2+} remains constant despite any variations in Mg/Ca_{sw} and therefore foraminiferal Mg/Ca follows a linear relationship with Mg/Ca_{sw} (Hasiuk and Lohmann, 2010; Evans and Müller, 2012). These studies suggest that in fact the partition coefficient is not independent of Mg/Ca_{sw} but rather decreases with increasing

Chapter Five: Refining Estimates of Deep Ocean Temperature across the Eocene-Oligocene Transition

Mg/Ca_{sw} and that a power function more accurately defines the relationship between foraminiferal Mg/Ca and Mg/Ca_{sw} (Hasiuk and Lohmann, 2010; Evans and Müller, 2012; Evans *et al.* 2014) (as shown in equation 5).

$$\text{Mg/Ca}_{\text{foram}} = F * \text{Mg/Ca}_{\text{sw}}^H$$

Eq. 5

F is the linear or exponential temperature dependency of that given species. The value of *H* is also species dependent. Many culture studies have focused their efforts on identifying the *H* value for different species (e.g. Evans and Müller, 2012; Lear *et al.* 2015; Hines *et al.* 2017). In this study, the approach of Lear *et al.* (2015) is adopted whereby the Mg/Ca_{sw} value for each sample is calculated using a third-order polynomial fit through a compilation of published Mg/Ca_{sw} values for the Cenozoic (equation 6).

$$\text{Mg/Ca}_{\text{sw}} = 5.2 - (0.238 * \text{Age}) + (0.00661 * \text{Age}^2) - (6.66e^{-5} * \text{Age}^3)$$

Eq. 6

The calibration used here to calculate paleotemperatures corrected for Mg/Ca_{sw} for *Oridorsalis umbonatus* uses a value of *H* estimated by Lear *et al.* (2015) and the temperature sensitivity determined from core-top samples (Lear *et al.* 2010). The *H* values used to calculate paleotemperatures corrected for Mg/Ca_{sw} for *Cibicidoides havanensis* and *Turborotalia ampliapertura* are taken from the calibration of Hines *et al.* (2017) with the exponential temperature sensitivities of Lear *et al.* (2002) and Anand *et al.* (2003), respectively. The calibration components are detailed in table 5.1.

Species	H	A	B	Calibration Reference
<i>Cibicidoides havanensis</i>	0.31	0.109	0.867	Hines <i>et al.</i> (2017)
<i>Turborotalia ampliapertura</i>	0.2	0.09	0.38	Hines <i>et al.</i> (2017)
	H	M	C	
<i>Oridorsalis umbonatus</i>	- 0.03	0.121	1.21	Lear <i>et al.</i> (2015)

Table 5.1 – Calibration components used to correct Mg/Ca-derived water temperatures for Mg/Ca_{sw} values different to modern at the EOT.

5.1.1.2.3 Diagenesis

A further potential source of error in the use of Mg/Ca as a paleothermometer is any change to the geochemical signal that occurs post-mortem; a process called diagenesis (Lear, 2007; Gasson *et al.* 2012). There are many diagenetic effects including dissolution, cementation, and recrystallisation. Dissolution lowers the Mg/Ca ratio within foraminiferal calcite; the Mg²⁺ impurity increases the solubility of the calcite lattice causing the less pure calcite to preferentially dissolve (Brown and Elderfield, 1996; Lear, 2007). As the process of dissolution progresses, the mass of the foraminifera test decreases, along with the ratio of Mg/Ca (Lear, 2007). Therefore, Rosenthal and Lohmann (2002) suggest that it is possible to use shell weights to correct for the dissolution effect on Mg/Ca. However, this approach must be used with caution as it assumes that foraminifera tests otherwise maintain their initial weight (Lear, 2007). It has also been proposed that the comparatively stable nature of a benthic foraminifer's habitat means that these deep ocean dwelling species are considerably less affected by dissolution than their planktonic counterparts (Rosenthal *et al.* 2000) although there is some doubt as to the validity of this idea.

In contrast to dissolution, cementation increases the Mg/Ca ratio of benthic foraminiferal calcite whereby inorganic calcite (which has a higher partition coefficient than biogenic calcite) overgrows on the foraminifer surface or infills the chambers (Lear, 2007). In the case of recrystallisation, the original biogenic calcite is replaced. Microcrystallites of biogenic calcite become larger through neomorphic recrystallisation whereby dissolution and precipitation reactions occur along very thin film of fluid passing through the foraminifer. This recrystallization happens in pore water, which tends to have a lower Mg/Ca ratio than seawater. The recrystallization of benthic foraminiferal calcite is heightened and reduced in carbonate-rich and clay-rich sediments, respectively, suggesting that preferentially sampling clay-rich sediments may reduce the effect of diagenesis on Mg/Ca ratios (Pearson *et al.* 2001; Lear, 2007). However, studies using samples from deeply-buried, carbonate-rich sediments have shown a far less pronounced effect of recrystallization on Mg/Ca ratios than could be reasonably expected from laboratory-based experiments (Baker *et al.* 1982; Sexton *et al.* 2006) suggesting that Mg/Ca ratios in benthic foraminifera

may be more resistant to this diagenetic effect than could be expected (Lear, 2007). In this study, IODP Site U1406 is characterised by clay-rich sediments and ODP Site 925 is more carbonate-rich. In addition, the samples with the greatest burial depth are those from ODP Site 925 (> 750 mbsf). Whilst the foraminifera were inspected under a standard binocular microscope and appeared moderately well-preserved, it is important to be mindful of the potential for substantial diagenetic alteration at such burial depths.

5.2 Methodology

5.2.1 Geological Setting

Samples spanning the EOT were analysed from sediment cores recovered from IODP Expedition 342, Site U1406 (Newfoundland Sediment Drifts - 40°21.0'N, 51°39.0'W), ODP Leg 154, Site 925 (Ceara Rise - 4°12.249'N, 43°29.334'W) and ODP Leg 121, Site 756 (Ninetyeast Ridge - 27°21.330'S, 87°35.805'E). Sites discussed in this chapter are shown in figure 5.1.

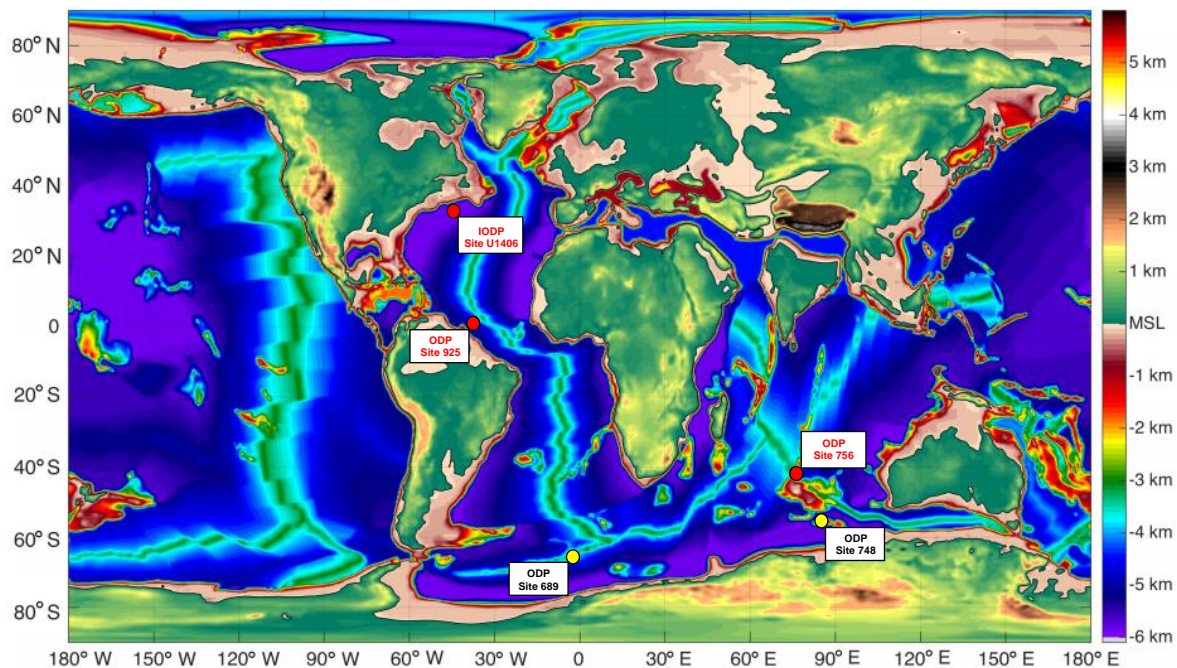


Figure 5.1 – Location of ocean drilling sites used, or discussed, in this study displayed on paleogeographic map from Baatsen *et al.* (2016). Red dots indicate sites from which new data has been generated in this thesis. Yellow dots indicate sites from which existing published data is presented for comparison purposes.

The Newfoundland ridges (J-Anomaly Ridge and Southeast Newfoundland Ridge) lie offshore of Newfoundland, north western Canada. These plastered ridges are mantled with contourite, pelagic carbonate drift deposits (Norris *et al.* 2014). IODP Site U1406 is located in the North Atlantic Ocean on J-Anomaly Ridge placing it directly underneath the path of the modern Atlantic DWBC. Its location and paleo water depth of 3300 metres at c. 50 Ma make it an ideal site to monitor changing ocean circulation and deep water formation in the North Atlantic through time (Boyle *et al.* 2017). With this in mind, samples of 20 cm³ from IODP Site U1406 were taken between 187.66 and 206.48 mbsf at an average temporal resolution of 10 kyr but

with intervals of higher resolution sampling (~ 2 – 5 kyr) across key intervals including the step-wise change in $\delta^{18}\text{O}$ and the EOGM.

ODP Site 925 is the shallowest site drilled as part of Leg 154 on Ceara Rise, an aseismic rise bounded by the Ceara abyssal plain to the west and the Amazon cone to the east, in the western equatorial Atlantic Ocean. Samples of 20 cm³ from ODP Site 925 were taken between 746.43 and 850.14 mbsf at an average temporal resolution of 50 kyr.

ODP Site 756 lies on Ninetyeast Ridge in the eastern Indian Ocean. Ninetyeast Ridge is a 5000 km north-south lineament stretching from 10°N to 34°S (Pierce *et al.* 1989). The 100 – 200 km wide ridge is composed of basalts that erupted onto a young, weak oceanic Indian plate in shallow waters (Zachos *et al.* 1992). Basement ages increase northward illustrating how the ridge formed near its present southern end due to the Kerguelen and Ninetyeast Ridge hotspot and gained its current south-north alignment by the northward movement of the Indian plate over the hotspot. The ridge is overlain by sediments derived from the Bengal Fan. ODP Site 756 is the southernmost site drilled on Ninetyeast Ridge as part of Leg 121 in a water depth of 1519 metres. The EOT section at ODP Site 756 is complete and composed of nannofossil ooze; samples were taken from between 113.67 and 142.66 mbsf.

5.2.2 Chronology

Chronology for ODP Sites 756 and 925 is based solely on biostratigraphy as magnetostratigraphic age control was unavailable for sites collected during Legs 121 and 154. Chronology for IODP Site U1406 is based on biostratigraphic and magnetostratigraphic datums. All age models are calibrated to the timescale of Cande and Kent (1995) and are presented in greater detail in chapter two of this thesis.

5.2.3 Sample Preparation and Analysis

5.2.3.1 Benthic Foraminiferal Stable Isotopes

Samples of benthic foraminifera used in this study were prepared and cleaned according to the protocol outlined in sections 2.2 and 2.4 of chapter two of this thesis.

For IODP Site U1406, between five and ten individuals of *Cibicidoides mundulus* were run from the 150 – 250 µm size fraction. These samples were analysed at the National Oceanography Centre (NOC). Analytical error for this dataset, based on analysis of in-house standard GS1, isotopically similar to NBS-19, is 0.03‰ for $\delta^{18}\text{O}$ and 0.04‰ for $\delta^{13}\text{C}$. For ODP Site 925 a minimum of five individuals of *Cibicidoides havanensis* and *Oridorsalis umbonatus* were run from specimens picked from the 250 – 355 µm size fraction. These samples were analysed at Cardiff University on a ThermoFinnigan MAT252 with online sample preparation by an automated Kiel II carbonate device. Analytical error for ODP the Site 925 data set, based on repeat analysis of standard NBS-19 (n=284), is 0.044‰ for $\delta^{18}\text{O}$ and 0.025‰ for $\delta^{13}\text{C}$. For ODP Sites 756 and 757, a minimum of two individuals of *Cibicidoides havanensis* or *Cibicidoides mundulus* were run from the 250 – 355 µm size fraction. These samples were analysed at Stockholm University by Max Holmström.

5.2.3.2 Foraminiferal Trace Elements

Benthic foraminifera samples used in this study were prepared and cleaned according to the protocol outlined in sections 2.2 and 2.5 of chapter two of this thesis. For planktic species, the second step of the cleaning protocol outlined in section 2.5.2 was omitted. For IODP Site U1406, a minimum of 10 individuals of *Oridorsalis umbonatus* were picked from the 250 - 355 µm size fraction to be analysed for their trace element composition. *Oridorsalis umbonatus* is a popular choice to produce trace element data as it has a wide geographic distribution allowing easy inter-site comparison. It is also a species present in the modern ocean allowing the development of accurate core-top calibrations. For ODP Site 925 a minimum of 10 individuals of *Cibicidoides havanensis*, *Nonion* sp and *Oridorsalis umbonatus* were analysed for their trace element composition. For ODP Site 756, a minimum of 10 individuals of *Cibicidoides havanensis* and *Oridorsalis umbonatus* were analysed. In addition, a minimum of 25 individuals of planktonic foraminifera *Turborotalia ampliapertura* were analysed for their trace element composition from ODP Site 756. All samples analysed were reported for ^6Li , ^7Li , ^{11}B , ^{24}Mg , ^{25}Mg , ^{27}Al , ^{43}Ca , ^{46}Ca , ^{48}Ca , ^{55}Mn , ^{87}Sr , ^{88}Sr , ^{111}Cd , ^{138}Ba , ^{146}Nd and ^{238}U . At the start and end of each analytical run, two independent in-house consistency standards were analysed to

Chapter Five: Refining Estimates of Deep Ocean Temperature across the Eocene-Oligocene Transition

allow calculation of the long-term precision and accuracy of each element (detailed in section 2.5.3 of chapter two of this thesis).

5.3 Results

5.3.1 Foraminiferal Sr/Ca as an Indicator of Diagenesis

Inaccuracies induced by diagenetic effects can be minimised by preferentially using well-preserved samples and avoiding those that are at risk of or show signs of diagenetic effects (Sexton *et al.* 2006; Lear, 2007; Gasson *et al.* 2012), and, where possible, correcting for these effects (Rosenthal and Lohmann, 2002). It is possible to identify samples with artificially enhanced Mg/Ca ratios due to diagenetic calcite by looking at paired Mg/Ca and Sr/Ca ratios; diagenesis alters these trace element ratios in opposite directions (Baker *et al.* 1982). As preservation decreases, Mg/Ca increases and Sr/Ca decreases (Cochran *et al.* 2010).

Figures 5.2 and 5.3 suggest no effect of diagenetic alteration at IODP Site U1406 and ODP Site 756. In contrast, there is a distinct inverse relationship between Mg/Ca and Sr/Ca in all three species at ODP Site 925 (figure 5.4). This is likely as a result of the substantial burial depth at this site and may explain the substantially lower values of $\delta^{18}\text{O}$ documented in chapter three of this thesis. With this in mind, the Mg/Ca values from ODP Site 925 will not be used to calculate paleotemperatures nor used in any further discussion of temperature changes across the EOT. In order to better understand the diagenetic effects on these samples, future work could include a comparative scanning electron microscope (SEM) imaging study.

Chapter Five: Refining Estimates of Deep Ocean Temperature across the Eocene-Oligocene Transition

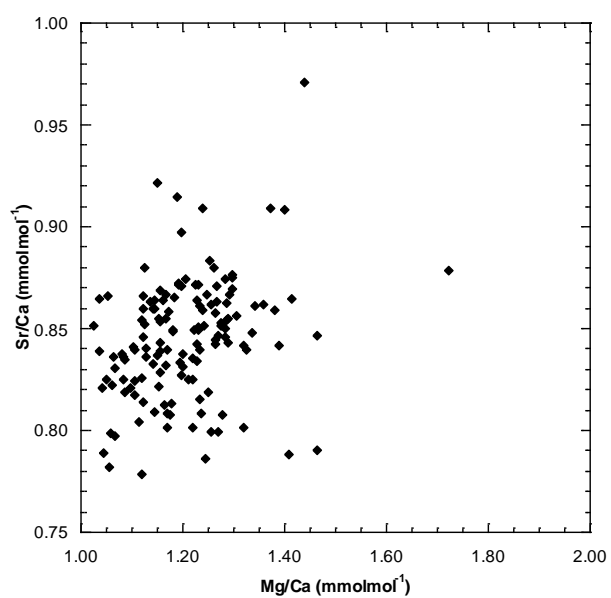


Figure 5.2 – Benthic foraminiferal Mg/Ca and Sr/Ca from *Oridorsalis umbonatus* at IODP Site U1406.

Chapter Five: Refining Estimates of Deep Ocean Temperature across the Eocene-Oligocene Transition

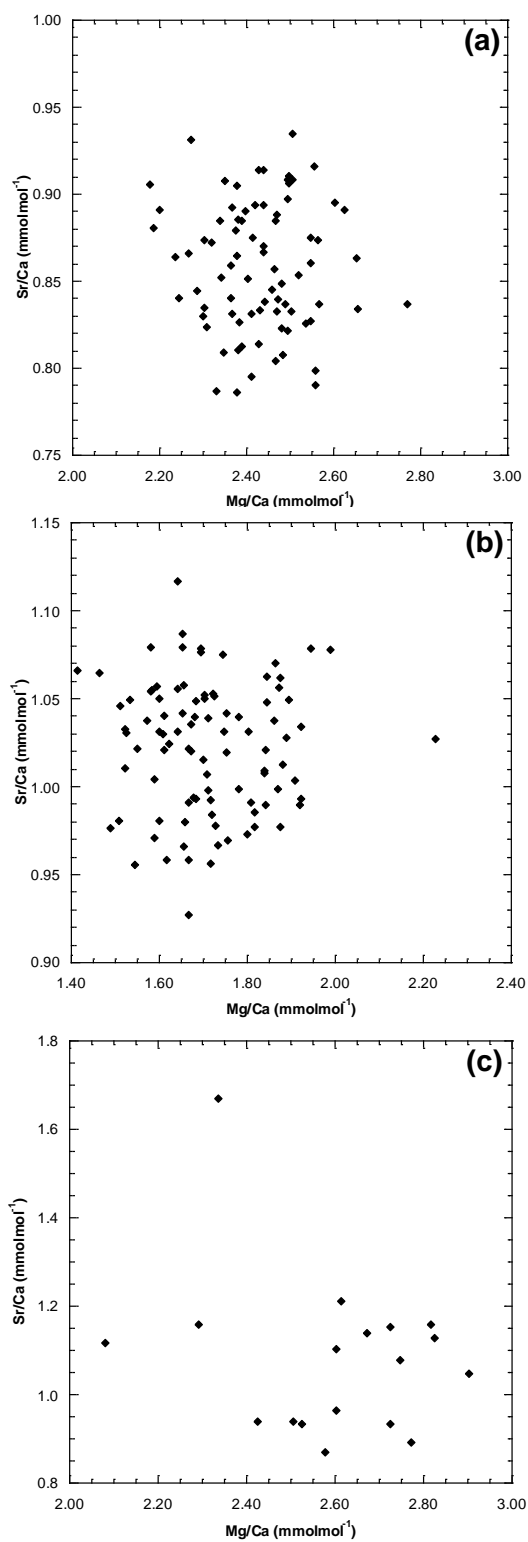


Figure 5.3 – Benthic foraminiferal Mg/Ca and Sr/Ca from (a) *Oridorsalis umbonatus*, (b) *Cibicidoides havanensis* and (c) *Turborotalia ampliapertura* at ODP Site 756.

Chapter Five: Refining Estimates of Deep Ocean Temperature across the Eocene-Oligocene Transition

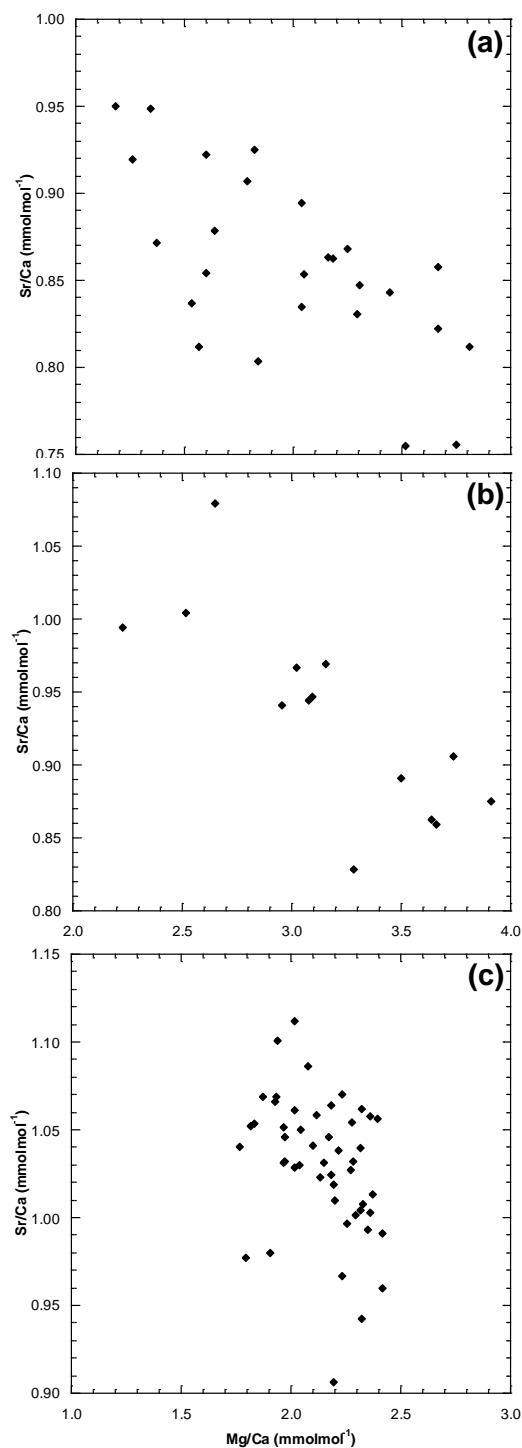


Figure 5.4 – Benthic foraminiferal Mg/Ca and Sr/Ca from (a) *Oridorsalis umbonatus*, (b) *Nonion* sp. and (c) *Cibicidoides havanensis* at ODP Site 925.

5.3.2 Foraminiferal Mg/Ca and Mn/Ca Covariance

Mn has a very short residence time in seawater (~50 years) (Klinkhammer *et al.* 2009) and exhibits a scavenged profile with increasing water depth (Tribovillard *et al.* 2006). The nature of Mn systematics at the seafloor is no less dynamic due to its redox-sensitive nature. In low oxygen conditions, solid-phase manganese oxides (MnO_x) are reduced to mobile soluble manganese (Mn^{2+}), which migrates upward along the oxygen concentration gradient where, upon reaching oxic conditions, Mn^{2+} is oxidised to MnO_x in the sediment once again. Under very low oxygen conditions, pore waters can become supersaturated with regard to Mn; it is here that Mn can inorganically precipitate as manganese carbonates (MnCO_3).

Both MnO_x and MnCO_3 phases may be considered contaminant phases when employing foraminiferal trace elements as proxy indicators of past ocean chemistry. Both MnO_x coatings and MnCO_3 overgrowths are enriched in a suite of other trace elements (Boyle, 1983; Barker *et al.* 2003; Reichart *et al.* 2003), thus impeding the accurate interpretation of paleotemperatures and other geochemical properties. A cleaning protocol developed by Boyle and Keigwin (1985) (outlined in section 2.5.2 of chapter two of this thesis) is commonly employed in foraminiferal trace element ratio studies to remove the potential contamination.

In cleaned foraminifera, unaffected by contaminant phases, ratios of Mn/Ca are typically less than 0.1 mol mol^{-1} (Barker *et al.* 2003). Above this threshold it is not uncommon to see covariance between Mn/Ca and other trace element to calcium ratios, particularly Cd/Ca. The reductive step of the cleaning protocol outlined in chapter two of this thesis was introduced specifically for analysis of Cd/Ca ratios due to the common covariance with Mn/Ca. However, here covariance has been identified between Mn/Ca and Mg/Ca in the trace element data generated from IODP Site U1406 for this study (figure 5.5). This high Mn/Ca has been attributed to a regional, intense productivity increase and reduced redox regime associated with glaciation at the EOT (see chapter four of this thesis). However, in order to accurately calculate paleotemperatures at IODP Site U1406 across the same interval, it is vital that the possible enrichment of Mg/Ca by a Mn-rich contaminant phase is accounted for.

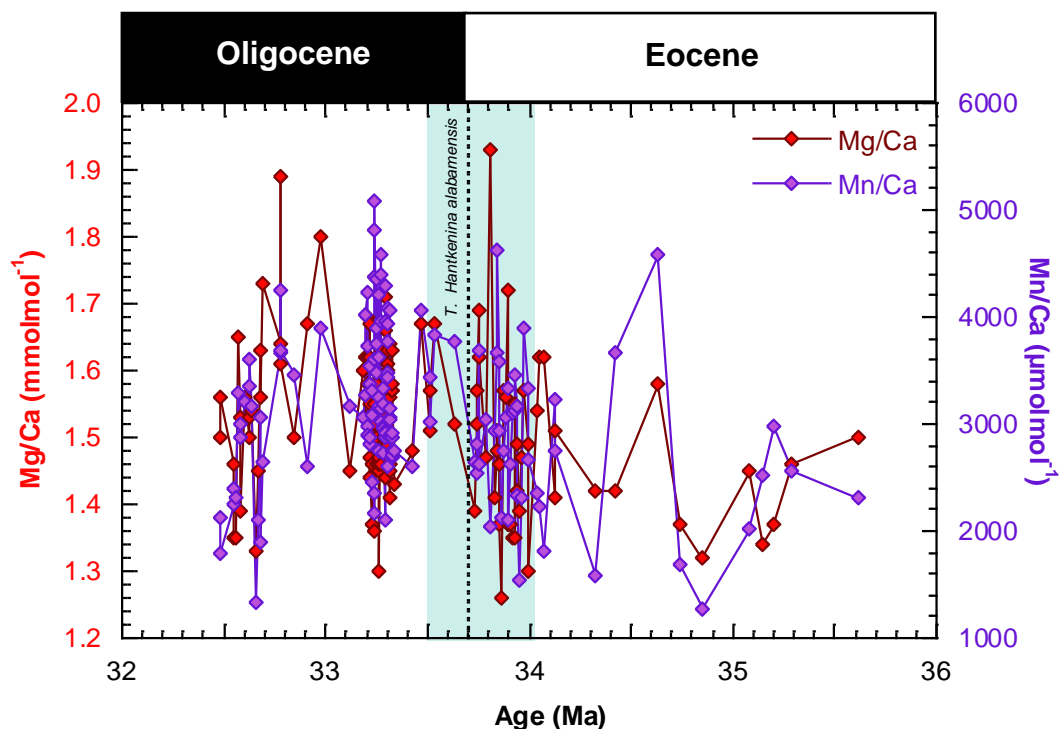


Figure 5.5 – Benthic foraminiferal Mg/Ca and Mn/Ca from *Oridorsalis umbonatus* at IODP Site U1406. Pale blue shaded bar indicates duration of the EOT. EOB marked by top of *Hantkenina alabamensis*. Age model calibrated to Cande and Kent (1995).

Mn/Ca values from IODP Site U1406 vary continuously across the sampling interval from a minimum of $1276 \mu\text{molmol}^{-1}$ to a maximum value of $5077 \mu\text{molmol}^{-1}$. Even the minimum value is around ten times the maximum recommended threshold of Mn/Ca values that could be considered a primary lattice-bound signal of $50 - 150 \mu\text{molmol}^{-1}$ (Boyle, 1983; Boyle and Keigwin, 1985). Four samples with differing solution HR-ICP-MS-derived Mn/Ca values were analysed by LA-ICP-MS. Considerable species-dependent variability exists as to where the contaminant phase resides within the test (Pena *et al.* 2005; 2008). Given that *Oridorsalis umbonatus* is not particularly porous, it could be reasonably expected that the Mn-rich contaminant was concentrated at the inner surface of the test wall. However, the results showed that the abnormally high values of Mn/Ca permeate the entire test in all samples (figure 5.6). At no point in any of the LA-ICP-MS profiles does Mn/Ca decrease below values that are greater than 20 times the values representative of a primary lattice-bound signal. It is difficult to ascertain the exact cause of this. However, it is possible that coatings have formed upon individual crystallites throughout the calcite lattice.

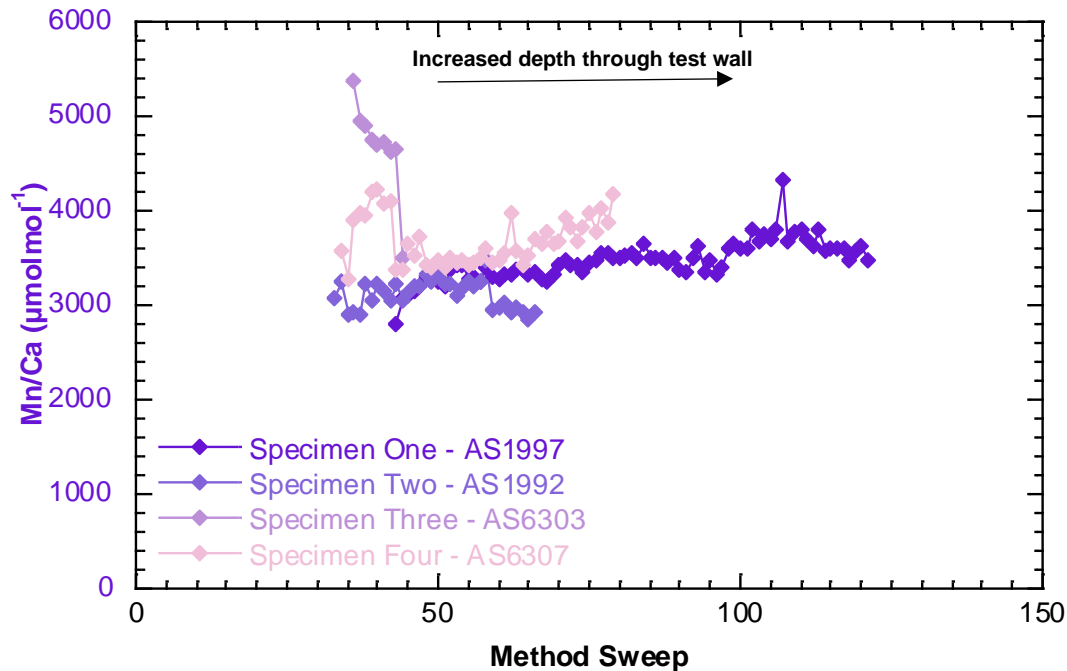


Figure 5.6 – Benthic foraminiferal Mn/Ca from IODP Site U1406 generated by LA-ICP-MS. Samples analysed include AS1997 (IODP Sample U1406A22X3 123 - 125), AS1992 (IODP Sample U1406A22X3 108 - 110), AS6303 (IODP Sample U1406A22H6 12 - 14) and AS6307 (IODP Sample U1406A22H6 24 - 26). Each data point represents the value of Mn/Ca at a given point through the foraminifer test wall. The method sweep represents the duration of the overall method. Increased method sweep represents increased duration of ablation. Hence, values at the low end of the method sweep represent ablation of the outermost test wall whereas values at the high end of the method sweep represent the innermost calcite of the test wall.

While there is a distinct covariance between Mn/Ca and Mg/Ca, the absolute values of Mg/Ca are not abnormal. A similar relationship has been observed in the Oligocene-Miocene section of IODP Site U1406 (Wilson, P. pers. comm.). However, the IODP Site U1406 Oligocene-Miocene *Oridorsalis umbonatus* Mg/Ca are lower than contemporaneous samples at Ceara Rise ODP Site 926, which lack Mn-rich coatings (Lear, pers. comm. 2019). This supports the suggestion that the Mg/Mn of the coatings is low (Hasenfratz et al. 2017). Therefore, mass balance considerations imply that it is unlikely that the marked covariance between Mg/Ca and Mn/Ca (figure 5.5) is entirely driven by varying amounts of Mg hosted in the contaminant phase. Instead, a significant portion of covariance must also be ascribed to an external control impacting both temperature and redox conditions. Therefore, a uniform correction has been applied to all Mg/Ca values discussed in the remainder of this chapter whereby it is assumed that the ratio of Mg to Mn in the contaminant phase is 0.1 molmol⁻¹. Figure 5.7 shows the measured and corrected Mg/Ca values for each

Chapter Five: Refining Estimates of Deep Ocean Temperature across the Eocene-Oligocene Transition

of the species and sites discussed in this chapter. It is clear that this correction makes a considerable difference to Mg/Ca values from IODP Site U1406 where an offset of as much as $0.5 \text{ mmol mol}^{-1}$ is seen. In essence, by applying this correction, the redox control exerted on the samples from IODP Site U1406 is removed. Figure 5.8 appears to validate this approach and suggests that the resulting Mg/Ca record contains a distinct climate signal. In contrast, values from ODP Site 756 are barely impacted at all suggesting that these samples have not been subjected to any Mn-rich contaminant phase and are, by contrast, preserving a primary signal.

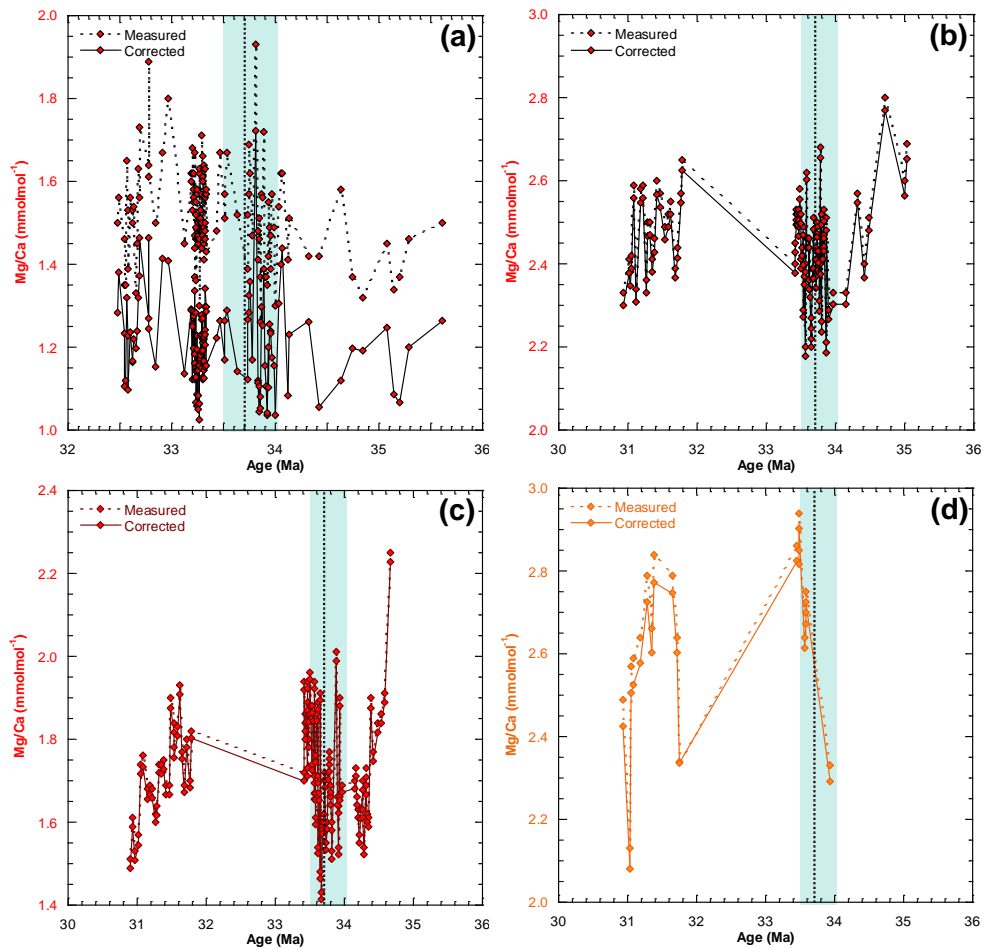


Figure 5.7 – Foraminiferal Mg/Ca from all sites discussed in this chapter corrected for a Mg/Mn ratio of 0.1 mol mol^{-1} ; (a) *Oridorsalis umbonatus* from IODP Site U1406, (b) *Oridorsalis umbonatus* from ODP Site 756, (c) *Cibicidoides havanensis* from Site 756, (d) *Turborotalia ampliapertura* from ODP Site 756. Pale blue shaded boxes indicate duration of EOT. EOB marked by top of *Hantkenina alabamensis* indicated by vertical dashed line. Age model calibrated to Cande and Kent (1995).

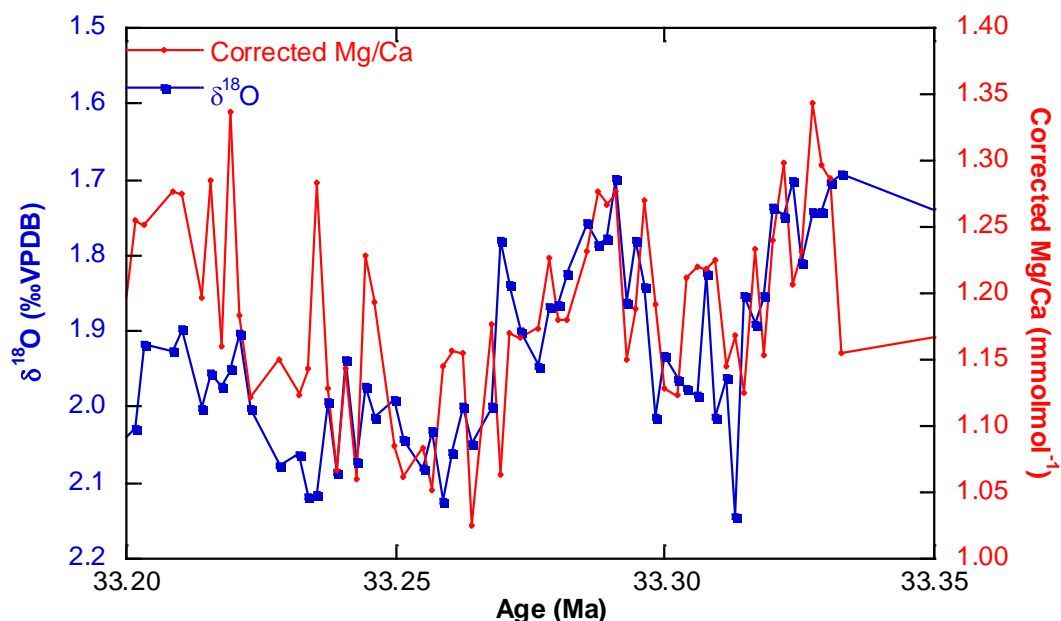


Figure 5.8 – Foraminiferal Mg/Ca corrected for a Mg/Mn ratio of 0.1 molmol⁻¹ alongside benthic foraminiferal δ¹⁸O from IODP Site U1406.

5.3.3 Correcting for Mg/Ca_{sw}

As discussed in section 5.1.1.2.2 of this chapter, the Mg/Ca of foraminiferal calcite is partly dependent on the Mg/Ca of seawater. In this study, the approach of Lear *et al.* (2015) is adopted whereby the Mg/Ca_{sw} value for each sample is calculated using a third-order polynomial fit through a compilation of published Mg/Ca_{sw} values for the Cenozoic (using equation 6). For IODP Site U1406, the H values used to calculate paleotemperatures corrected for Mg/Ca_{sw} for *Oridorsalis umbonatus* are derived from the exponential calibration of Lear *et al.* (2015) which uses the temperature sensitivity of Lear *et al.* (2002). The Mg/Ca values used are those corrected for Mn contamination assuming a 0.1 molmol⁻¹ Mg/Mn ratio of the coatings (as shown in figure 5.7). As shown in figure 5.9, correcting for seawater Mg/Ca results in paleotemperatures almost 2°C greater than their uncorrected counterparts.

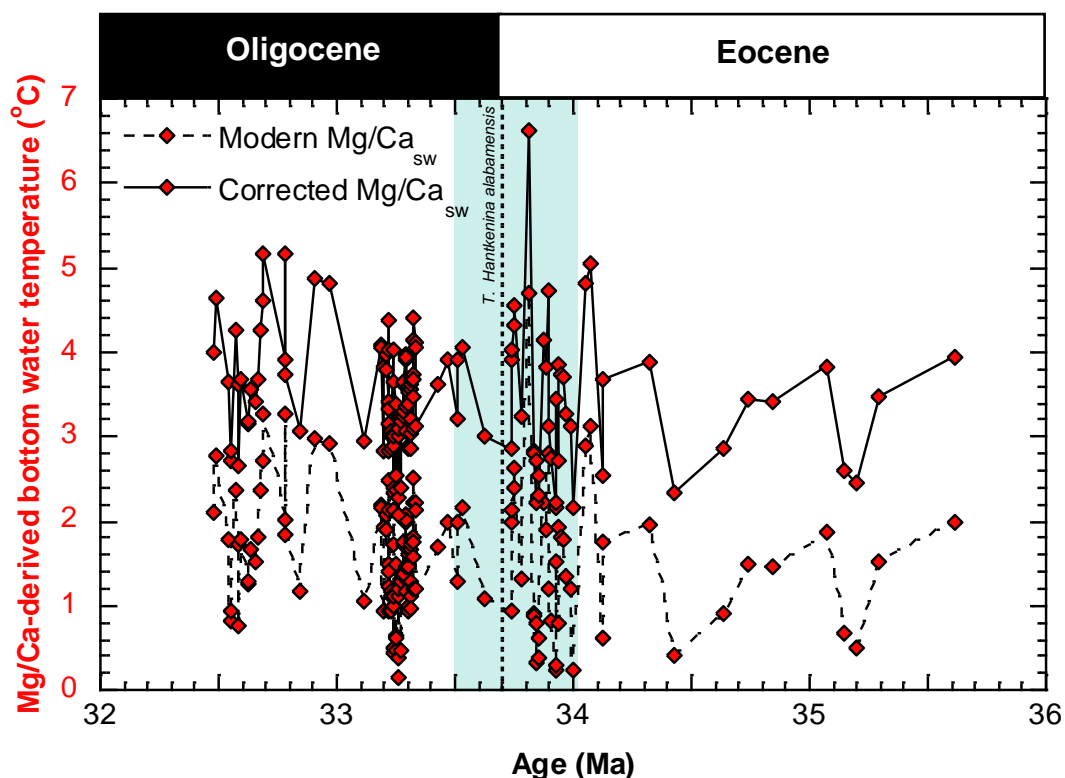


Figure 5.9 – *Oridorsalis umbonatus* Mg/Ca-derived BWT from IODP Site U1406. Dashed lines show Mg/Ca-derived temperatures corrected only for Mn contamination as outlined in the previous section and hence assume a Mg/Ca_{sw} at the EOT equivalent to modern. Solid lines represent Mg/Ca-derived temperatures corrected for both Mn contamination and EOT Mg/Ca_{sw} . Shaded pale blue bar indicates duration of the EOT. EOB marked by top of *Hantkenina alabamensis*. Age model calibrated to Cande and Kent (1995).

For ODP Site 756, the H values used to calculate paleotemperatures corrected for Mg/Ca_{sw} for *Oridorsalis umbonatus* are derived from the exponential calibration of Lear *et al.* (2015) which uses the temperature sensitivity of Lear *et al.* (2002). The H values used to calculate paleotemperatures corrected for Mg/Ca_{sw} for *Cibicidoides havanensis* and *Turborotalia ampliapertura* are taken from the exponential calibration of Hines *et al.* (2017) with the temperature sensitivities of Lear *et al.* (2002) and Anand *et al.* (2003), respectively. The components of these calibrations are detailed in table 5.1. As with *Oridorsalis umbonatus* at IODP Site U1406, when corrected for Mg/Ca_{sw} the paleotemperatures calculated from this shallow infaunal species at ODP Site 756 are approximately 2°C offset from uncorrected Mg/Ca. The other two species, *Cibicidoides havanensis* and *Turborotalia ampliapertura*, are offset by ~ 2.5°C and 1.6°C, respectively (see figure 5.10).

Chapter Five: Refining Estimates of Deep Ocean Temperature across the Eocene-Oligocene Transition

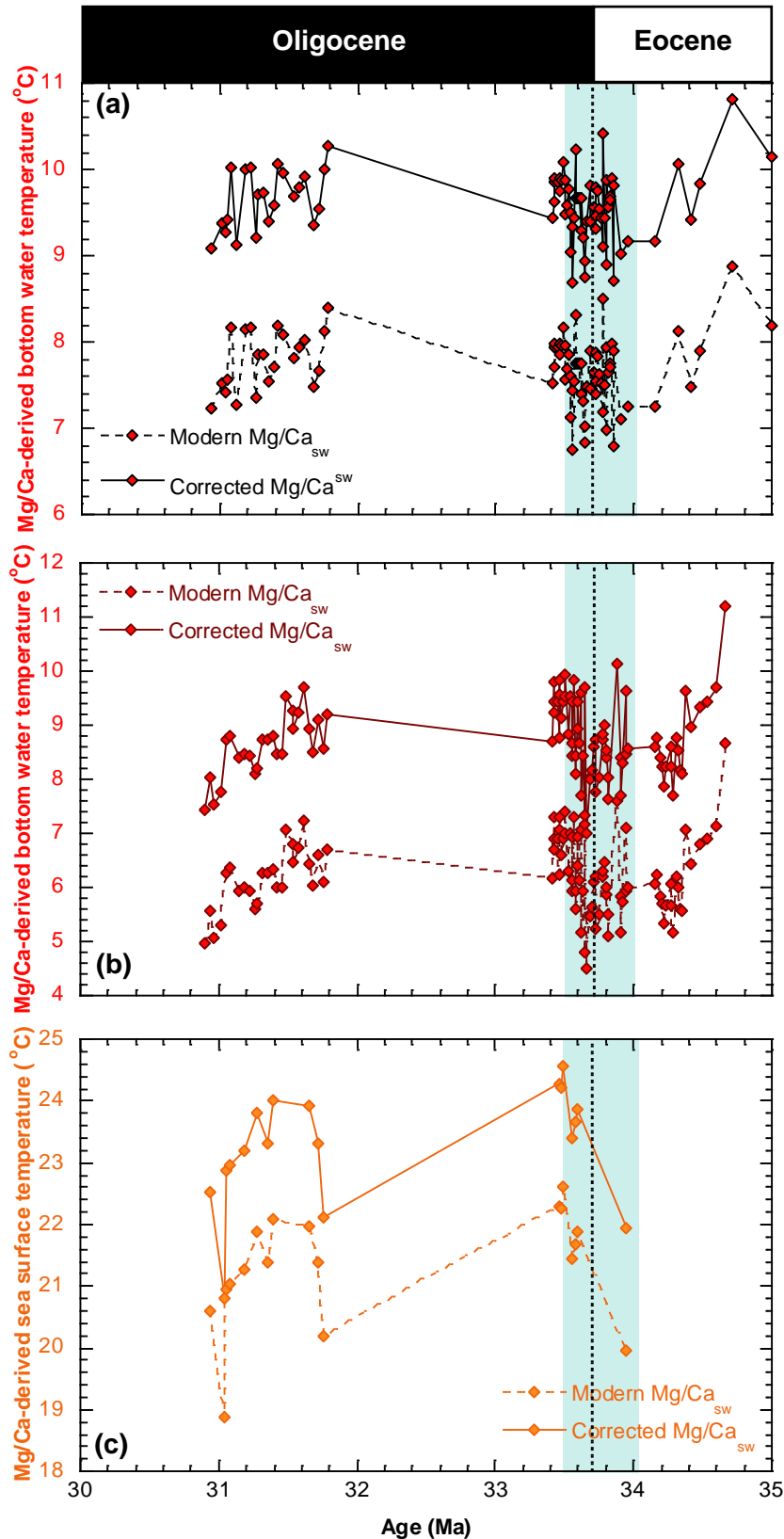


Figure 5.10 – Benthic foraminiferal Mg/Ca-derived BWT from ODP Site 756 from (A) *Oridorsalis umbonatus*, (B) *Cibicidoides havanensis*, and (C) *Turborotalia ampliapertura*. Dashed lines show Mg/Ca-derived temperatures corrected only for Mn contamination as outlined in the previous section. Solid lines represent Mg/Ca-derived temperatures corrected for both Mn contamination and Mg/Ca_{sw} at the EOT. Pale blue shaded bars represent duration of the EOT. EOB marked by top of *Hantkenina alabamensis* as indicated by vertical dashed line. Age model calibrated to Cande and Kent (1995).

5.3.4 Mg/Ca Change across the EOT

As shown in figure 5.11 the Mg/Ca-derived BWT record from IODP Site U1406 is highly variable throughout its duration. Large oscillations on the order of ~ 2 – 5 °C precede the isotope shift during the interval 34 Ma to 33.75 Ma. Maximum values of > 6°C are also seen during this time. It is quite clear that there is a significant absence of permanent cooling across the isotope shift at this northern hemisphere site. This could perhaps be related to the absence of cooling documented in surface waters from the region across the EOT (Liu *et al.* 2018). However there seems to be a slight and gradual warming when comparing the pre- to post-shift periods. Given the water depth of IODP Site U1406 (~ 3300 metres) and the clay-rich nature of the sediments, it is quite possible that the benthic foraminifera were not protected by buffering in the sediments and have been subjected to the influence of $\Delta[\text{CO}_3^{2-}]$. This is supported by very low abundance of planktic foraminifera throughout the sampled section. This possibility will be evaluated in the discussion section of this chapter. Following the isotope shift during the EOGM, between 33.5 Ma and 33 Ma, temperatures continue to oscillate between 2 – 4.5°C.

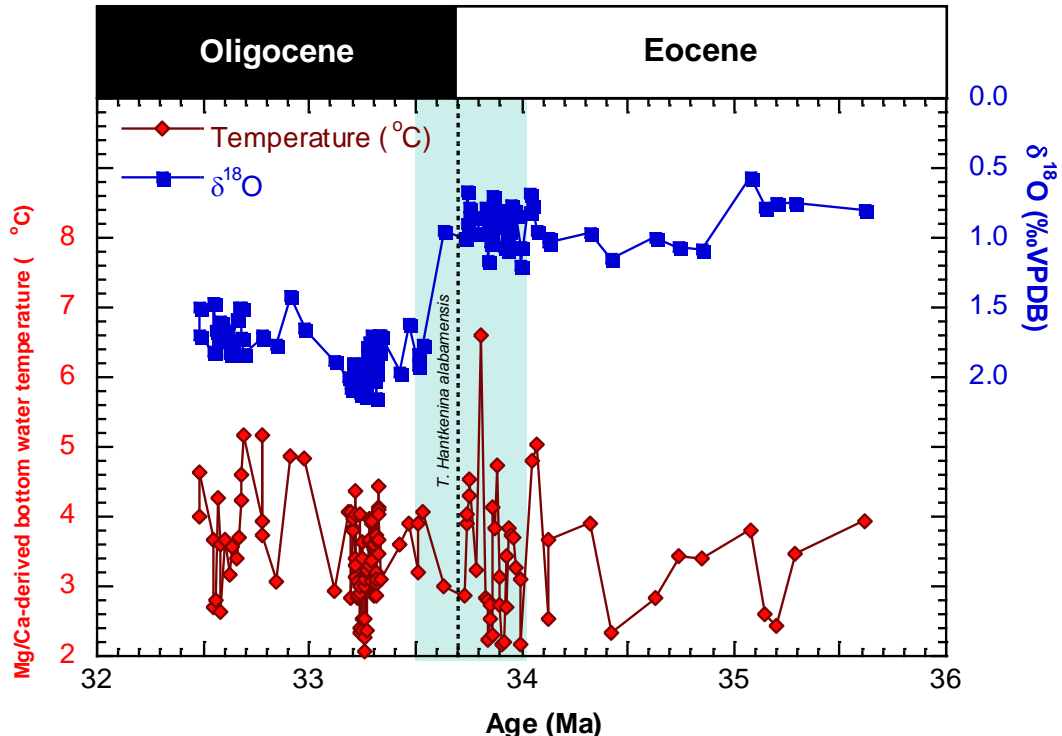


Figure 5.11 – Benthic foraminiferal Mg/Ca-derived BWT from IODP Site U1406 from *Oridorsalis umbonatus* along with benthic foraminiferal $\delta^{18}\text{O}$ from *Cibicoides* sp. Pale blue shaded bar indicates duration of EOT. EOB marked by top of *Hantkenina alabamensis* shown by vertical dashed line. Age model calibrated to Cande and Kent (1995).

Chapter Five: Refining Estimates of Deep Ocean Temperature across the Eocene-Oligocene Transition

ODP Site 756 is a much shallower site (~ 1500 metres) with carbonate-rich sediments and abundant planktonic foraminifera indicating no evidence of dissolution. Benthic foraminiferal Mg/Ca is therefore less likely to be affected by changes in bottom water $\Delta[\text{CO}_3^{2-}]$ at this site.

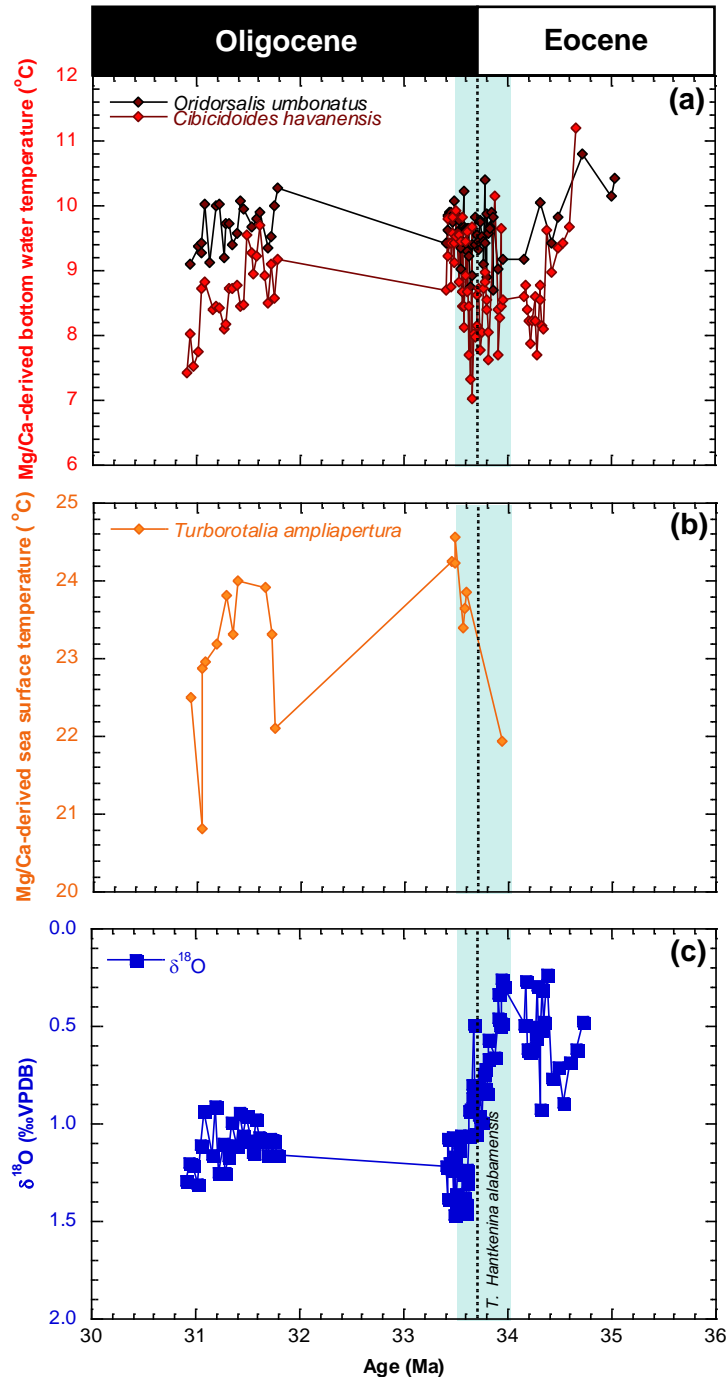


Figure 5.12 – From ODP Site 756 (a) Benthic foraminiferal Mg/Ca-derived BWT from *Oridorsalis umbonatus* and *Cibicidoides* sp. (b) Planktic foraminiferal Mg/Ca-derived SST from *Turborotalia ampliapertura* and (c) benthic foraminiferal $\delta^{18}\text{O}$ from *Cibicidoides* sp. (H.K. Coxall, unpublished). Pale blue shaded bar indicates duration of EOT. EOB marked by top of *Hantkenina alabamensis*. Age model calibrated to Cande and Kent (1995).

Chapter Five: Refining Estimates of Deep Ocean Temperature across the Eocene-Oligocene Transition

As shown in figure 5.12, a distinct cooling is seen in both species of benthic foraminifera. *Oridorsalis umbonatus* records a cooling of $\sim 1.6^{\circ}\text{C}$ from 10.8°C at 34.71 Ma to 9.2°C at 34.15 Ma. *Cibicidoides havanensis* records a decrease in BWT of 2.4°C from 11.2°C at 34.66 Ma to 8.8°C at 34.17 Ma. The disparity in the magnitude of BWT cooling is possibly due to the use of a generic *Cibicidoides* calibration rather than one specifically calculated for *Cibicidoides havanensis*. Across the isotope shift, both benthic species and the near-surface dwelling planktonic species, *Turborotalia ampliapertura*, record an increase in BWT and SST respectively. Bottom waters appear to warm by 1.5°C between 33.91 Ma and 33.43 Ma whereas SST increases by 2.6°C between 33.94 Ma and 33.49 Ma. It is impossible to make interpretations as to changes in temperature in the early EOGM due to a substantial hiatus that persists until 31.8 Ma. Thereafter a period of significant cooling ensues in both the bottom water and surface ocean temperature records. BWT decreases by 2.3°C between 31.62 Ma and 30.93 Ma. A similar magnitude of cooling is seen in SST whereby temperature cools from 23.9°C at 31.65 Ma to 20.8°C at 31.04 Ma.

5.4 Discussion

5.4.1 Influence of Saturation State at IODP Site U1406

In section 2.3.4 it was observed that there is a significant absence of cooling across the isotope shift at IODP Site U1406. Given the water depth of IODP Site U1406 (~3300 m) and the clay-rich nature of the sediments, it is quite possible that the benthic foraminifera were not protected by buffering in the sediments and have been subjected to the influence of $\Delta[\text{CO}_3^{2-}]$; an idea supported by very low abundance of planktic foraminifera throughout the sampled section. Previous work has suggested that paired Li/Ca and Mg/Ca analysis offers a method by which the $\Delta[\text{CO}_3^{2-}]$ and temperature controls on Mg/Ca can be deconvolved (Lear and Rosenthal, 2006; Lear *et al.* 2010; Mawbey and Lear, 2013) even when significant changes in $\Delta[\text{CO}_3^{2-}]$ have occurred (Lear *et al.* 2010).

Li/Ca in benthic foraminifera exhibits a strong negative correlation with temperature; as temperature decreases, Li/Ca increases (Hall and Chan, 2004; Marriot *et al.* 2004a; 2004b). This inverse relationship with temperature may lend itself to the use of Li/Ca as a paleothermometer at lower temperatures (Marriot *et al.* 2004b). However, down-core comparison of Li/Ca and $\delta^{18}\text{O}$ suggest variations too sizeable to be explained solely by temperature change, rather some other factor must exert a control on Li/Ca ratios in benthic foraminifera (Marriot *et al.* 2004b). Indeed, Li/Ca ratios are positively correlated with saturation state (Lear and Rosenthal, 2006). Benthic foraminiferal Li/Ca ratios give support to the hypothesis that increased $\Delta[\text{CO}_3^{2-}]$ in the deep ocean exerts a strong influence on Mg/Ca ratios across the EOT (Lear *et al.* 2010; Pusz *et al.* 2011; Mawbey and Lear, 2013). In contrast to Mg/Ca ratios, the linear relationship between Li/Ca ratios and $\Delta[\text{CO}_3^{2-}]$ endures into well-saturated waters and does not appear to reach a threshold (Lear *et al.* 2010).

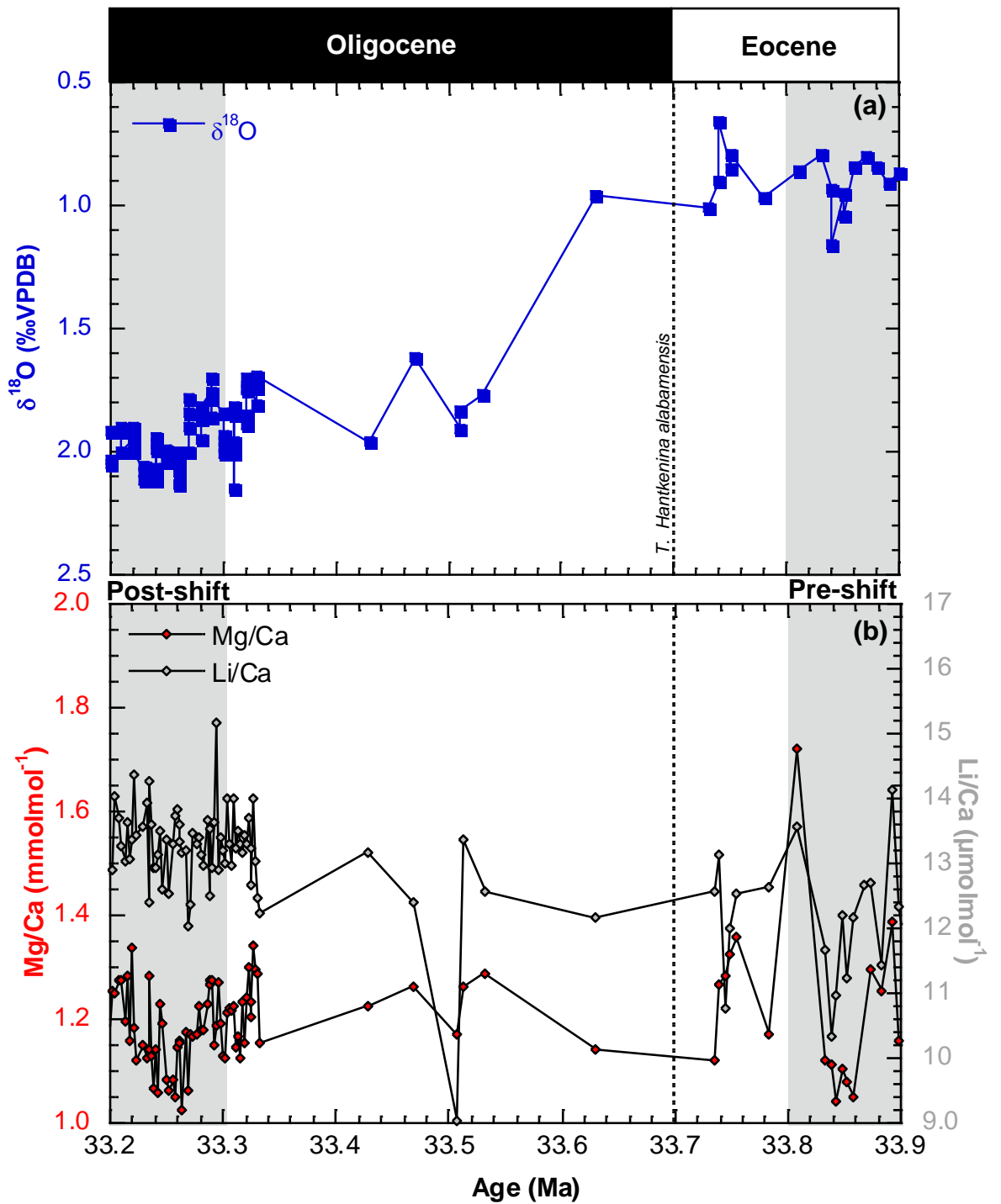


Figure 5.13 - (a) Benthic foraminiferal $\delta^{18}\text{O}$ and (b) Mg/Ca and Li/Ca from *Oridorsalis umbonatus* at IODP Site U1406. Mg/Ca values corrected for Mn-rich contaminant phase. EOB marked by top of *Hantkenina alabamensis*. Age model calibrated to Cande and Kent (1995).

Chapter Five: Refining Estimates of Deep Ocean Temperature across the Eocene-Oligocene Transition

	Average Mg/Ca (mmolmol ⁻¹)	Average Li/Ca (μmolmol ⁻¹)	Average Temperature (°C)* <small>*assuming no saturation state influence on Mg/Ca</small>
Pre-Shift 33.9 - 33.8 Ma	1.21	12.12	3.44
Post-Shift 33.3 - 33.2 Ma	1.18	13.32	3.24
Difference	-0.03	1.20	-0.20
Change in temperature (°C)	-0.98		
Change in saturation state (μmolkg ⁻¹)	10.15		

Table 5.2 – Values taken from intervals highlighted with grey bars in figure 5.13 and used to calculate the influence of relative changes in both temperature and carbonate ion saturation state on Mg/Ca and Li/Ca.

Table 5.2 details the intervals shown by grey bars in figure 5.13. These intervals are defined as pre-shift (33.9 – 33.8 Ma) and post-shift (33.3 – 33.2 Ma). Average values of both Li/Ca and Mg/Ca are taken across these two intervals. Average Li/Ca increases from 12.12 μmolmol⁻¹ to 13.32 μmolmol⁻¹. Concurrently, average Mg/Ca decreases from 1.21 mmolmol⁻¹ to 1.18 mmolmol⁻¹. An increase in Li/Ca could suggest either a decrease in temperature, an increase in saturation state or a combination of both. While it is possible that the Li/Ca might also be impacted by Mn/Ca contamination, comparison of the two ratios across the studied interval suggests this is unlikely (see appendix 4). In this study, the approach of Lear *et al.* (2010) is used to try to deconvolve the relative change in temperature and Δ[CO₃²⁻] contributing to both the Mg/Ca and Li/Ca records at IODP Site U1406. This study used a combination of temperature and Δ[CO₃²⁻] calibrations to do so:

$$\Delta\text{Mg} = 0.0086.\Delta\text{CO}_3^{2-} + 0.12.\Delta\text{T} \quad \text{Eq. 7}$$

$$\Delta\text{Li} = 0.047.\Delta\text{CO}_3^{2-} - 0.74.\Delta\text{T} \quad \text{Eq. 8}$$

When applied to the section from IODP Site U1406, this approach documents an increase in bottom water $\Delta[\text{CO}_3^{2-}]$ of $10.15 \mu\text{molkg}^{-1}$ and a BWT cooling of 0.98°C . This approach assumes that the foraminiferal Mg/Ca record has been affected by changing saturation state. If it is assumed that the change in average Mg/Ca between the two intervals can be attributed solely to temperature change this suggests a decrease in temperature of 0.2°C . Using the same approach of Lear *et al.* (2010) this would imply that $\Delta[\text{CO}_3^{2-}]$ increased by $25.85 \mu\text{molkg}^{-1}$ between the two intervals. When previously applied to sections across the EOT, this approach suggested a change in $\Delta[\text{CO}_3^{2-}]$ of $19 \mu\text{molkg}^{-1}$ and $36 \mu\text{molkg}^{-1}$ respectively at DSDP Site 522 and ODP Site 1218 (Lear *et al.* 2010). The influence of $\Delta[\text{CO}_3^{2-}]$ appears to be most similar between sites in the Atlantic Ocean; this is true no matter what assumption is made about the influence of temperature on Mg/Ca. However, the estimate where an influence of $\Delta[\text{CO}_3^{2-}]$ on Mg/Ca is assumed is in closest agreement with those from elsewhere in the Atlantic Ocean (e.g. DSDP Site 522).

It would appear that, across the isotope shift, combining Mg/Ca and Li/Ca is a better approach to reconstructing the bottom water temperature trend in the North Atlantic. When applied to the section from IODP Site U1406, this approach documents a cooling of 0.98°C ; a lower magnitude of cooling than that documented at DSDP Site 522 in the South Atlantic (Lear *et al.* 2010) and other sites in the high southern latitudes. This is the first record of BWT change across the EOT from the North Atlantic region and supports earlier conclusions that a transient interhemispheric temperature asymmetry occurred coeval with glaciation at the EOT (Liu *et al.* 2018) whereby BWT and SST cooled to a much greater degree in the high southern latitudes than in their northern counterparts. Modelling efforts attribute this to changes in ocean circulation and interhemispheric heat transport due to growth of the AIS (Goldner *et al.* 2014). This theory supports an earlier idea discussed in chapter three of this thesis as an explanation of greater oscillations in the ϵNd record from ODP Site 1263. Following the onset of glaciation on Antarctica it is likely that the highly dynamic nature of the AIS during its infancy prompted oscillations in the relative strengthening and weakening of the two polar-sourced water masses whereby intensification of deep water formation at one pole may occur at the expense of deep

water formation at the other. Increasing ice volume on Antarctica is known to enhance production of AABW by the growth of sea ice and associated brine rejection (Ohshima *et al.* 2016) and hence would enhance cooling in the high southern latitudes.

5.4.2 Indian Ocean Circulation

In the modern ocean, the Indian Ocean presents a much more complicated picture than both the Atlantic and Pacific serving as an oceanographic go-between for both of these larger ocean basins (Trujillo and Thurman, 2008). The northern reaches of the surface Indian Ocean are controlled predominantly by seasonal changes due to its basin shape and surrounding areas of high relief resulting in oscillations between the northeast monsoon and the southwest monsoon (Trujillo and Thurman, 2008). The southern reaches of the surface Indian Ocean are dominated by the Indian Ocean subtropical gyre. The north and south are characterised by low dissolved oxygen and high nutrient content, and high dissolved oxygen and low nutrient content, respectively (Tchernia, 1980). The influence of these northern- and southern-derived systems is divided by a salinity minimum at around 10°S (Tchernia, 1980). Given the tropical and sub-tropical setting of the Indian Ocean basin oscillations in both surface temperature and salinity are much smaller than elsewhere in the world's ocean leading to an absence of deep water formation. Hence, at depth the Indian Ocean is characterised by a collection of different water masses; including AABW, NADW and AAIW. The northward progression of these water masses is halted at 10°S; beyond this latitude bottom waters are composed of a mix of Red Sea, Persian Gulf and Arabian Sea Water.

However, circulation patterns of the latest Eocene and earliest Oligocene were likely very different. Historically, understanding of oceanographic changes in the Indian Ocean has been limited in comparison to that of the Atlantic and the Pacific. It was not until the late 1950s and early 1960s that concerted efforts were made as part of the International Indian Ocean Expedition to increase the understanding of modern Indian Ocean oceanography. In terms of paleoceanography, Indian Ocean deep sea drilling efforts have traditionally been impeded by hiatuses and poor recovery. However, the ODP studies of the early and mid-1990s made a significant

contribution to the spatial and temporal resolution of Cenozoic paleoceanographic records of the Paleogene and the Neogene.

In this section records generated by Max Holström from ODP Site 756 in the Indian Ocean are compared with those from ODP Site 689 (Maud Rise, Atlantic sector of the Southern Ocean) and ODP Site 748 (Kerguelen Plateau, Indian sector of the Southern Ocean) (figure 5.15). It is clear that some key similarities and differences exist when comparing these three records.

5.4.2.1 Temperature Disparity in the Indian Ocean: The Influence of Tethyan-Sourced Waters or NCW?

It is thought that the Paleocene and early Eocene Indian Ocean was reasonably homogenous in terms of water masses and temperature gradients. The ocean was much warmer at this time with BWTs of around 10 – 16°C (Zachos *et al.* 1992). A divergence between $\delta^{18}\text{O}$ values at ODP Site 757 (Ninety East Ridge) and ODP Site 748 (Kerguelen Plateau) occurred at c. 42 Ma likely representing a thermal segregation of intermediate water masses in the Indian Ocean (Zachos *et al.* 1992). Kerguelen Plateau, in the higher southern latitudes, was bathed by a colder, southern-sourced deep-water mass akin to AAIW whereas Ninety East Ridge remained under the influence of a low latitude, warm and saline water mass. Evidence from neodymium isotopes at ODP Site 689 supports this theory; the onset to more radiogenic values occurs at c. 40.8 Ma suggesting the presence of a colder, southern-sourced bottom water mass (Scher and Martin, 2004). This thermal segregation intensified following glaciation and remained until the late Oligocene (Zachos *et al.* 1992) and hence is a reasonable explanation for the disparity between temperature records in the Southern Ocean (ODP Sites 689 and 748) and the Indian Ocean (ODP Site 756) in the latest Eocene (figure 5.15).

Figure 5.15 shows a BWT cooling on the order of 2 – 3°C over the course of 400 kyr at ODP Site 756 between 34.7 Ma and 34.3 Ma. This cooling is not evident in the Southern Ocean records over the same interval. However, a substantial (~ 2 – 3°C) cooling of both SST and BWT between 34.3 Ma and the onset of the isotope shift at the EOT occurs at both ODP Site 689 and ODP Site 748. This magnitude of cooling is distinctly absent from the BWT record at ODP Site 756 where temperature

remains stable across this interval. Average temperatures also appear to be on the order of 3 – 4°C cooler at the deeper, high latitude sites than at ODP Site 756. It is likely that this difference occurred due to the different water masses present at these sites across the late Eocene. The cooler nature of and similarity between temperature changes at ODP Sites 689 and 748 suggest that they were both bathed by the colder high latitude water mass. Conversely, BWT at ODP Site 756 is more likely a result of a warmer, more saline water mass derived from the northern region of the Indian Ocean basin. One possible candidate for this southerly flowing warm, saline water mass has been termed Tethyan-Indian Saline Water (TISW) after its likely source region (Woodruff and Savin, 1989; Zachos *et al.* 1992).

The Tethys Ocean has undergone many stages of evolution from its greatest extent during the Mesozoic era to its compartmentalisation in the Cenozoic. This ocean became a seaway following the opening of the Indian Ocean with the northward movement of the African, Australian and Indian plates and allowed surface throughflow from the Indian to the Atlantic Ocean and the passage of waters at depth in the opposing direction. While much debate surrounds the precise timing of its closure with estimates varying from the Late Eocene to Middle Miocene (Rögl, 1999; Jovane *et al.* 2007; Allen and Armstrong, 2008; Bialik *et al.* 2019), earliest estimates of c. 35 Ma align well with the significant cooling at ODP Site 756 between 34.7 Ma and 34.3 Ma. A narrowing of the Tethys seaway due to the collision of the Eurasian and Arabian plates would diminish the influence of warm, saline Tethyan-sourced water on sites in the northerly regions of the Indian Ocean basin. The absence of this signal in the high southern latitude sites is to be expected given that this region was already bathed by a Southern Ocean sourced water mass. This idea is supported by an increase in ϵNd at ODP Site 757 (also on Ninety East Ridge) over this time interval; ϵNd decreases from -7.5 to -6 between 36 Ma and 28.5 Ma which might suggest a diminished influence of non-radiogenic Tethyan seawater (Scher *et al.* 2002). It has been suggested that TISW was replaced in the northern Indian Ocean by Indonesian Throughflow in the earliest Oligocene (Scher *et al.* 2002), however subsequent studies have found no evidence for this (Wright *et al.* 2018). It is more likely that the influence of TISW waxed and waned during the final stages of

narrowing (Jovane *et al.* 2007) before its replacement by a Southern Ocean-derived intermediate water mass.

However, given that TISW is thought to have been both warm and saline, it is surprising that a significant change in salinity is not seen in records of $\delta^{18}\text{O}_{\text{sw}}$ from ODP Site 756. If a saline water mass bathed ODP Site 756 $\delta^{18}\text{O}_{\text{sw}}$ could reasonably be expected to be higher than at other sites within the Indian Ocean basin; something that is not evident upon comparison of ODP Sites 689, 748 and 756 (see figure 5.15). The timing of significant cooling at ODP Site 756 coincides with the onset of NCW in the North Atlantic at 34.7 Ma (see chapter three of this thesis). Hence it is possible that, as NCW exerted greater influence in the Atlantic, Southern Ocean-derived bottom waters were diverted elsewhere. The colder high latitude-derived deep waters increased their northward influence in the Indian Ocean as NCW began to fill the Atlantic. The warmer temperatures at ODP Site 756 were perhaps simply because of a difference in water depth between the Ninety East Ridge site and those at higher latitudes.

Recent work has focused on modelling the impacts of NCW onset due to closure of the Arctic gateway to the North Atlantic (Hutchinson *et al.* 2019). Figure 5.14 shows modelled temperature along a north-south transect through the Indian Ocean at 38 Ma. The difference between panel a and b of figure 5.14 results from closure of the Arctic gateway in the model. Prior to gateway closure deep waters bathing ODP Site 756 stemmed from the North Pacific. However, following gateway closure deep waters from the Southern Ocean bathed Ninety East Ridge. This change in bottom water mass appears to have been associated with a $\sim 1 - 2^\circ\text{C}$ cooling likely due to the colder and fresher nature of Southern Ocean-driven bottom waters. While the same modelling simulations suggest some change in the Tethys region, no deep water formation appears to occur there either pre- or post-gateway closure. Hence the cooling discussed above is most likely associated with changes in Indian Ocean bottom water masses due to onset of NCW in the North Atlantic.

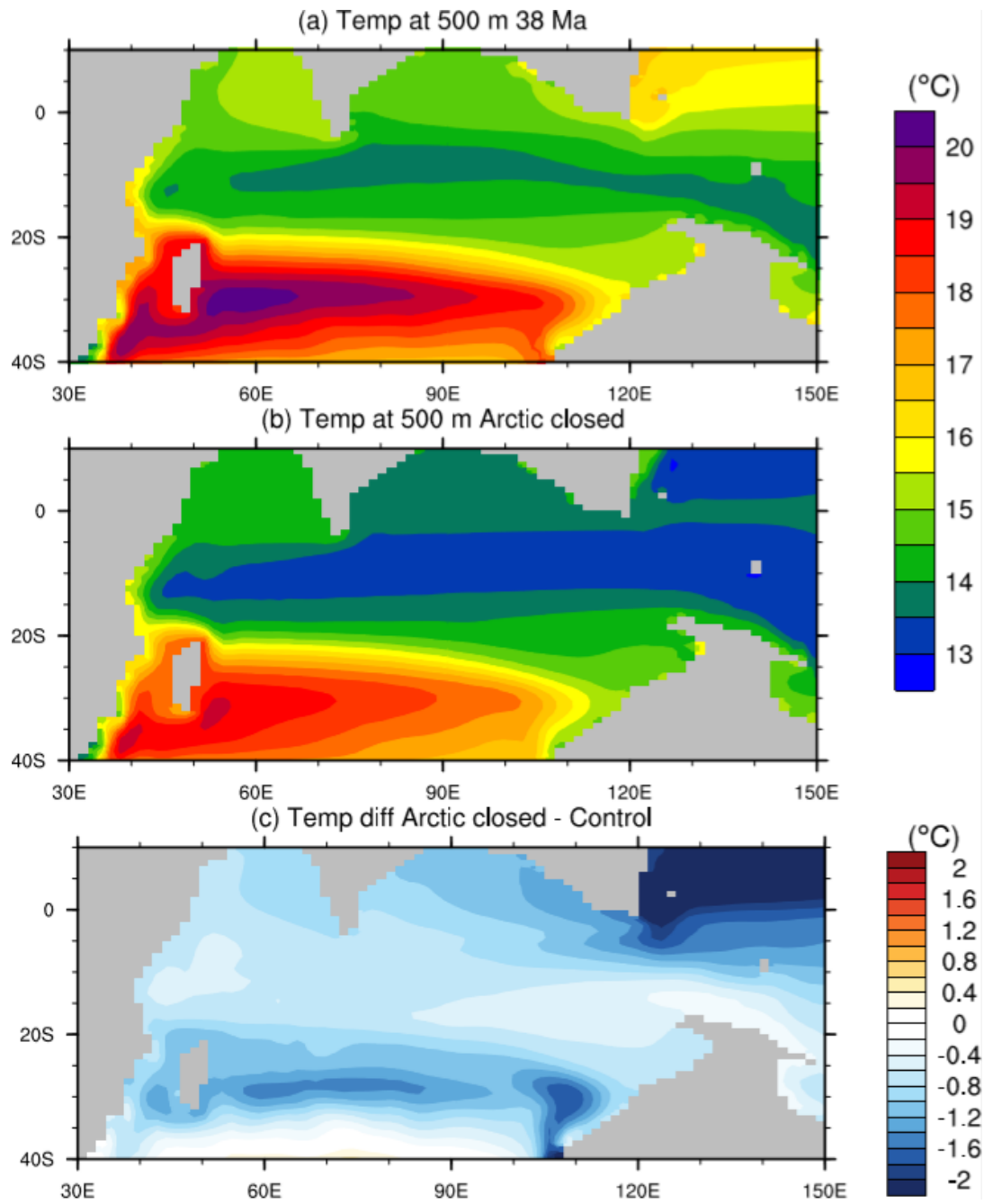


Figure 5.14 – Modelling simulation of temperature change due to onset of AMOC as a result of closure of the Arctic-North Atlantic gateway. Panels show a north-south transect through the Indian Ocean at 500 metre water depth. Difference between panels a and b is closure of the Arctic-North Atlantic gateway. Simulations, provided by David Hutchinson (pers. comm), were developed using the GFDL CM2.1 model adapted to Late Eocene boundary conditions including paleogeography of Baatsen *et al.* (2016).

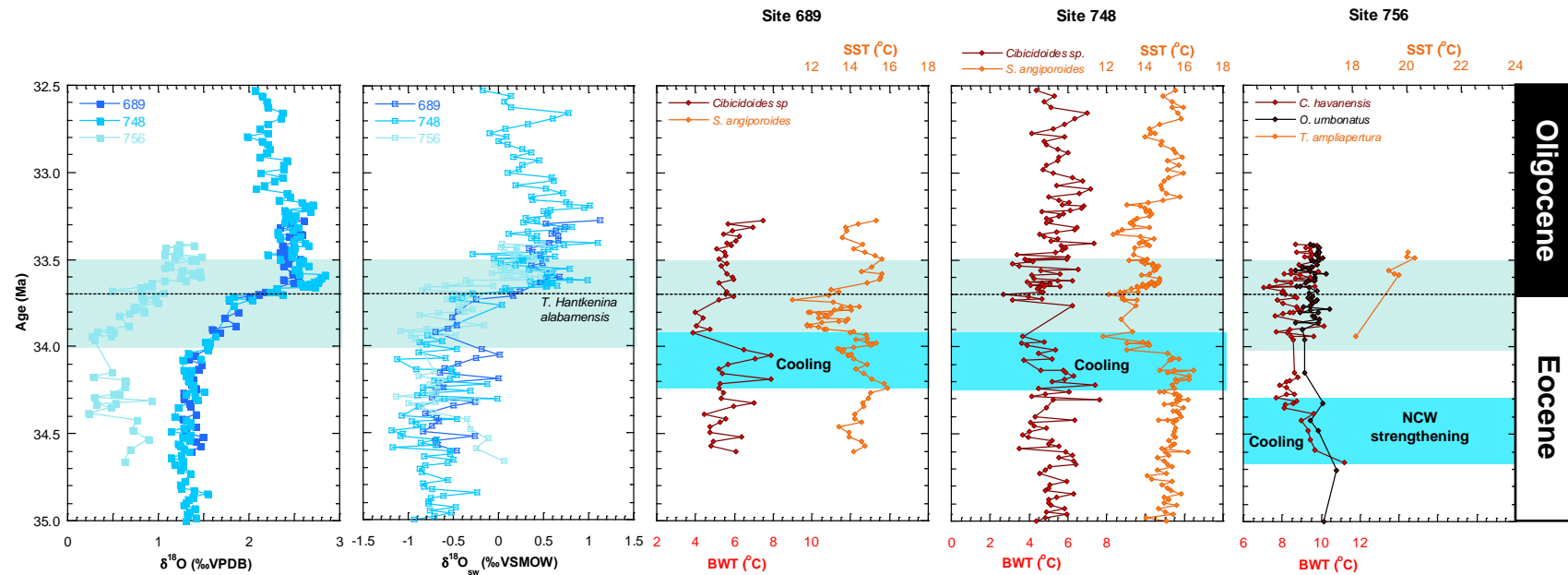


Figure 5.15 – Records of benthic foraminiferal $\delta^{18}\text{O}$ and $\delta^{18}\text{O}_{\text{sw}}$ from Indian Ocean including ODP Site 756 (H.K. Coxall - unpublished), ODP Site 689 and ODP Site 748 (Bohaty *et al.* 2012). Foraminiferal SST and BWT from Indian Ocean including ODP Site 756 (this study), ODP Site 689 and ODP Site 748 (Bohaty *et al.* 2012). Pale blue shaded bar indicates duration of the EOT. EOB marked by top of *Hantkenina alabamensis*. Turquoise bars show periods of cooling and strengthening of NCW. Age model calibrated to Cande and Kent (1995).

5.4.2.2 A Regional Indian Ocean Warming?

A substantial (~ 2 – 3°C) cooling of both SST and BWT between 34.3 Ma and the step one of the isotope shift at the EOT occurs at both ODP Site 689 and ODP Site 748. This magnitude of cooling is distinctly absent from the BWT record at ODP Site 756 where temperature remains stable across this interval. Thereafter however figure 5.15 depicts some interesting trends across the isotope shift. At ODP Site 756, a 1.8°C increase in temperature is seen in the record from *Cibicidoides havanensis* between 33.62 Ma and 33.55 Ma from 7.7°C to 9.6°C. An even greater degree of warming is seen across the same interval at ODP Site 748; bottom water temperature increases by 3.4°C from 3.1°C at 33.77 Ma to 6.5°C at 33.55 Ma (Bohaty *et al.* 2012).

While acknowledging that it is possible, if unlikely, that SST cooling at the onset of the isotope shift was not accompanied by a concomitant bottom water cooling, Bohaty *et al.* (2012) attribute the lack of deep ocean cooling across the EOT at ODP Sites 689 and 748 to the influence of carbonate saturation state changes despite their somewhat shallow paleo water depths (1500 metres and 800 metres, respectively). However, an absence of paired Li/Ca or B/Ca data from both sites prevented the authors from drawing more concrete conclusions as to the influence of $\Delta[\text{CO}_3^{2-}]$. Given the relatively shallow paleo water depth of ODP Site 756 (~ 450 m), a significant influence from $\Delta[\text{CO}_3^{2-}]$ might be surprising. However, BWTs derived from *Oridorsalis umbonatus* do not indicate substantial warming across the same interval; infaunal species are thought to be less susceptible to the influence of $\Delta[\text{CO}_3^{2-}]$ and hence may not be recording the same signal as *Cibicidoides havanensis* (Elderfield *et al.* 2006). Given the availability of Li/Ca data from this site and the significant increase in Li/Ca across the isotope shift (figure 5.16), the approach of Lear *et al.* (2010) is employed to try to deconvolve any effect of temperature and $\Delta[\text{CO}_3^{2-}]$. Table 5.3 details the intervals shown by grey bars in figure 5.16. These intervals are defined as pre-shift (34 – 33.9 Ma) and post-shift (33.6 – 33.5 Ma). Average values of both Li/Ca and Mg/Ca are taken across these two intervals. Average Li/Ca increases from 10.53 μmolmol^{-1} to 11.75 μmolmol^{-1} . Concurrently, average Mg/Ca increases from 1.66 mmolmol^{-1} to 1.78 mmolmol^{-1} . An

Chapter Five: Refining Estimates of Deep Ocean Temperature Across the Eocene Oligocene Transition

increase in Li/Ca could suggest either a decrease in temperature, an increase in saturation state or a combination of both.

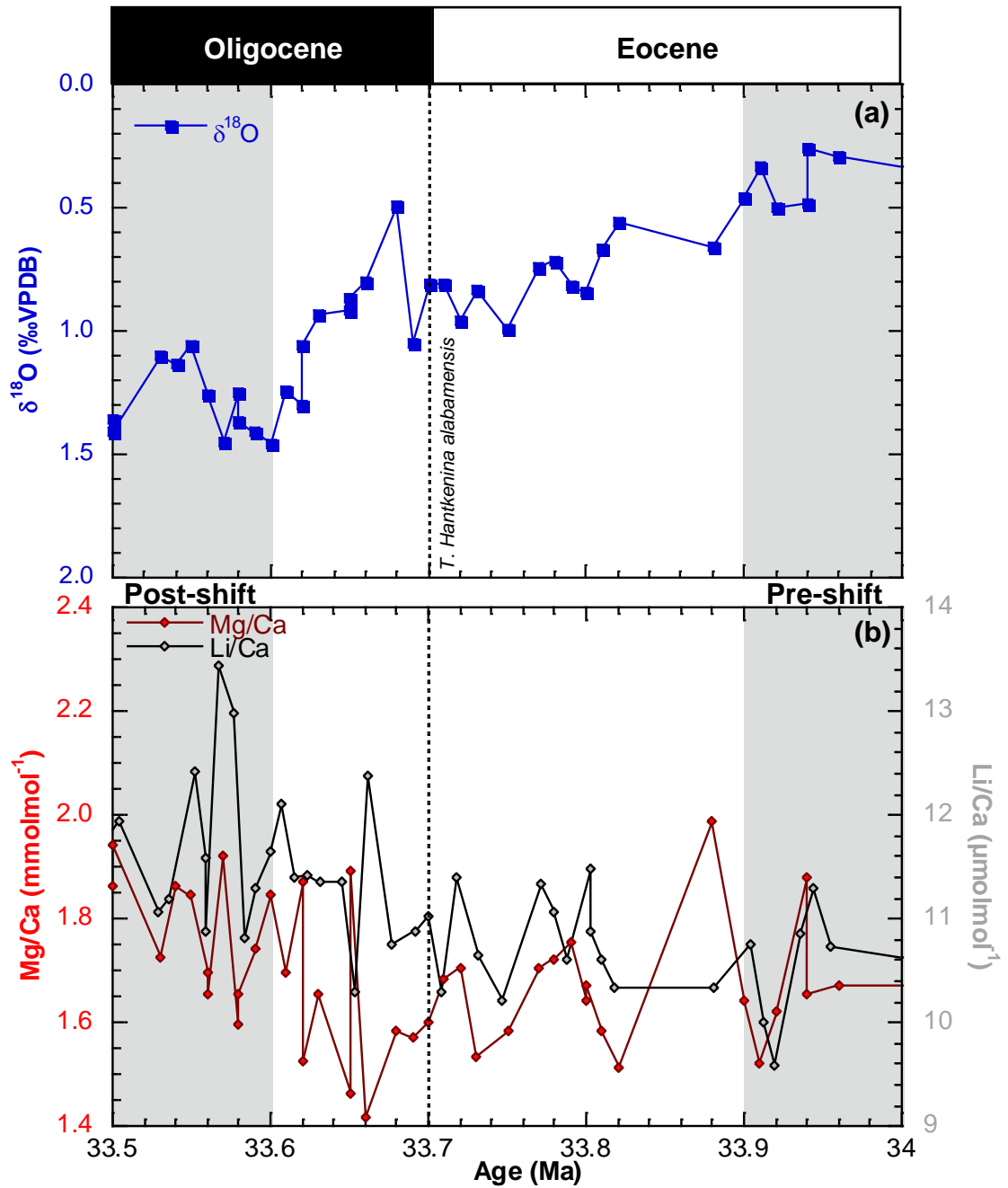


Figure 5.16 – Records of benthic foraminiferal $\delta^{18}\text{O}$ (a) and Mg/Ca and Li/Ca (b) from *Cibicidoides havanensis* at ODP Site 756. Mg/Ca values corrected for Mn-rich contaminant phase. EOB marked by top of *Hantkenina alabamensis*. Age model calibrated to Cande and Kent (1995).

Chapter Five: Refining Estimates of Deep Ocean Temperature Across the Eocene Oligocene Transition

	Average Mg/Ca <i>C. havanensis</i> (mmolmol ⁻¹)	Average Temperature (°C) <small>*assuming no saturation state influence on Mg/Ca</small>	Average Li/Ca <i>C. havanensis</i> (μmolmol ⁻¹)	Average B/Ca <i>C. havanensis</i> (μmolmol ⁻¹)
Pre-Shift 34 - 33.9 Ma	1.66	8.50	10.53	123.57
Post-Shift 33.6 - 33.5 Ma	1.78	9.07	11.75	156.95
Difference	0.12	0.57	1.22	33.38
Change in temperature (°C)	-0.40			
Change in saturation state (μmolkg ⁻¹)	19.60			

Table 5.3 – Values taken from intervals highlighted with grey bars in figure 5.16 and used to calculate the influence of relative changes in both temperature and carbonate ion saturation state on Mg/Ca and Li/Ca.

When applied to the section from ODP Site 756, this approach documents an increase in $\Delta[\text{CO}_3^{2-}]$ of 19.6 μmolkg^{-1} and a temperature decrease of 0.4°C. This approach assumes that the foraminiferal Mg/Ca record has been affected by changing saturation state. If it is assumed that the change in average Mg/Ca between the two intervals can be attributed solely to temperature change this suggests an increase in temperature of 0.57°C. In an attempt to corroborate the estimates of $\Delta[\text{CO}_3^{2-}]$ made using the approach of Lear *et al.* (2010), B/Ca in *Cibicidoides havanensis* from ODP Site 756 is used to calculate changing $\Delta[\text{CO}_3^{2-}]$ across the same interval using the approach of Yu and Elderfield (2007). In the absence of a calibration specifically for *Cibicidoides havanensis* two different calibrations are used; one for *Cibicidoides wuellerstorfi* and another for *Cibicidoides mundulus*. These two calibrations suggest a change in $\Delta[\text{CO}_3^{2-}]$ between the pre-shift and post-shift intervals of 48 μmolkg^{-1} and 29 μmolkg^{-1} ; estimates suggesting a potentially significant influence of $\Delta[\text{CO}_3^{2-}]$ on Mg/Ca at this site. However, there is great disparity between estimates dependent on the species-specific calibration used. It is important to remember that: (i) neither of these calibrations are for

Cibicidoides havanensis; and (ii) there is a strong influence of vital effects on the B/Ca of different species (Yu and Elderfield, 2007) meaning that only speculative conclusions can be drawn from these values. However, it is perhaps more likely that the change in $\Delta[\text{CO}_3^{2-}]$ at ODP Site 756 is towards the lower end of these estimated values given: (i) the shallow water depth at ODP Site 756; and (ii) when considering the uncertainty associated with these calculations ($\pm 10 \mu\text{mol kg}^{-1}$), the *Cibicidoides mundulus* estimate of $29 \mu\text{mol kg}^{-1}$ is closer to the estimate calculated using the approach of Lear *et al.* (2010) ($19.6 \mu\text{mol kg}^{-1}$). Therefore, assuming that none of the values used to perform these calculations are impacted by diagenesis, the change in saturation state appears to be lower in the Indian Ocean than in the Atlantic and much lower than in the Pacific across the EOT.

By the EOT the dominant water masses bathing ODP Site 756 were likely derived from the Southern Ocean. Given that there is no significant change in water mass at Kerguelen Plateau in the latest Eocene and earliest Oligocene (Wright *et al.* 2018), it is likely that the water mass that bathed ODP Site 748 simply increased its influence northward to the lower latitudes of ODP Site 756 at the EOT. The most likely candidate for inducing change in the EOT Indian Ocean has previously been proposed as Subantarctic Mode Water (SAMW) (Dunkley-Jones *et al.* 2008). In the modern ocean, SAMW forms on the northern edge of the ACC within close proximity of the Subantarctic Front (SAF). It is largely responsible for communicating change in high latitude climate parameters to the low latitude Indian Ocean. The incursion of SAMW is also a plausible cause for a lesser change in $\Delta[\text{CO}_3^{2-}]$ at Site 756. In the modern ocean, nutrients transported northward in SAMW account for as much as 75% of biological productivity north of 30°S (Sarmiento *et al.* 2004; Dunkley-Jones *et al.* 2008). An increased flux of nutrients to the Southern Ocean as a result of glaciation-induced sea level fall and weathering of newly exposed shelf sediments transported in enhanced SAMW likely increased productivity and associated export production in the low-latitude Indian Ocean. This interpretation is in line with evidence of regional changes in nannofossil abundance; assemblage diversity decreased and the abundance of eutrophic taxa increased at this time (Dunkley-Jones *et al.* 2008; Villa *et al.* 2014).

Greater rates of export production are also associated with higher rates of organic carbon burial. A localised increase in the preservation of organic matter due to cooling bottom waters may also have compounded this effect. Therefore, the incursion of nutrient-rich waters derived from the Southern Ocean would likely lead to a lesser change in $\Delta[\text{CO}_3^{2-}]$. Conversely, regions of the Pacific have documented declining productivity across the EOT (e.g. Moore *et al.* 2014) with a traceable decline in productivity in a northerly direction through the basin (Griffith *et al.* 2010). This could perhaps suggest that waters leaving the Indian and Indian sector of the Southern Ocean for the Pacific were nutrient depleted and hence explain the greater change in $\Delta[\text{CO}_3^{2-}]$ documented at ODP Site 1218 (Lear *et al.* 2010).

As shown in figure 5.15, there is a slight ($\sim 1.5^\circ\text{C}$) SST warming at both ODP Site 689 and ODP Site 748 associated with the second step of the isotope shift; the interval associated with the greatest magnitude of AIS growth. The resolution of the record at ODP Site 756 is too coarse to precisely determine any concomitant warming at this site. While there is significant doubt cast on the authenticity of the concomitant BWT warming, the occurrence of a SST warming is potentially more plausible. Modelling studies focused on the regional variation in SST change due to growth of the AIS find SST warming reaching from the high southern latitudes to the tropical latitudes of the Indian Ocean which they attribute to changes in thermal stratification due to intensification of AABW formation (Goldner *et al.* 2013; 2014). While these simulations are heavily dependent on the choice of paleogeography used, the modelling output in figure 5.14 appears to corroborate the presence of warmer waters in the upper water column (> 500 m) in the high latitude Indian Ocean.

5.4.3 Ice Growth at the EOT

Changes in $\delta^{18}\text{O}$ of benthic foraminifera provide a signal of both change in ice volume and BWT. $\delta^{18}\text{O}_{\text{sw}}$ records changing continental ice volume as, when polar ice sheets expand, the lighter oxygen isotope (^{16}O) is preferentially evaporated at lower latitudes and precipitated over the poles due to Rayleigh fractionation where it is stored in the ice sheet. This leaves the heavier oxygen isotope (^{18}O) at a greater relative abundance in the therefore isotopically heavier ocean. This means that,

Chapter Five: Refining Estimates of Deep Ocean Temperature Across the Eocene Oligocene Transition

where robust estimates of temperature change can be made, the $\delta^{18}\text{O}_{\text{sw}}$ can be calculated. Here, $\delta^{18}\text{O}_{\text{sw}}$ is calculated using the approach outlined in Marchitto *et al.* (2014). Given the uncertainties described in the previous section, $\delta^{18}\text{O}_{\text{sw}}$ presented here are uncorrected for changes in $\Delta[\text{CO}_3^{2-}]$. Figure 5.17 shows the calculated $\delta^{18}\text{O}_{\text{sw}}$ of ODP Sites 689, 748 and 756. It is clear from figure 5.17 that estimates of $\delta^{18}\text{O}_{\text{sw}}$ from ODP Site 756 are in reasonable agreement with those from ODP Sites 689 and 748; all sites show a change in $\delta^{18}\text{O}_{\text{sw}}$ across the transition of $\sim 0.6\text{‰}$. This is also in alignment with published estimates generated from extremely well-preserved samples (e.g. Lear *et al.* 2008). The fact that the $\delta^{18}\text{O}_{\text{sw}}$ values are so similar between sites despite large differences in $\delta^{18}\text{O}$, could suggest that despite the potential influence of secondary effects Mg/Ca accurately records temperature changes.

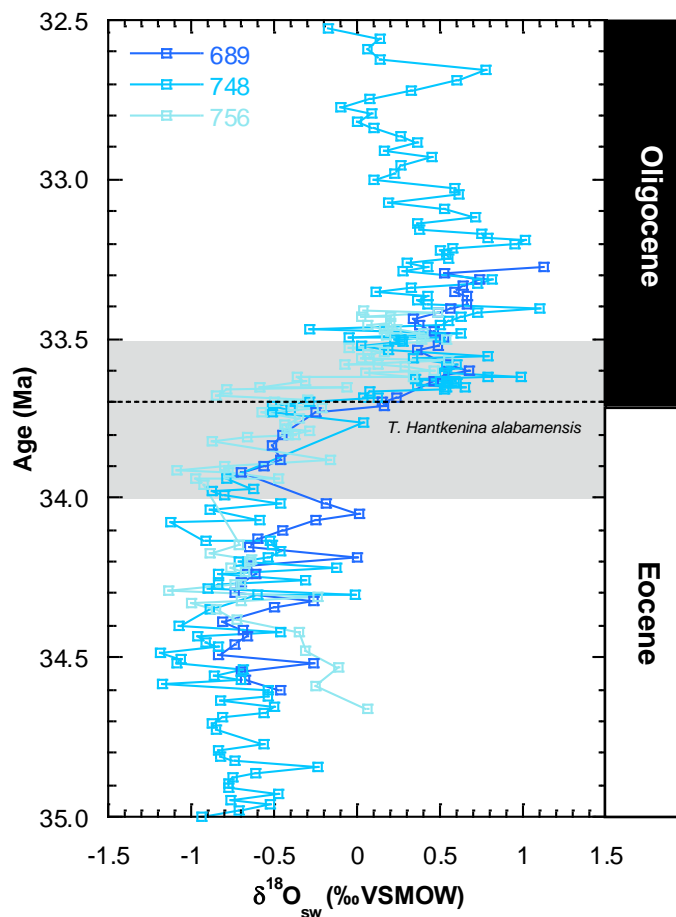


Figure 5.17 – Benthic foraminiferal $\delta^{18}\text{O}_{\text{sw}}$ calculated from ODP Sites 689 and 748 (Bohaty *et al.* 2012) and ODP Site 756 (this study). Grey shaded bar represents duration of the EOT. EOB marked by top of *Hantkenina alabamensis*. Age model calibrated to Cande and Kent (1995).

It is important to recognise that these estimates of $\delta^{18}\text{O}_{\text{sw}}$ may be offset due to inaccuracies in Mg/Ca-derived temperature estimates caused by $\Delta[\text{CO}_3^{2-}]$. The likely offset in $\delta^{18}\text{O}_{\text{sw}}$ due to $\Delta[\text{CO}_3^{2-}]$ is between 0.01 and 0.03 ‰ $\mu\text{mol kg}^{-1}$ (Elderfield *et al.* 2006). However, the reasonable agreement in the amplitude of relative change between the records shown in figure 5.17 suggests that inferences may be made as to the relative change in ice volume across the transition and casts some doubt as to the influence of $\Delta[\text{CO}_3^{2-}]$ on Mg/Ca at ODP Site 756.

Calculation of $\delta^{18}\text{O}_{\text{sw}}$ allows an estimate of the amount of ice volume present following the EOT. In order to calculate ice volume, an estimate of the isotopic composition of Oligocene age ice sheets is required. Most studies assume a value between -45‰ and -35‰ based on modelling results (DeConto *et al.* 2008) and the fact that warmer than modern air temperatures at higher latitudes would likely have caused the isotopic composition of the AIS to be considerably different to modern (Lhomme *et al.* 2005) (Bohaty *et al.* 2012). Therefore, ODP Site 756 suggests an estimate of ice volume very similar to that of previously published estimates that suggest growth of an AIS similar in size to that of the modern (between 80% and 110% of the modern AIS) (e.g. Lear *et al.* 2008; Bohaty *et al.* 2012). An estimate of ice volume equivalent to the modern AIS leaves no magnitude of $\delta^{18}\text{O}_{\text{sw}}$ attributable to northern hemisphere glaciation ruling out the idea of bipolar glaciation at the EOT discussed in section 5.1.1.1 of this chapter.

5.5 Chapter Summary

It has long been known that the use of foraminiferal Mg/Ca ratios in developing paleotemperature estimates across the EOT is not without its complications. Many efforts have been made to account for various secondary effects. Evidence presented in this chapter, while highlighting the need for further strides in this area, holds promise in the ability to correct for the influence of both Mn-rich contaminant phases and $\Delta[\text{CO}_3^{2-}]$ on Mg/Ca. In particular, these results suggest that further work should consider applying the approach of Lear *et al.* (2010) to records from other deep ocean sites where paired Mg/Ca and Li/Ca records are available, and highlight the importance of collecting paired foraminiferal Li/Ca with Mg/Ca in new trace element studies from deep sea sediments. This chapter has shown that this approach allows the development of records of Mg/Ca-derived BWT and can provide useful insights into changing bottom water chemistry at sites previously understudied due to the likely impact of $\Delta[\text{CO}_3^{2-}]$. This chapter provides two prime examples.

Results from the North Atlantic region provide the very first BWT record from this region across the EOT and show a distinct similarity in the temperature response of the surface and deep ocean. Previously published records of SST from this region have failed to record any cooling across this critical climate transition. Similarly the new record of BWT at IODP Site U1406 suggests cooling of 0.98°C supporting earlier conclusions that a transient interhemispheric temperature asymmetry occurred coeval with glaciation at the EOT (Liu *et al.* 2018) whereby BWT and SST cooled to a much greater degree in the high southern latitudes than in their northern counterparts. Onset of glaciation on Antarctica has been suggested to enhance production of AABW by the growth of sea ice and associated brine rejection (Ohshima *et al.* 2016) and hence would enhance cooling in the high southern latitudes and diminish cooling in the North Atlantic. This effect is likely also responsible for the warming associated with the isotope shift in the Indian Ocean region.

Further insights into changing ocean circulation are documented by comparative study of benthic foraminiferal trace elements within the Indian Ocean basin. A BWT cooling of 2 – 3°C over the course of 400 kyr at ODP Site 756 is unparalleled at high

latitude Southern Ocean sites and likely represents a change in water mass bathing this region of the Indian Ocean: either (i) the diminishing influence of TISW following the onset of the gradual closure of the Tethys gateway at c. 35 Ma; or (ii) displacement of Southern Ocean-derived bottom water to the Indian Ocean due to newly onset NCW filling the Atlantic. In either case, the replacement water mass was likely derived from the Southern Ocean; the formation of which intensified following cooling and associated glaciation of Antarctica. A 0.4°C cooling and increase in $\Delta[\text{CO}_3^{2-}]$ of approximately $20 \mu\text{molkg}^{-1}$ is associated with the increased northern influence of this southerly-derived water mass – likely akin to SAMW. These high latitude-sourced cold waters carry northward an abundance of weathered nutrients from the Antarctic continent resulting in a regional pulse of primary productivity and associated increase in organic carbon burial. This may explain the lower $\Delta[\text{CO}_3^{2-}]$ response of the Indian Ocean compared to the Pacific and warrants further investigation into regional controls on CCD deepening at the EOT.

Chapter Six

Synthesis

6.1 Major Findings

The overall aim of this thesis was to explore the evolution of temperature, ice volume and ocean circulation across the EOT and the interactions between key climatic parameters that served as forcing and feedback mechanisms across this landmark climate transition. Particular emphasis has been placed on the role played by paleoceanographic changes in the North Atlantic region and the subsequent interaction with changing Antarctic ice volume. This thesis has adopted a multi-proxy approach to investigating changes in ocean circulation, temperature and ice volume. Benthic foraminiferal stable isotope and trace element data have been used to develop records of temperature, ice volume and perturbations to the carbon cycle. Neodymium isotopes derived from fossil fish teeth have been used to develop records of changing weathering regime and ocean circulation. The use of these techniques have resulted in the major findings summarised below.

6.1.1 Strengthening of NCW Conditioned Climate for Landmark Change at the EOT

Prior to the work presented in this thesis much conflict remained over the precise timing of the onset of bipolar deep water formation in the Cenozoic oceans. A switch from a single southerly-sourced deep water mass to a bipolar configuration that included NCW (the paleo precursor to NADW) had been dated to various points during the Cenozoic; from the Early Eocene to Middle Miocene (Wright and Miller, 1996; Hohbein, 2012). Some evidence had placed NCW onset in the interval spanning the Late Eocene and Early Oligocene (Davies *et al.* 2001; Via and Thomas, 2006; Abelson and Erez, 2017), yet the precise timing of this onset with regard to the isotope shift and growth of ice on Antarctica had remained poorly refined. The aim of work carried out in chapter three of this thesis was to better constrain the timing of any reorganisation in North Atlantic Ocean circulation associated with the EOT and growth of the AIS. Do changes in bottom water mass properties suggest a change in Atlantic Ocean circulation between the Late Eocene and Early Oligocene? If so, did these changes pre- or post-date growth of the Antarctic Ice Sheet? Using ϵNd generated from fossil fish teeth at ODP Site 1263 (Walvis Ridge) in the South Atlantic, this thesis has presented the first record that shows, without ambiguity, the geochemical signature of NCW penetrating into the South Atlantic prior to the EOT. This high resolution record of ϵNd from Walvis Ridge

documents the primary phase of northern-sourced deep water occurring in the latest Eocene; just under 1 My prior to the EOT. In contrast to earlier suggestions that a reorganisation of ocean circulation occurred in response to changing heat and salinity patterns associated with growth of the AIS, this thesis suggests that the increasing influence of northern-sourced deep waters provided optimal conditions for landmark climate change prior to the occurrence of the ultimate trigger of the Earth's greenhouse-icehouse transition; the coincidence of low eccentricity and low-amplitude change in obliquity. Priming of the climate system by the onset of NCW and associated northern hemisphere heat piracy made it more susceptible to undergo previously unparalleled changes in Cenozoic climate at Earth's greenhouse-icehouse transition. Comparison of the Walvis Ridge ϵNd record with records documenting the waxing and waning of the AIS suggests that NCW was climatically modulated with a strong control exerted by the orbitally-paced dynamics of the AIS.

There is significant scope for future work to investigate paleoceanographic changes further back into the late Eocene, focusing in particular on key periods such as the regional negative excursion in $\delta^{13}\text{C}$. Can initial overflows of NCW be identified in the ϵNd record at Walvis Ridge and other sites in the Atlantic Ocean? In addition, an increased resolution of this record in the early Oligocene, across the EOGM, would be very useful in corroborating the link between orbitally-paced waxing and waning of the AIS and the strength of NCW flux by use of spectral analysis.

6.1.2 A Glacially-Induced Transient Productivity Increase

Prior to the work presented in this thesis, numerous studies had detailed changes in primary productivity and export production from the Late Eocene to Early Oligocene. However, there was a distinct lack of records from the northern high latitudes in the Atlantic; a region thought to have undergone significant oceanographic changes at this time. More recent research that proposed the southward export of nutrient-rich, low $\delta^{13}\text{C}$ water imprinted by Arctic-sourced fossil carbon to the North Atlantic region in the million years leading up to the EOT warranted greater investigation of the role played by the Arctic and North Atlantic in productivity changes at the EOT (Coxall *et al.* 2018). The aim of the work presented in chapter four of this thesis was to

investigate changes in primary productivity and export production in the North Atlantic at the EOT. Did the initiation of NCW impact primary productivity and export production in the Atlantic Ocean? What role did changes in primary productivity have on the carbon cycle perturbation and $p\text{CO}_2$ at the EOT? This work presents a suite of benthic foraminiferal stable isotopes and trace element (U/Ca and Mn/Ca) data from IODP Site U1406 (Newfoundland Sediment Drifts) and ODP Site 925 (Ceara Rise) in the North and Equatorial Atlantic, respectively. Chapter four documents a regional transient excursion in Atlantic Ocean primary productivity that begins coeval with Antarctic glaciation at the EOT and suggests that the Arctic Ocean continental shelves served as the nutrient-rich source fuelling this productivity pulse. This new source of bioavailable nutrients was distributed through the North Atlantic region causing increased primary productivity and associated export production following the exposure of organic-rich shelf sediment nutrients to weathering upon glacially-induced sea level fall. This transient pulse in productivity is associated with a temporary steepening of the overall decline in $p\text{CO}_2$.

There are several avenues that future work in this area could focus on including: (i) generation of productivity records from the higher northern latitudes within the Arctic region to allow the source region of this productivity pulse to be corroborated; (ii) increase the spatial resolution of productivity records across the EOT to search for evidence of this mechanism acting on a more global scale; (iii) extension of the record back into the late Eocene to cover documented precursor glaciations (e.g. PrOM (Scher *et al.* 2014)) to identify the influence of the Shelf-Nutrient mechanism over a different scale in deep time; and (iv) use of an EMIC to effectively test the scale of the possible effect on $p\text{CO}_2$ under boundary conditions of the late Eocene and early Oligocene.

6.1.3 Refined Estimates of Temperature Change at the EOT

Early studies that adopted foraminiferal Mg/Ca as a BWT paleothermometer failed to recognise any deep ocean cooling signal across the EOT. Subsequent studies have recognised that in some instances this was caused by the influence of secondary controls Mg/Ca. Evidence presented in chapter five of this thesis, while highlighting the need for further strides in this area, holds promise in the ability to correct for the influence of both Mn-rich contaminant phases and $\Delta[\text{CO}_3^{2-}]$ on Mg/Ca. By applying

methods of correction, chapter five presents refined estimates of deep ocean temperature change in both the North Atlantic and Indian Ocean regions.

Chapter five presents the first record of BWT across the EOT from the North Atlantic region. Interestingly, this record supports earlier conclusions that a transient interhemispheric temperature asymmetry occurred coeval with glaciation at the EOT whereby BWT and SST cooled to a much greater degree in the high southern latitudes. It is likely that changes in ocean circulation and interhemispheric heat transport due to growth of the AIS significantly affected the relative strength of polar water masses and interhemispheric heat transport. This is supported by evidence presented in chapter three of this thesis suggesting the onset of glaciation on Antarctica, and the highly dynamic nature of the AIS during its infancy, prompted oscillations in the relative strengthening and weakening of the two polar-sourced water masses whereby intensification of deep water formation at one pole occurred at the expense of deep water formation at the other.

Chapter five presents further insights as to changes in ocean circulation and temperature in the Indian Ocean. A BWT cooling of 2 – 3°C over the course of 400 kyr between 34.7 Ma and 34.3 Ma at ODP Site 756, unparalleled at high latitude Southern Ocean sites, suggests an increased influence of Southern Ocean-derived water due to either: (i) the diminishing influence of TISW following the onset of the gradual closure of the Tethys gateway at c. 35 Ma; or (ii) displacement of Southern Ocean-derived bottom water to the Indian Ocean due to newly formed (c. 34.7 Ma) NCW filling the Atlantic. The formation of this northerly flowing water mass intensified coeval with glaciation. An increased flux of nutrients to the Southern Ocean as a result of glaciation-induced sea level fall and weathering of newly exposed shelf sediments transported in this water mass likely increased productivity and associated export production in the low-latitude Indian Ocean. It is proposed that by the time waters reached the Pacific Ocean they were somewhat nutrient depleted explaining the disparity in $\Delta[\text{CO}_3^{2-}]$ between the two ocean basins.

Future work in this area could focus on two key areas: (i) proxy accuracy in the face of secondary effects and contaminant phases; and (ii) generation of additional

surface water and bottom water temperature records from a multitude of proxies at sites in the high northern latitudes. Specifically, it would be useful to further investigate the effect of Mn/Ca on Mg/Ca-derived temperatures and test the idea that a Mn-rich contaminant phase could reside on individual crystallites through a foraminifer test. A comparative diagenetic study using SEM imaging of specimens from ODP Site 925 would also be useful in identifying whether the $\delta^{18}\text{O}$ and Mg/Ca-derived paleotemperatures from this site are perturbed due to burial-depth induced diagenetic overprinting. Finally, not only would the generation of further bottom water and surface water temperature records from the North Atlantic and Arctic regions increase confidence in the idea of NCW-induced temperature asymmetry, but the use of, and the extent of agreement between, multiple proxy archives (e.g. TEX_{86} , clumped isotopes) would aid identification of secondary effects on Mg/Ca paleotemperatures.

6.2 Implications

6.2.1 *The Chronology of the EOT*

This thesis has made significant strides towards resolving the timeline of key climatic events in the Atlantic Ocean region in the lead up to and across the EOT that highlight the importance of the influence of the Arctic Ocean and North Atlantic at the EOT; the link between changes in this region and changes in AIS volume highlight the role of both in modulating climate and ocean chemistry across this critical interval in Earth's climate history. Figure 6.1 brings together all the new data collected and presented in this work along with relevant existing published data and clearly illustrates an improved understanding of the timeline of events across the EOT that was not possible prior to this work.

A compilation of $\delta^{13}\text{C}$ records from across the North Atlantic region, including that generated in this study from IODP Site U1406, document a region-wide negative excursion from ~ 35.5 Ma. This excursion likely stemmed from Arctic-sourced waters enriched in light fossil carbon breaching the GSR and flowing in to the North Atlantic (Coxall *et al.* 2018). It is highly likely this represents initial overflows of NCW prior to its intensification at 34.7 Ma where NCW formation matures to include an

interhemispheric AMOC; shown for the first time without ambiguity by ϵNd data from ODP Site 1263 generated by this study. The convergence of ϵNd at Walvis Ridge and in the Labrador Sea (ODP Site 647) to values akin to ISOW and DSOW suggest a Nordic Sea source for NCW along with a notable absence of a contribution from LSW; this represents the first stage of the long-term, Cenozoic evolution of NADW occurring one million years prior to the EOT. It is highly likely that the intensification of deep water formation in the North Atlantic serves as the long sought after link between the extreme orbital parameters of the period and the widespread changes in climate seen at the EOT. The increasing influence of northern-sourced deep waters, and associated cross-hemisphere heat piracy, conditioned Earth for landmark climate change prior to the occurrence of the orbital parameters considered to be the ultimate trigger of the EOT.

Glaciation of the AIS occurs at the Eocene-Oligocene boundary, c. 33.7 Ma, coincident with the occurrence of low eccentricity and low-amplitude change in obliquity, and the decline of $p\text{CO}_2$ below the critical threshold for Antarctic glaciation (DeConto *et al.* 2008). The impacts of glaciation identified in this study are twofold. Firstly greater variation in the ϵNd record during an interval when a young and dynamic AIS was paced over shorter orbital timescales (Galeotti *et al.* 2016) suggests waxing and waning of the ice sheet modulated the competing formation of NCW and AABW. This complex interhemispheric balancing act between northern and southern high latitude deep water masses likely explains the significant temperature asymmetry between the two regions documented in this thesis. Secondly, falling sea level associated with growth of the AIS generated a regional productivity pulse in the Atlantic Ocean due to exposure and weathering of organic-rich Arctic continental shelves and a redistribution of these newly bioavailable nutrients southward through the Atlantic. The pulse of productivity acted as a positive feedback on glaciation by drawing down atmospheric CO_2 . Upon stabilisation of an AIS now paced over longer eccentricity timescales, Arctic riverine systems reached a new equilibrium and the supply of nutrients diminished. In addition, deep water formation in the North Atlantic intensified once again.

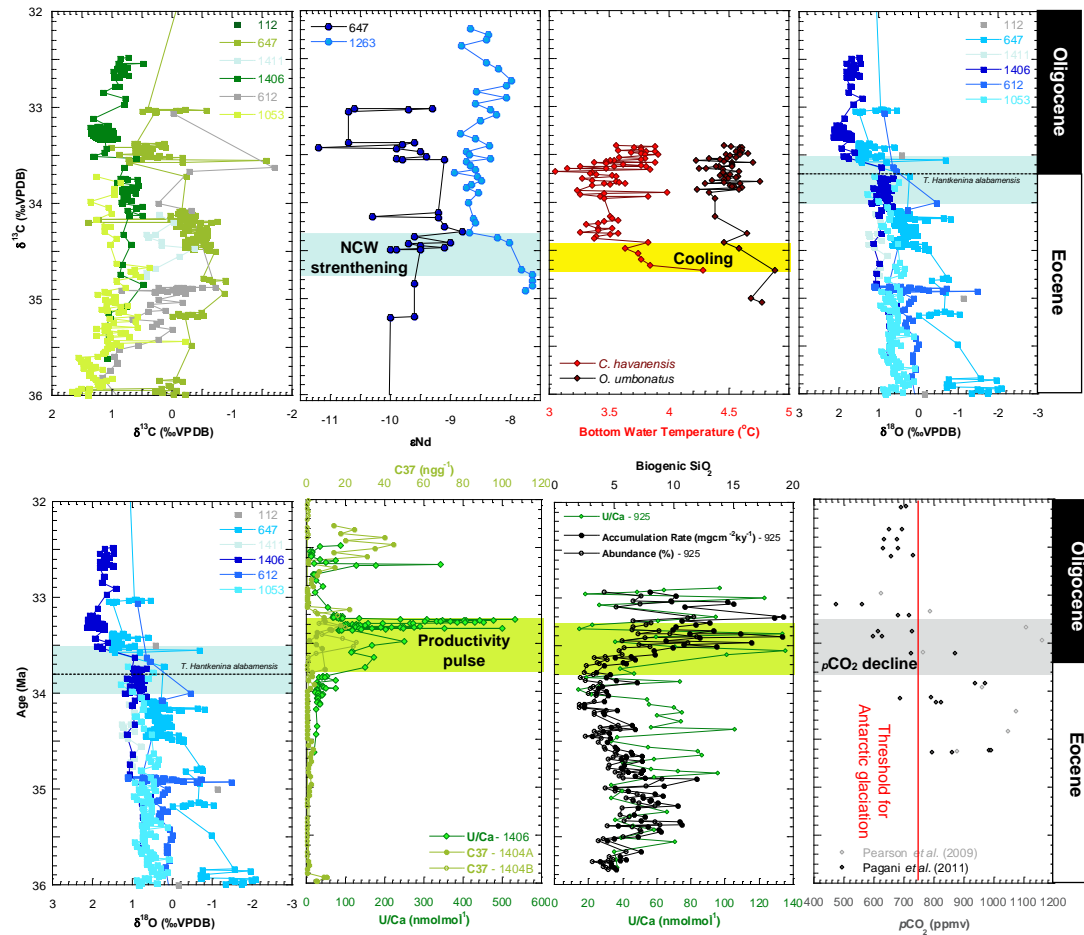


Figure 6.1 - Summary of the EOT. Benthic foraminiferal isotopes from ODP Site 112, 612, 647, IODP Sites U1411 (Coxall *et al.* 2018), ODP Site 1053 (Borelli *et al.* 2014) and IODP Site U1406 (this study). ϵNd from ODP Sites 647 (Coxall *et al.* 2018) and 1263 (this study). Productivity proxies from ODP Sites 647 (Coxall, H.K. and Lear, C.H., pers. comm.) and 925 (Diester-Haas and Zachos, 2003; this study), and IODP Sites U1404 (Liu *et al.* 2018) and U1406 (this study). $p\text{CO}_2$ reconstructions from Pearson *et al.* (2009) and Pagani *et al.* (2011). Threshold for Antarctic glaciation taken from DeConto *et al.* (2008). EOB marked by top of *Hantkenina alabamensis*. Age model calibrated to Cande and Kent (1995).

6.2.2 Climate System Feedbacks

The implications of the work conducted in this thesis are three-fold. Not only has this work enabled the development of an improved chronology of events that occurred across the EOT and highlighted the substantial benefits of a multi-proxy approach in paleoceanographic studies, it has wider implications for understanding the manner in which key elements of the climate system interact. An improved understanding of the interactions that played a key role in forcing and modulating climatic change across the EOT allows emphasis to be placed on relevant forcing mechanisms and feedbacks in studies focused on possible future changes in climate.

Prior to this work, significant debate remained within the scientific community as to the ultimate forcing mechanism responsible for the EOT. Was drawdown of atmospheric CO₂ more important than changing ocean gateways? Did the onset of bipolar deep water formation change heat and salinity distributions globally resulting in growth of an ice sheet on Antarctica? This work has shown that it is highly unlikely one key forcing mechanism alone was responsible for such landmark change at the EOT. The ultimate trigger for glaciation at the EOT and the pacemaker for subsequent ice sheet growth was the interval of coinciding low eccentricity and low-amplitude change in obliquity. In addition, growth of the AIS would not have occurred if atmospheric CO₂ had not declined below a critical threshold (DeConto and Pollard, 2003a; 2003b; DeConto *et al.* 2008). These two forcing mechanisms could be considered largely global drivers of change at the EOT. However, this study has also clearly demonstrated a potential role for the significant strengthening of deep water formation in the North Atlantic in priming the regional Antarctic climate for glaciation. In addition, the subsequent link between the waxing and waning of the AIS and the strength of the proto-AMOC yields key insights into how changing patterns of heat and salt in the oceans exert a strong effect on regional temperature changes. Finally, this work has suggested that falling sea level may have led to a previously unexplored positive carbon cycle feedback. Future work should explore the scale of possible effects of this mechanism while being mindful of other carbon cycle feedbacks that are outside the scope of this particular study.

The EOT serves as a prime example of the value of combining multi-proxy paleoceanographic research with climate model simulations. Modelling studies are vitally important experimental arenas that facilitate better understanding of the manner in which various climatic parameters interact. However, paleoceanographic studies, such as this one, are instrumental in providing realistic boundary conditions that allow accurate hindcasting of the geological past so that models may better forecast Earth's possible future.

References

Appendices

Abelson, M., Agnon, A. and Almogi-Labin, A. 2008. 'Indications for control of the Iceland plume on the Eocene-Oligocene 'greenhouse-icehouse' climate transition', *Earth and Planetary Science Letters*, 265: 33 – 48.

Abelson, M. and Erez, J. 2017. 'The onset of modern-like Atlantic meridional overturning circulation at the Eocene-Oligocene transition: Evidence, causes, and possible implications for global cooling', *Geochemistry, Geophysics, Geosystems*, 18: 2177 – 2199.

Allègre, C.J., Dupré, B., Négrel, P. and Gaillardet, J., 1996. 'Sr, Nd, Pb isotope systematics in Amazon and Congo River systems: constraints about erosion processes', *Chemical Geology*, 131 (1-4): 93 – 112.

Allen, M.B. and Armstrong, H.A. 2008. 'Arabia–Eurasia collision and the forcing of mid-Cenozoic global cooling', *Palaeogeography, Palaeoclimatology, Palaeoecology*, 265 (1-2): 52 – 58.

Anand, P., Elderfield, H. and Conte, M.H. 2003. 'Calibration of Mg/Ca thermometry in planktonic foraminifera from a sediment trap time series', *Paleoceanography*, 18 (2).

Armstrong McKay, D.I., Tyrell, T. and Wilson, P.A. 2016. 'Global carbon cycle perturbation across the Eocene-Oligocene climate transition', *Paleoceanography*, 31: 311 – 329.

Arz, H.W., Pätzold, J. and Wefer, G. 1998. 'Correlated millennial-scale changes in surface hydrography and terrigenous sediment yield inferred from last-glacial marine deposits off northeastern Brazil', *Quaternary Research*, 50 (2): 157 – 166.

Baatsen, M., van Hinsbergen, D.J.J., von der Heydt, A.S., Dijkstra, H.A., Sluijs, A., Abels, H.A. and Bijl, P.K. 2016. 'Reconstructing geographical boundary conditions for palaeoclimate modelling during the Cenozoic', *Climate of the Past*, 12, 1635 – 1644.

Appendices

Bacon, M.P. and Rosholt, J.N. 1982. 'Accumulation rates of Th-230, Pa-231, and some transition metals on the Bermuda Rise', *Geochimica et Cosmochimica Acta*, 46 (4): 651 – 666.

Baker, P.A., Gieskes, J.M. and Elderfield, H. 1982. 'Diagenesis of carbonates in deep-sea sediments – evidence from Sr/Ca ratios and interstitial dissolved Sr²⁺ data', *Journal of Sedimentary Petrology*, 52: 71 – 82.

Bamber, J.L., Riva, R.E., Vermeersen, B.L. and LeBrocq, A.M. 2009. 'Reassessment of the potential sea-level rise from a collapse of the West Antarctic Ice Sheet', *Science*, 324 (5929): 901 – 903.

Barker, P.F. 2001. 'Scotia Sea regional tectonic evolution: implications for mantle flow and palaeocirculation', *Earth Science Reviews*, 55: 1 – 39.

Barker, P.F. and Burrell, J. 1976. 'The opening of Drake Passage', *in: Proceedings of the Joint Oceanographic Assembly*, Food and Agricultural Organization of the United Nations, Rome: 103.

Barker, S., Greaves, M. and Elderfield, H. 2003. 'A study of cleaning procedures used for foraminiferal Mg/Ca paleothermometry', *Geochemistry, Geophysics, Geosystems*, 4 (9): 8407.

Barnes, C.E. and Cochran, J.K. 1990. 'Uranium removal in oceanic sediments and the oceanic U balance', *Earth and Planetary Science Letters*, 97 (1-2): 94 – 101.

Barras, C., Mouret, A., Nardelli, M. P., Metzger, E., Petersen, J., La, C., Filipsson, H. L., and Jorissen, F. J. 2018. 'Experimental calibration of Mn incorporation in foraminiferal calcite', *Geochimica Cosmochimica Acta*, In Review.

Basak, C. and Martin, E.E. 2013. 'Antarctic weathering and carbonate compensation at the Eocene-Oligocene transition', *Nature Geoscience*, 6: 121 – 124.

Appendices

Bates, N.R. and Mathis, J.T. 2009. 'The Arctic Ocean marine carbon cycle: evaluation of air-sea CO₂ exchanges, ocean acidification impacts and potential feedbacks', *Biogeosciences*, 6 (11): 2433 – 2459.

Bender, M., Grande, K., Johnson, K., Marra, J., Williams, P.J., Sieburth, J., Pilson, M., Langdon, C., Hitchcock, G., Orchardo, J., Hunt, C., Donaghay, P., Heinemann, K. 1987. 'A comparison of four methods for determining planktonic community production', *Limnology and Oceanography*, 32 (5): 1085 – 1098.

Berner, R.A. 1982. 'Burial of organic carbon and pyrite sulfur in the modern ocean: its geochemical and environmental significance', *American Journal of Science*: 282.

Bemis, B.E., Spero, H.J., Bijma, J. and Lea, D.W. 1998. 'Reevaluation of the oxygen isotopic composition of planktonic foraminifera: Experimental results and revised paleotemperature equations', *Paleoceanography*, 13 (2): 150 – 160.

Bertine, K.K., Chan, L.H. and Turekian, K.K. 1970. 'Uranium determinations in deep-sea sediments and natural waters using fission tracks', *Geochimica et Cosmochimica Acta*, 34 (6): 641 – 648.

Bialik, O.M., Frank, M., Betzler, C., Zammit, R. and Waldmann, N.D. 2019. 'Two-step closure of the Miocene Indian Ocean Gateway to the Mediterranean', *Scientific Reports*, 9 (1): 8842.

Bijl, P.K., Bendle, J.A.P., Bohaty, S.M., Pross, J., Schouten, S., Tauxe, L., Stickley, C.E., McKay, R.M., Röhl, U., Olney, M., Slujs, A., Escutia, C., Brinkhuis, H. and Expedition 318 Scientists. 2013. 'Eocene cooling linked to early flow across the Tasmanian Gateway', *Proceedings of the National Academy of Sciences*, 100 (24).

Billups, K. and Schrag, D.P. 2003. 'Application of benthic foraminiferal Mg/Ca ratios to questions of Cenozoic climate change', *Earth and Planetary Science Letters*, 209: 181 – 195.

Appendices

Blard, P.H., Sylvestre, F., Tripathi, A.K., Claude, C., Causse, C., Coudrain, A., Condom, T., Seidel, J.L., Vimeux, F., Moreau, C. and Dumoulin, J.P. 2011. 'Lake highstands on the Altiplano (Tropical Andes) contemporaneous with Heinrich 1 and the Younger Dryas: new insights from ^{14}C , U–Th dating and $\delta^{18}\text{O}$ of carbonates', *Quaternary Science Reviews*, 30 (27-28): 3973 – 3989.

Bohaty, S. M. and Zachos, J. C. 2003. 'Significant Southern Ocean warming event in the late middle Eocene', *Geology*, 31: 1017 – 1020.

Bohaty, S. M., Zachos, J. C., Florindo, F. & Delaney, M. L. 2009. 'Coupled greenhouse warming and deep-sea acidification in the middle Eocene', *Paleoceanography*, 24.

Bohaty, S.M., Zachos, J.C. and Delaney, M.L. 2012. 'Foraminiferal Mg/Ca evidence for Southern Ocean cooling across the Eocene-Oligocene transition', *Earth and Planetary Science Letters*, 317 – 318: 251 – 261.

Boiteau, R., Greaves, M. and Elderfield, H. 2012. 'Authigenic uranium in foraminiferal coatings: A proxy for ocean redox chemistry', *Paleoceanography*, 27 (3).

Borrelli, C., Cramer, B.S. and Katz, M.E. 2014. 'Bipolar Atlantic deepwater circulation in the middle-late Eocene: Effects of Southern Ocean gateway openings', *Paleoceanography*, 29 (4): 308 – 327.

Boyle, E.A. 1983. 'Manganese carbonate overgrowths on foraminifera tests', *Geochimica et Cosmochimica Acta*, 47 (10): 1815 – 1819.

Boyle, E.A. and Keigwin, L.D. 1985. 'Comparison of Atlantic and Pacific paleochemical records for the last 215,000 years: changes in deep ocean circulation and chemical inventories', *Earth and Planetary Science Letters*, 76 (1-2): 135 – 150.

Boyle, P.R., Romans, B.W., Tucholke, B.E., Norris, R.D., Swift, S.A. and Sexton, P.F. 2017. 'Cenozoic North Atlantic deep circulation history recorded

Appendices

in contourite drifts, offshore Newfoundland, Canada', *Marine Geology*, 385: 185 – 203.

Brinkhuis, H., Schouten, S., Collinson, M.E., Sluijs, A., Damsté, J.S.S., Dickens, G.R., Huber, M., Cronin, T.M., Onodera, J., Takahashi, K. and Bujak, J.P. 2006. 'Episodic fresh surface waters in the Eocene Arctic Ocean', *Nature*, 441 (7093): 606.

Bristow, L.A., Mohr, W., Ahmerkamp, S. and Kuypers, M.M. 2017. 'Nutrients that limit growth in the ocean', *Current Biology*, 27 (11): R474 - R478.

Broecker, W.S. 1982. 'Ocean chemistry during glacial time', *Geochimica et Cosmochimica Acta*, 46 (10): 1689 – 1705.

Broecker, W. S. 1991. 'The great ocean conveyor', *Oceanography*, 4: 79 – 89.

Broecker, W.S. and Peng, T. 1982. *Tracers in the Sea*, Lamont-Doherty Geological Observatory, Columbia University.

Cande, S.C. and Kent, D.V. 1995. 'Revised calibration of the geomagnetic polarity timescale for the Late Cretaceous and Cenozoic', *Journal of Geophysical Research*, 100 (B4): 6093 – 6095.

Chappell, J. and Shackleton, N.J. 1986. 'Oxygen isotopes and sea level', *Nature*, 324: 137 – 140.

Chave, K.E. 1954. 'Aspects of biochemistry of magnesium: 1. Calcareous marine organisms', *Journal of Geology*, 62: 266 – 283.

Chen, P., Yu, J. and Jin, Z. 2017. 'An evaluation of benthic foraminiferal U/Ca and U/Mg proxies for deep ocean carbonate chemistry and redox conditions', *Geochemistry, Geophysics, Geosystems*, 18 (2): 617 – 630.

Chun, C.O., Delaney, M.L. and Zachos, J.C. 2010. 'Paleoredox changes across the Paleocene-Eocene thermal maximum, Walvis Ridge (ODP Sites

Appendices

1262, 1263, and 1266): Evidence from Mn and U enrichment factors', *Paleoceanography*, 25 (4).

Clark, D.L., Hobart, D.E. and Neu, M.P. 1995. 'Actinide carbonate complexes and their importance in actinide environmental chemistry', *Chemical Reviews*, 95 (1): 25 – 48.

Clift, P., 1996. 'Plume tectonics as a cause of mass wasting on the southeast Greenland continental margin', *Marine and Petroleum Geology*, 13 (7): 771 – 780.

Cochran, J.K., Kallenberg, K., Landman, N.H., Harries, P.J., Weinreb, D., Turekian, K.K., Beck, A.J. and Cobban, W.A. 2010. 'Effect of diagenesis on the Sr, O, and C isotope composition of late Cretaceous mollusks from the Western Interior Seaway of North America', *American Journal of Science*, 310 (2): 69 – 88.

Coggon, R.M. and Teagle, D.A.H. 2011. 'Hydrothermal calcium-carbonate veins reveal past ocean chemistry', *Trends in Analytical Chemistry*, 30 (8): 1252 – 1268.

Coggon, R.M., Teagle, D.A.H., Smith-Duque, C.E., Alt, J.C. and Cooper, M.J. 2010. 'Reconstructing Past Seawater Mg/Ca and Sr/Ca from Mid-Ocean Ridge Flank Calcium Carbonate Veins', *Science*, 327: 1114 – 1117.

Colbourn, G., Ridgwell, A. and Lenton, T.M. 2015. 'The time scale of the silicate weathering negative feedback on atmospheric CO₂', *Global Biogeochemical Cycles*, 29 (5): 583 – 596.

Compton, J., Mallinson, D., Glenn, C.R., Filippelli, G., Föllmi, K., Shields, G. and Zanin, Y. 2000. 'Variations in the global phosphorus cycle', *in*: Glenn, C.R., Prevot-Lucas, J. and Lucas, J. (eds) *Marine Authigenesis: From Global to Microbial*, SEPM Society of Sedimentary Geology.

Coxall, H.K. and Pearson, P.N. 2007. 'The Eocene Oligocene Transition' *in*: Williams, M., Haywood, A.M., Gregory, F.J. and Schmidt, D.N. (eds) *Deep-*

Appendices

Time Perspectives on Climate Change: Marrying the Signal from Computer Models and Biological Proxies, The Micropalaeontological Society, Special Publications, The Geological Society, London: 351 – 387.

Coxall, H.K. and Wilson, P.A. 2011. 'Early Oligocene glaciation and productivity in the eastern equatorial Pacific: Insights into global carbon cycling', *Paleoceanography*, 26 (2): 1 – 18.

Coxall, H.K., Wilson, P.A., Pälike, H., Lear, C.H. and Backman, J. 2005. 'Rapid stepwise onset of Antarctic glaciation and deeper calcite compensation in the Pacific Ocean', *Nature*, 433: 53 – 57.

Coxall, H.K., Huck, C.E., Huber, C.E., Huber, M., Lear, C.H., Legarda-Lisarri, A., O'Regan, M., Sliwinska, K.K., van de Flierdt, T., de Boer, A.M., Zachos, J.C. and Backman, J. 2018. 'Export of nutrient rich Northern Component Water preceded early Oligocene Antarctic glaciation', *Nature Geoscience*, 11 (3): 190 – 196.

Brown, S.J. and Elderfield, H. 1996. 'Variations in Mg/Ca and Sr/Ca ratios of planktonic foraminifera caused by postdepositional dissolution: Evidence of shallow Mg-dependent dissolution', *Paleoceanography*, 11: 543 – 551.

Curry, W.B., Shackleton, N.J., Richer, C. and the Leg 154 Scientists. 1995. *Proceedings of the Ocean Drilling Program Initial Reports*, 154.

Davies, R., Cartwright, J., Pike, J. and Line, C. 2001. 'Early Oligocene initiation of North Atlantic Deep Water formation', *Nature*, 410: 917 – 920.

DeConto, R.M. and Pollard, D. 2003a. 'Rapid Cenozoic glaciation of Antarctica induced by declining atmospheric CO₂', *Nature*, 421: 245 – 249.

DeConto, R.M. and Pollard, D. 2003b. 'A coupled climate-ice sheet modelling approach to the Early Cenozoic history of the Antarctic ice sheet', *Palaeogeography, Palaeoclimatology, Palaeoecology*, 198: 39 – 52.

Appendices

DeConto, R., Pollard, D. and Harwood, D. 2007. 'Sea ice feedback and Cenozoic evolution of Antarctic climate and ice sheets', *Paleoceanography*, 22 (3).

DeConto, R.M., Pollard, D., Wilson, P.A., Pälike, H., Lear, C.H. and Pagani, M. 2008. 'Thresholds for Cenozoic bipolar glaciation', *Nature*, 652 – 656.

Delaney, M.L. and Boyle, E.A. 1983. 'Uranium and thorium isotope concentrations in foraminiferal calcite', *Earth and Planetary Science Letters*, 62 (2): 258 – 262.

Demicco, R.V., Lowenstein, T.K., Hardie, L.A. and Spencer, R.J. 2005. 'Model of seawater composition for the Phanerozoic', *Geology*, 33 (11): 877 – 880.

Dickson, J.A.D. 2004. 'Echinoderm Skeletal Preservation: Calcite-Aragonite Seas and the Mg/Ca Ratio of Phanerozoic Oceans', *Journal of Sedimentary Research*, 74 (3): 355 – 365.

Diester-Haass, L. 1995. 'Middle Eocene to early Oligocene paleoceanography of the Antarctic Ocean (Maud Rise, ODP Leg 113, Site 689): change from a low to a high productivity ocean', *Palaeogeography, Palaeoclimatology, Palaeoecology*, 113 (2-4): 311 – 334.

Diester-Haass, L. and Zahn, R. 1996. 'Eocene-Oligocene transition in the Southern Ocean: History of water mass circulation and biological productivity', *Geology*, 24 (2): 163 – 166.

Diester-Haass, L. and Zahn, R. 2001. 'Paleoproductivity increase at the Eocene–Oligocene climatic transition: ODP/DSDP Sites 763 and 592', *Palaeogeography, Palaeoclimatology, Palaeoecology*, 172 (1-2): 153 – 170.

Diester-Haass, L. and Zachos, J. 2003. 'The Eocene-Oligocene Transition in the Equatorial Atlantic (ODP Site 925): Paleoproductivity Increase and

Appendices

Positive $\delta^{13}\text{C}$ excursion', *Greenhouse to Icehouse: The Marine Eocene-Oligocene Transition*, 397 – 416.

Dobson, D.M., Dickens, G.R. and Rea, D.K. 2001. 'Terrigenous sediment on Ceara Rise: a Cenozoic record of South American orogeny and erosion', *Palaeogeography, Palaeoclimatology, Palaeoecology*, 165 (3-4): 215 – 229.

Dunkley Jones, T., Bown, P.R., Pearson, P.N., Wade, B.S., Coxall, H.K. and Lear, C.H. 2008. 'Major shifts in calcareous phytoplankton assemblages through the Eocene-Oligocene transition of Tanzania and their implications for low-latitude primary production', *Paleoceanography*, 23 (4).

Eagles, G., Livermore, R. and Morris, P. 2006. 'Small basins in the Scotia Sea: The Eocene Drake Passage gateway', *Earth and Planetary Science Letters*, 242: 343 – 353.

Edgar, K.M., Wilson, P.A., Sexton, P.F. and Suganuma, Y. 2007. 'No extreme bipolar glaciation during the main Eocene calcite compensation shift', *Nature*, 448: 908 – 911.

Elderfield, H. & Pagett, R. 1986. 'Rare earth elements in ichthyoliths: variations with redox conditions and depositional environment', *Science of the Total Environment*, 49: 175 – 197.

Elderfield, H. and Ganssen, G. 2000. 'Past temperature and $\delta^{18}\text{O}$ of surface ocean waters inferred from foraminiferal Mg/Ca ratios', *Nature*, 405: 442 – 445.

Elderfield, H., Bertram, C.J., Erez, J. 1996. 'A biomineralization model for the incorporation of trace elements into foraminiferal calcium carbonate', *Earth and Planetary Science Letters*, 142 (3 – 4): 409 – 423.

Elderfield, H., Yu, J., Anand, P., Kiefer, T. and Nyland, B. 2006. 'Calibrations for benthic foraminiferal Mg/Ca paleothermometry and the carbonate ion hypothesis', *Earth and Planetary Science Letters*, 250: 633 – 649.

Appendices

Eldrett, J.S., Harding, I.C., Wilson, P.A., Butler, E. and Roberts, A.P. 2007. 'Continental ice in Greenland during the Eocene and Oligocene', *Nature*, 446: 176 – 179.

Elsworth, G., Galbraith, E., Halverson, G. and Yang, S. 2017. 'Enhanced weathering and CO₂ drawdown caused by latest Eocene strengthening of the Atlantic meridional overturning circulation', *Nature Geoscience*, 10: 213 – 217.

Epstein, S., Buchsbaum, R., Lowenstam, H.A. and Urey, H.C. 1953. 'Revised carbonate-water isotopic temperature scale', *Geological Society of America Bulletin*, 64 (11): 1315 – 1326.

Epstein, S., Buchsbaum, R., Lowenstam, H.A. and Urey, H.C. 1953. 'Revised carbonate-water isotopic temperature scale', *Geological Society of America Bulletin*, 64 (11): 1315 – 1326.

Erhardt, A.M., Pälike, H. and Paytan, A. 2013. 'High-resolution record of export production in the eastern equatorial Pacific across the Eocene-Oligocene transition and relationships to global climatic records', *Paleoceanography*, 28 (1): 130 – 142.

Evans, D. and Müller, W. 2012. 'Deep time foraminifera Mg/Ca paleothermometry: Nonlinear correction for secular change in seawater Mg/Ca', *Paleoceanography*, 27: 1 – 11.

Evans, D., Erez, J., Oron, S. and Müller, W. 2014. 'Mg/Ca-temperature and seawater-test chemistry relationships in the shallow-dwelling large benthic foraminifera *Operculina ammonoides*', *Geochimica et Cosmochimica Acta*, 148 (1): 325 – 342.

Evans, D., Sahoo, N., Renema, W., Cotton, L. J., Müller, W., Todd, J. A., Saraswati, P. K., Stassen, P., Ziegler, M., Pearson, P. N., Valdes, P. J. & Affek, H. P. 2018. 'Eocene greenhouse climate revealed by coupled clumped isotope-Mg/Ca thermometry', *Proceedings of the National Academy of Sciences of the United States of America*, 115: 1174 – 1179.

Appendices

Exon, N.F., Kennett, J.P., Malone, M.J., The Leg 189 Shipboard Scientific Party. 2001. *Proceedings of the Ocean Drilling Programme*, Initial Reports 189, Ocean Drilling Program.

Figueiredo, J.J.J.P., Hoorn, C., Van der Ven, P. and Soares, E. 2009. 'Late Miocene onset of the Amazon River and the Amazon deep-sea fan: Evidence from the Foz do Amazonas Basin', *Geology*, 37 (7): 619 – 622.

Filippelli, G.M., Latimer, J.C., Murray, R.W. and Flores, J.A. 2007. 'Productivity records from the Southern Ocean and the equatorial Pacific Ocean: testing the glacial shelf-nutrient hypothesis', *Deep Sea Research Part II: Topical Studies in Oceanography*, 54 (21-22): 2443 – 2452.

Flores, J.A., Philippelli, G.M., Sierro, F.J. and Latimer, J.C. 2012. 'The "White Ocean" hypothesis: a late Pleistocene Southern Ocean governed by coccolithophores and driven by phosphorus', *Frontiers in microbiology*, 3: 233.

Fyke, J.G., D'Orgeville, M., Weaver, A.J. 2015. 'Drake Passage and Central American Seaway controls on the distribution of the oceanic carbon reservoir', *Global and Planetary Change*, 128: 72 – 82.

Galeotti, S., DeConto, R., Naish, T., Stocchi, P., Florindo, F., Pagani, M., Barrett, P., Bohaty, S.M., Lanci, L., Pollard, D., Sandroni, S., Talarico, F.M. and Zachos, J.C. 2016. 'Antarctic Ice Sheet variability across the Eocene-Oligocene boundary climate transition', *Science*, 352 (6281): 76 – 80.

Gasson, E., Siddall, M., Lunt, D.J., Rackham, O.J.L., Lear, C.H. and Pollard, D. 2012. 'Exploring uncertainties in the relationship between temperature, ice volume, and sea level over the past 50 million years', *Reviews of Geophysics*, 50: 1 – 35.

Gasson, E., Lunt, D.J., DeConto, R., Goldner, A., Heinemann, M., Huber, M., LeGrande, A.N., Pollard, D., Sagoo, N., Siddall, M., Winguth, A. and Valdes, P.J. 2014. 'Uncertainties in the modelled CO₂ threshold for Antarctic glaciation', *Climate of the Past*, 10: 451 – 466.

Appendices

Gelderloos, R., Straneo, F. and Katsman, C.A. 2012. 'Mechanisms behind the temporary shutdown of deep convection in the Labrador Sea: Lessons from the Great Salinity Anomaly years 1968–71', *Journal of Climate*, 25 (19): 6743 – 6755.

Glock, N., Eisenhauer, A., Liebetrau, V., Wiedenbeck, M., Hensen, C. and Nehrke, G. 2012. 'EMP and SIMS studies on Mn/Ca and Fe/Ca systematics in benthic foraminifera from the Peruvian OMZ: a contribution to the identification of potential redox proxies and the impact of cleaning protocols', *Biogeosciences*, 9 (1): 341 – 359.

Goldner, A., Herold, N. and Huber, M. 2014. Antarctic glaciation caused ocean circulation changes at the Eocene–Oligocene transition. *Nature*, 511(7511): 574.

Grandjean, P., Cappetta, H., Michard, A. & Albarede, F. 1987. 'The assessment of REE patterns and $^{143}\text{Nd}/^{144}\text{Nd}$ Nd ratios in fish remains', *Earth and Planetary Science Letters*, 84: 181 – 196.

Gray, W. R., Weldeab, S., Lea, D. W., Rosenthal, Y., Gruber, N., Donner, B. & Fischer, G. 2018. 'The effects of temperature, salinity, and the carbonate system on Mg/Ca in *Globigerinoides ruber* (white): A global sediment trap calibration', *Earth and Planetary Science Letters*, 482: 607 – 620.

Griffith, E.M., Paytan, A., Eisenhauer, A., Bullen, T.D. and Thomas, E. 2011. 'Seawater calcium isotope ratios across the Eocene-Oligocene transition', *Geology*, 39: 683 – 686.

Groeneveld, J. and Filipsson, H.L. 2013. 'Mg/Ca and Mn/Ca ratios in benthic foraminifera: the potential to reconstruct past variations in temperature and hypoxia in shelf regions', *Biogeosciences*, 10 (7): 5125 – 5138.

Guidry, M.W. and Mackenzie, F.T. 2003. 'Experimental study of igneous and sedimentary apatite dissolution: control of pH, distance from equilibrium, and temperature on dissolution rates', *Geochimica et Cosmochimica Acta*, 67 (16): 2949 – 2963.

Appendices

Hall, J.M. and Chan, L.-H. 2004. 'Li/Ca in multiple species of benthic and planktonic foraminifera: Thermocline, latitudinal, and glacial-interglacial variation', *Geochimica et Cosmochimica Acta*, 68: 529 – 545.

Hasenfratz, A.P., Martínez-García, A., Jaccard, S.L., Vance, D., Wälle, M., Greaves, M. and Haug, G.H. 2017. 'Determination of the Mg/Mn ratio in foraminiferal coatings: An approach to correct Mg/Ca temperatures for Mn-rich contaminant phases', *Earth and Planetary Science Letters*, 457: 335 – 347.

Hasiuk, F.J. and Lohmann, K.C. 2010. 'Application of calcite Mg partitioning functions to the reconstruction of paleocean Mg/Ca', *Geochimica et Cosmochimica Acta*, 74: 6751 – 6763.

Holbourn, A., Henderson, A.S. and Macleod, N. 2013. *Atlas of Benthic Foraminifera*, Wiley-Blackwell, Natural History Museum, London.

Herguera, J.C. and Berger, W. 1991. 'Paleoproductivity from benthic foraminifera abundance: Glacial to postglacial change in the west-equatorial Pacific', *Geology*, 19 (12): 1173 – 1176.

Heureux, A.M.C. and Rickaby, R.E.M. 2015. 'Refining our estimate of atmospheric CO₂ across the Eocene-Oligocene climatic transition', *Earth and Planetary Science Letters*, 409: 329 – 338.

Hill, D.J., Haywood, A.M., Valdes, P.J., Francis, J.E., Lunt, D.J., Wade, B.S. and Bowman, V.C. 2013. 'Paleogeographic controls on the onset of the Antarctic circumpolar current', *Geophysical Research Letters*, 40 (19): 5199 – 5204.

Hillaire-Marcel, C., De Vernal, A., Bilodeau, G. & Weaver, A. 2001. 'Absence of deepwater formation in the Labrador Sea during the last interglacial period', *Nature*, 410: 1073 – 1077.

Hines, B. R., Hollis, C. J., Atkins, C. B., Baker, J. A., Morgans, H. E. & Strong, P. C. 2017. 'Reduction of oceanic temperature gradients in the early

Appendices

Eocene Southwest Pacific Ocean', *Palaeogeography, Palaeoclimatology, Palaeoecology*, 475, 41 – 54.

Hoffman, P. F. 1988. 'United Plates of America, the birth of a craton-Early Proterozoic assembly and growth of Laurentia', *Annual Review of Earth and Planetary Sciences*, 16: 543 – 603.

Hohbein, M.W., Sexton, P.F. and Cartwright, J.A. 2012. 'Onset of North Atlantic Deep Water production coincident with inception of the Cenozoic global cooling trend', *Geology*, 40 (3): 255 – 258.

Hoorn, C., Guerrero, J., Sarmiento, G.A. and Lorente, M.A. 1995. 'Andean tectonics as a cause for changing drainage patterns in Miocene northern South America', *Geology*, 23 (3): 237 – 240.

Houben, A.J.P., van Mourik, C.A., Montanari, A., Coccioni, R. and Brinkhuis, H. 2012. 'The Eocene-Oligocene transition: Changes in sea level, temperature or both?', *Palaeogeography, Palaeoclimatology, Palaeoecology*, 335 – 336: 75 – 83.

Howe, J.A., Stoker, M.S. and Woolfe, K.J. 2001. 'Deep-marine seabed erosion and gravel lags in the northwestern Rockfall Trough, North Atlantic Ocean', *Geological Society of London Journal*, 158: 427 – 438.

Huber, M., Brinkhuis, H., Stickley, C.E., Döös, K., Slujs, A., Warnaar, J., Schellenberg, S.A. and Williams, G.L. 2004. 'Eocene circulation of the Southern Ocean: Was Antarctica kept warm by subtropical waters?', *Paleoceanography*, 19: 1 – 12.

Hutchinson, D.K., Boer, A.M.D., Coxall, H.K., Caballero, R., Nilsson, J. and Baatsen, M. 2018. 'Climate sensitivity and meridional overturning circulation in the late Eocene using GFDL CM2. 1', *Climate of the Past*, 14 (6): 789 – 810.

Appendices

Hutchinson, D.K., Coxall, H.K., O'Regan, M., Nilsson, J., Caballero, R. & de Boer, A.M. 2019. 'Arctic closure as a trigger for Atlantic overturning at the Eocene-Oligocene Transition', *Nature Communications*, 10 (3797).

Hyeong, K., Kuroda, J., Seo, I. and Wilson, P.A. 2016. 'Response of the Pacific inter-tropical convergence zone to global cooling and initiation of Antarctic glaciation across the Eocene Oligocene Transition', *Nature Scientific Reports*, 6: 30647.

Izuka, S.K. 1988. 'Relationship of magnesium and other minor elements in tests of *Cassidulina subglobosa* and *corriangulata* to physical oceanic properties', *Journal of Foraminiferal Research*, 18: 151 – 157.

Jacobsen, S. B. and Wasserburg, G. 1980. 'Sm-Nd isotopic evolution of chondrites', *Earth and Planetary Science Letters*, 50, 139 – 155.

Jasper, J.P. and Gagosian, R.B. 1989. 'Alkenone molecular stratigraphy in an oceanic environment affected by glacial freshwater events', *Paleoceanography*, 4 (6): 603 – 614.

Jeandel, C., Bishop, J.K. and Zindler, A., 1995. 'Exchange of neodymium and its isotopes between seawater and small and large particles in the Sargasso Sea', *Geochimica et Cosmochimica Acta*, 59 (3): 535 – 547.

Jeandel, C., Arsouze, T., Lacan, F., Téchiné, P. and Dutay, J.C. 2007. 'Isotopic Nd compositions and concentrations of the lithogenic inputs into the ocean: A compilation, with an emphasis on the margins', *Chemical Geology*, 239 (1-2): 156 – 164.

Jochum, K.P., Nohl, U., Herwig, K., Lammel, E., Stoll, B. and Hofmann, A.W. 2005. 'GeoReM: a new geochemical database for reference materials and isotopic standards', *Geostandards and Geoanalytical Research*, 29 (3): 333 – 338.

Jovane, L., Sprovieri, M., Florindo, F., Acton, G., Coccioni, R., D'all Antonia, B. and Dinares-Turell, J. 2007. 'Eocene-Oligocene paleoceanographic

Appendices

changes in the stratotype section, Massignano, Italy: Clues from rock magnetism and stable isotopes', *Journal of Geophysical Research*, 112: 1 – 16.

Katz, A. 1973. 'The interaction of magnesium with calcite during crystal growth at 25–90°C and one atmosphere', *Geochimica et Cosmochimica Acta*, 37: 1563 – 1586.

Katz, M., Katz, D., Wright, J., Miller, K., Pak, D., Shackleton, N. and Thomas, E. 2003. 'Early Cenozoic benthic foraminiferal isotopes: Species reliability and interspecies correction factors', *Paleoceanography*, 18 (2): 1024.

Katz, M.E., Miller, K.G., Wright, J.D., Wade, B.S., Browning, J.V., Cramer, B.S. and Rosenthal, Y. 2008. 'Stepwise transition from the Eocene greenhouse to the Oligocene icehouse', *Nature Geoscience*, 1: 329 – 334.

Katz, M.E., Cramer, B.S., Toggweiler, J.R., Esmay, G., Liu, C., Miller, K.G., Rosenthal, Y., Wade, B.S. and Wright, J.D. 2011. 'Impact of Antarctic Circumpolar Current Development on Late Paleogene Ocean Structure', *Science*, 332: 1076 – 1079.

Kelly, D.C., Nielsen, T.M., McCarren, H.K., Zachos, J.C. and Röhl, U. 2010. 'Spatiotemporal patterns of carbonate sedimentation in the South Atlantic: Implications for carbon cycling during the Paleocene–Eocene thermal maximum', *Palaeogeography, Palaeoclimatology, Palaeoecology*, 293 (1-2): 30 – 40.

Kennet, J.P. 1977. 'Cenozoic Evolution of Antarctic Glaciation, the Circum-Antarctic Ocean, and Their Impact on Global Paleoceanography', *Journal of Geophysical Research*, 82 (27): 3843 – 3860.

Keul, N., Langer, G., de Nooijer, L.J., Nehrke, G., Reichart, G.J. and Bijma, J. 2013. 'Incorporation of uranium in benthic foraminiferal calcite reflects seawater carbonate ion concentration', *Geochemistry, Geophysics, Geosystems*, 14 (1): 102 – 111.

Appendices

Kipp, L.E., Charette, M.A., Moore, W.S., Henderson, P.B. and Rigor, I.G. 2018. 'Increased fluxes of shelf-derived materials to the central Arctic Ocean', *Science Advances*, 4 (1): 1302.

Klinkhammer, G.P., Mix, A.C. and Haley, B.A. 2009. 'Increased dissolved terrestrial input to the coastal ocean during the last deglaciation', *Geochemistry, Geophysics, Geosystems*, 10 (3).

Koho, K.A., García, R.D., De Stigter, H.C., Epping, E., Koning, E., Kouwenhoven, T.J. and Van der Zwaan, G.J. 2008. 'Sedimentary labile organic carbon and pore water redox control on species distribution of benthic foraminifera: A case study from Lisbon–Setúbal Canyon (southern Portugal)', *Progress in Oceanography*, 79 (1): 55 – 82.

Koho, K.A., de Nooijer, L.J. and Reichart, G.J. 2015. 'Combining benthic foraminiferal ecology and shell Mn/Ca to deconvolve past bottom water oxygenation and paleoproductivity', *Geochimica et Cosmochimica Acta*, 165: 294 – 306.

Koho, K.A., de Nooijer, L.J., Fontanier, C., Toyofuku, T., Oguri, K., Kitazato, H. and Reichart, G.J. 2017. 'Benthic foraminiferal Mn/Ca ratios reflect microhabitat preferences', *Biogeosciences*.

Kominz, M.A. and Pekar, S.F. 2001. 'Oligocene eustasy from two-dimensional sequence stratigraphic backstripping', *GSA Bulletin*, 113 (3): 291 – 304.

Ku, T.L., 1965. 'An evaluation of the U^{234}/U^{238} method as a tool for dating pelagic sediments', *Journal of Geophysical Research*, 70 (14): 3457 – 3474.

Ku, T.L., Knauss, K.G. and Mathieu, G.G. 1977. 'Uranium in open ocean: concentration and isotopic composition', *Deep Sea Research*, 24 (11): 1005 – 1017.

Lacan, F. & Jeandel, C. 2001. 'Tracing Papua New Guinea imprint on the central Equatorial Pacific Ocean using neodymium isotopic compositions and

Appendices

Rare Earth Element patterns', *Earth and Planetary Science Letters*, 186: 497 – 512.

Lacan, F. & Jeandel, C. 2005. 'Neodymium isotopes as a new tool for quantifying exchange fluxes at the continent–ocean interface', *Earth and Planetary Science Letters*, 232: 245 – 257.

Ladant, J-B., Donnadieu, Y., Lefebvre, V. and Dumas, C. 2014. 'The respective role of atmospheric carbon dioxide and orbital parameters on ice sheet evolution at the Eocene-Oligocene transition', *Paleoceanography*, 29: 810 – 823.

Ladant, J.B., Donnadieu, Y., Bopp, L., Lear, C.H. and Wilson, P.A. 2018. 'Meridional contrasts in productivity changes driven by the opening of Drake Passage', *Paleoceanography and Paleoclimatology*, 33 (3): 302 – 317.

Lambelet, M., van de Flierdt, T., Crocket, K., Rehkämper, M., Kreissig, K., Coles, B., Rijkenberg, M.J., Gerringa, L.J., de Baar, H.J. and Steinfeldt, R. 2016. 'Neodymium isotopic composition and concentration in the western North Atlantic Ocean: results from the GEOTRACES GA02 section', *Geochimica et Cosmochimica Acta*, 177: 1 – 29.

Latimer, J.C. and Filippelli, G.M. 2002. 'Eocene to Miocene terrigenous inputs and export production: geochemical evidence from ODP Leg 177, Site 1090', *Palaeogeography, Palaeoclimatology, Palaeoecology*, 182 (3-4): 151 – 164.

Lea, D.W., Mashiotta, T.A. and Spero, H.J. 1999. 'Controls on magnesium and strontium uptake in planktonic foraminifera determined by live culturing', *Geochimica et Cosmochimica Acta*, 63: 2369 – 2379.

Lear, C.H. 2007. 'Mg/Ca palaeothermometry: a new window into Cenozoic climate change' *in*: Williams, M., Haywood, A.M., Gregory, F.J. and Schmidt, D.N. (eds) *Deep-Time Perspectives on Climate Change: Marrying the Signal from Computer Models and Biological Proxies*, The Micropalaeontological Society, Special Publications, The Geological Society, London: 313 – 349.

Appendices

Lear, C.H. and Rosenthal, Y. 2006. 'Benthic foraminiferal Li/Ca: Insights into Cenozoic seawater carbonate saturation state', *Geology*, 34 (11): 985 – 988.

Lear, C.H. and Lunt, D.J. 2016. 'How Antarctica got its ice', *Science*, 352 (6281): 34 – 35.

Lear, C.H., Elderfield, H. and Wilson, P.A. 2000. 'Cenozoic Deep-Sea Temperatures and Global Ice Volumes from Mg/Ca in Benthic Foraminiferal Calcite', *Science*, 287: 269 – 272.

Lear, C.H., Rosenthal, Y. and Slowey, N. 2002. 'Benthic foraminiferal Mg/Ca-paleothermometry: A revised core-top calibration', *Geochimica et Cosmochimica Acta*, 66 (19): 3375 – 3387.

Lear, C.H., Rosenthal, Y., Coxall, H.K. and Wilson, P.A. 2004. 'Late Eocene to early Miocene ice sheet dynamics and the global carbon cycle', *Paleoceanography*, 19: 1 – 11.

Lear, C.H., Bailey, T.R., Pearson, P.N., Coxall, H.K. and Rosenthal, Y. 2008. 'Cooling and ice growth across the Eocene-Oligocene transition', *Geology*, 36 (3): 251 – 254.

Lear, C.H., Mawbey, E.H. and Rosenthal, Y. 2010. 'Cenozoic benthic foraminiferal Mg/Ca and Li/Ca records: Toward unlocking temperatures and saturation states', *Paleoceanography*, 25: 1 – 11.

Lear, C. H., Coxall, H. K., Foster, G. L., Lunt, D. J., Mawbey, E. M., Rosenthal, Y., Sossian, S. M., Thomas, E. & Wilson, P. A. 2015. 'Neogene ice volume and ocean temperatures: Insights from infaunal foraminiferal Mg/Ca paleothermometry', *Paleoceanography*, 30 (11): 1437 – 1454.

Lefebvre, V., Donnadiou, Y., Sepulchre, P., Swingedouw, D. and Zhang, Z-S. 2012. 'Deciphering the role of southern gateways and carbon dioxide on the onset of the Antarctic Circumpolar Current', *Paleoceanography*, 27: 1 – 9.

Appendices

Lenton, T.M. and Britton, C. 2006. 'Enhanced carbonate and silicate weathering accelerates recovery from fossil fuel CO₂ perturbations', *Global Biogeochemical Cycles*, 20 (3).

Lhomme, N., Clarke, G.K. and Ritz, C. 2005. 'Global budget of water isotopes inferred from polar ice sheets', *Geophysical Research Letters*, 32 (20).

Liu, Z., Pagani, M., Zinniker, D., DeConto, R., Huber, M., Brinkhuis, H., Shah, S.R., Leckie, M. and Pearson, A. 2009. 'Global Cooling During the Eocene-Oligocene Climate Transition', *Science*, 323: 1187 – 1190.

Liu, Z., He, Y., Jiang, Y., Wang, H., Liu, W., Bohaty, S.M. and Wilson, P.A. 2018. 'Transient temperature asymmetry between hemispheres in the Palaeogene Atlantic Ocean', *Nature Geoscience*, 11 (9): 656.

Livermore, R., Eagles, G., Morris, P. and Maldonado, A. 2004. 'Shackleton Fracture Zone: No barrier to early circumpolar ocean circulation', *Geology*, 32: 797 – 800.

Livermore, R., Nankivell, A., Eagles, G. and Morris, P. 2005. 'Paleogene opening of Drake Passage', *Earth and Planetary Science Letters*, 236: 459 – 470.

Livermore, R., Hillenbrand, C.D., Meredith, M. and Eagles, G. 2007. 'Drake Passage and Cenozoic climate: An open and shut case?', *Geochemistry, Geophysics, Geosystems*, 8 (1): 1 – 11.

Longerich, H.P., Jackson, S.E. and Günther, D. 1996. 'Inter-laboratory note. Laser ablation inductively coupled plasma mass spectrometric transient signal data acquisition and analyte concentration calculation', *Journal of Analytical Atomic Spectrometry*, 11 (9): 899 – 904.

Lowenstein, T.K., Timofeeff, M.N., Brennan, S.T., Hardie, L.A. and Demicco, R.V. 2001. 'Oscillations in Phanerozoic Seawater Chemistry: Evidence from Fluid Inclusions', *Science*, 294: 1086 – 1088.

Appendices

Lyle, M., Gibbs, S., Moore, T.C. and Rea, D.K. 2007. 'Late Oligocene initiation of the Antarctic Circumpolar Current: Evidence from the South Pacific', *Geology*, 35: 691 – 694.

Lynch-Stieglitz, J., Curry, W.B. and Slowey, N. 1999. 'A geostrophic transport estimate for the Florida Current from the oxygen isotope composition of benthic foraminifera', *Paleoceanography*, 14 (3): 360 – 373.

Marriot, C.S., Henderson, G.M., Belshaw, N.S., Tudhope, A.W. 2004a. 'Temperature dependence of $\delta^7\text{Li}$, $\delta^{44}\text{Ca}$ and Li/Ca incorporation into calcium carbonate', *Earth and Planetary Science Letters*, 222: 615 – 624.

Marriot, C.S., Henderson, G.M., Crompton, R., Staubwasser, M. and Shaw, S. 2004b. 'Effect of mineralogy, salinity, and temperature on Li/Ca and Li isotope composition of calcium carbonate', *Chemical Geology*, 212: 5 – 15.

Marshall, J. & Schott, F. 1999. 'Open-ocean convection: Observations, theory, and models', *Reviews of Geophysics*, 37: 1 – 64.

Martin, E.E. and Haley, B.A. 2000. 'Fossil fish teeth as proxies for seawater Sr and Nd isotopes', *Geochimica et Cosmochimica Acta*, 64 (5): 835 – 847.

Martin, E.E. and Scher, H.D. 2004. 'Preservation of seawater Sr and Nd isotopes in fossil fish teeth: Bad news and good news', *Earth and Planetary Science Letters*, 220: 25 – 39.

Martin, E. E. and Scher, H. 2006. 'A Nd isotopic study of southern sourced waters and Indonesian throughflow at intermediate depths in the Cenozoic Indian Ocean', *Geochemistry Geophysics Geosystems*, 7 (9).

Martin, P.A., Lea, D.W., Rosenthal, Y., Shackleton, N.J., Sarnthein, M. and Papenfuss, T. 2002. 'Quaternary deep sea temperature histories derived from benthic foraminiferal Mg/Ca', *Earth and Planetary Science Letters*, 198: 193 – 209.

Appendices

Mawbey, E.M. and Lear, C.H. 2013. 'Carbon cycle feedbacks during the Oligocene-Miocene transient glaciation', *Geology*, 41 (9): 963 – 966.

McConnaughey, T. 1989. '¹³C and ¹⁸O isotopic disequilibrium in biological carbonates: I. Patterns', *Geochimica et Cosmochimica Acta*, 53 (1): 151 – 162.

McCoy-West, A.J., Millet, M.A. and Burton, K.W. 2017. 'The neodymium stable isotope composition of the silicate Earth and chondrites', *Earth and Planetary Science Letters*, 480: 121 – 132.

McKay, C.L., Groeneveld, J., Filipsson, H.L., Gallego-Torres, D., Whitehouse, M.J., Toyofuku, T. and Romero, O.E. 2015. 'A comparison of benthic foraminiferal Mn/Ca and sedimentary Mn/Al as proxies of relative bottom-water oxygenation in the low-latitude NE Atlantic upwelling system', *Biogeosciences*, 12: 5415 – 5428.

McKinley, C.C., Thomas, D.J., LeVay, L.J. and Zachary, R. 2019. 'Nd isotopic structure of the Pacific Ocean 40 – 10 Ma, and evidence for the reorganisation of deep North Pacific Ocean circulation between 36 and 25 Ma', *Earth and Planetary Science Letters*, 521: 139 – 149.

McManus, J., Berelson, W.M., Klinkhammer, G.P., Hammond, D.E. and Holm, C. 2005. 'Authigenic uranium: relationship to oxygen penetration depth and organic carbon rain', *Geochimica et Cosmochimica Acta*, 69 (1): 95 – 108.

Merico, A., Tyrrell, T. and Wilson, P.A. 2008. 'Eocene/Oligocene ocean de-acidification linked to Antarctic glaciation by sea-level fall', *Nature*, 452: 979 – 983.

Miller, K. G., Browning, J. V., Aubry, M.-P., Wade, B. S., Katz, M. E., Kulpecz, A. A. & Wright, J. D. 2008. 'Eocene–Oligocene global climate and sea-level changes: St. Stephens Quarry, Alabama', *Geological Society of America Bulletin*, 120, 34 – 53.

Appendices

Miller, K., Wright, J.D., Katz, M.E., Wade, B.S., Browning, J.V., Cramer, B.S. and Rosenthal, Y. 2009. 'Climate threshold at the Eocene-Oligocene transition: Antarctic ice sheet influence on ocean circulation' *in*: Koeberl, C. and Montanari, A. (eds) *The Late Eocene Earth – Hothouse, Icehouse and Impacts*, Special Paper 452, The Geological Society of America, Ch11: 169 – 178.

Mitrovica, J.X., Tamisiea, M.E., Davis, J.L. and Milne, G.A. 2001. 'Recent mass balance of polar ice sheets inferred from patterns of global sea-level change', *Nature*, 409 (6823): 1026.

Mitrovica, J.X., Gomez, N. and Clark, P.U. 2009. 'The sea-level fingerprint of West Antarctic collapse', *Science*, 323 (5915): 753.

Moore Jr, T.C., Wade, B.S., Westerhold, T., Erhardt, A.M., Coxall, H.K., Baldauf, J. and Wagner, M. 2014. 'Equatorial Pacific productivity changes near the Eocene-Oligocene boundary', *Paleoceanography*, 29 (9): 825 – 844.

Mudelsee, M., Bickert, T., Lear, C.H. and Lohmann, G. 2014. 'Cenozoic climate changes: A review based on time series analysis of marine benthic $\delta^{18}\text{O}$ records', *Reviews of Geophysics*, 52: 333 – 374.

Nairn, M.G. (2018) 'Mid-Late Miocene climate constrained by a new Laser Ablation ICP-MS set up' PhD Thesis.

Ní Fhlaithearta, S., Reichert, G.J., Jorissen, F.J., Fontanier, C., Rohling, E.J., Thomson, J. and De Lange, G.J. 2010. 'Reconstructing the seafloor environment during sapropel formation using benthic foraminiferal trace metals, stable isotopes, and sediment composition', *Paleoceanography*, 25 (4).

Nilsen, E.B., Anderson, L.D. and Delaney, M.L. 2003. 'Paleoproductivity, nutrient burial, climate change and the carbon cycle in the western equatorial Atlantic across the Eocene/Oligocene boundary', *Paleoceanography*, 18 (3).

Appendices

Norris, R.D., Wilson, P.A., Blum, P., and the Expedition 342 Scientists. 2014. *Proceedings of the Integrated Ocean Drilling Program*, 342.

Nürnberg, D., Buma, J. and Hemleben, C. (1996) 'Assessing the reliability of magnesium in foraminiferal calcite as a proxy for water mass temperatures', *Geochimica et Cosmochimica Acta*, 60 (5): 803 – 814.

O'Regan, M., Williams, C.J., Frey, K.E. and Jakobsson, M. 2011. 'A synthesis of the long-term paleoclimatic evolution of the Arctic', *Oceanography*, 24 (3): 66 – 80.

Ohshima, K.I., Nihashi, S. and Iwamoto, K. 2016. 'Global view of sea-ice production in polynyas and its linkage to dense/bottom water formation', *Geoscience Letters*, 3 (1): 13.

Onodera, J., Takahashi, K. and Jordan, R.W. 2008. 'Eocene silicoflagellate and ebridian paleoceanography in the central Arctic Ocean', *Paleoceanography*, 23 (1).

Pagani, M., Zachos, J.C. and Freeman, K.H. 2002. 'Eocene/Oligocene alkenone-based CO₂ estimates', Goldschmidt Conference Abstracts.

Pagani, M., Zachos, J.C., Freeman, K.H., Tipple, B. and Bohaty, S.M. 2005. 'Marked Decline in Atmospheric Carbon Dioxide Concentrations During the Paleogene', *Science*, 309: 600 – 603.

Pagani, M., Huber, M., Liu, Z., Bohaty, S.M., Henderiks, J., Sijp, W., Krishnan, S. and DeConto, R.M. 2011. 'The Role of Carbon Dioxide During the Onset of Antarctic Glaciation', *Science*, 334: 1261 – 1264.

Pälike, C., Delaney, M.L. and Zachos, J.C. 2014. 'Deep-sea redox across the Paleocene-Eocene thermal maximum', *Geochemistry, Geophysics, Geosystems*, 15 (4): 1038 – 1053.

Park, R. and Epstein, S. 1960. 'Carbon isotope fractionation during photosynthesis', *Geochimica. et cosmochimica acta*, 21 (1-2): 110 – 126.

Appendices

Parnell-Turner, R., White, N., Henstock, T., Murton, B., Maclennan, J. and Jones, S.M. 2014. 'A continuous 55-million-year record of transient mantle plume activity beneath Iceland', *Nature Geoscience*, 7: 914 – 919.

Pearson, P.N. and Chaisson, W.P. 1997. 'Late Paleocene to Middle Miocene Planktonic Foraminifera Biostratigraphy of the Ceara Rise', *in*: Shackleton, N.J., Curry, W.B., Richter, C. and Bralower, T.J. (eds) 1997. *Proceedings of the Ocean Drilling Program, Scientific Results*, 154.

Pearson, P.N., Ditchfield, P.W., Singano, J., Harcourt-Brown, K.G., Nicholas, C.J., Olsson, R.K., Shackleton, N.J. and Hall, M.A. 2001. 'Warm tropical sea surface temperatures in the Late Cretaceous and Eocene epochs', *Nature*, 413: 481 – 487.

Pearson, P.N., Olsson, R.K., Huber, B.T., Hemleben, C. and Berggren, W.A. (eds) 2006. *Atlas of Eocene Planktonic Foraminifera*, Cushman Foundation for Foraminiferal Research Special Publication, 41, Fredericksburg, USA.

Pearson, P.N., Foster, G.L., and Wade, B.S. 2009. 'Atmospheric carbon dioxide through the Eocene-Oligocene climate transition', *Nature*, 461: 1110 – 1113.

Peck, V.L., Yu, J., Kender, S. and Riesselman, C.R. 2010. 'Shifting ocean carbonate chemistry during the Eocene-Oligocene climate transition: Implications for deep-ocean Mg/Ca paleothermometry', *Paleoceanography*, 25.

Pena, L.D., Calvo, E., Cacho, I., Eggins, S. and Pelejero, C. 2005. 'Identification and removal of Mn-Mg-rich contaminant phases on foraminiferal tests: Implications for Mg/Ca past temperature reconstructions', *Geochemistry, Geophysics, Geosystems*, 6 (9).

Pena, L.D., Cacho, I., Calvo, E., Pelejero, C., Eggins, S. and Sadekov, A. 2008. 'Characterization of contaminant phases in foraminifera carbonates by electron microprobe mapping', *Geochemistry, Geophysics, Geosystems*, 9 (7).

Appendices

Peterson, R.G. and Stramma L. 1991. 'Upper-level circulation in the South Atlantic Ocean', *Progress in Oceanography*, 26 (1): 1 – 73.

Piepgras, D.J. and Wasserburg, G.J. 1980. 'Neodymium isotopic variations in seawater', *Earth and Planetary Science Letters*, 50 (1): 128 – 138.

Piepgras, D.J. and Wasserburg, G.J. 1982. 'Isotopic composition of neodymium in waters from the Drake Passage', *Science*, 217 (4556): 207 – 214.

Piepgras, D.J. and Wasserburg, G.J. 1987. 'Rare earth element transport in the western North Atlantic inferred from Nd isotopic observations', *Geochimica et Cosmochimica Acta*, 51 (5): 1257 – 1271.

Piepgras, D.J. and Jacobsen, S.B. 1988. 'The isotopic composition of neodymium in the North Pacific', *Geochimica et Cosmochimica Acta*, 52 (6): 1373 – 1381.

Piepgras, D.J., Wasserburg, G.J. and Dasch, E.J. 1979. 'The isotopic composition of Nd in different ocean masses', *Earth and Planetary Science Letters*, 45 (2): 223 – 236.

Pierce, J., Weisel, J. and the Leg 121 Scientists. (1989) *Proceedings of the Ocean Drilling Program*, 121.

Poore, H., White, N. and Maclennan, J. 2011. 'Ocean circulation and mantle melting controlled by radial flow of hot pulses in the Iceland plume', *Nature Geoscience*, 4: 558 – 561.

Pusz, A.E., Thunell, R.C. and Miller, K.G. 2011. 'Deep water temperature, carbonate ion, and ice volume changes across the Eocene-Oligocene climate transition', *Paleoceanography*, 26: 1 – 15.

Raitzsch, M., Kuhnert, H., Hathorne, E.C., Groeneveld, J. and Bickert, T. 2011. 'U/Ca in benthic foraminifers: A proxy for the deep-sea carbonate saturation', *Geochemistry, Geophysics, Geosystems*, 12 (6).

Appendices

Reichart, G.-J., Jorissen, F., Anschutz, P. & Mason, P. R. 2003. 'Single foraminiferal test chemistry records the marine environment', *Geology*, 31, 355 – 358.

Reynard, B., Lécuyer, C. & Grandjean, P. 1999. 'Crystal-chemical controls on rareearth element concentrations in fossil biogenic apatites and implications for paleoenvironmental reconstructions', *Chemical Geology*, 155: 233 – 241.

Rickers, F., Fichtner, A. and Trampert, J. 2013. 'The Iceland Jan Mayen plume system and its impact on mantle dynamics in the North Atlantic region: Evidence from full-waveform inversion', *Earth and Planetary Science Letters*, 367: 39 – 51.

Riesselman, C.R., Dunbar, R.B., Mucciarone, D.A. and Kitasei, S.S. 2007. 'High resolution stable isotope and carbonate variability during the early Oligocene climate transition: Walvis Ridge (ODP Site 1263)', US Geological Survey Open File Repository, 1047 (7).

Rögl, F., 1999. 'Mediterranean and Paratethys. Facts and hypotheses of an Oligocene to Miocene paleogeography (short overview)', *Geologica carpathica*, 50 (4): 339 – 349.

Rosenthal, Y. and Lohmann, G.P. 2002. 'Accurate estimation of sea surface temperatures using dissolution-corrected calibrations for Mg/Ca paleothermometry', *Paleoceanography*, 17 (3): 1 – 6.

Rosenthal, Y., Boyle, E.A. and Slowey, N. 1997. 'Temperature control on the incorporation of magnesium, strontium, fluorine and cadmium into benthic foraminiferal shells from Little Bahama Bank: Prospects for thermocline paleoceanography', *Geochimica et Cosmochimica Acta*, 61 (17): 3633 – 3643.

Rosenthal, Y., Lohmann, G.P., Lohmann, K.C. and Sherrell, R.M. 2000. 'Incorporation and preservation of Mg in *Globeriginoidea sacculifer*.

Appendices

Implications for reconstructing the temperature and $^{18}\text{O}/^{16}\text{O}$ of seawater', *Paleoceanography*, 15 (1): 133 – 145.

Rostek, F., Bard, E., Beaufort, L., Sonzogni, C. and Ganssen, G. 1997. 'Sea surface temperature and productivity records for the past 240 kyr in the Arabian Sea', *Deep Sea Research Part II: Topical Studies in Oceanography*, 44 (6-7): 1461 – 1480.

Rousseau, T.C., Sonke, J.E., Chmeleff, J., Van Beek, P., Souhaut, M., Boaventura, G., Seyler, P. and Jeandel, C. 2015. 'Rapid neodymium release to marine waters from lithogenic sediments in the Amazon estuary', *Nature communications*, 6: 7592.

Russell, A.D., Emerson, S., Nelson, B.K., Erez, J. and Lea, D.W. 1994. 'Uranium in foraminiferal calcite as a recorder of seawater uranium concentrations', *Geochimica et Cosmochimica Acta*, 58 (2): 671 – 681.

Russell, A.D., Emerson, S., Mix, A.C. and Peterson, L.C. 1996. 'The use of foraminiferal uranium/calcium ratios as an indicator of changes in seawater uranium content', *Paleoceanography*, 11 (6): 649 – 663.

Russell, A.D., Hönisch, B., Spero, H.J. and Lea, D.W. 2004. 'Effects of seawater carbonate ion concentration and temperature on shell U, Mg, and Sr in cultured planktonic foraminifera', *Geochimica et Cosmochimica Acta*, 68 (21): 4347 – 4361.

Salamy, K.A. and Zachos, J.C. 1999. 'Latest Eocene-Early Oligocene climate change and Southern Ocean fertility: inferences from sediment accumulation and stable isotope data', *Palaeogeography, Palaeoclimatology, Palaeoecology*, 145: 61 – 77.

Sarmiento, J.L., Slater, R., Barber, R., Bopp, L., Doney, S.C., Hirst, A.C., Kleypas, J., Matear, R., Mikolajewicz, U., Monfray, P. and Soldatov, V. 2004. 'Response of ocean ecosystems to climate warming', *Global Biogeochemical Cycles*, 18 (3).

Appendices

Scher, H. D. & Martin, E. E. 2004. 'Circulation in the Southern Ocean during the Paleogene inferred from neodymium isotopes', *Earth and Planetary Science Letters*, 228: 391 – 405.

Scher, H. D. & Martin, E. E. 2006. 'Timing and climatic consequences of the opening of Drake Passage', *Science*, 312: 428 – 430.

Scher, H. D. & Martin, E. E. 2008. 'Oligocene deep water export from the North Atlantic and the development of the Antarctic Circumpolar Current examined with neodymium isotopes', *Paleoceanography*, 23 (1).

Scher, H.D., Martin, E.E. and Haase, A.A. (2002) 'Circulation of Eocene to Pliocene intermediate water masses in the Indian Ocean: Evidence from fossil fish teeth Nd isotopes', *Goldschmidt Conference Abstracts*.

Scher, H. D., Bohaty, S. M., Zachos, J. C. & Delaney, M. L. 2011. 'Two-stepping into the icehouse: East Antarctic weathering during progressive ice-sheet expansion at the Eocene–Oligocene transition', *Geology*, 39: 383 – 386.

Scher, H. D., Bohaty, S. M., Smith, B. W. & Munn, G. H. 2014. 'Isotopic interrogation of a suspected late Eocene glaciation', *Paleoceanography*.

Schneider, T., Bischoff, T. and Haug, G.H. 2014. 'Migrations and dynamics of the intertropical convergence zone', *Nature*, 513 (7516): 45.

Schumacher, S. and Lazarus, D. 2004. 'Regional differences in pelagic productivity in the late Eocene to early Oligocene—a comparison of southern high latitudes and lower latitudes', *Palaeogeography, Palaeoclimatology, Palaeoecology*, 214 (3): 243 – 263.

Scotese, C.R. 2014. 'Atlas of Paleogene Paleogeographic Maps (Mollweide Projection), Maps 8-15, Volume 1, The Cenozoic, PALEOMAP Atlas for ArcGIS', PALEOMAP Project, Evanston, IL.

Appendices

Seidov, D. and Maslin, M. 2001. 'Atlantic ocean heat piracy and the bipolar climate see-saw during Heinrich and Dansgaard–Oeschger events', *Journal of Quaternary Science: Published for the Quaternary Research Association*, 16 (4): 321 – 328.

Sexton, P. F., Wilson, P. A. & Pearson, P. N. 2006. 'Microstructural and geochemical perspectives on planktic foraminiferal preservation: "Glassy" versus "Frosty"', *Geochemistry, Geophysics, Geosystems*, 7.

Shackleton, N.J. 1987. 'Oxygen isotopes, ice volume and sea level', *Quaternary Science Reviews*, 6: 183 – 190.

Shaw, H. & Wasserburg, G. 1985. 'Sm-Nd in marine carbonates and phosphates: Implications for Nd isotopes in seawater and crustal ages', *Geochimica et Cosmochimica Acta*, 49: 503 – 518.

Siesser, W.G., 1995. 'Paleoproductivity of the Indian Ocean during the Tertiary period', *Global and Planetary Change*, 11 (1-2): 71 – 88.

Sijp, W.P. and England, M.H. 2003. 'Effect of the Drake Passage throughflow on global climate', *Journal of Physical Oceanography*, 34: 1254 – 1266.

Sijp, W.P., England, M.H. and Huber, M. 2011. 'Effect of the deepening of the Tasman Gateway on the global ocean', *Paleoceanography*, 26 (4).

Silva, P.I. and Jenkins, D. 1993. 'Decision on the Eocene-Oligocene boundary stratotype', *Episodes*, 16: 379 – 382.

Smith, A.G. and Pickering, K.T. 2003. 'Oceanic gateways as a critical factor to initiate icehouse Earth', *Journal of the Geological Society*, 160: 337 – 340.

Smith, A.G., Smith, D.G. and Funnell, B.M. 1994. *Atlas of Mesozoic and Cenozoic coastlines*, Cambridge University Press, Cambridge.

Appendices

Spero, H.J., Bijma, J., Lea, D.W. and Bemis, B.E. 1997. 'Effect of seawater carbonate concentration on foraminiferal carbon and oxygen isotopes', *Nature*, 390 (6659): 497.

Spray, J.F., Bohaty, S.M., Davies, A., Bailey, I., Romans, B.W., Cooper, M.J., Milton, J.A. and Wilson, P.A. 2019. 'North Atlantic evidence for a unipolar icehouse climate state at the Eocene-Oligocene Transition', *Paleoceanography and Paleoclimatology*.

Stärz, M., Jokat, W., Knorr, G. and Lohmann, G. 2017. 'Threshold in North Atlantic-Arctic Ocean circulation controlled by the subsidence of the Greenland-Scotland Ridge', *Nature Communications*, 8: 15681.

Staudigel, H., Doyle, P. & Zindler, A. 1985. 'Sr and Nd isotope systematics in fish teeth', *Earth and Planetary Science Letters*, 76: 45 – 56.

Stewart, J.A., Gutjahr, M., James, R.H., Anand, P. and Wilson, P.A. 2016. 'Influence of the Amazon River on the Nd isotope composition of deep water in the western equatorial Atlantic during the Oligocene–Miocene transition', *Earth and Planetary Science Letters*, 454: 132 – 141.

Stickley, C.E., Brinkhuis, H., Schellenberg, S.A., Slujs, Röhl, A., Fuller, U., Grauert, M., Huber, M., Warnaar, J. and Williams, G.L. 2004. 'Timing and nature of the deepening of the Tasmanian Gateway', *Paleoceanography*, 19.

Stille, P. & Fischer, H. 1990. 'Secular variation in the isotopic composition of Nd in Tethys seawater', *Geochimica et Cosmochimica Acta*, 54: 3139 – 3145.

Straneo, F. 2006. 'On the Connection between Dense Water Formation, Overturning, and Poleward Heat Transport in a Convective Basin', *Journal of Physical Oceanography*, 36: 1822 – 1840.

Sundby, S., Drinkwater, K.F. and Sigurd Kjesbu, O. 2016. 'The North Atlantic Spring-Bloom System – Where the Changing Climate Meets the Winter Dark', *Frontiers in Marine Science*, 3 (28).

Appendices

Sundquist, E.T. 1991. 'Steady-and non-steady-state carbonate-silicate controls on atmospheric CO₂', *Quaternary Science Reviews*, 10 (2-3): 283 – 296.

Tachikawa, K., Jeandel, C. and Roy-Barman, M. 1999. 'A new approach to the Nd residence time in the ocean: the role of atmospheric inputs', *Earth and Planetary Science Letters*, 170 (4): 433 – 446.

Tamburini, F. and Föllmi, K.B. 2009. 'Phosphorus burial in the ocean over glacial-interglacial time scales', *Biogeosciences*, 6 (4): 501 – 513.

Tchernia, P. (1980) 'The Indian Ocean' in: *Descriptive Regional Oceanography*, Oxford: Pergamon Press Ltd, 171 – 215. Ch 6.

Tessier, A., Campbell, P.G. and Bisson, M. 1979. 'Sequential extraction procedure for the speciation of particulate trace metals', *Analytical Chemistry*, 51 (7): 844 – 851.

Thomas, D.J. 2004. 'Evidence for deep-water production in the North Pacific Ocean during the early Cenozoic warm interval', *Nature*, 430: 65 – 68.

Thomas, D.J. and Via, R.K. (2007) 'Neogene evolution of Atlantic thermohaline circulation: Perspective from Walvis Ridge, southeastern Atlantic Ocean', *Paleoceanography and Paleoclimatology*, 22.

Thomas, D.J., Korty, R., Huber, M., Schubert, J.A. and Haines, B. 2014. 'Nd isotopic structure of the Pacific Ocean 70 – 30 Ma and numerical evidence for vigorous ocean circulation and ocean heat transport in a greenhouse world', *Paleoceanography and Paleoclimatology*, 29 (5): 454 – 469.

Tigchelaar, M., von der Heydt, A.S. and Dijkstra, H.A. 2011. 'A new mechanism for the two-step $\delta^{18}\text{O}$ signal at the Eocene-Oligocene boundary', *Climate of the Past*, 7: 235 – 247.

Tilstone, G., Miller, P.I., Brewin, B. and Priede, I.G. 2014. 'Enhancement of primary production in the North Atlantic outside of the spring bloom, identified

Appendices

by remote sensing of ocean colour and temperature', *Remote Sensing of Environment*, 146: 77 – 86.

Toyoda, K. and Tokonami, M., 1990. 'Diffusion of rare-earth elements in fish teeth from deep-sea sediments'. *Nature*, 345 (6276): 607.

Tribovillard, N., Algeo, T. J., Lyons, T. and Riboulleau, A. 2006. 'Trace metals as paleoredox and paleoproductivity proxies: an update', *Chemical Geology*, 232: 12 – 32.

Tripati, A., Backman, J., Elderfield, H. and Ferretti, P. 2005. 'Eocene bipolar glaciation associated with global carbon cycle changes', *Nature*, 341 – 346.

Trujillo, A.P. and Thurman, H.V. (2008) 'Ocean Circulation' *in: Essentials of Oceanography*, London: Pearson Education Ltd, 202 – 243. Ch 7.

Tschumi, T., Joos, F., Gehlen, M. and Heinze, C. 2010. 'Deep ocean ventilation, carbon isotopes, marine sedimentation and the deglacial CO₂ rise', *Climate of the Past*, 6 (5): 1895 – 1958.

Tyrrell, T. 1999. 'The relative influences of nitrogen and phosphorus on oceanic primary production', *Nature*, 400 (6744): 525.

Urey, H. C. 1947. 'The thermodynamic properties of isotopic substances', *Journal of the Chemical Society*, 562 – 581.

Urey, H.C., Lowenstam, H.A., Epstein, S. and McKinney, C.R. 1951. 'Measurement of paleotemperatures and temperatures of the Upper Cretaceous of England, Denmark, and the southeastern United States', *Geological Society of America Bulletin*, 62 (4): 399 – 416.

Vahlenkamp, M., Niezgodzki, I., Vleeschouwer, De. D., Bickert, T., Harper, D., Kirtland Turner, S., Lohmann, G., Sexton, P., Zachos, J. and Pälike, H. 2018a. 'Astronomically paced changes in deep-water circulation in the western North Atlantic during the middle Eocene', *Earth and Planetary Science Letters*, 484: 329 – 340.

Appendices

Vahlenkamp, M., Niezgodzki, I., Vleeschouwer, De. D., Lohmann, G., Bickert, T. and Pälike, H. 2018b. 'Ocean and climate response to North Atlantic seaway changes at the onset of long-term Eocene cooling', *Earth and Planetary Science Letters*, 498: 185 – 195.

van de Flierdt, T., Griffiths, A.M., Lambelet, M., Little, S.H., Stichel, T. and Wilson, D.J. 2016. 'Neodymium in the oceans: a global database, a regional comparison and implications for palaeoceanographic research', *Philosophical Transactions of the Royal Society A: Mathematical, Physical and Engineering Sciences*, 374 (2081).

Van Peer, T.E., Liebrand, D., Xuan, C., Lippert, P.C., Agnini, C., Blum, N., Blum, P., Bohaty, S.M., Bown, P.R., Greenop, R. and Kordesch, W.E.. 2017. 'Data report: revised composite depth scale and splice for IODP Site UU1406', *Proceedings of the Integrated Ocean Drilling Program*, 342.

van Soelen, E.E., Kim, J.H., Santos, R.V., Dantas, E.L., de Almeida, F.V., Pires, J.P., Roddaz, M. and Damste, J.S.S. 2017. 'A 30 Ma history of the Amazon River inferred from terrigenous sediments and organic matter on the Ceará Rise', *Earth and Planetary Science Letters*, 474: 40 – 48.

Via, R.K. and Thomas, D.J. 2006. 'Evolution of Atlantic thermohaline circulation: Early Oligocene onset of deep-water production in the North Atlantic', *Geology*, 34: 441 – 444.

Viers, J., Roddaz, M., Filizola, N., Guyot, J.L., Sondag, F., Brunet, P., Zouiten, C., Boucayrand, C., Martin, F. and Boaventura, G.R. 2008. 'Seasonal and provenance controls on Nd–Sr isotopic compositions of Amazon rivers suspended sediments and implications for Nd and Sr fluxes exported to the Atlantic Ocean', *Earth and Planetary Science Letters*, 274 (3-4): 511 – 523.

Villa, G., Fioroni, C., Persico, D., Roberts, A.P. and Florindo, F. 2014. 'Middle Eocene to Late Oligocene Antarctic glaciation/deglaciation and southern ocean productivity', *Paleoceanography*, 29 (3): 223 – 237.

Appendices

Vleeschouwer, De. D., Vahlenkamp, M., Crucifix, M. and Pälike, H. 2017. 'Alternating Southern and Northern Hemisphere climate response to astronomical forcing during the past 35 my', *Geology*, 45 (4): 375 – 378.

Wade, B.S., Pearson, P.N., Berggren, W.A. and Pälike, H. 2011. 'Review and revision of Cenozoic tropical planktonic foraminiferal biostratigraphy and calibration to the geomagnetic polarity and astronomical time scale', *Earth Science Reviews*, 104 (13): 111 – 142.

Wade, B.S., Houben, A.J.P., Quaijtaal, W., Schouten, S., Rosenthal, Y., Miller, K.G., Katz, M.E., Wright, J.D., Brinkhuis, H. 2012. 'Multiproxy record of abrupt sea-surface cooling across the Eocene-Oligocene transition in the Gulf of Mexico', *Geology*, 40 (2): 159 – 162.

Walsh, J.J. 1989. 'Arctic carbon sinks: present and future', *Global Biogeochemical Cycles*, 3 (4): 393 – 411.

Weis, D., Kieffer, B., Maerschalk, C., Barling, J., De Jong, J., Williams, G.A., Hanano, D., Pretorius, W., Mattielli, N., Scoates, J.S. and Goolaerts, A. 2006. 'High-precision isotopic characterization of USGS reference materials by TIMS and MC-ICP-MS', *Geochemistry, Geophysics, Geosystems*, 7 (8).

Werne, J.P., Hollander, D.J., Lyons, T.W. and Peterson, L.C. 2000. 'Climate-induced variations in productivity and planktonic ecosystem structure from the Younger Dryas to Holocene in the Cariaco Basin, Venezuela', *Paleoceanography*, 15 (1): 19 – 29.

Westerhold, T., Röhl, U., Pälike, H., Wilkens, R., Wilson, P.A. and Acton, G. 2014. 'Orbitally tuned timescale and astronomical forcing in the middle Eocene to early Oligocene', *Climate of the Past*, 10: 955 – 973.

White, R.S. 1997. 'Rift-plume interaction in the North Atlantic', *Philosophical Transactions of the Royal Society of London A*, 355: 319 – 399.

Wilkinson, B. and Algeo, T. 1989. 'Sedimentary carbonate record of calcium-magnesium cycling', *American Journal of Science*, 289 (10): 1158 – 1194.

Appendices

Wilson, D. J., Piotrowski, A. M., Galy, A. & Clegg, J. A. 2013. 'Reactivity of neodymium carriers in deep sea sediments: Implications for boundary exchange and paleoceanography', *Geochimica et Cosmochimica Acta*, 109: 197 – 221.

Woodruff, F. and Savin, S.M. (1989) 'Miocene deepwater oceanography', *Paleoceanography*, 4: 87 – 140.

Wright, J. 1984. 'REE and Nd isotopes in conodont apatite: Variations with geological age and depositional environment. In Conodont Biofacies and Provincialism', *Geological Society of America Bulletin*, 196: 325 – 340.

Wright, J.D. and Miller, K.G. 1996. 'Southern Ocean influence on late Eocene to Miocene deep-water circulation' in: Kennet, J.P. (ed.) 'The Antarctic paleoenvironment: A perspective on global change, Part 2', *Antarctic Research Series*, 60: 1 – 25.

Wright, N.M., Scher, H.D., Seton, M., Huck, C.E. and Duggan, B.D. 2018. 'No change in Southern Ocean circulation in the Indian Ocean from the Eocene through late Oligocene', *Paleoceanography and Paleoclimatology*, 33 (2): 152 – 167.

Wu, J., Sunda, W., Boyle, E.A. and Karl, D.M. 2000. 'Phosphate depletion in the western North Atlantic Ocean', *Science*, 289 (5480): 759 – 762.

Yu, J. and Elderfield, H. 2007. 'Benthic foraminiferal ratios reflect deep water carbonate saturation state', *Earth and Planetary Science Letters*, 258: 73 – 86.

Yu, J. and Elderfield, H. 2008. 'Mg/Ca in the benthic foraminifera *Cibicidoides wuellerstorfi* and *Cibicidoides mundulus*: Temperature versus carbonate ion saturation', *Earth and Planetary Science Letters*, 276: 129 – 139.

Appendices

Yu, J., Elderfield, H., Jin, Z. and Booth, L. 2008. 'A strong temperature effect on U/Ca in planktonic foraminiferal carbonates', *Geochimica et Cosmochimica Acta*, 72 (20): 4988 – 5000.

Yu, J., Foster, G.L., Elderfield, H., Broecker, W.S. and Clark, E. 2010. 'An evaluation of benthic foraminiferal B/Ca and $\delta^{11}\text{B}$ for deep ocean carbonate ion and pH reconstructions', *Earth and Planetary Science Letters*, 293: 114 – 120.

Zachos, J.C. and Kump, L.R. 2005. 'Carbon cycle feedbacks and the initiation of Antarctic glaciation in the earliest Oligocene', *Global and Planetary Change*, 47: 51 – 66.

Zachos, J.C., Rea, D.K., Seto, K., Nomura, R. and Niitsuma, N. (1992) 'Paleogene and Early Neogene Deep Water Paleoceanography of the Indian Ocean as Determined from Benthic Foraminifer Stable Carbon and Oxygen Isotope Records', in: Duncan, R.A., Rea, D.K., Kidd, R.B., von Rad, U. and Weissel, J.K. (eds) *Synthesis of Results from Scientific Drilling in the Indian Ocean*, American Geophysical Union, Washington DC.

Zachos, J.C., Quinn, T.M. and Salamy, K.A. 1996. 'High-resolution (10^4 years) deep-sea foraminiferal stable isotope records of the Eocene-Oligocene climate transition', *Paleoceanography*, 11: 251 – 266.

Zachos, J.C., Opdyke, B.N., Quinn, T.M., Jones, C.E. and Hallid, A.N. 1999. 'Early Cenozoic glaciation, Antarctic weathering, and seawater $^{87}\text{Sr}/^{86}\text{Sr}$: is there a link?', *Chemical Geology*, 161: 165 – 180.

Zachos, J.C., Pagani, M., Sloan, L.C., Thomas, E. and Billups, K. 2001. 'Trends, rhythms and aberrations in global climate: 65 Ma to present', *Science*, 292: 686 – 693.

Zachos, J.C., Kroon, D.C., Blum, P. and the Leg 208 Scientists. 2004. *Proceedings of the Ocean Drilling Program, Initial Reports*, 208.

Appendices

Zachos, J.C., Dickens, G.R. and Zeebe, R.E. 2008. 'An early Cenozoic perspective on greenhouse warming and carbon-cycle dynamics', *Nature*, 45: 279 – 283.

Zeebe, R.E. 1999. 'An explanation of the effect of seawater carbonate concentration on foraminiferal oxygen isotopes', *Geochimica et Cosmochimica Acta*, 63 (13-14): 2001 – 2007.

Appendices

Appendix 1: Cleaning procedure for foraminiferal stable isotope and trace element analysis

Before You Start

1. Set your tubes of crushed forams in a clean, perspex rack. Randomize samples prior to cleaning.
2. All reagents necessary reagents should be prepared and stored in new, acid-leached PE bottles, including:
 - 10% HCl and DI H₂O for rinsing pipette tips
 - DI H₂O for foraminifera cleaning
 - Trace grade methanol for foraminifera cleaning
 - Reducing reagent
 - Oxidizing reagent
 - DI H₂O for sample transfers
 - 0.02HNO₃ for foraminifera leaching
3. Turn on flow bench at least 15 minutes before using, wipe down all work surfaces and mop floor of clean lab with DI water before starting.

Removal of Fine Clays

1. Drain the ultrasonic bath in the flow bench and refill with fresh DI H₂O to the base of perspex rack.
2. Tap sample rack firmly on the bench to shake foraminifera to base of tubes.
3. Open tube tops slowly in case fragments are stuck to sides or lids.
4. Using DI H₂O for foraminifera cleaning, gently fill each tube most of the way.
5. If forams are visible in tube lids, add a small amount of water to the lids as well. Close tubes.
6. Tap rack firmly on the bench to settle forams and get rid of any air bubbles.
7. Rinse pipette tip in 10% HCl (3x) and then DI H₂O (3x) tip rinses.
8. Siphon off as much water as possible from the tubes.
9. Open all tubes and fill ~1/3 full with water. Close tubes.
10. Tap rack as necessary to remove air bubbles.

Appendices

13. Ultrasonicate for one minute. Fine clays should now be dislodged and held in suspension.

14. Turn off bath and remove rack. Open all tubes and vigorously squirt DI H₂O for foraminifera cleaning into each tube so as to agitate the sample and mix clays throughout. Close tubes.

15. Tap rack firmly on the bench, invert and shake, then wait for foraminifera to settle. Don't wait too long, or suspended clays will also settle. If necessary, tap the rack again to encourage foraminifera to settle.

16. Clean siphon tip (3x 10% HCl and 3x DI H₂O).

17. Siphon off as much water as possible leaving foraminifera behind.

18. Repeat steps 11-17 a total of 3x with DI H₂O. To avoid systematic variations in the effectiveness of clay removal, begin siphoning at a different row or side of the rack during each rinse step. Change the orientation of the rack in the sonic bath during each sonication.

19. Fill 125 mL spray bottle ~1/5 full with trace grade methanol. Loosen cap of spray bottle when not in use to keep methanol from dripping from the tip.

20. Repeat steps 11-17 1-2x with trace grade methanol, depending on the degree of clay contamination in your samples. Special instructions for methanol:

- *Always wear goggles when working with methanol*
- *Fill tubes to the top of the rack with methanol (rather than just 1/3 full)*
- *Do not add additional methanol after ultrasonication; simply siphon off existing methanol*
- *Methanol is less viscous than water, so take special care when siphoning; don't go to quite to the bottom of the tube*
- *When siphoning methanol, it may work better to press siphon tip against the rear of the tube (rather than the front)*
- *Dispose of any leftover methanol in the labelled waste container*

21. Repeat steps 11-17 an additional 2x with DI H₂O.

22. Pipette off all remaining water using a clean (3x 10% HCl and 3x DI H₂O), 100 µL pipette tip. It is not necessary to rinse the tip between samples.

Removal of Metal Oxides (Reducing Step)

1. Turn on power source for hotplate in the fume cupboard and set to 300 °C.

Appendices

2. Rinse and fill the glass evaporating dish in the fume cupboard with DI H₂O. Set on hotplate.
3. Rinse and fill tall form beaker containing thermometer with DI H₂O from the ELGA tap. Set on hot plate. Use this to top up the evaporating dish as water evaporates.
4. Drain the ultrasonic bath in the fume cupboard and refill with fresh DI H₂O.
5. Prepare your reducing reagent in the labelled, empty 60 mL bottle. Please note that hydrous hydrazine is volatile, carcinogenic, and explosive. Always work in the fume cupboard and take care to minimize exposure. Dispose of all related waste (pipette tips, parafilm, gloves) in a plastic bag and seal bag before removing from fume cupboard.
6. Pour 10 mLs ammonia solution and 10 mLs citric acid/ammonia solution (both stored in the fridge) into the empty bottle; pour these reagents directly from the bottles (no pipettes) and take care not to touch the lids of reagent bottles to any other surfaces.
7. Prepare a waste bag, a fresh strip of parafilm, and a clean (3x 10% HCl and 3x DI H₂O) 1000 µL (blue) pipette tip.
8. Remove hydrous hydrazine from fridge.
9. Pipette 1200 µL hydrous hydrazine into the reducing reagent, cap and invert to mix. Re-parafilm hydrous hydrazine and return to fridge.
10. Before proceeding, ensure hot water bath is hot (on verge of boiling, 80-90 °C). This can take about 30 minutes.
11. Open tubes. Using a clean (3x 10% HCl and 3x DI H₂O) 100 µL pipette tip, add 100 µL reducing reagent to each tube. Be aware that the reagent has a low viscosity and tends to drip. Close tubes firmly.
12. Because ammonia has a high vapor pressure, tube caps will tend to blow open in the hot water bath. To prevent this, clamp tubes shut by screwing a perspex plate to the top of your rack. Ensure your tubes are firmly closed and that they are in good contact with the plate surface.
13. Place racks in the hot water bath for a total of 30 minutes. Calcium carbonate is slightly soluble in ammonia, so avoid letting your sample fragments sit in the reducing agent for longer than the necessary 30 minutes. Every 2 minutes:
 - *Remove rack*
 - *Tighten screws on perspex clamp*
 - *Invert, shake, and tap rack to settle forams and remove bubbles*

Appendices

- *Ultrasonicate rack for a few seconds (this will agitate the reagent into all parts of the sample and discourage dissolved oxides from re-precipitating)*
- *Tap rack firmly and return to hot water bath*
- *Top off the water bath as necessary using hot water from the beaker*

14. After 30 minutes, remove rack and clamp and carefully open and close all tubes to release gas. Keep one finger on the top of the tube and use your thumb to open the tube in a peeling motion.

15. Pipette off as much reducing reagent as possible using a clean (3x 10% HCl and 3x DI H₂O) 100 µL pipette tip. Do not use siphon. Eject waste into the reducing reagent bottle.

16. Fill tube caps and tubes with DI H₂O for foraminifera cleaning. Close tubes. Tap rack firmly to settle foraminifera.

17. Rinse pipette tip (3x 10% HCl and 3x DI H₂O). Siphon caps and then siphon off as much water as possible from tubes.

18. Repeat steps 12 and 13 two more times.

19. Fill tubes half full with DI H₂O for foram cleaning, close tubes, then set in the hot water bath for 5 minutes.

20. In the meantime, prepare a fresh strip of parafilm.

21. Remove hydrazine waste container (brown bottle) from fridge and place in fume cupboard. Dump leftover reducing reagent into waste container.

22. Fill the empty 60 mL bottle for rinsing reducing reagent with DI H₂O.

23. Rinse the reducing reagent bottle 2-3x with DI H₂O, dumping rinse water into the waste container. Re-parafilm waste container and return to fridge.

24. If five minutes have passed, remove rack from hot water bath, clean pipette tip (3x 10% HCl and 3x DI H₂O), siphon caps, and then siphon off as much water as possible from tubes.

25. Repeat steps 12 and 13 two more times.

24. Repeat step 15.

25. Repeat step 22. It is now safe to remove the rack from the fume hood.

26. Turn hotplate off or down as appropriate (you will need it again in Section V).

Sample Transfer

1. In the flow bench, label a new set of acid-leached tubes for your samples.
2. Using a disposable scalpel, cut off ~1/4 of a 100 μL pipette tip.
3. Set the pipettor to 70 μL and thoroughly clean the pipette tip (6x 10% HCl and 6x DI H_2O).
4. If you have not already, rinse and refill your DI H_2O for sample transfers.
5. Open old tube. Hold pipette tip directly over sample fragments and pipette and expel fragments ($\pm \text{H}_2\text{O}$) into the new tube of the same sample number.
6. Add a small amount of DI H_2O for sample transfers to the old tube. Repeat transfer until no fragments are visible in the old tube and then again once more (usually 2-3x).
7. Between samples, rinse the pipette tip 2-3x in your DI H_2O for sample transfers.
8. Once all samples have been transferred into new tubes, rinse pipette tip (3x 10% HCl and 3x DI H_2O), and siphon off as much water as possible.

Removal of Organic Matter (Oxidizing Step)

1. In the fume cupboard, ensure water bath is hot (on verge of boiling, 80-90 $^{\circ}\text{C}$) and filled to the base of your perspex rack.
2. Prepare your oxidizing reagent in the labelled, empty 60 mL bottle.
 - *Pour 15 mL 0.1 N NaOH (stored in the fridge) into the empty bottle; pour this reagent directly from the bottle (no pipettes) and take care not to touch the lid of the reagent bottle to any other surface.*
 - *Using a clean (3x 10% HCl and 3x DI H_2O) 100 μL pipette tip, add 50 μL H_2O_2 ; please pour a small quantity of H_2O_2 into the H_2O_2 bottle cap, pipette from the cap, and dispose of cap contents before re-capping the bottle.*
 - *Cap reagent bottle and invert to mix.*
3. Open tubes and add 250 μL oxidizing reagent to each sample. Close tubes.
4. Set rack in hot water bath for 5 minutes.

Appendices

5. Remove rack and invert, shake, and tap the rack to settle foraminifera and remove bubbles. Ultrasonicate rack for a few seconds, then tap rack firmly and return to hot water bath.
6. Repeat steps 4 and 5.
7. Open tubes and top them off with DI H₂O for foram cleaning.
8. Clean pipette tip (3x 10% HCl and 3x DI H₂O), and siphon off oxidizing reagent.
9. Repeat steps 7 and 8 two more times.

Dilute Acid Leach

1. In the flow bench, clean a 1000 µL pipette tip (3x 10% HCl and 3x DI H₂O).
2. Add 250 µL 0.002 N HNO₃ to each tube. Because HNO₃ will dissolve carbonate, you may wish to use 0.001 N HNO₃ for small samples. You may also wish to skip ultrasonication and do fewer (or no) repetitions of the leach.
3. Tap the rack firmly and check for air bubbles. If necessary, tap some more.
4. Ultrasonicate the rack for 30 seconds.
5. Remove rack from bath. Invert, shake, and tap rack firmly to settle foraminifera.
6. Open tubes. While waiting for fragments to settle, clean pipette tip (3x 10% HCl and 3x DI H₂O).
7. Once fragments have settled, siphon off as much acid as possible.
8. Repeat steps 2-7 4x as quickly as possible to avoid dissolving your samples. To avoid systematic variations in the effectiveness of the acid leach, begin siphoning at a different row or side of the rack during each rinse step. Change the orientation of the rack in the sonic bath during each sonication.
9. Fill tubes and caps with DI H₂O for foraminifera cleaning. Close tubes.
10. Tap rack firmly, check for bubbles, and ultrasonicate for a few seconds.
11. Remove rack from bath. Invert, shake, and tap rack firmly to settle foraminifera.

Appendices

12. Turn on siphon and clean siphon tip (3x 10% HCl and 3x DI H₂O). Once foraminifera have settled, siphon caps and then siphon off as much water as possible from tubes.

13. Repeat steps 10-13.

14. Pipette off all remaining water using a clean (3x 10% HCl and 3x DI H₂O), 100 μ L pipette tip. It is important to remove as much water as possible. Use a new, freshly-cleaned tip for each sample.

Appendix 2: Column chemistry procedure used on samples from ODP Site 925

Dissolution of fish teeth samples

1. Using a clean 1000 μ l pipette tip, add 0.5ml of 1M HCl to each centrifuge tube of fish teeth sample.
2. Ultrasonicate samples until teeth have dissolved.
3. Make up a blank and STD (e.g. BCR-2 – a basaltic rock STD). Add 1.0ml of 1M HCl to each.
4. Once sufficiently ultrasonicated, add 0.5ml of 1M HCl to each 6ml Teflon vials. Add each sample to its respective Teflon vial.
5. Leave samples on a hot plate at 120°C overnight. By the following morning, samples should be dissolved. If they are not yet dissolved, alternate ultrasonication with the hot plate until they are. Always allow dissolved samples to cool before starting the next step. Increased temperature causes an increase in the K_D , thus you may decrease the Nd yield by using a sample at too high a temperature.

Separation stage one (REEs from matrix)

1. Columns are stored in 0.3M HCl. Carefully remove these using tweezers provided.
2. Wash columns through with 10ml (a full column) of 6M HCl. Gently add the first 1ml with a clean 1000 μ l pipette tip by holding the pipette tip close to, but not touching, the inside of the upper column and allowing the HCl to drip into the column. Use the squeeze bottle to top up to the 10ml mark. This avoids disturbing the resin too much.
3. Condition the columns by washing through with 2 x 0.5ml 1M HCl to ensure the column/resin is at the same concentration as the sample. Using a clean 1000 μ l pipette tip, add 0.5ml of 1M HCl and wait for that to drip through before adding a further 0.5ml of 1M HCl.
4. Using a clean, new 1000 μ l pipette tip for each sample, load the sample into the columns by adding 2 x 0.5ml (i.e. add 0.5ml to each column, then repeat). Drip the sample in gently straight down the middle of the column trying not to lose any droplets on the side of the column.
5. Wash the sample through by adding to the column, with a clean 1000 μ l pipette tip, 2 x 0.5ml of 1M HCl. Again, add 0.5ml of 1M HCl and wait for that to drip through before adding a further 0.5ml of 1M HCl.
6. In the meantime, label a new set of clean vials.
7. In stages, with a clean 1000 μ l pipette tip, add 0.5ml, 2.5ml and 4ml of 3M HCl to each column in order to elute the matrix. Add the 0.5ml in a

Appendices

gentle dripping fashion before adding the 2.5ml and 4ml portions more quickly. This is again to avoid disturbing the surface of the resin.

8. Using a clean pipette tip, add 0.5ml of 6M HCl to each column in a gentle dripping fashion.
9. Take two long, clean strips of parafilm. Remove the lids from the clean vials and place rim down on the parafilm. Place the vials on top of their respective lids and position underneath columns.
10. To each column, with a clean pipette tip, add 7ml (2 x 3.5ml), of 6M HCl. Allow this to drip through (15 – 30 minutes) and collect into the clean, labelled sample vials.
11. Put the sample vials onto the hot plate at approximately 120°C to evaporate the REE fraction. Before you leave for the end of the day, check the vials. If the sample has diminished by less than 50%, turn the hotplate down to 90°C. If the sample has diminished by more than 50%, turn the hotplate down to 70°C.

Each of the columns and resin now need to be washed before their next use.

12. Wash columns and resin through by adding, with a clean pipette tip, 2ml of DI water. Add this in a gentle, dripping fashion.
13. With a clean 1000µl pipette tip, add 1ml of 4M HNO₃. Add this in a gentle, dripping fashion before using the squeeze bottle to add a further 9ml of 4M HNO₃.
14. Repeat step 13.
15. With a clean 1000µl pipette tip, add 1ml of 6M HCl. Add this in a gentle, dripping fashion before using the squeeze bottle to add a further 9ml of 6M HCl.
16. With a clean 1000µl pipette tip, add 1ml of DI water. Add this in a gentle, dripping fashion before using the squeeze bottle to add a further 9ml of DI water.
17. Once columns are empty, with a clean 1000µl pipette tip, add 1ml of DI water to the top of the resin before placing columns back in their respective containers. Mark on the outside of the container that they been used an additional time. Columns are stored in 0.5M HCl. Do not allow the resin to dry out.

Separation stage two (Nd from REEs)

1. Before starting, the columns and resin need to be backflushed with DI water. Siphon up a full syringe of DI water. Ensure there are no air bubbles in the syringe or tube; otherwise these will become lodged in the resin. Attach the tube to the base of the column (an upside down pipette tip in the end of the tube allows it to slot on nicely). In a smooth and gradual motion, flush water through the column until the resin is sitting at the base of the main reservoir and astride the narrowing

Appendices

column. If air bubbles are present in the resin, do this step again. If air bubbles remain, extract them with a clean pipette tip. Allow the resin to settle for around 30 minutes.

2. Take samples off the hotplate and ensure they are fully evaporated. You will not be able to see any sample at the base of the vial; it will look virtually empty! Using a clean pipette tip, add 0.2ml of 0.2M HCl to each sample and ultrasonicate for up to 30 minutes.
3. When samples have finished ultrasonication, hold the vials up to the light. You will be able to find a spot of 'friction' that appears to 'catch' the droplet of acid in the bottom of the vial. This seemingly sticky point denotes the presence of your sample.
4. Ready the columns with the same concentration of acid as the forthcoming step by adding 1ml of 0.2M HCl. This can take up to 30 minutes to drip through.
5. Repeat step 4.
6. Using a clean, new pipette tip for each sample, add the sample to the column. The best way in which to do this is to first find the 'sticking point'. Take up the sample and, using the pipette tip, rinse around the vial. Repeat this process until the 'sticking point' is diminished and you are confident that you can pick up your sample in the pipette.
7. Wash the sample with 1.5ml of 0.2M HCl. Add this in a gentle, dripping fashion.
8. Repeat step 7.
9. Using a clean pipette tip, add 4ml of 0.2M HCl to each column. This will take approximately two and a quarter hours to drip through.
10. In the meantime, squirt 6M HCl into each empty sample vial and place onto a hotplate at approx. 120°C. This reflux will clean the vials before they are reused.
11. Remove cleaned vials from hotplate and pour away the 6M acid used to clean them.
12. Place the new vials underneath the columns and, using a clean pipette tip, add 3.5ml of 0.2M HCl. Collect this in the clean vials. This should take approximately 2 hours.
13. Place samples on the hot plate overnight at around 70°C.

Sample preparation and column cleaning

1. Backflush the columns with DI water. Siphon up a full syringe of DI water. Ensure there are no air bubbles in the syringe or tube; otherwise these will become lodged in the resin. Attach the tube to the base of the column (an upside down pipette tip in the end of the tube allows it to slot on nicely). In a smooth and gradual motion, flush water through the column until the resin is sitting at the base of the main reservoir and astride the narrowing column. If air bubbles are present

Appendices

in the resin, do this step again. If air bubbles remain, extract them with a clean pipette tip. Allow the resin to settle for around 30 minutes.

2. Add 10 drops (approximately 300 μ l) of concentrated HNO₃ to each sample. Reflux (lids on) on the hot plate at 120°C for approximately 30 minutes.
3. Remove lids from the sample and evaporate at 120°C. This takes approximately 1 hour.
4. Fill the columns with 6M HCl and allow to drip through. This will take approximately 2½ to 3 hours.
5. Once again, add 10 drops (approximately 300 μ l) of concentrated HNO₃ to each vial and reflux (lids on) on the hotplate at 120°C for 30 minutes.
6. After 30 minutes, remove the lids and allow to evaporate. The purpose of this step is to change the Nd from the chloride to a nitrate complex in preparation for the MC-ICP-MS.
7. Fill the columns with DI water and allow to drip through (approximately 2 ½ to 3 hours).
8. Once this water has passed through, add a few drops of DI water to the columns and place them back in their containers (in clean water). Make sure that the water level in the tube is higher than the water level in the column. Mark onto the outside of the tube to indicate a further use of the columns.

Appendix 3: Column chemistry procedure used on samples from ODP Site 1263 taken from McCoy-West *et al.* (2017).

Dissolution of fish teeth samples

1. Using a clean 1000 μ l pipette tip, add 0.5ml of 1M HCl to each centrifuge tube of fish teeth sample.
2. Ultrasonicate samples until teeth have mostly dissolved.
3. Make up a blank and STD (e.g. BCR-2 – a basaltic rock STD). Add 1.0ml of 1M HCl to each.
4. Once sufficiently ultrasonicated, add 0.5ml of 1M HCl to each 6ml Teflon vials. Add each sample to its respective Teflon vial.
5. Leave samples on a hot plate at 120°C overnight. By the following morning, samples should be dissolved. If they are not yet dissolved, alternate ultrasonication with the hot plate until they are. Always allow dissolved samples to cool before starting the next step. Increased temperature causes an increase in the K_D , thus you may decrease the Nd yield by using a sample at too high a temperature.

Separation stage one (REEs from matrix)

1. Clean cation columns sequentially with 2ml MQ (3x), 8ml 6M HCl (3x) and 8ml MQ (3x).
2. Condition columns with 6ml 1M HCl (x1).
3. Load 2ml 1M HCl (x1).
4. Wash columns sequentially with 5ml 1M HCl + 1M HF (x2), 6ml 2.5M HCl (x2) and 8ml 2M HNO₃ (x1).
5. Collect in 7ml 6M HCl (x2).

Separation stage two (Nd from REEs)

1. Clean columns with a full volume of MQ (x1), 3ml 6M HCl (x4) and a further full volume of MQ.
2. Condition columns with 3ml 0.2M HCl (x1).
3. Load samples in 0.5ml 0.2M HCl (x1).
4. Wash columns with 3ml 0.2M HCl (x2).
5. Collect in 3ml 0.2m HCl (x2)
6. Clean columns with a full volume of MQ (x1), 3ml 6M HCl (x1) and a further full volume of MQ (x2).

Appendix 4: Benthic foraminiferal stable isotope and trace element data from *Oridorsalis umbonatus* at IODP Site U1406. Age calibrated to Cande and Kent (1995).

Depth (mbsf)	Age (Ma)	Normalised $\delta^{13}\text{C}$ (‰VPDB) Mean	Normalised $\delta^{18}\text{O}$ (‰VPDB) Mean	Mg/Ca (mmolmol ⁻¹)	Li/Ca (μmolmol ⁻¹)	Sr/Ca (mmolmol ⁻¹)	Cd/Ca (μmolmol ⁻¹)	U/Ca (nmolmol ⁻¹)	Al/Ca (μmolmol ⁻¹)	Mn/Ca (μmolmol ⁻¹)	B/Ca (μmolmol ⁻¹)	Fe/Ca (μmolmol ⁻¹)
187.66	32.483	0.73	1.50	1.50	13.77	0.85	0.12	87.52	27.33	2135.11	46.21	335.08
187.69	32.486	0.87	1.70	1.56	11.77	0.86	0.12	36.21	60.75	1799.12	40.10	299.63
188.26	32.544	0.90	1.82	1.46	13.33	0.84	0.12	15.87	80.56	2258.33	35.70	358.08
188.29	32.547	0.49	1.47	1.35	13.16	0.82	0.12	8.77	32.80	2403.33	55.60	380.15
188.38	32.556	0.88	1.66	1.35	13.00	0.83	0.11	14.70	25.46	2324.28	31.50	363.46
188.53	32.571	0.81	1.73	1.65	13.56	0.80	0.13	11.54	11.54	3301.82	45.39	537.79
188.62	32.580	0.75	1.60	1.53	13.19	0.83	0.13	11.59	72.49	3001.72	45.38	449.88
188.65	32.584	0.82	1.64	1.39	12.74	0.82	0.13	14.15	25.78	2875.58	36.96	445.79
188.83	32.599	0.92	1.66	1.56	13.15	0.81	0.14	12.53	16.22	3205.33	33.35	544.75
189.04	32.623	0.80	1.82	1.50	13.19	0.81	0.14	35.24	9.11	3351.42	36.62	578.75
189.07	32.626	0.99	1.83	1.53	12.57	0.83	0.15	34.51	4.56	3597.24	43.95	613.12
189.16	32.636	0.87	1.73	1.54	12.80	0.83	0.14	75.14	11.41	3175.23	34.22	559.99
189.40	32.660	0.83	1.58	1.33	12.82	0.90	0.11	48.91	181.34	1345.22	54.19	245.92
189.46	32.666	0.74	1.51	1.45	13.28	0.86	0.12	19.07	12.14	2097.27	38.95	322.39
189.58	32.678	0.97	1.50	1.63	13.55	0.84	0.14	343.60	6.01	3068.46	71.81	433.21
189.64	32.684	0.89	1.71	1.56	13.28	0.91	0.11	177.17	9.61	1908.03	35.77	292.33
189.67	32.688	0.96	1.84	1.73	13.32	0.85	0.13	128.14	12.19	2641.86	37.45	433.38
190.54	32.776	0.89	1.72	1.64	12.54	0.80	0.18	18.66	11.79	3672.34	37.10	501.40
190.57	32.779	0.96	1.70	1.89	12.04	0.79	0.17	24.54	93.49	4257.84	51.61	2823.04
190.60	32.782	0.96	1.70	1.61	12.46	0.79	0.13	20.20	18.43	3693.07	36.55	457.57
191.20	32.843	1.16	1.77	1.50	10.87	0.82	0.16	24.21	29.11	3470.53	52.22	456.57
191.83	32.908	0.78	1.42	1.67	12.83	0.86	0.15	41.94	6.90	2596.44	33.25	326.05
192.46	32.972	0.80	1.66	1.80	12.19	0.79	0.17	21.47	472.58	3906.41	46.29	537.99
195.39	33.119	1.31	1.89	1.45	13.41	0.86	0.11	54.12	12.76	3175.32	34.22	364.84
196.56	33.189	1.07	2.00	1.60	10.59	0.87	0.12	76.59	42.87	3066.31	45.11	382.26

196.59	33.191	1.10	2.08	1.62	9.54	0.86	0.11	69.91	27.13	3271.41	49.01	397.91
196.71	33.198	1.25	2.05	1.53	12.77	0.81	0.12	72.66	17.19	4032.19	32.09	496.20
196.77	33.201	1.22	2.03	1.68	12.89	0.80	0.13	86.97	5.18	4223.42	32.69	543.05
196.80	33.203	1.33	1.92	1.62	14.05	0.82	0.14	92.58	14.59	3722.91	34.42	477.41
196.89	33.209	1.37	1.92	1.58	13.69	0.85	0.12	66.54	33.33	2976.72	32.98	366.23
196.92	33.210	1.37	1.90	1.56	13.26	0.85	0.13	77.35	6.63	2895.64	37.16	392.94
196.98	33.214	1.33	2.00	1.55	13.05	0.83	0.19	70.09	25.65	3535.95	39.15	454.87
197.01	33.216	1.13	1.95	1.62	13.63	0.85	0.12	87.14	6.86	3373.98	33.51	442.98
197.04	33.218	1.21	1.97	1.44	13.08	0.86	0.11	83.73	23.12	2824.35	35.17	323.84
197.07	33.219	1.33	1.95	1.67	13.37	0.85	0.12	89.86	4.17	3378.54	33.58	417.96
197.1	33.221	1.21	1.90	1.47	14.36	0.87	0.11	92.89	12.44	2870.89	33.29	313.58
197.13	33.223	1.22	2.00	1.37	13.43	0.86	0.13	133.99	10.00	2455.57	36.14	286.04
197.22	33.228	1.16	2.08	1.46	13.58	0.84	0.12	239.24	9.70	3093.98	33.68	358.78
197.28	33.232	1.16	2.06	1.46	13.94	0.85	0.13	531.27	12.99	3321.62	35.01	350.60
197.31	33.234	1.25	2.12	1.36	12.39	0.86	0.11	307.88	15.38	2173.64	31.93	268.96
197.34	33.235	1.22	2.12	1.52	14.28	0.87	0.12	406.77	11.43	2362.02	38.66	281.09
197.37	33.237	1.23	1.99	1.49	13.61	0.84	0.20	402.62	12.66	3604.07	31.49	374.54
197.40	33.239	1.22	2.09	1.55	12.93	0.80	0.15	477.99	12.57	4823.23	30.84	506.72
197.43	33.241	1.21	1.94	1.58	12.94	0.81	0.12	346.86	18.61	4367.50	31.31	465.71
197.46	33.243	1.18	2.07	1.57	13.15	0.80	0.16	441.70	16.41	5077.89	34.77	557.73
197.49	33.244	1.00	1.97	1.58	13.51	0.86	0.12	331.40	26.13	3478.03	40.08	343.66
197.52	33.246	1.13	2.01	1.58	12.59	0.83	0.13	366.96	47.04	3888.49	37.26	469.27
197.58	33.250	1.22	1.99	1.46	13.36	0.83	0.13	303.51	14.87	3750.25	31.93	384.66
197.61	33.252	1.07	2.04	1.50	12.54	0.82	0.13	341.38	18.46	4347.24	30.78	448.45
197.67	33.255	1.31	2.08	1.45	13.29	0.84	0.14	385.71	11.47	3636.05	29.07	388.60
197.7	33.257	1.17	2.03	1.47	13.73	0.83	0.13	429.08	12.76	4200.23	33.53	419.21
197.73	33.259	1.19	2.13	1.46	13.83	0.86	0.14	406.09	15.53	3147.46	33.80	329.15
197.76	33.260	1.21	2.06	1.47	13.61	0.84	0.12	453.68	22.80	3159.23	34.11	371.26
197.79	33.262	1.09	2.00	1.48	13.34	0.84	0.13	265.18	13.29	3251.93	33.19	367.20
197.82	33.264	0.98	2.05	1.30	13.17	0.85	0.13	271.64	10.32	2758.40	34.23	316.94

197.88	33.268	1.13	2.00	1.62	13.19	0.81	0.12	193.97	11.84	4404.60	34.35	556.21
197.91	33.269	1.27	1.78	1.46	12.03	0.84	0.13	156.25	10.69	3959.98	35.18	449.38
197.94	33.271	1.35	1.84	1.63	12.37	0.80	0.15	117.60	5.77	4578.04	29.48	595.21
197.97	33.273	1.14	1.90	1.48	13.48	0.86	0.13	104.00	16.90	3147.36	32.83	377.48
198.03	33.277	1.31	1.95	1.48	13.30	0.86	0.12	98.87	13.22	3027.61	31.25	417.43
198.06	33.278	1.25	1.87	1.53	13.39	0.84	0.12	127.36	60.56	2978.78	34.64	362.07
198.09	33.280	1.07	1.86	1.50	13.13	0.85	0.13	132.53	10.71	3183.81	32.12	376.39
198.12	33.282	1.20	1.82	1.51	12.98	0.85	0.14	151.13	18.16	3340.01	30.80	386.91
198.18	33.286	1.15	1.76	1.50	13.66	0.85	0.14	136.41	9.05	2729.46	34.16	324.89
198.21	33.287	1.13	1.78	1.57	12.51	0.85	0.13	126.07	10.23	2952.25	36.99	348.72
198.24	33.289	1.12	1.78	1.48	13.55	0.87	0.11	94.20	8.10	2097.27	38.59	261.23
198.27	33.291	1.06	1.70	1.71	12.93	0.81	0.12	129.41	12.81	4290.82	36.63	607.93
198.3	33.293	1.06	1.86	1.44	13.64	0.92	0.10	91.09	9.88	2882.00	33.11	346.52
198.33	33.294	1.32	1.78	1.48	15.17	0.91	0.13	122.93	4.00	2947.91	32.04	335.83
198.36	33.296	1.18	1.84	1.66	12.90	0.85	0.13	247.99	15.55	3953.49	30.28	488.76
198.39	33.298	1.27	2.01	1.48	13.42	0.87	0.11	291.00	23.71	2915.93	34.32	351.51
198.42	33.300	1.31	1.93	1.48	13.20	0.84	0.12	275.05	12.67	3474.72	34.80	390.91
198.46	33.302	1.26	1.96	1.47	13.02	0.85	0.12	240.09	16.21	3431.46	32.63	382.54
198.49	33.304	1.19	1.98	1.61	14.00	0.82	0.12	190.07	15.56	3929.91	36.59	457.01
198.52	33.306	1.27	1.98	1.60	13.30	0.84	0.12	124.10	11.14	3781.12	30.70	427.10
198.55	33.308	1.29	1.82	1.63	12.98	0.80	0.12	216.84	10.74	4088.61	37.29	540.97
198.58	33.309	1.27	2.01	1.49	13.99	0.87	0.12	168.53	3.65	2613.31	38.18	396.03
198.61	33.311	1.19	1.96	1.45	13.24	0.86	0.13	351.27	22.31	3069.02	36.16	329.15
198.64	33.313	1.19	2.15	1.46	13.50	0.87	0.13	500.23	13.76	2888.60	35.38	330.07
198.67	33.315	1.07	1.85	1.41	13.31	0.88	0.13	246.59	9.25	2868.79	32.93	298.38
198.70	33.317	1.18	1.89	1.64	13.18	0.82	0.14	135.69	24.97	4061.26	38.84	530.81
198.73	33.318	1.04	1.85	1.46	13.42	0.85	0.12	203.05	548.46	3046.91	31.60	353.45
198.76	33.320	1.20	1.74	1.56	13.30	0.85	0.13	140.04	16.18	3144.73	33.61	371.29
198.79	33.322	1.23	1.75	1.57	13.71	0.87	0.12	92.49	18.32	2680.60	30.95	305.24
198.82	33.324	0.93	1.70	1.48	13.24	0.87	0.11	117.61	10.29	2758.43	31.99	309.03

198.85	33.326	1.13	1.81	1.50	12.66	0.87	0.12	117.79	13.10	2688.11	29.15	333.32
198.88	33.327	1.15	1.74	1.63	14.01	0.86	0.12	81.96	59.01	2885.12	36.88	379.92
198.91	33.329	1.00	1.74	1.57	13.04	0.87	0.12	84.30	231.50	2717.31	38.34	345.10
198.94	33.331	1.21	1.70	1.58	12.48	0.86	0.11	89.72	16.01	2917.37	31.04	369.42
198.97	33.333	1.12	1.69	1.43	12.24	0.85	0.11	116.71	33.72	2749.18	36.40	319.23
196.07	33.429	1.11	1.96	1.48	13.16	0.85	0.13	248.88	18.15	2607.89	36.57	427.53
196.73	33.468	1.14	1.62	1.67	12.40	0.84	0.16	167.69	6.26	4054.22	34.71	507.91
197.39	33.507	1.31	1.91	1.51	9.03	0.81	0.12	116.85	29.87	3435.70	37.38	471.08
197.48	33.513	1.31	1.83	1.57	13.38	0.86	0.12	115.44	20.52	3018.05	46.84	349.45
197.81	33.532	0.61	1.77	1.67	12.56	0.84	0.12	171.55	105.87	3831.63	36.88	479.70
198.53	33.629	0.81	0.96	1.52	12.16	0.83	0.14	150.38	11.21	3767.56	28.76	489.92
199.17	33.734	0.87	1.01	1.39	12.59	0.87	0.12	42.40	24.52	2644.54	29.75	343.99
199.20	33.739	0.87	0.90	1.52	13.14	0.86	0.12	53.21	22.08	2535.03	36.86	306.70
199.23	33.744	0.79	0.66	1.57	10.76	0.85	0.13	32.16	14.28	2821.70	35.56	436.27
199.26	33.749	0.59	0.85	1.69	12.02	0.84	0.14	38.92	66.77	3680.99	29.18	535.45
199.29	33.754	0.75	0.79	1.62	12.53	0.86	0.14	47.22	21.44	2634.82	34.45	291.52
199.47	33.784	0.92	0.97	1.47	12.64	0.84	0.14	75.81	8.19	3040.71	34.99	347.95
199.62	33.809	0.57	0.86	1.93	13.55	0.88	0.11	28.34	168.79	2046.81	50.32	454.25
199.77	33.833	0.67	0.79	1.41	11.67	0.85	0.11	32.23	10.58	2933.99	30.34	417.46
199.8	33.838	0.59	0.93	1.48	10.33	0.80	0.12	27.82	18.89	3663.08	26.70	457.93
199.83	33.843	0.77	1.16	1.51	10.98	0.79	0.12	30.78	10.01	4626.82	31.32	570.35
199.86	33.848	0.80	0.95	1.46	12.21	0.82	0.12	27.44	25.58	3593.36	34.82	452.94
199.89	33.853	0.83	1.04	1.37	11.23	0.84	0.11	27.97	20.86	2936.47	29.94	363.44
199.92	33.858	0.83	0.84	1.26	12.19	0.87	0.11	41.40	4.70	2119.52	30.74	235.83
199.98	33.868	0.68	0.70	2.14	12.67	0.87	0.10	44.56	26.67	2197.89	42.18	300.69
200.01	33.873	0.84	0.80	1.57	12.72	0.88	0.11	73.75	12.47	2749.20	35.88	361.89
200.07	33.883	0.83	0.84	1.56	11.44	0.88	0.11	50.08	16.68	3067.99	48.94	402.74
200.13	33.892	0.62	0.91	1.72	14.15	0.84	0.12	27.95	57.20	3330.91	34.34	556.70
200.16	33.897	0.77	0.87	1.37	12.32	0.87	0.10	25.80	15.03	2115.93	34.59	302.06
200.22	33.907	0.77	0.80	1.37	10.88	0.84	0.12	28.41	24.52	2634.20	65.09	181.78

200.31	33.922	0.81	1.06	1.35	11.39	0.84	0.11	25.67	7.38	3107.47	31.82	438.64
200.34	33.927	0.76	1.08	1.35	11.62	0.82	0.10	23.36	79.34	3117.41	28.51	470.29
200.37	33.932	0.79	0.98	1.55	12.07	0.83	0.18	36.03	8.43	3459.61	28.80	447.48
200.40	33.937	0.83	0.90	1.42	11.37	0.84	0.13	31.55	19.26	3160.45	49.12	368.87
200.43	33.942	0.80	0.96	1.49	12.29	0.86	0.11	30.06	16.69	2330.71	31.80	304.06
200.49	33.952	0.78	0.76	1.39	10.79	0.91	0.11	41.52	34.55	1544.59	28.43	172.26
200.52	33.957	0.79	0.80	1.47	14.36	0.86	0.14	39.18	21.07	2323.41	36.77	258.72
200.61	33.972	0.68	0.84	1.57	11.93	0.81	0.12	30.84	14.96	3903.00	29.74	546.35
200.73	33.991	0.85	1.07	1.49	12.71	0.83	0.12	28.58	20.70	3325.29	30.90	435.42
200.76	33.996	0.84	1.20	1.30	11.93	0.86	0.12	29.71	11.16	2673.50	31.70	314.02
201.00	34.036	0.50	0.68	1.54	12.52	0.86	0.13	29.45	12.93	2350.38	47.05	297.64
201.03	34.041	0.61	0.82	2.11	16.38	0.89	0.13	28.71	364.38	2050.89	117.03	439.27
201.09	34.051	0.60	0.77	1.62	11.95	0.91	0.11	35.39	14.21	2229.00	53.15	276.44
201.21	34.070	0.75	0.95	1.62	13.15	0.97	0.11	34.33	48.97	1820.91	237.66	328.31
201.54	34.125	0.50	0.99	1.41	11.80	0.83	0.11	24.41	7.17	3223.55	31.88	566.99
201.57	34.130	0.72	1.03	1.51	12.25	0.85	0.11	25.51	74.81	2757.47	49.63	391.78
202.33	34.321	0.82	0.96	1.42	11.99	0.88	0.10	27.88	14.32	1583.11	44.30	218.72
202.96	34.423	0.68	1.14	1.42	10.79	0.78	0.09	24.06	12.14	3665.32	25.77	600.15
204.22	34.630	0.83	0.99	1.58	11.05	0.78	0.13	21.16	11.15	4595.51	30.05	723.17
204.88	34.740	0.86	1.07	1.37	13.00	0.87	0.10	26.66	14.12	1698.45	33.92	204.41
205.51	34.846	0.49	1.08	1.32	9.25	0.87	0.09	23.98	82.36	1276.87	41.09	157.41
206.89	35.077	0.77	0.57	1.45	12.61	0.87	0.13	26.62	23.22	2022.04	36.09	279.40
207.28	35.142	1.07	0.78	1.34	11.77	0.82	0.13	14.83	34.74	2522.34	41.63	334.78
203.99	35.196	1.04	0.75	1.37	12.11	0.83	0.13	14.41	13.27	2989.22	32.64	373.78
204.56	35.291	1.10	0.75	1.46	12.96	0.84	0.13	14.97	18.84	2559.73	36.63	306.66
206.48	35.612	1.08	0.81	1.50	13.38	0.84	0.13	30.39	19.20	2310.83	35.27	297.96
190.3		1.11	1.95	1.47	13.56	0.87	0.13	340.25	29.23	2849.23	35.29	307.01

Appendices

Appendix 5: Benthic foraminiferal Mg/Ca-derived temperatures corrected for Mg/Ca_{sw} using the approach of Lear *et al.* (2015) from *Oridorsalis umbonatus* at IODP Site U1406. Age calibrated to Cande and Kent (1995).

Depth (mbsf)	Age (Ma)	Mg/Ca (mmolmol ⁻¹)	Mn-Corrected Mg/Ca (mmolmol ⁻¹)	Mg/Casw (molmol ⁻¹)	Temperature (°C)
187.660	32.483	1.50	1.28	2.1609	2.45
187.690	32.486	1.56	1.38	2.1608	2.95
188.260	32.544	1.46	1.23	2.1597	2.11
188.290	32.547	1.35	1.11	2.1597	1.19
188.380	32.556	1.35	1.12	2.1595	1.19
188.530	32.571	1.65	1.32	2.1592	3.70
188.620	32.580	1.53	1.23	2.1590	2.70
188.650	32.584	1.39	1.10	2.1589	1.53
188.830	32.599	1.56	1.24	2.1586	2.95
189.040	32.623	1.50	1.16	2.1582	2.45
189.070	32.626	1.53	1.17	2.1581	2.70
189.160	32.636	1.54	1.22	2.1579	2.78
189.400	32.660	1.33	1.20	2.1575	1.03
189.460	32.666	1.45	1.24	2.1573	2.03
189.580	32.678	1.63	1.32	2.1571	3.53
189.640	32.684	1.56	1.37	2.1570	2.95
189.670	32.688	1.73	1.47	2.1569	4.37
190.540	32.776	1.64	1.27	2.1552	3.61
190.570	32.779	1.89	1.46	2.1552	5.70
190.600	32.782	1.61	1.24	2.1551	3.36
191.200	32.843	1.50	1.15	2.1539	2.45
191.830	32.908	1.67	1.41	2.1527	3.87
192.460	32.972	1.80	1.41	2.1514	4.95
195.390	33.119	1.45	1.14	2.1486	2.03
196.560	33.189	1.60	1.29	2.1472	3.28
196.590	33.191	1.62	1.29	2.1472	3.45
196.710	33.198	1.53	1.12	2.1471	2.70
196.770	33.201	1.68	1.26	2.1470	3.95
196.800	33.203	1.62	1.25	2.1470	3.45
196.890	33.209	1.58	1.28	2.1469	3.11
196.920	33.210	1.56	1.27	2.1468	2.95
196.980	33.214	1.55	1.20	2.1468	2.86
197.010	33.216	1.62	1.29	2.1467	3.45
197.040	33.218	1.44	1.16	2.1467	1.94
197.070	33.219	1.67	1.34	2.1466	3.87
197.100	33.221	1.47	1.18	2.1466	2.19
197.130	33.223	1.37	1.12	2.1466	1.36
197.220	33.228	1.46	1.15	2.1465	2.11
197.280	33.232	1.46	1.12	2.1464	2.11
197.310	33.234	1.36	1.14	2.1464	1.28
197.340	33.235	1.52	1.28	2.1463	2.61

Appendices

197.370	33.237	1.49	1.13	2.1463	2.36
197.400	33.239	1.55	1.07	2.1463	2.86
197.430	33.241	1.58	1.14	2.1462	3.11
197.460	33.243	1.57	1.06	2.1462	3.03
197.490	33.244	1.58	1.23	2.1462	3.11
197.520	33.246	1.58	1.19	2.1461	3.11
197.580	33.250	1.46	1.08	2.1461	2.11
197.610	33.252	1.50	1.06	2.1460	2.45
197.670	33.255	1.45	1.08	2.1460	2.03
197.700	33.257	1.47	1.05	2.1459	2.19
197.730	33.259	1.46	1.14	2.1459	2.11
197.760	33.260	1.47	1.16	2.1459	2.19
197.790	33.262	1.48	1.15	2.1458	2.28
197.820	33.264	1.30	1.03	2.1458	0.77
197.880	33.268	1.62	1.18	2.1457	3.45
197.910	33.269	1.46	1.06	2.1457	2.11
197.940	33.271	1.63	1.17	2.1456	3.53
197.970	33.273	1.48	1.17	2.1456	2.28
198.030	33.277	1.48	1.17	2.1455	2.28
198.060	33.278	1.53	1.23	2.1455	2.70
198.090	33.280	1.50	1.18	2.1455	2.45
198.120	33.282	1.51	1.18	2.1454	2.53
198.180	33.286	1.50	1.23	2.1454	2.45
198.210	33.287	1.57	1.28	2.1453	3.03
198.240	33.289	1.48	1.27	2.1453	2.28
198.270	33.291	1.71	1.28	2.1453	4.20
198.300	33.293	1.44	1.15	2.1452	1.94
198.330	33.294	1.48	1.19	2.1452	2.28
198.360	33.296	1.66	1.27	2.1452	3.78
198.390	33.298	1.48	1.19	2.1451	2.28
198.420	33.300	1.48	1.13	2.1451	2.28
198.460	33.302	1.47	1.12	2.1450	2.19
198.490	33.304	1.61	1.21	2.1450	3.36
198.520	33.306	1.60	1.22	2.1450	3.28
198.550	33.308	1.63	1.22	2.1449	3.53
198.580	33.309	1.49	1.23	2.1449	2.36
198.610	33.311	1.45	1.15	2.1449	2.03
198.640	33.313	1.46	1.17	2.1448	2.11
198.670	33.315	1.41	1.12	2.1448	1.69
198.700	33.317	1.64	1.23	2.1448	3.61
198.730	33.318	1.46	1.15	2.1447	2.11
198.760	33.320	1.56	1.24	2.1447	2.95

Appendices

198.790	33.322	1.57	1.30	2.1447	3.03
198.820	33.324	1.48	1.21	2.1446	2.28
198.850	33.326	1.50	1.23	2.1446	2.45
198.880	33.327	1.63	1.34	2.1446	3.53
198.910	33.329	1.57	1.30	2.1445	3.03
198.940	33.331	1.58	1.29	2.1445	3.11
198.970	33.333	1.43	1.16	2.1445	1.86
196.070	33.429	1.48	1.22	2.1426	2.28
196.730	33.468	1.67	1.26	2.1418	3.87
197.390	33.507	1.51	1.17	2.U1411	2.53
197.480	33.513	1.57	1.26	2.1410	3.03
197.810	33.532	1.67	1.29	2.U1406	3.87
198.530	33.629	1.52	1.14	2.1387	2.61
199.170	33.734	1.39	1.12	2.1367	1.53
199.200	33.739	1.52	1.27	2.1366	2.61
199.230	33.744	1.57	1.28	2.1365	3.03
199.260	33.749	1.69	1.32	2.1364	4.03
199.290	33.754	1.62	1.36	2.1363	3.45
199.470	33.784	1.47	1.17	2.1357	2.19
199.620	33.809	1.93	1.72	2.1352	6.04
199.770	33.833	1.41	1.12	2.1348	1.69
199.800	33.838	1.48	1.11	2.1347	2.28
199.830	33.843	1.51	1.04	2.1346	2.53
199.860	33.848	1.46	1.10	2.1345	2.11
199.890	33.853	1.37	1.08	2.1344	1.36
199.920	33.858	1.26	1.05	2.1343	0.44
200.010	33.883	1.57	1.30	2.1338	3.03
200.070	33.892	1.56	1.25	2.1336	2.95
200.130	33.897	1.72	1.39	2.1335	4.28
200.160	33.907	1.37	1.16	2.1333	1.36
200.220	33.922	1.37	1.11	2.1330	1.36
200.310	33.927	1.35	1.04	2.1329	1.19
200.340	33.932	1.35	1.04	2.1328	1.19
200.370	33.937	1.55	1.20	2.1327	2.86
200.400	33.942	1.42	1.10	2.1326	1.78
200.430	33.952	1.49	1.25	2.1325	2.36
200.490	33.957	1.39	1.24	2.1324	1.53
200.520	33.972	1.47	1.23	2.1321	2.19
200.610	33.991	1.57	1.18	2.1317	3.03
200.730	33.996	1.49	1.16	2.1316	2.36
200.760	34.041	1.30	1.04	2.1307	0.77
201.000	34.051	1.54	1.91	2.1305	2.78
201.090	34.125	1.62	1.40	2.1291	3.45
201.210	34.130	1.62	1.44	2.1290	3.45
201.540	34.321	1.41	1.08	2.1252	1.69
201.570	34.423	1.51	1.23	2.1232	2.53

Appendices

202.330	34.630	1.42	1.26	2.1191	1.78
202.960	34.740	1.42	1.05	2.1170	1.78
204.220	34.846	1.58	1.12	2.1149	3.11
204.880	35.077	1.37	1.20	2.1102	1.36
205.510	35.142	1.32	1.19	2.1089	0.94
206.890	35.196	1.45	1.25	2.1078	2.03
207.280	35.291	1.34	1.09	2.1059	1.11
203.990	35.612	1.37	1.07	2.0993	1.36
204.560	35.291	1.46	1.20	2.1059	2.11
206.480	35.612	1.50	1.26	2.0993	2.44

Appendix 6: Benthic foraminiferal stable isotope and trace element data from *Oridorsalis umbonatus* at ODP Site 925. Age calibrated to Cande and Kent (1995).

Depth (mbsf)	Age (Ma)	Mg/Ca (mmolmol ⁻¹)	Li/Ca (μ molmol ⁻¹)	Sr/Ca (mmolmol ⁻¹)	Cd/Ca (μ molmol ⁻¹)	U/Ca (nmolmol ⁻¹)	Al/Ca (μ molmol ⁻¹)	Mn/Ca (μ molmol ⁻¹)	B/Ca (μ molmol ⁻¹)	Fe/Ca (μ molmol ⁻¹)
746.45	32.83	3.30	9.38	0.85	0.06	115.05	44.83	891.56	17.04	9408.91
747.50	32.85	3.18	9.00	0.86	0.09	45.05	97.43	880.26	20.49	7548.14
748.07	32.87	3.04	9.08	0.89	0.08	47.51	172.90	909.01	16.61	8642.91
748.73	32.89	3.25	8.68	0.87	0.07	18.44	12.79	960.40	16.88	8695.83
750.22	32.93	2.60	10.69	0.85	0.15	107.53	992.75	936.62	26.90	4528.10
757.13	33.12	3.45	9.78	0.84	0.08	114.00	29.75	1188.16	24.07	9289.05
758.91	33.17	2.60	12.29	0.92	0.14	72.46	1158.88	1234.24	27.48	4441.58
761.84	33.25	3.67	9.06	0.86	0.05	13.10	100.15	1246.65	25.11	11203.73
764.64	33.33	3.05	9.58	0.85	0.11	64.15	225.59	1117.71	17.27	8680.26
768.26	33.43	3.75	8.97	0.76	0.08	77.34	16.47	1490.77	14.10	12297.40
769.75	33.47	3.52	9.97	0.75	0.06	179.07	75.73	1347.60	23.83	11949.36
771.21	33.51	2.54	10.51	0.84	0.09	120.32	252.74	1279.46	22.52	5744.23
782.69	33.82	2.37	9.30	0.87	0.06	23.79	468.26	538.14	23.98	4433.69
785.88	33.91	3.66	9.21	0.82	0.05	22.98	82.50	836.72	22.42	9912.89
789.65	34.01	2.57	9.03	0.81	0.08	50.51	54.84	654.40	21.19	5685.71
792.72	34.10	3.04	9.36	0.83	0.12	90.87	74.61	816.29	20.04	7243.09
795.95	34.19	2.84	9.51	0.80	0.07	74.10	25.52	707.46	18.52	6769.77
798.02	34.24	2.19	9.97	0.95	0.10	45.16	94.68	575.29	20.44	2554.32
798.97	34.27	3.81	8.34	0.81	0.04	134.35	30.54	1134.46	12.71	12226.29
807.06	34.49	2.82	12.68	0.93	1.84	103.39	1172.64	893.14	63.41	5976.78
808.56	34.53	2.64	9.17	0.88	0.07	106.02	269.70	791.01	22.11	5539.12
810.06	34.57	3.29	9.30	0.83	0.18	71.02	306.29	1087.37	15.40	9833.47
811.41	34.61	2.79	9.84	0.91	0.08	42.53	540.34	629.47	32.73	5792.09
813.71	34.68	2.26	9.94	0.92	0.08	66.05	72.33	734.00	20.51	3096.58
815.16	34.71	2.35	10.17	0.95	0.10	72.12	913.10	679.26	21.52	3377.68
836.08	35.29	3.16	8.66	0.86	0.09	65.57	143.39	734.15	24.02	7143.66

Appendix 7: Benthic foraminiferal stable isotope and trace element data from *Cibicidoides havanensis* at ODP Site 925. Age calibrated to Cande and Kent (1995).

Depth (mbsf)	Age (Ma)	$\delta^{18}\text{O}$ (‰VPDB)	Mg/Ca (mmolmol ⁻¹)	Li/Ca (μmolmol^{-1})	Sr/Ca (mmolmol ⁻¹)	Cd/Ca (μmolmol^{-1})	U/Ca (nmolmol ⁻¹)	Al/Ca (μmolmol^{-1})	Mn/Ca (μmolmol^{-1})	B/Ca (μmolmol^{-1})	Fe/Ca (μmolmol^{-1})
746.45	32.83	0.04	1.97	12.95	1.03	0.09	79.07	36.21	549.63	134.39	3210.72
747.50	32.85	0.15	1.77	13.90	1.04	0.12	72.43	115.58	804.80	129.07	2395.98
748.07	32.87	0.48	2.12	13.76	1.06	0.10	44.01	315.12	652.87	127.19	3378.01
748.73	32.89	0.48	2.17	12.57	1.05	0.11	21.98	189.74	714.97	130.89	3434.17
750.22	32.93	-0.47	2.32	10.80	0.94	0.14	115.64	184.17	1002.47	96.08	5598.87
753.01	33.01	0.60	1.94	12.98	1.10	0.09	26.13	271.43	761.66	132.60	3120.79
757.13	33.12	-0.04	2.36	11.50	1.06	0.10	74.44	133.30	846.50	118.15	5185.51
758.91	33.17	0.22	2.36	12.89	1.00	0.12	49.15	317.55	1041.09	129.26	4123.83
760.37	33.21	0.10	2.10	13.04	1.04	0.08	22.07	153.41	764.40	125.82	3334.85
761.84	33.25	0.11	2.32	13.18	1.06	0.07	12.87	99.07	778.66	125.66	4243.99
763.53	33.30	0.27	1.97	13.28	1.05	0.10	133.77	405.09	877.00	129.45	3480.43
764.64	33.33	-0.48	2.37	13.71	1.04	0.15	60.48	435.86	957.49	119.36	4951.63
768.26	33.43	-0.01	2.02	11.80	1.06	0.08	63.66	95.36	924.57	124.66	3954.79
769.75	33.47	0.47	1.93	12.47	1.07	0.10	92.08	36.25	839.32	127.11	3460.84
771.21	33.51	-0.23	1.82	13.06	1.05	0.08	81.66	92.83	914.27	134.91	3379.39
775.61	33.63	-0.62	2.17	11.58	0.93	0.07	895.88	49.78	944.60	101.53	4773.81
776.62	33.66	-0.37	2.24	11.31	0.97	0.09	38.53	48.54	833.20	106.72	4512.23
778.17	33.70	-0.07	2.18	12.50	1.02	0.10	45.60	96.90	709.96	115.43	4392.30
779.67	33.74	-0.13	2.27	12.62	1.03	0.05	18.38	94.99	590.23	121.18	4053.08
781.17	33.78	-0.34	2.01	13.95	1.11	0.05	73.24	31.09	532.24	138.82	2646.41
782.69	33.82	-0.70	2.15	13.05	1.03	0.07	30.36	95.55	520.70	123.12	3261.36
784.17	33.86	-0.18	1.93	13.11	1.07	0.05	14.22	43.60	426.12	125.42	3050.74
785.88	33.91	-1.00	2.26	11.92	1.00	0.08	22.87	130.40	505.11	109.87	4630.13
787.87	33.96	-0.49	1.90	11.89	0.98	0.11	54.49	72.17	545.84	103.32	3421.58

789.65	34.01		3.33	9.57	0.83	0.08	61.43	47.67	736.81	79.09	7052.47
790.87	34.05	-0.27	2.20	11.25	0.91	0.08	70.06	39.40	660.28	95.34	4443.67
792.72	34.10	-0.36	2.04	12.42	1.03	0.07	58.59	62.10	502.78	112.98	3536.39
793.87	34.13	-0.07	1.80	12.64	0.98	0.10	60.08	77.46	689.30	118.23	1801.00
798.02	34.24	-0.73	1.97	12.92	1.03	0.09	47.38	161.10	609.34	118.12	3378.20
798.97	34.27		2.59	12.05	1.01	0.09	76.88	182.68	742.36	107.85	5096.75
801.98	34.35		2.04	14.09	1.07	0.12	39.61	260.01	727.79	121.13	3350.99
803.47	34.39	-0.34	2.08	12.99	1.09	0.10	33.16	330.46	648.66	119.46	3190.54
805.57	34.45	-0.85	2.20	12.12	1.01	0.06	54.55	315.32	679.37	106.18	3963.15
807.06	34.49	-0.27	2.13	12.89	1.02	0.11	69.84	493.11	857.67	112.76	3724.59
808.56	34.53		2.09	12.86	1.02	0.12	81.84	243.15	730.66	102.50	3525.50
810.06	34.57	-0.46	2.37	13.71	1.01	0.12	45.85	440.91	676.65	108.92	3304.05
811.41	34.61	-0.77	2.32	11.79	1.00	0.07	37.51	212.95	583.01	103.19	4378.24
813.71	34.68	-0.35	2.28	12.24	1.05	0.05	47.29	85.18	719.62	108.15	3677.34
814.40	34.69	-0.37	2.05	18.11	1.05	0.18	55.04	1417.57	733.52	112.77	1686.89
815.16	34.71	-0.27	2.24	14.73	1.07	0.09	74.97	752.17	627.67	126.89	3543.67
816.65	34.76	-0.30	2.21	12.23	1.04	0.09	58.35	250.53	581.14	118.16	3543.32
819.67	34.84	-1.03	2.33	10.87	1.01	0.07	33.38	93.18	546.81	100.84	4053.78
821.56	34.89	-0.17	1.87	12.81	1.07	0.06	39.69	27.39	429.59	128.16	2242.31
824.13	34.96	-0.55	1.83	13.27	1.05	0.08	33.03	84.63	407.88	116.20	2340.81
829.39	35.11	0.06	2.32	12.84	1.04	0.11	65.63	192.00	525.80	117.24	3495.21
830.88	35.15	-0.60	2.19	11.66	1.02	0.06	44.38	172.85	532.45	105.33	4216.83
832.37	35.19	-0.36	2.02	12.09	1.03	0.08	35.71	95.89	494.68	117.11	2719.48
834.56	35.25	-0.27	2.42	11.35	0.96	0.15	45.85	100.57	621.03	97.39	4520.43
836.08	35.29	-0.81	2.35	11.34	0.99	0.09	51.31	151.16	567.71	108.68	4359.07
839.08	35.37	-0.49	2.39	12.29	1.06	0.06	39.22	46.40	523.84	117.73	3773.24
844.19	35.51	-0.35	2.42	10.70	0.99	0.06	34.80	56.59	528.81	106.71	4218.08
847.15	35.59	-0.56	1.97	11.39	1.05	0.06	36.40	18.42	347.74	116.57	2774.99
850.15	35.68	-0.68	2.28	11.41	1.03	0.08	25.02	155.87	527.85	119.13	4301.26

Appendices

Appendix 8: ϵNd from fossil fish teeth at ODP Site 925. Age calibrated to Cande and Kent (1995).

Depth (mbsf)	Age (Ma)	ϵNd
747.50	32.85	-12.99
748.73	32.89	-14.06
764.64	33.33	-13.54
768.26	33.43	-13.44
771.21	33.51	-13.84
772.93	33.55	-15.07
778.17	33.70	-14.23
782.69	33.82	-13.19
785.67	33.90	-13.11
801.98	34.35	-14.89
816.65	34.76	-13.92
832.37	35.19	-14.47
840.57	35.41	-13.81

Appendices

Appendix 9: Benthic foraminiferal Mg/Ca-derived temperatures corrected for Mg/Ca_{sw} using the approach of Lear *et al.* (2015) from *Oridorsalis umbonatus* at ODP Site 925. Age calibrated to Cande and Kent (1995).

Depth (mbsf)	Age (Ma)	Mg/Ca (mmolmol ⁻¹)	Mg/Ca _{sw} (molmol ⁻¹)	Temperature (°C)
746.45	32.83	1.97	2.15	10.04
747.50	32.85	1.77	2.15	9.05
748.07	32.87	2.12	2.15	10.71
748.73	32.89	2.17	2.15	10.92
750.22	32.93	2.32	2.15	11.54
753.01	33.01	1.94	2.15	9.90
757.13	33.12	2.36	2.15	11.70
758.91	33.17	2.36	2.15	11.70
760.37	33.21	2.10	2.15	10.63
761.84	33.25	2.32	2.15	11.55
763.53	33.30	1.97	2.15	10.05
764.64	33.33	2.18	2.14	10.98
768.26	33.43	2.02	2.14	10.28
769.75	33.47	1.93	2.14	9.86
771.21	33.51	1.82	2.14	9.33
776.62	33.66	2.24	2.14	11.24
778.17	33.70	2.18	2.14	10.99
779.67	33.74	2.27	2.14	11.36
781.17	33.78	2.01	2.14	10.24
782.69	33.82	2.15	2.14	10.86
784.17	33.86	1.93	2.13	9.87
785.88	33.91	2.26	2.13	11.32
787.87	33.96	1.90	2.13	9.73
790.87	34.05	2.20	2.13	11.08
792.72	34.10	2.04	2.13	10.39
793.87	34.13	1.80	2.13	9.24
798.02	34.24	1.97	2.13	10.07
803.47	34.39	2.08	2.12	10.57
805.57	34.45	2.20	2.12	11.09
807.06	34.49	2.13	2.12	10.80
810.06	34.57	2.37	2.12	11.78
811.41	34.61	2.32	2.12	11.58
813.71	34.68	2.28	2.12	11.42
814.40	34.69	2.05	2.12	10.45
815.16	34.71	2.24	2.12	11.26
816.65	34.76	2.21	2.12	11.14
819.67	34.84	2.33	2.11	11.63
821.56	34.89	1.87	2.11	9.61
824.13	34.96	1.83	2.11	9.42
829.39	35.11	2.32	2.11	11.60
830.88	35.15	2.19	2.11	11.07

Appendices

832.37	35.19	2.02	2.11	10.33
834.56	35.25	2.42	2.11	11.99
836.08	35.29	2.35	2.11	11.72
839.08	35.37	2.39	2.10	11.88
840.57	35.41	2.29	2.10	11.48
844.19	35.51	2.42	2.10	11.99
847.15	35.59	1.97	2.10	10.11
850.15	35.68	2.28	2.10	11.45

Appendices

Appendix 10: Benthic foraminiferal Mg/Ca-derived temperatures corrected for Mg/Ca_{sw} using the approach of Hines *et al.* (2017) from *Cibicidoides havanensis* at ODP Site 925. Age calibrated to Cande and Kent (1995).

Depth (mbsf)	Age (Ma)	Mg/Ca (mmolmol ⁻¹)	Mg/Ca _{sw} (molmol ⁻¹)	Temperature (°C)
746.45	32.83	1.97	2.15	10.04
747.50	32.85	1.77	2.15	9.05
748.07	32.87	2.12	2.15	10.71
748.73	32.89	2.17	2.15	10.92
750.22	32.93	2.32	2.15	11.54
753.01	33.01	1.94	2.15	9.90
757.13	33.12	2.36	2.15	11.70
758.91	33.17	2.36	2.15	11.70
760.37	33.21	2.10	2.15	10.63
761.84	33.25	2.32	2.15	11.55
763.53	33.30	1.97	2.15	10.05
764.64	33.33	2.18	2.14	10.98
768.26	33.43	2.02	2.14	10.28
769.75	33.47	1.93	2.14	9.86
771.21	33.51	1.82	2.14	9.33
776.62	33.66	2.24	2.14	11.24
778.17	33.70	2.18	2.14	10.99
779.67	33.74	2.27	2.14	11.36
781.17	33.78	2.01	2.14	10.24
782.69	33.82	2.15	2.14	10.86
784.17	33.86	1.93	2.13	9.87
785.88	33.91	2.26	2.13	11.32
787.87	33.96	1.90	2.13	9.73
790.87	34.05	2.20	2.13	11.08
792.72	34.10	2.04	2.13	10.39
793.87	34.13	1.80	2.13	9.24
798.02	34.24	1.97	2.13	10.07
803.47	34.39	2.08	2.12	10.57
805.57	34.45	2.20	2.12	11.09
807.06	34.49	2.13	2.12	10.80
810.06	34.57	2.37	2.12	11.78
811.41	34.61	2.32	2.12	11.58
813.71	34.68	2.28	2.12	11.42
814.40	34.69	2.05	2.12	10.45
815.16	34.71	2.24	2.12	11.26
816.65	34.76	2.21	2.12	11.14
819.67	34.84	2.33	2.11	11.63
821.56	34.89	1.87	2.11	9.61
824.13	34.96	1.83	2.11	9.42
829.39	35.11	2.32	2.11	11.60

Appendices

830.88	35.15	2.19	2.11	11.07
832.37	35.19	2.02	2.11	10.33
834.56	35.25	2.42	2.11	11.99
836.08	35.29	2.35	2.11	11.72
839.08	35.37	2.39	2.10	11.88
840.57	35.41	2.29	2.10	11.48
844.19	35.51	2.42	2.10	11.99
847.15	35.59	1.97	2.10	10.11
850.15	35.68	2.28	2.10	11.45

Appendices

Appendix 11: Benthic foraminiferal stable isotope from *Oridorsalis umbonatus* at ODP Site 1263. Age calibrated to Cande and Kent (1995).

Depth (mbsf)	Age (Ma)	$\delta^{13}\text{C}$ (VPDB)	$\delta^{18}\text{O}$ (VPDB)
69.60	31.89	-0.06	2.37
70.61	32.02	-0.45	1.87
71.61	32.15	0.06	2.16
73.61	32.41	0.25	2.50
74.61	32.55	0.28	2.45
75.62	32.68	0.04	2.15
76.61	32.82	0.50	2.64
77.62	32.95	0.29	2.47
79.09	33.16	0.22	2.38
80.11	33.30	0.54	2.40
81.92	33.55	0.20	2.22
83.12	33.72	0.08	2.00
84.33	33.90	0.10	1.77
85.10	34.01	0.24	2.04
89.11	34.60	-0.06	1.60
89.90	34.72	-0.29	1.53
90.31	34.79	-0.09	1.64

Appendices

Appendix 12: ϵNd from fossil fish teeth at ODP Site 1263. Age calibrated to Cande and Kent (1995).

Depth (mbsf)	Age (Ma)	$\epsilon\text{Nd}(t)$
69.60	31.89	-8.66
70.11	31.96	-8.37
70.61	32.02	-8.40
71.11	32.09	-8.82
72.63	32.28	-8.40
73.11	32.35	-8.20
74.12	32.48	-7.99
74.61	32.55	-8.07
75.10	32.61	-8.57
75.62	32.68	-8.06
76.11	32.75	-8.58
76.61	32.82	-8.33
77.11	32.88	-8.24
77.62	32.95	-8.50
78.61	33.09	-8.83
79.09	33.16	-8.58
79.61	33.23	-8.35
80.11	33.30	-8.73
80.41	33.34	-8.68
80.71	33.38	-8.33
81.01	33.42	-8.74
81.33	33.47	-8.67
81.61	33.51	-8.58
81.92	33.55	-8.93
82.21	33.59	-8.55
82.52	33.64	-8.49
82.88	33.69	-8.65
83.12	33.72	-8.73
83.50	33.78	-8.53
84.33	33.90	-8.70
85.61	34.08	-8.61
85.91	34.13	-8.58
86.73	34.25	-8.68
87.11	34.31	-8.22
87.52	34.37	-8.01
88.31	34.48	-7.81
88.71	34.54	-7.64
89.11	34.60	-7.63
89.51	34.66	-7.63
89.90	34.72	-7.75

Appendix 13: Benthic foraminiferal trace element data from *Oridorsalis umbonatus* at ODP Site 756. Age calibrated to Cande and Kent (1995).

Depth (mbsf)	Age (Ma)	Mg/Ca (mmolmol ⁻¹)	Li/Ca (μmolmol ⁻¹)	Sr/Ca (mmolmol ⁻¹)	Cd/Ca (μmolmol ⁻¹)	U/Ca (nmolmol ⁻¹)	Al/Ca (μmolmol ⁻¹)	Mn/Ca (μmolmol ⁻¹)	B/Ca (μmolmol ⁻¹)	Fe/Ca (μmolmol ⁻¹)
113.67	30.94	2.33	12.18	0.83	0.14	17.70	41.67	301.77	37.86	16.17
114.07	31.01	2.41	11.96	0.79	0.15	18.07	5.81	326.91	30.36	15.24
114.26	31.04	2.38	11.96	0.81	0.16	15.58	5.27	314.97	31.65	11.44
114.29	31.05	2.42	11.88	0.81	0.14	15.86	3.14	321.69	32.75	23.20
114.49	31.08	2.59	12.46	0.80	0.15	16.48	17.71	321.47	29.45	13.43
114.69	31.12	2.34	12.27	0.82	0.14	17.45	7.49	303.97	29.34	13.71
115.08	31.19	2.58	12.53	0.83	0.14	13.83	97.03	312.99	50.18	23.76
115.29	31.22	2.59	12.09	0.79	0.18	17.13	16.94	320.85	29.73	15.68
115.49	31.26	2.36	12.10	0.79	0.14	15.29	4.09	299.50	29.39	12.39
115.62	31.28	2.50	11.57	0.80	0.15	15.90	8.27	324.26	34.95	18.06
115.82	31.32	2.50	12.45	0.83	0.14	17.49	22.36	303.70	30.22	16.83
116.02	31.35	2.41	11.98	0.81	0.14	18.60	18.65	293.40	41.79	17.39
116.22	31.39	2.46	12.16	0.81	0.15	15.66	18.57	324.21	28.62	11.19
116.41	31.42	2.60	11.85	0.84	0.16	16.18	9.47	333.47	32.89	14.43
116.62	31.46	2.57	12.22	0.83	0.18	18.13	13.37	339.70	25.70	23.94
117.02	31.53	2.49	12.24	0.84	0.18	20.89	10.83	315.14	32.41	14.30
117.32	31.58	2.52	12.10	0.84	0.18	16.26	13.21	297.10	28.77	12.63
117.52	31.62	2.55	11.76	0.85	0.18	17.95	34.55	307.68	33.98	23.62
117.91	31.68	2.39	12.54	0.89	0.21	16.54	23.48	243.29	38.59	18.46
118.12	31.72	2.44	12.12	0.87	0.18	19.18	16.72	248.54	34.44	16.40
118.33	31.76	2.57	13.06	0.87	0.16	19.46	71.13	228.10	32.32	17.28
118.48	31.78	2.65	13.24	0.89	0.18	21.40	32.81	250.67	33.43	13.96
120.31	33.41	2.40	12.52	0.90	0.18	17.43	10.00	232.45	32.65	13.45
120.41	33.42	2.45	12.22	0.91	0.19	18.13	23.37	232.65	40.44	24.09
120.51	33.43	2.52	11.92	0.91	0.22	19.10	6.31	244.66	31.04	18.61
120.61	33.43	2.53	12.88	0.91	0.20	19.58	60.97	249.20	41.62	21.52

120.81	33.45	2.52	12.70	0.90	0.19	18.87	14.22	259.16	32.88	23.97
120.91	33.46	2.53	12.99	0.93	0.18	20.83	13.52	231.50	37.81	19.22
121.11	33.47	2.49	12.66	0.88	0.21	21.56	9.18	244.79	35.62	18.58
121.21	33.48	2.52	12.85	0.91	0.23	19.99	17.25	233.39	35.77	25.47
121.31	33.49	2.58	12.95	0.92	0.19	21.29	50.61	232.63	35.60	17.50
121.41	33.50	2.52	13.07	0.91	0.19	22.28	27.09	231.46	33.15	18.56
121.51	33.50	2.41	12.51	0.88	0.18	18.48	24.26	214.74	32.62	19.56
121.61	33.51	2.44	12.78	0.89	0.17	20.45	12.70	199.16	33.62	18.33
121.81	33.53	2.49	12.49	0.89	0.39	21.50	14.74	215.96	33.29	18.36
121.91	33.54	2.42	12.22	0.89	0.15	19.24	26.94	219.55	32.48	12.55
122.00	33.54	2.29	12.20	0.93	0.16	20.37	12.84	187.86	59.85	15.51
122.11	33.55	2.37	12.11	0.91	0.16	20.68	9.48	191.89	36.45	15.78
122.21	33.56	2.20	12.02	0.91	0.17	21.83	19.45	209.75	39.37	20.16
122.31	33.57	2.40	11.73	0.89	0.16	20.23	11.68	203.33	36.19	17.60
122.43	33.58	2.62	13.12	0.90	0.15	22.20	67.20	180.18	54.98	297.69
122.52	33.58	2.46	13.01	0.91	0.14	20.13	49.50	204.94	34.89	1068.57
122.72	33.60	2.46	13.06	0.89	0.14	20.47	23.64	222.82	36.51	14.54
122.81	33.61	2.46	12.68	0.87	0.13	19.72	5.23	213.71	36.77	13.85
122.92	33.62	2.36	12.82	0.88	0.13	18.61	37.54	202.36	37.03	12.79
123.03	33.62	2.46	12.34	0.87	0.12	20.78	25.87	223.73	32.01	12.85
123.13	33.63	2.34	12.55	0.87	0.12	18.59	10.44	210.54	36.33	12.73
123.31	33.65	2.22	12.12	0.89	0.10	17.74	6.67	211.79	33.53	12.01
123.41	33.65	2.27	11.70	0.84	0.12	19.78	63.78	263.56	31.40	15.93
123.51	33.66	2.39	12.31	0.86	0.12	17.33	19.70	257.72	32.59	16.05
123.81	33.68	2.51	11.69	0.81	0.12	19.25	11.59	279.25	36.70	15.38
123.90	33.69	2.39	11.79	0.84	0.12	19.57	11.71	272.49	31.18	13.93
124.11	33.71	2.44	11.60	0.80	0.12	19.51	21.21	296.20	34.71	17.31
124.24	33.72	2.37	12.34	0.85	0.12	18.48	8.14	269.41	30.80	14.74
124.33	33.73	2.41	11.91	0.83	0.11	19.11	24.70	275.39	31.04	15.42
124.41	33.73	2.50	12.10	0.84	0.12	15.51	5.61	267.93	28.87	12.35

124.51	33.74	2.49	12.74	0.86	0.11	17.30	71.16	260.46	31.67	14.36
124.61	33.75	2.43	14.12	0.85	0.13	19.72	6.84	260.72	29.96	18.92
124.81	33.76	2.40	13.62	0.86	0.12	15.17	41.40	218.55	56.01	90.83
124.91	33.77	2.31	12.14	0.84	0.11	19.46	26.96	243.76	35.16	15.62
125.01	33.78	2.68	13.89	0.83	0.16	20.65	62.24	245.77	59.79	68.43
125.13	33.79	2.40	12.62	0.88	0.11	17.89	25.16	258.46	40.08	13.85
125.31	33.80	2.26	12.03	0.86	0.10	19.15	13.84	245.72	62.28	17.32
125.31	33.80	2.52	12.14	0.82	0.11	18.51	71.10	249.29	68.93	32.41
125.51	33.82	2.44	12.43	0.83	0.10	17.39	12.56	291.22	30.87	12.97
125.61	33.83	2.47	12.12	0.84	0.10	15.97	12.02	283.55	28.96	14.27
125.71	33.83	2.46	11.96	0.83	0.10	17.28	14.86	282.46	28.07	14.69
125.81	33.84	2.53	12.04	0.83	0.10	17.28	10.25	275.66	29.61	11.81
126.00	33.86	2.21	11.92	0.88	0.09	16.69	10.79	238.36	42.34	21.82
126.11	33.86	2.51	12.56	0.85	0.10	18.77	77.60	285.37	39.21	23.64
126.61	33.90	2.29	11.06	0.87	0.10	16.99	90.02	241.70	101.93	33.76
127.26	33.96	2.33	11.97	0.87	0.09	18.51	116.46	264.39	35.45	16.28
129.81	34.15	2.33	11.70	0.83	0.10	16.78	29.05	267.24	37.61	23.88
131.91	34.32	2.57	12.58	0.86	0.11	16.83	73.15	239.70	111.61	33.05
133.21	34.42	2.40	11.50	0.83	0.13	18.64	42.90	320.06	34.39	17.42
133.96	34.48	2.51	11.69	0.82	0.12	15.84	49.25	293.92	43.46	28.81
136.91	34.71	2.80	11.70	0.84	0.19	16.42	42.81	296.45	49.32	36.92
140.56	35.00	2.60	11.65	0.87	0.21	18.61	13.46	356.26	30.09	17.19
141.08	35.04	2.69	12.34	0.86	0.25	20.84	29.09	357.37	44.49	29.77

Appendix 14: Benthic foraminiferal stable isotope and trace element data from *Cibicidoides havanensis* at ODP Site 756. Age calibrated to Cande and Kent (1995).

Depth (mbsf)	Age (Ma)	$\delta^{13}\text{C}$ (‰VPDB)	$\delta^{18}\text{O}$ (‰VPDB)	Mg/Ca (mmolmol ⁻¹)	Li/Ca (μmolmol ⁻¹)	Sr/Ca (mmolmol ⁻¹)	Cd/Ca (μmolmol ⁻¹)	U/Ca (nmolmol ⁻¹)	Al/Ca (μmolmol ⁻¹)	Mn/Ca (μmolmol ⁻¹)	B/Ca (μmolmol ⁻¹)	Fe/Ca (μmolmol ⁻¹)
113.47	30.90	1.01	1.29	1.51	9.43	0.98	0.13	14.28	10.02	213.25	134.86	10.25
113.67	30.94	0.93	1.20	1.61	11.03	0.97	0.12	13.33	8.22	208.65	140.70	10.14
113.87	30.97	1.08	1.20	1.53	10.89	0.98	0.13	13.33	5.44	221.21	142.86	11.17
114.07	31.01	1.01	1.31	1.57	10.60	0.96	0.14	15.66	11.71	243.96	131.35	9.82
114.29	31.05	0.86	1.11	1.74	11.25	0.96	0.17	15.54	27.12	237.07	137.13	18.76
114.49	31.08	1.04	0.93	1.76	11.39	0.97	0.12	10.99	4.48	255.27	128.04	0.21
114.89	31.15	0.96	1.15	1.68	10.77	0.97	0.15	14.38	11.82	239.22	125.25	16.25
115.08	31.19	1.06	0.91	1.69	11.12	0.93	0.14	12.35	13.89	233.19	120.82	10.33
115.29	31.22	0.98	1.25	1.68	10.82	0.98	0.13	14.77	32.24	207.89	135.62	17.51
115.49	31.26	1.16	1.10	1.62	11.38	0.98	0.12	13.57	6.91	203.56	131.65	9.91
115.62	31.28	1.14	1.25	1.64	11.29	0.96	0.13	13.23	10.14	223.42	134.84	10.37
115.82	31.32	0.98	1.17	1.74	11.25	0.98	0.14	16.22	11.46	214.10	131.18	15.50
116.02	31.35	0.85	0.99	1.74	11.41	0.99	0.13	13.45	15.16	223.47	134.88	12.12
116.22	31.39	0.92	1.11	1.75	11.01	0.98	0.15	13.76	8.63	228.54	129.25	10.54
116.41	31.42	0.79	0.94	1.69	11.19	0.96	0.15	13.35	8.90	242.18	135.26	12.62
116.62	31.46	0.92	1.06	1.69	12.02	0.99	0.15	14.97	24.44	227.11	133.57	10.01
116.82	31.49	0.99	0.96	1.90	11.51	0.98	0.16	14.72	11.90	246.57	131.13	24.61
117.02	31.53	1.07	1.08	1.84	11.16	0.98	0.14	14.27	99.47	222.18	131.95	37.90
117.12	31.54	1.09	1.15	1.78	11.03	0.97	0.16	14.44	12.71	235.61	130.59	16.81
117.32	31.58	0.98	0.97	1.83	10.92	0.99	0.15	15.29	19.58	214.14	138.33	11.47
117.52	31.62	0.99	1.07	1.93	11.09	1.00	0.16	14.19	8.06	219.42	142.86	10.70
117.72	31.65	1.02	1.08	1.77	11.13	1.02	0.17	13.88	39.75	184.83	151.89	26.87
117.91	31.68	0.89	1.16	1.69	11.51	1.02	0.15	13.23	9.11	180.12	141.05	12.17
118.12	31.72	1.07	1.08	1.80	10.68	1.04	0.16	14.54	8.57	180.93	141.30	18.50
118.33	31.76	1.14	1.08	1.70	10.73	1.05	0.14	17.28	14.58	161.92	141.00	9.32
118.48	31.78	1.42	1.16	1.82	10.87	1.03	0.14	16.79	13.46	173.99	140.05	25.13

120.31	33.41	1.17	1.22	1.72	11.78	1.02	0.15	13.93	9.71	188.64	146.49	12.20
120.41	33.42	1.39	1.39	1.94	12.14	0.99	0.15	16.58	12.32	213.56	147.60	14.15
120.51	33.43	1.37	1.08	1.82	12.07	0.97	0.17	17.29	35.79	207.62	142.19	31.78
120.61	33.43	1.26	1.20	1.86	12.17	1.01	0.16	16.65	6.95	204.90	144.73	11.32
120.81	33.45	1.39	1.20	1.86	12.04	0.99	0.15	16.57	16.80	191.36	144.56	15.35
120.91	33.46	1.32	1.23	1.73	12.24	1.00	0.16	16.07	25.00	180.86	147.93	14.51
121.01	33.47	1.41	1.06	1.94	12.23	0.99	0.18	17.30	21.27	175.63	165.35	17.64
121.11	33.47	1.44	1.20	1.89	12.17	1.00	0.15	16.75	16.60	193.59	144.07	13.73
121.21	33.48	1.65	1.47	1.80	12.40	1.00	0.15	16.14	16.52	187.79	148.69	18.79
121.31	33.49	1.52	1.17	1.86	12.31	1.02	0.15	17.36	18.37	185.07	150.38	17.37
121.41	33.50	1.70	1.36	1.88	11.77	1.04	0.14	16.53	10.40	179.35	151.58	13.85
121.51	33.50	1.57	1.41	1.96	11.94	1.08	0.14	14.35	7.65	167.10	156.96	11.02
121.81	33.53	1.73	1.10	1.74	11.07	1.05	0.12	16.37	35.48	153.68	145.01	10.48
121.91	33.54	1.63	1.13	1.88	11.18	1.07	0.13	13.84	38.75	159.50	150.56	11.74
122.11	33.55	1.73	1.06	1.86	12.41	1.06	0.13	15.79	44.93	148.60	178.69	13.84
122.21	33.56	1.66	1.26	1.71	11.58	1.08	0.13	13.89	12.76	143.32	163.18	12.14
122.21	33.56	1.66	1.26	1.69	10.88	1.06	0.12	9.85	10.02	158.63	152.16	10.65
122.31	33.57	1.87	1.45	1.67	13.45	1.03	0.11	13.77	21.07	155.67	161.52	10.39
122.43	33.58	1.93	1.25	1.94	12.99	1.06	0.12	15.74	170.84	171.10	163.83	13.98
122.52	33.58	1.81	1.37	1.61	10.81	1.08	0.11	12.19	32.76	141.77	149.47	11.07
122.61	33.59	1.83	1.41	1.67	11.29	1.08	0.12	15.18	15.54	162.80	153.51	11.61
122.72	33.60	1.81	1.46	1.76	11.64	1.05	0.12	8.51	7.39	163.10	148.02	11.50
122.81	33.61	1.65	1.24	1.86	12.10	1.08	0.10	13.95	13.86	152.15	155.52	14.48
122.92	33.62	1.77	1.30	1.71	11.39	1.06	0.10	15.42	20.02	157.22	146.98	11.54
123.03	33.62	1.45	1.06	1.89	11.42	1.03	0.11	12.98	29.98	167.04	149.25	21.45
123.13	33.63	1.49	0.93	1.54	11.35	1.09	0.13	15.09	21.68	146.74	155.92	14.71
123.31	33.65	1.46	0.92	1.67	11.36	1.06	0.12	15.28	10.95	163.96	153.42	14.64
123.41	33.65	1.61	0.87	1.48	10.28	1.05	0.12	14.65	14.44	158.21	142.33	10.24
123.51	33.66	1.35	0.80	1.91	12.38	1.07	0.10	13.30	22.35	166.15	155.80	20.52
123.71	33.68	1.40	0.49	1.43	10.75	1.08	0.09	11.94	13.34	147.48	147.89	10.68

123.90	33.69	1.33	1.05	1.60	10.87	1.04	0.10	15.27	9.25	181.89	139.35	10.17
124.00	33.70	1.42	0.81	1.59	11.03	1.03	0.10	13.41	20.22	183.40	141.37	13.65
124.11	33.71	1.33	0.81	1.62	10.29	0.99	0.10	12.31	14.40	186.51	130.65	12.72
124.24	33.72	1.30	0.96	1.70	11.39	1.05	0.10	12.52	6.62	166.78	140.47	9.91
124.41	33.73	1.31	0.83	1.72	10.66	1.05	0.10	10.72	30.83	174.08	140.67	18.15
124.61	33.75	1.31	0.99	1.55	10.22	1.05	0.09	13.69	14.05	153.26	140.40	13.93
124.91	33.77	1.27	0.74	1.60	11.34	1.05	0.10	13.71	9.24	167.74	138.80	11.27
125.01	33.78	1.07	0.72	1.72	11.06	1.05	0.09	14.21	12.65	173.47	150.65	12.15
125.13	33.79	1.19	0.82	1.74	10.61	1.04	0.09	13.59	25.35	179.34	134.30	13.85
125.31	33.80	1.35	0.84	1.77	11.48	1.03	0.10	14.82	32.83	166.97	164.64	16.99
125.31	33.80	1.35	0.84	1.66	10.87	1.04	0.10	15.79	12.91	185.64	135.21	10.50
125.41	33.81	1.36	0.67	1.69	10.60	1.05	0.10	14.97	13.74	187.06	138.49	11.72
125.51	33.82	1.39	0.56	1.60	10.33	1.05	0.08	13.13	29.32	179.72	134.08	10.22
126.31	33.88	0.85	0.66	1.53	10.33	1.08	0.09	12.90	7.21	180.00	130.40	25.02
126.61	33.90	0.97	0.46	2.01	10.75	1.12	0.11	15.55	8.48	214.06	102.54	13.29
126.71	33.91	0.98	0.33	1.66	10.01	1.03	0.10	14.70	41.46	192.96	122.42	13.10
126.81	33.92	1.17	0.50	1.54	9.58	1.02	0.09	12.94	20.38	174.42	125.69	11.54
127.01	33.94	1.01	0.48	1.64	10.85	1.01	0.10	13.49	10.05	169.67	140.03	17.45
127.11	33.94	1.00	0.26	1.90	11.29	1.04	0.09	11.22	168.32	198.80	127.19	12.74
127.26	33.96	1.19	0.29	1.66	10.72	1.91	1.12	17.51	19.58	64.23	1011.48	113.12
129.81	34.15	1.06	0.49	1.69	10.19	1.04	0.10	10.84	30.74	185.93	122.73	12.79
130.01	34.17	1.29	0.27	1.70	10.35	1.04	0.11	15.36	22.21	194.71	122.67	24.68
130.22	34.19	1.27	0.62	1.73	10.85	1.06	0.10	14.96	19.30	197.94	131.93	15.86
130.41	34.20	1.14	0.64	1.66	10.28	1.04	0.09	14.67	12.28	193.96	121.75	14.77
130.61	34.22	1.11	0.62	1.63	10.16	1.02	0.09	12.74	5.79	185.30	128.93	11.15
130.80	34.23	1.30	0.62	1.57	10.24	1.03	0.11	14.85	11.01	192.60	131.63	15.81
131.23	34.27	0.98	0.50	1.63	10.35	0.99	0.11	14.26	16.42	209.88	126.84	13.00
131.31	34.27	1.17	0.56	1.70	10.50	1.02	0.11	16.38	20.22	217.26	126.12	13.75
131.50	34.29	0.98	0.29	1.63	10.45	1.01	0.10	14.93	9.78	200.93	129.15	14.74
131.79	34.31	1.35	0.93	1.54	13.07	1.01	0.11	8.76	215.97	185.40	130.79	17.89

131.91	34.32	1.30	0.52	1.73	10.50	1.02	0.11	13.32	16.37	219.21	127.88	16.34
132.11	34.33	0.87	0.31	1.69	10.31	1.05	0.11	16.37	17.35	222.70	127.99	13.69
132.30	34.35	1.15	0.48	1.62	10.40	1.00	0.11	8.71	76.08	202.94	128.68	11.12
132.71	34.38	1.22	0.23	1.61	10.30	1.06	0.11	13.69	18.46	208.97	134.85	16.69
133.21	34.42	1.34	0.76	1.90	10.82	1.03	0.13	16.02	13.28	239.40	122.61	21.69
133.96	34.48	1.28	0.71	1.77	9.87	0.99	0.12	13.74	13.72	232.10	127.33	13.33
134.66	34.53	1.31	0.89	1.84	10.85	1.01	0.13	13.54	23.59	223.09	136.06	18.05
135.41	34.59	1.37	0.69	1.86	10.24	1.03	0.13	11.87	42.80	222.67	128.73	14.18
136.31	34.66	1.40	0.62	1.91	10.36	1.03	0.13	14.77	12.70	218.70	133.47	16.22
136.91	34.71	1.26	0.47	2.25	10.86	1.02	0.13	14.27	33.52	223.11	129.62	13.30

Appendix 15: Benthic foraminiferal trace element data from *Turborotalia ampliapertura* at ODP Site 756. Age calibrated to Cande and Kent (1995).

Depth (mbsf)	Age (Ma)	Mg/Ca (mmolmol ⁻¹)	Li/Ca (μmolmol ⁻¹)	Sr/Ca (mmolmol ⁻¹)	Cd/Ca (μmolmol ⁻¹)	U/Ca (nmolmol ⁻¹)	Al/Ca (μmolmol ⁻¹)	Mn/Ca (μmolmol ⁻¹)	B/Ca (μmolmol ⁻¹)	Fe/Ca (μmolmol ⁻¹)
113.67	30.94	2.49	9.30	0.94	0.19	19.29	68.66	659.80	37.90	42.12
114.26	31.04	2.13	10.87	1.12	0.18	18.41	92.91	493.77	68.43	29.89
114.29	31.05	2.57	9.27	0.94	0.18	17.45	19.63	641.92	33.19	21.00
114.49	31.08	2.59	9.50	0.93	0.23	21.47	13.61	662.17	32.06	17.95
115.08	31.19	2.64	8.35	0.87	0.23	15.76	79.38	634.76	29.82	16.01
115.62	31.28	2.79	9.50	0.93	0.22	18.08	30.01	659.58	38.25	15.89
116.02	31.35	2.66	9.84	0.96	0.23	16.80	35.07	571.12	48.75	24.28
116.22	31.39	2.84	9.54	0.89	0.21	17.64	39.52	688.16	33.68	37.09
117.72	31.65	2.79	10.21	1.08	0.24	32.36	163.21	434.85	51.47	32.53
118.12	31.72	2.64	10.95	1.10	0.22	23.37	40.87	373.30	36.70	16.06
118.33	31.76	2.34	11.10	1.67	6.68	2.54	26.73	40.59	467.33	529.48
120.91	33.46	2.86	11.28	1.13	0.31	16.72	145.64	358.29	130.77	38.68
121.21	33.48	2.85	11.42	1.16	0.24	28.04	50.84	319.15	90.02	41.16
121.31	33.49	2.94	9.78	1.05	0.26	23.69	86.96	362.95	97.43	64.76
122.21	33.56	2.64	11.60	1.21	0.22	27.98	935.16	259.90	62.53	26.52
122.43	33.58	2.70	11.74	1.14	0.21	24.13	285.89	264.93	70.82	27.10
122.61	33.59	2.75	11.28	1.15	0.18	26.11	69.65	250.58	54.70	48.13
127.01	33.94	2.33	10.22	1.16	0.15	21.65	16.26	387.88	37.58	16.66

Appendices

Appendix 16: Benthic foraminiferal Mg/Ca-derived temperatures corrected for Mg/Ca_{sw} using the approach of Lear *et al.* (2015) from *Oridorsalis umbonatus* at ODP Site 756. Age calibrated to Cande and Kent (1995).

Depth (mbsf)	Age (Ma)	Mg/Ca (mmolmol ⁻¹)	Mn-Corrected Mg/Ca (mmolmol ⁻¹)	Mg/Casw (molmol ⁻¹)	Temperature (°C)
113.67	30.94	2.33	2.30	2.19	9.13
114.07	31.01	2.41	2.38	2.19	9.77
114.26	31.04	2.38	2.35	2.19	9.53
114.29	31.05	2.42	2.39	2.19	9.86
114.49	31.08	2.59	2.56	2.19	11.28
114.69	31.12	2.34	2.31	2.19	9.21
115.08	31.19	2.58	2.55	2.19	11.21
115.29	31.22	2.59	2.56	2.19	11.28
115.49	31.26	2.36	2.33	2.18	9.38
115.62	31.28	2.50	2.47	2.18	10.53
115.82	31.32	2.50	2.47	2.18	10.55
116.02	31.35	2.41	2.38	2.18	9.80
116.22	31.39	2.46	2.43	2.18	10.19
116.41	31.42	2.60	2.57	2.18	11.36
116.62	31.46	2.57	2.54	2.18	11.10
117.02	31.53	2.49	2.46	2.18	10.45
117.32	31.58	2.52	2.49	2.18	10.72
117.52	31.62	2.55	2.52	2.18	10.96
117.91	31.68	2.39	2.37	2.18	9.68
118.12	31.72	2.44	2.42	2.18	10.09
118.33	31.76	2.57	2.55	2.17	11.19
118.48	31.78	2.65	2.62	2.17	11.84
120.31	33.41	2.40	2.38	2.14	9.77
120.41	33.42	2.45	2.43	2.14	10.19
120.51	33.43	2.52	2.50	2.14	10.76
120.61	33.43	2.53	2.51	2.14	10.84
120.81	33.45	2.52	2.49	2.14	10.75
120.91	33.46	2.53	2.51	2.14	10.85
121.11	33.47	2.49	2.47	2.14	10.51
121.21	33.48	2.52	2.50	2.14	10.77
121.31	33.49	2.58	2.56	2.14	11.27
121.41	33.50	2.52	2.50	2.14	10.77
121.51	33.50	2.41	2.39	2.14	9.87
121.61	33.51	2.44	2.42	2.14	10.13
121.81	33.53	2.49	2.47	2.14	10.53
121.91	33.54	2.42	2.40	2.14	9.95
122.00	33.54	2.29	2.27	2.14	8.89
122.11	33.55	2.37	2.35	2.14	9.55
122.21	33.56	2.20	2.18	2.14	8.12
122.31	33.57	2.40	2.38	2.14	9.79

Appendices

122.43	33.58	2.62	2.60	2.14	11.65
122.52	33.58	2.46	2.44	2.14	10.29
122.72	33.60	2.46	2.44	2.14	10.28
122.81	33.61	2.46	2.44	2.14	10.28
122.92	33.62	2.36	2.34	2.14	9.46
123.03	33.62	2.46	2.44	2.14	10.28
123.13	33.63	2.34	2.32	2.14	9.29
123.31	33.65	2.22	2.20	2.14	8.28
123.41	33.65	2.27	2.24	2.14	8.66
123.51	33.66	2.39	2.36	2.14	9.66
123.81	33.68	2.51	2.48	2.14	10.65
123.90	33.69	2.39	2.36	2.14	9.65
124.11	33.71	2.44	2.41	2.14	10.05
124.24	33.72	2.37	2.34	2.14	9.49
124.33	33.73	2.41	2.38	2.14	9.82
124.41	33.73	2.50	2.47	2.14	10.57
124.51	33.74	2.49	2.46	2.14	10.50
124.61	33.75	2.43	2.40	2.14	10.00
124.81	33.76	2.40	2.38	2.14	9.78
124.91	33.77	2.31	2.29	2.14	9.01
125.01	33.78	2.68	2.66	2.14	12.10
125.13	33.79	2.40	2.37	2.14	9.75
125.31	33.80	2.26	2.24	2.14	8.59
125.31	33.80	2.52	2.50	2.14	10.76
125.51	33.82	2.44	2.41	2.14	10.05
125.61	33.83	2.47	2.44	2.13	10.31
125.71	33.83	2.46	2.43	2.13	10.23
125.81	33.84	2.53	2.50	2.13	10.82
126.00	33.86	2.21	2.19	2.13	8.18
126.11	33.86	2.51	2.48	2.13	10.64
126.61	33.90	2.29	2.27	2.13	8.84
127.26	33.96	2.33	2.30	2.13	9.16
129.81	34.15	2.33	2.30	2.13	9.15
131.91	34.32	2.57	2.55	2.13	11.18
133.21	34.42	2.40	2.37	2.12	9.69
133.96	34.48	2.51	2.48	2.12	10.64
136.91	34.71	2.80	2.77	2.12	13.05
140.56	35.00	2.60	2.56	2.11	11.33
141.08	35.04	2.69	2.65	2.11	12.09

Appendices

Appendix 17: Benthic foraminiferal Mg/Ca-derived temperatures corrected for Mg/Ca_{sw} using the approach of Hines *et al.* (2017) from *Cibicidoides havanensis* at ODP Site 756. Age calibrated to Cande and Kent (1995).

Depth (mbsf)	Age (Ma)	Mg/Ca (mmolmol ⁻¹)	Mn-Corrected Mg/Ca (mmolmol ⁻¹)	Mg/Casw (molmol ⁻¹)	Temperature (°C)
113.47	30.90	1.51	1.49	2.19	7.42
113.67	30.94	1.61	1.59	2.19	8.02
113.87	30.97	1.53	1.51	2.19	7.54
114.07	31.01	1.57	1.55	2.19	7.76
114.29	31.05	1.74	1.72	2.19	8.73
114.49	31.08	1.76	1.73	2.19	8.82
114.89	31.15	1.68	1.66	2.19	8.40
115.08	31.19	1.69	1.67	2.19	8.46
115.29	31.22	1.68	1.66	2.19	8.42
115.49	31.26	1.62	1.60	2.18	8.09
115.62	31.28	1.64	1.62	2.18	8.19
115.82	31.32	1.74	1.72	2.18	8.74
116.02	31.35	1.74	1.72	2.18	8.74
116.22	31.39	1.75	1.73	2.18	8.79
116.41	31.42	1.69	1.67	2.18	8.46
116.62	31.46	1.69	1.67	2.18	8.47
116.82	31.49	1.90	1.88	2.18	9.55
117.02	31.53	1.84	1.82	2.18	9.27
117.12	31.54	1.78	1.76	2.18	8.95
117.32	31.58	1.83	1.81	2.18	9.22
117.52	31.62	1.93	1.91	2.18	9.71
117.72	31.65	1.77	1.75	2.18	8.93
117.91	31.68	1.69	1.67	2.18	8.50
118.12	31.72	1.80	1.78	2.18	9.09
118.33	31.76	1.70	1.68	2.17	8.57
118.48	31.78	1.82	1.80	2.17	9.19
120.31	33.41	1.72	1.70	2.14	8.70
120.41	33.42	1.94	1.92	2.14	9.81
120.51	33.43	1.82	1.80	2.14	9.22
120.61	33.43	1.86	1.84	2.14	9.42
120.81	33.45	1.86	1.84	2.14	9.43
120.91	33.46	1.73	1.71	2.14	8.76
121.01	33.47	1.94	1.92	2.14	9.83
121.11	33.47	1.89	1.87	2.14	9.58
121.21	33.48	1.80	1.78	2.14	9.13
121.31	33.49	1.86	1.84	2.14	9.43
121.41	33.50	1.88	1.86	2.14	9.54
121.51	33.50	1.96	1.94	2.14	9.93
121.81	33.53	1.74	1.72	2.14	8.83
121.91	33.54	1.88	1.86	2.14	9.55
122.11	33.55	1.86	1.85	2.14	9.45

Appendices

122.21	33.56	1.71	1.70	2.14	8.68
122.21	33.56	1.69	1.65	2.14	8.45
122.31	33.57	1.67	1.92	2.14	9.83
122.43	33.58	1.94	1.60	2.14	8.12
122.52	33.58	1.61	1.65	2.14	8.45
122.61	33.59	1.67	1.74	2.14	8.94
122.72	33.60	1.76	1.84	2.14	9.45
122.81	33.61	1.86	1.69	2.14	8.67
122.92	33.62	1.71	1.87	2.14	9.59
123.03	33.62	1.89	1.53	2.14	7.71
123.13	33.63	1.54	1.65	2.14	8.45
123.31	33.65	1.67	1.46	2.14	7.33
123.41	33.65	1.48	1.89	2.14	9.69
123.51	33.66	1.91	1.42	2.14	7.02
123.71	33.68	1.43	1.58	2.14	8.04
123.90	33.69	1.60	1.57	2.14	7.99
124.00	33.70	1.59	1.60	2.14	8.16
124.11	33.71	1.62	1.68	2.14	8.62
124.24	33.72	1.70	1.70	2.14	8.72
124.41	33.73	1.72	1.53	2.14	7.77
124.61	33.75	1.55	1.58	2.14	8.05
124.91	33.77	1.60	1.70	2.14	8.72
125.01	33.78	1.72	1.72	2.14	8.83
125.13	33.79	1.74	1.75	2.14	8.99
125.31	33.80	1.77	1.64	2.14	8.39
125.31	33.80	1.66	1.67	2.14	8.55
125.41	33.81	1.69	1.58	2.14	8.05
125.51	33.82	1.60	1.51	2.14	7.63
126.31	33.88	1.53	1.99	2.13	10.15
126.61	33.90	2.01	1.64	2.13	8.39
126.71	33.91	1.66	1.52	2.13	7.70
126.81	33.92	1.54	1.62	2.13	8.29
127.01	33.94	1.64	1.88	2.13	9.64
127.11	33.94	1.90	1.65	2.13	8.46
127.26	33.96	1.66	1.67	2.13	8.56
129.81	34.15	1.69	1.68	2.13	8.61
130.01	34.17	1.70	1.71	2.13	8.77
130.22	34.19	1.73	1.64	2.13	8.39
130.41	34.20	1.66	1.61	2.13	8.23
130.61	34.22	1.63	1.55	2.13	7.88
130.80	34.23	1.57	1.61	2.13	8.22
131.23	34.27	1.63	1.68	2.13	8.60
131.31	34.27	1.70	1.61	2.13	8.22
131.50	34.29	1.63	1.52	2.13	7.70
131.79	34.31	1.54	1.71	2.13	8.77
131.91	34.32	1.73	1.67	2.13	8.55

Appendices

132.11	34.33	1.69	1.60	2.13	8.16
132.30	34.35	1.62	1.59	2.12	8.10
132.71	34.38	1.61	1.88	2.12	9.63
133.21	34.42	1.90	1.75	2.12	8.97
133.96	34.48	1.77	1.82	2.12	9.34
134.66	34.53	1.84	1.84	2.12	9.44
135.41	34.59	1.86	1.89	2.12	9.69
136.31	34.66	1.91	2.23	2.12	11.21

Appendices

Appendix 18: Benthic foraminiferal Mg/Ca-derived temperatures corrected for Mg/Ca_{sw} using the approach of Hines *et al.* (2017) from *Turborotalia ampliapertura* at ODP Site 756. Age calibrated to Cande and Kent (1995).

Depth (mbsf)	Age (Ma)	Mg/Ca (mmolmol ⁻¹)	Mn-Corrected Mg/Ca (mmolmol ⁻¹)	Mg/Casw (molmol ⁻¹)	Temperature (°C)
113.67	30.94	2.49	2.42	2.19	22.51
114.26	31.04	2.13	2.08	2.19	20.81
114.29	31.05	2.57	2.51	2.19	22.88
114.49	31.08	2.59	2.52	2.19	22.96
115.08	31.19	2.64	2.58	2.19	23.19
115.62	31.28	2.79	2.72	2.18	23.81
116.02	31.35	2.66	2.60	2.18	23.31
116.22	31.39	2.84	2.77	2.18	24.01
117.72	31.65	2.79	2.75	2.18	23.91
118.12	31.72	2.64	2.60	2.18	23.32
118.33	31.76	2.34	2.34	2.17	22.11
120.91	33.46	2.86	2.82	2.14	24.26
121.21	33.48	2.85	2.82	2.14	24.23
121.31	33.49	2.94	2.90	2.14	24.57
122.21	33.56	2.64	2.61	2.14	23.40
122.43	33.58	2.70	2.67	2.14	23.65
122.61	33.59	2.75	2.72	2.14	23.86
127.01	33.94	2.33	2.29	2.13	21.94